Anomalous transport and interaction effects in Weyl metals

E.C.I. van der Wurff

Anomalous transport and interaction effects in Weyl metals

E.C.I. van der Wurff

PhD thesis, Utrecht University, June 2019

Printed by: ProefschriftMaken.nl

ISBN: 978-94-6380-394-6

About the cover: reproduction of the painting "*Doppelzelt*, 1923, 114", by Swiss-German artist Paul Klee. The painting resembles two tilted Weyl cones that are separated in energy-momentum space. The Museum Collection Rosengart, Lucerne (Switzerland) is gratefully acknowledged for providing a high-resolution photograph of the painting and giving the permission to use the painting as a cover. Cover design by Bastiaan Schravendeel.

Anomalous transport and interaction effects in Weyl metals

Anomaal transport en interactie-effecten in Weyl metalen

(met een samenvatting in het Nederlands)

Proefschrift

ter verkrijging van de graad van doctor aan de Universiteit Utrecht op gezag van de rector magnificus, prof. dr. H.R.B.M. Kummeling, ingevolge het besluit van het college voor promoties in het openbaar te verdedigen op maandag 24 juni 2019 des middags te 4.15 uur

door

Erik Christian Ingrid van der Wurff

geboren op 23 augustus 1991 te Maastricht

Promotor: prof. dr. ir. H.T.C. Stoof

Dit werk maakt deel uit van het onderzoeksprogramma van de Stichting voor Fundamenteel Onderzoek der Materie (FOM), die deel uitmaakt van de Nederlandse Organisatie voor Wetenschappelijk Onderzoek (NWO).

Contents

Preface

> *"Hay muchas personas que tienen talento y ganas, y muchas de ellas nunca llegan a nada. Ése es sólo el principio para hacer cualquier cosa en la vida. El talento natural es como la fuerza de un atleta. Se puede nacer con más o menos facultades, pero nadie llega a ser un atleta sencillamente porque ha nacido alto o fuerte o rápido. Lo que hace al atleta, o al artista, es el trabajo, el oficio y la técnica. La inteligencia con la que naces es simplemente munición. Para llegar a hacer algo con ella es necesario que transformes tu mente en una arma de precisión."*
>
> – Carlos Ruiz Zafón, *El juego del ángel*

This thesis is the result of four years of research, done at the Institute for Theoretical Physics of Utrecht University under the supervision of prof. dr. ir. Henk Stoof. Although part of the research was aimed at Bose-Einstein condensates of photons, we focus here on our study of Weyl metals instead.

Chapter 1 gives an introduction to the topics discussed in this thesis and ends with an outline of the research presented in the remaining chapters. The results of our research are described in Chapters 2-5. As the title of the thesis suggests, the research is presented in two parts. Chapters 2 and 3 treat anomalous transport properties of Weyl metals with tilted cones, whereas in Chapters 4 and 5 we focus on interaction effects in Weyl metals.

At the end of the thesis the reader will find the bibliography, a Dutch summary for the layman, acknowledgments and some information about the author.

I sincerely hope that the reader learns something from my thesis.

Erik van der Wurff
May 2019, Utrecht

List of publications

This thesis is based on the following publications:

- [1] E.C.I. van der Wurff and H.T.C. Stoof, *Large anomalous magnetic moment in three-dimensional Dirac and Weyl semimetals*,
  Physical Review B **94**, 155118 (2016).

- [2] E.C.I. van der Wurff and H.T.C. Stoof, *Anisotropic chiral magnetic effect from tilted Weyl cones*,
  Physical Review B **96**, 121116 (R) (2017).

- [3] E.C.I. van der Wurff and H.T.C. Stoof, *Magnetovortical and thermoelectric transport in type-I Weyl metals*,
  Submitted, arXiv:1903.10985.

- [4] E.C.I. van der Wurff and A. Cortijo, *Many-body fermionic excitations in Weyl semimetals due to elastic gauge fields*,
  Submitted, arXiv:1905.00908.

Other publications to which the author has contributed:

- [5] E.C.I. van der Wurff, A.-W. de Leeuw, R.A. Duine, and H.T.C. Stoof, *Interaction effects on number fluctuations in a Bose-Einstein condensate of light*,
  Physical Review Letters **113**, 135301 (2014).

- [6] A.-W. de Leeuw, E.C.I. van der Wurff, R.A. Duine, and H.T.C. Stoof, *Phase diffusion in a Bose-Einstein condensate of light*,
  Physical Review A **90**, 043627 (2014).

- [7] A.-W. de Leeuw, E.C.I. van der Wurff, R.A. Duine, D. van Oosten, and H.T.C. Stoof, *Theory for Bose-Einstein condensation of light in nanofabricated semiconductor microcavities*,
  Physical Review A **94**, 013615 (2016).

Popular-scientific articles by the author:

1 Introduction

The American physicist Richard Feynman once famously wrote that if, by some catastrophic event, all scientific knowledge were to be destroyed, he would choose the following sentence to be passed on to the next generation: "*All things are made of atoms - little particles that move around in perpetual motion, attracting each other when they are a little distance apart, but repelling upon being squeezed into one another.*"[9]. The importance of this so-called *atomic hypothesis* is hard to overstate: a large part of our prevailing knowledge of the world surrounding us is based on it. One could even argue that, roughly speaking, the atomic hypothesis divides current-day research in physics into two main directions: high-energy, or elementary-particle, physics and low-energy, or condensed-matter, physics.

On the one hand, particle physics takes the reductionist route and tries to answer the question of what the atom itself consists and how those constituent particles interact among themselves. At the time that Feynman made the case for the atomic hypothesis it was already an established fact that the atom consisted of electrons, protons and neutrons. In the decades after, it became increasingly clear that of these three types of particles only the electron is a fundamental, indivisible particle, whereas the proton and neutron consist of quarks.[a]

Condensed-matter physics, on the other hand, is devoted to understanding the behavior of large collections of atoms. When a collection of atoms is brought close enough together, the interactions between atoms become typically strong enough such that a solid-state material is formed in which the atoms are neatly arranged in a periodic lattice. Depending on the type of atoms and the amount of available electrons, such a material can be a good conductor (metal) or a poor conductor (insulator). Understanding the fundamental reasons for this difference was a great triumph of twentieth-century

[a] String theory speculates that all fundamental particles, also the electron, are tiny, vibrating strings. Up until now, no experimental evidence for this idea has been found.

physics.

Even though these two research directions have different aims, they frequently interact with each other through the exchange of conceptual ideas and computational techniques [10]. Richard Feynman himself, for instance, contributed a great amount to both directions of research. This thesis is no exception to this fact and centers around electrons in a solid-state material that resemble the massless Weyl fermions known from particle physics.

In the next section we discuss this puzzling claim, thereby introducing the physical system of interest of this thesis: *Weyl metals*. Subsequently, we consecutively introduce the other parts of the title of this thesis, i.e., *anomalous transport* (Section 1.2) and *interaction effects* (Section 1.3) in said Weyl metals. Finally, we give an outline of the rest of the thesis in Section 1.4.

1.1 Weyl metals

With the development of quantum mechanics in the roaring twenties came the realization that at the quantum scale, elementary particles sometimes behave as if they were waves. Indeed, the Schrödinger equation for a non-relativistic electron in a vacuum of volume V is solved by plane waves of the form $\Psi(\boldsymbol{x}) = e^{i\boldsymbol{k}\cdot\boldsymbol{x}}/\sqrt{V}$. The wavevector $\boldsymbol{k}$ determines the energy of such a free electron via the dispersion relation $\varepsilon_{\boldsymbol{k}}^{\text{free}} = \hbar^2|\boldsymbol{k}|^2/2m_e$, with m_e the (rest) mass of the electron.

1.1.1 Quasiparticles in solid-state physics

The wave nature of electrons led the Swiss physicist Felix Bloch to ask the following question in 1928: what happens to the wavefunction of an electron when it is subjected to a periodic potential, as is the case for the electrons roaming around in the periodic potential landscape enforced by the atoms in a solid-state lattice? The answer to this question is given by what is nowadays known as *Bloch's theorem*. This theorem states that the wavefunction of an electron in a periodic potential can be written as $\Psi_{n\boldsymbol{k}}(\boldsymbol{x}) = u_{n\boldsymbol{k}}(\boldsymbol{x})e^{i\boldsymbol{k}\cdot\boldsymbol{x}}$ with n a discrete index and $\hbar\boldsymbol{k}$ the so-called crystal momentum [11].[b] The function $u_{n\boldsymbol{k}}(\boldsymbol{x})$ encodes the periodicity of the un-

[b] In fact, Bloch's theorem only holds for lattices without imperfections and impurities.

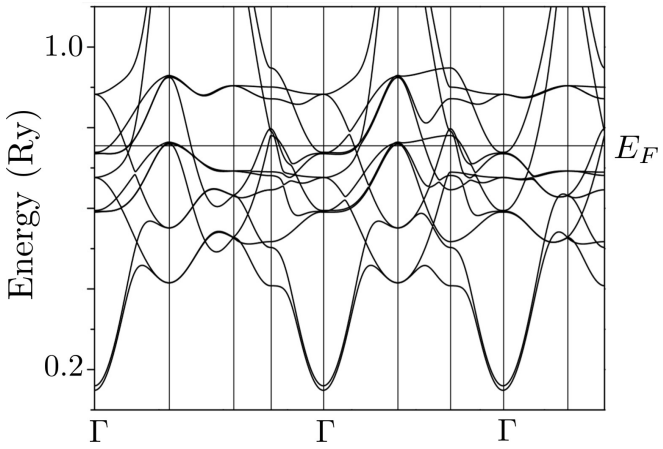

Figure 1.1: Electronic band structure of ferromagnetic bcc Fe (iron) along high-symmetry lines in the Brillouin zone, with high-symmetry points indicated by vertical lines. The energy is given in units of Ry, with 1 Ry $\simeq$ 13.6 eV. The Γ-point is the center of the Brillouin zone ($\boldsymbol{k} = \boldsymbol{0}$). Figure adapted from Ref. [12].

derlying lattice, i.e., $u_{n\boldsymbol{k}}(\boldsymbol{x}) = u_{n\boldsymbol{k}}(\boldsymbol{x} + \boldsymbol{a})$, with $\boldsymbol{a}$ the vector that translates between lattice points.

Using Bloch's theorem to solve Schrödinger's equation in a weak periodic potential leads to periodicity in momentum space and shows that the electrons destructively interfere such that there are only solutions to the Schrödinger equation for certain ranges of energies, called bands. These bands are labeled by the index n introduced in Bloch's theorem. The occurence of bands should be contrasted to the free case, where any energy is allowed, and ultimately explains the difference between metals, semiconductors and insulators. Knowing the band structure is therefore of paramount importance to understand the properties of any solid-state material. Nowadays, advanced numerical techniques like density functional theory can very accurately compute the complicated band structure of any solid-state material. A typical band structure obtained using such techniques is displayed in Fig. 1.1 for Fe (iron).

Closer inspection of the band around the Fermi energy in Fig. 1.1 shows that near the Γ-point ($\boldsymbol{k} = \boldsymbol{0}$), it looks very much like the quadratic dispersion of a free nonrelativistic electron. As it turns out, very often the

electrons in a certain band can be described by the effective dispersion $\varepsilon_{\boldsymbol{k}} = \hbar^2|\boldsymbol{k}|^2/2m^*$, with m^* the so-called effective mass that typically takes on values ranging from $m_e/10$ up to $10m_e$.[c] With the introduction of this effective mass we have introduced the concept of a *quasiparticle*. That is to say, an electron in a solid-state material behaves, due to its interactions with the environment, as if it were a heavier or lighter fermion.[d]

The idea of quasiparticles has proven to be extremely versatile in physics and a whole range of quasiparticles has been introduced over time. Another fermionic example is the hole quasiparticle, which can be assigned to concave bands and represents the absence of an electron. Besides these fermionic examples, there are also bosonic quasiparticles, although they are more commonly referred to as *collective excitations*. Prominent examples of collective excitations are plasmons and phonons, which are quantized plasma and lattice vibrations, respectively. We return to both of these in Section 1.3.

1.1.2 Massless particles

Now we might wonder if also massless fermionic quasiparticles can exist in a solid-state material. But what characterizes a massless fermion? From particle physics we know that relativistic spin-1/2 fermions with mass m obey the Dirac equation [16]

$$-\big(i\hbar c\gamma^\mu\partial_\mu + mc^2\big)\psi(x) = 0, \tag{1.1}$$

where c is the speed of light, $\psi(x)$ a four-component spinor, $\partial_\mu = (c^{-1}\partial_t, \boldsymbol{\nabla})$, and γ^μ are the gamma matrices.[e] If we now take the mass to zero, the Dirac

[c] Heavy fermion materials have electrons with an effective mass of up to a thousand times the electron rest mass [13]. These types of materials are strongly correlated and we will not consider them here.

[d] The idea of quasiparticles was put on a firm footing with the development of *Fermi liquid theory*, which was first proposed by Russian physicist Lev Landau in 1956 [14]. Soon after, his colleagues Abrikosov and Khalatnikov used the mathematical toolbox of quantum many-body physics that was developed in the decades prior to show that in most materials, the lifetime of said quasiparticles becomes large at low enough energies, thereby warranting the name quasi*particles* in the first place [15].

[e] They obey the Clifford algebra $\gamma^\mu\gamma^\nu + \gamma^\nu\gamma^\mu = 2\eta^{\mu\nu}$, with $\eta^{\mu\nu} = \mathrm{diag}(-1, +1, +1, +1)$ the (mostly-plus) Minkowski metric.

equation simplifies to two decoupled two-by-two equations, reading

$$i\hbar c \begin{pmatrix} 0 & c^{-1}\partial_t + \sigma^j \partial_j \\ -c^{-1}\partial_t + \sigma^j \partial_j & 0 \end{pmatrix} \begin{pmatrix} \psi_-(x) \\ \psi_+(x) \end{pmatrix} = 0, \tag{1.2}$$

where σ^j are the three Pauli matrices and $\psi_\pm(x)$ are two-component spinors.[f] Eq. (1.2) is known as the Weyl equation, after the German mathematician Hermann Weyl [17]. The energy eigenvalues of the Weyl equation are the same for $\psi_\pm(x)$ and form cones of the form $\varepsilon_{\boldsymbol{k}} = \pm\hbar c|\boldsymbol{k}|$, with $\boldsymbol{k}$ the corresponding wavevector. The solutions $\psi_\pm(x)$ differ in the fact that they are eigenstates of the helicity operator $\hat{\boldsymbol{k}}\cdot\boldsymbol{\sigma}/2$ with opposite sign, which is called the chirality. Physically, a positive (negative) chirality means that the spin and momentum of the cone are pointing in the same (opposite) direction for the positive energy states.

The problem of finding massless particles in a solid-state material has thus been reformulated into the question: where can we find a band structure that contains a conduction and valence band that touch at the Fermi energy in a linear fashion? Around such a *band-crossing point* the dispersion relation of the quasiparticles can be linearized, thereby mimicking a massless particle with a certain chirality.

1.1.3 Linear band-crossing points

Determining the prerequisites for a band-crossing point is an old problem that was solved in the early days of quantum mechanics and band theory [18, 19]. The reasoning is as follows. Using the fact that the three Pauli matrices and the unit matrix σ^0 form a basis for all two-by-two matrices, any two-band Hamiltonian can be written as

$$\mathcal{H}(\boldsymbol{k}) = B_0(\boldsymbol{k})\sigma^0 + B_j(\boldsymbol{k})\sigma^j \equiv B_\mu(\boldsymbol{k})\sigma^\mu, \tag{1.3}$$

with $B_\mu(\boldsymbol{k})$ real-valued functions. The eigenvalues of this Hamiltonian are given by $\varepsilon_{\boldsymbol{k}} = B_0(\boldsymbol{k}) \pm \sqrt{B_1(\boldsymbol{k})^2 + B_2(\boldsymbol{k})^2 + B_3(\boldsymbol{k})^2}$. From these eigenvalues it becomes clear that there can only be a band-crossing point $\boldsymbol{k}_{\mathrm{BCP}}$ when the three requirements $B_i(\boldsymbol{k}_{\mathrm{BCP}}) = 0$ are met. In a three-dimensional Brillouin

[f] In going from Eq. (1.1) to Eq. (1.2), we used the representation $\gamma^0 = i\sigma^y \otimes \mathbb{1}_2$ and $\gamma^j = \sigma^x \otimes \sigma^j$, which we use throughout the whole thesis.

zone the wavenumber $\boldsymbol{k}$ has three components, such that this condition is met at the intersection of three planes, which can happen at generic points in the Brillouin zone. Such band-crossing points are called *accidental* degeneracies [20]. In lower dimensions accidental degeneracies cannot exist because the wavenumber $\boldsymbol{k}$ only has two components. Therefore, additional symmetries are necessary to enforce so-called *essential* band-crossings at high-symmetry points in the Brillouin zone [21].

Historically, it was this last type of degeneracies that was discussed in a concrete material for the first time. Already in 1947, the Canadian physicist Philip Wallace used a tight-binding model to compute the band structure of a single, two-dimensional layer of graphite, which we today know as *graphene* [22]. Around the Fermi level, he found linearly dispersing quasiparticles with energy-dispersion relation $\varepsilon_{\boldsymbol{k}} = \hbar v_F |\boldsymbol{k}|$, with v_F the Fermi velocity that is three hundred times smaller than the speed of light. The lattice of graphene consists of two superimposed inequivalent triangular sublattices, yielding a hexagonal Brillouin zone. It is in fact a combination of reflection symmetry that relates the two sublattices, and a threefold rotational symmetry that enforces the Dirac cones to be at the so-called K and K'-corners of the hexagonal Brillouin zone [21]. Despite its theoretical simplicity, it took until 2004 to isolate graphene for the first time. Amazingly, the extraction technique comprised of simply sticking a piece of scotch tape on graphite, pulling it off and repeating this several times [23].

As discussed, three-dimensional materials can have accidental degeneracies at generic points in $\boldsymbol{k}$-space. If they are located around the Fermi level they are nowadays referred to as Weyl semimetals and the corresponding degeneracies as Weyl nodes. In the case of a non-zero chemical potential, we speak of a Weyl metal. The Hamiltonian around such a Weyl node is given in linearized form by[g]

$$\mathcal{H}_\chi(\boldsymbol{k}) = \chi \hbar v_F \boldsymbol{\sigma} \cdot \boldsymbol{k}, \tag{1.4}$$

where we assumed isotropy for simplicity. Note that just like in the case of the Weyl equation from particle physics introduced in Eq. (1.2), we assigned a chirality to the Hamiltonian in Eq. (1.4). Even though the Weyl Hamiltonian looks deceivingly simple, it has many interesting properties and leads to a large amount of interesting physics.

[g] Here we ignore the possibility of a term proportional to σ^0, but we return to this in Section 1.1.8.

1.1.4 Topological protection

One such interesting property is the fact that the Weyl node given by the Hamiltonian in Eq. (1.4) is topologically protected. As explained in the previous section, all Pauli matrices have been exhausted, such that adding a perturbation to the Hamiltonian proportional to any of the Pauli matrices only shifts the location of the Weyl node. In addition, the topology associated with the Hamiltonian is ingrained in its eigenstates $|u_{n\chi\boldsymbol{k}}\rangle$, where n labels the conduction/valence band [24]. To see this, we compute the Berry curvature $\boldsymbol{\Omega}_{n,\chi}(\boldsymbol{k})$ associated with these eigenstates, finding

$$\boldsymbol{\Omega}_{n,\chi}(\boldsymbol{k}) = \partial_{\boldsymbol{k}} \times \langle u_{n\chi\boldsymbol{k}} | i\partial_{\boldsymbol{k}} | u_{n\chi\boldsymbol{k}} \rangle = -\frac{n\chi\boldsymbol{k}}{2|\boldsymbol{k}|^3}. \tag{1.5}$$

The Berry curvature has the form of a monopole with charge χ [25], as can be seen from the identity[h] $\partial_{\boldsymbol{k}} \cdot \boldsymbol{\Omega}_{-,\chi}(\boldsymbol{k}) = 2\pi\chi\delta(\boldsymbol{k})$. The presence of a non-zero Berry curvature with the form of a monopole provides us with valuable information.

First of all, we note from Eq. (1.5) that the sign of the monopole charge is determined by the chirality χ. As the Brillouin zone is periodic (in fact, it is a torus), this means that a single Weyl cone cannot exist in the Brillouin zone. The solution to this conundrum lies in the chirality χ: for every Weyl cone with positive chirality there must be another Weyl cone with negative chirality. In other words, Weyl cones always come in pairs in the Brillouin zone [26]. Only when two Weyl cones are put on top of each other, do the monopoles 'annihilate' and a so-called Dirac cone is formed, which has doubly degenerate eigenstates for each value of $\boldsymbol{k}$ (except at $\boldsymbol{k} = \boldsymbol{0}$, where the degeneracy is fourfold). Such a state of matter is called a three-dimensional Dirac semimetal.

1.1.5 From Dirac to Weyl semimetals

In what circumstances do we have a Dirac semimetal, instead of a Weyl semimetal? Again, the Berry curvature provides the answer. Generically,

[h] For physical observables the appropriate object to consider is $\boldsymbol{\Omega}_{\chi}(\boldsymbol{k}) \equiv \sum_n \boldsymbol{\Omega}_{n,\chi}(\boldsymbol{k}) N_{\mathrm{F}}(\varepsilon_{n\boldsymbol{k}})$, with $N_{\mathrm{F}}(x) = (e^{x/k_BT}+1)^{-1}$ the Fermi-Dirac distribution function. At $T = 0$, we have $\boldsymbol{\Omega}_{\chi}(\boldsymbol{k}) = \boldsymbol{\Omega}_{-,\chi}(\boldsymbol{k})$ because the conduction band does not participate in the sum.

the Berry curvature obeys $\boldsymbol{\Omega}_n(-\boldsymbol{k}) = \boldsymbol{\Omega}_n(\boldsymbol{k})$ in the presence of inversion symmetry (IS) and $\boldsymbol{\Omega}_n(-\boldsymbol{k}) = -\boldsymbol{\Omega}_n(\boldsymbol{k})$ when time-reversal symmetry (TRS) is present [27]. If both these symmetries are present, the Berry curvature must be zero. Thus, the fact that the Berry curvature is non-zero for the low-energy Hamiltonian in Eq. (1.4) tells us that it has emerged from a microscopic model which either breaks time-reversal symmetry (TRS), or inversion symmetry (IS). We can turn this reasoning around and say that pairs of Weyl cones emerge from breaking either TRS or IS in a Dirac semimetal. In field-theoretical language[i], this can be achieved by supplementing the free, massless Dirac Lagrangian $\mathcal{L} = -i\hbar c\psi^\dagger(x)\gamma^0\gamma^\mu\partial_\mu\psi(x)$ with a vector b_μ as follows [30]

$$\mathcal{L} = \hbar c\psi^\dagger(x)\gamma^0\big(-i\gamma^\mu\partial_\mu + b_\mu\gamma^\mu\gamma^5\big)\psi(x), \tag{1.6}$$

where $\gamma^5 \equiv i\gamma^0\gamma^1\gamma^2\gamma^3$ anticommutes with all other gamma matrices. When $b_\mu = (b_0, \mathbf{0})$, the above Lagrangian breaks parity (IS), whereas in the case $b_\mu = (0, \boldsymbol{b})$ it breaks TRS. Replacing c by v_F, the Hamiltonian resulting from a Legendre transformation on Eq. (1.6) is given for one cone with chirality χ by

$$\mathcal{H}_\chi(\boldsymbol{k}) = \chi\hbar v_F b_0\sigma^0 + \hbar v_F\chi\boldsymbol{\sigma}\cdot(\boldsymbol{k} + \chi\boldsymbol{b}), \tag{1.7}$$

which has eigenenergies $\varepsilon_{n\boldsymbol{k}} = \chi\hbar v_F b_0 + n\hbar v_F|\boldsymbol{k} + \chi\boldsymbol{b}|$. Thus, when only TRS is broken the cones with opposite chirality are split by $2\boldsymbol{b}$ in momentum space, while they are split by $2\hbar b_0 v_F$ in energy when only IS is broken. Physically, TRS is broken in materials that are, for instance, doped with nondynamic magnetic impurities, whereas IS is broken when the underlying lattice of the material is not inversion-symmetric.

Finally, it is important to remark that the minimum amount of cones for an inversion-symmetry broken Weyl semimetal is four. The reason is that under time-reversal symmetry both spin and momentum change sign, such that we necessarily go from a cone with a certain chirality to a cone with the same chirality (assuming that the cones are not located at $\boldsymbol{k} = \mathbf{0}$ in the first place). As Weyl cones in a band structure always come in pairs of opposite chirality, this means the minimum amount of Weyl cones is four for an inversion-symmetry broken Weyl semimetal.

[i] In fact, we know that the combination of Charge conjugation, Parity and Time reversal (CPT) is a symmetry of any Lorentz invariant local quantum field theory with a hermitian Hamiltonian, but consequences of its breaking have been studied in the high-energy physics literature with Lagrangians like Eq. (1.6) [28, 29].

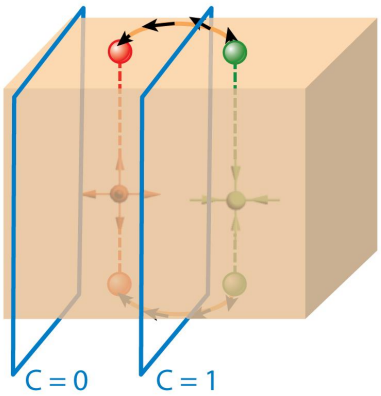

Figure 1.2: Illustration of two Weyl nodes with chirality $\chi = +1$ (red) and $\chi = -1$ (green). The Chern number is only non-zero in between the Weyl nodes and consequently there are surface states that connect into Fermi arcs on the top, bottom, front and back (the latter two are not shown here). Reprinted with permission from Ref. [31].

1.1.6 Fermi arcs

How can we distinguish experimentally between a Dirac and Weyl semimetal? Measuring a linear dispersion relation is not enough, as the previous section showed. Luckily, the non-zero Berry curvature of Weyl cones gives rise to a distinct type of surface states, which we discuss next. Suppose we have a pair of Weyl nodes that are separated in momentum space in the x-direction by an amount $2b_x$. In a plane between the nodes the spectrum is gapped, such that for every plane $A(k_y, k_z)$ at fixed k_x that is perpendicular to the straight line separating the cones, we may define a Chern number $\mathcal{C}_{k_x}$ as follows

$$\mathcal{C}_{k_x} = \frac{1}{2\pi} \sum_n \int_{A(k_y,k_z)} \mathrm{d}^2\boldsymbol{k} \cdot \boldsymbol{\Omega}_{n\chi}(\boldsymbol{k}), \tag{1.8}$$

where the band index n runs over the occupied bands. The Chern number is quantized and non-zero only in between the Weyl nodes. An important consequence of this result is that there are non-trivial surface states on the surfaces surrounding the line separating the Weyl nodes. This in turn is a consequence of the *bulk-boundary correspondence*, which states that on the surface between two materials with different Chern numbers, there is

necessarily a surface state [32]. In particular, vacuum is a trivial insulator with Chern number zero, such that at the boundary of a material with a non-zero Chern number, there must be a surface state. In the present case there is one (chiral) surface state for every value of k_x in between the Weyl nodes, such that in fact there is a so-called *Fermi arc* of surface states, which is depicted in Fig. 1.2. The existence of a Fermi arc is an important result that has no counterpart in high-energy physics and was used as an experimental smoking gun to verify the existence of the first Weyl semimetal, to which we turn next.

1.1.7 Experimental realizations of Weyl semimetals

There are many materials with band structures that display linear band-crossing points. It is, however, like looking for a needle in a haystack to find the ones that are located close to the Fermi level, such that the accessible low-energy excitations are indeed Weyl fermions.[j] The first proposals for materials obeying this criterion emerged in 2011 and were a topological insulator multilayer [35] and the pyrochlore iridate $Y_2Ir_2O_7$ [36]. Nevertheless, neither of these materials was the first solid-state material in which a Weyl semimetal was observed. Instead, band structure calculations showed in 2015 that the transition-metal monophosphides Tantalum Arsenide (TaAs), Tantalum Phosphide (TaP), Niobium Arsenide (NbAs) and Niobium Phosphide (NbP) are Weyl semimetals [37, 38]. The lattices of these materials break inversion symmetry and due to their complicated lattice structure, they host a minimum of twelve pairs of Weyl nodes.

Within months after the theoretical prediction, experiments on all four of these materials showed the existence of topological Fermi arcs on the surface and a conical band dispersion in the bulk [39–44]. The experimental technique used to do so was ARPES, which stands for Angle-Resolved Photoemission Spectroscopy. It entails irradiating a material with photons which excite electrons that are subsequently emitted. The band structure can then be determined from the angular and energy distribution of the emitted electrons. The ARPES measurements of the bulk conical dispersion and Fermi arcs in TaAs are displayed in Fig. 1.3.

[j] For an exhaustive overview of all proposals and experimental realizations of Weyl semimetals, see Refs. [33] and [34], which were vital to the overview presented here.

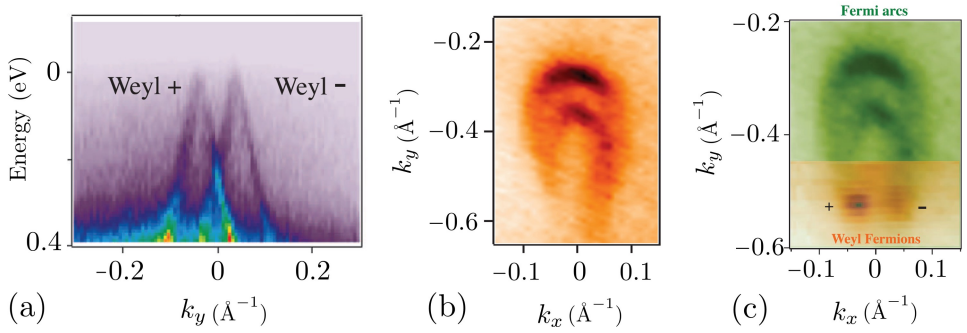

Figure 1.3: Experimental observation of a Weyl semimetal in TaAs. (a) ARPES measurements of the bulk dispersion relation along a fixed plane in the Brillouin zone, demonstrating two Weyl cones. (b) ARPES measurements of the surface Fermi arcs. (c) The first two plotted together to show the termination of the Fermi arc at the bulk Weyl node projections on the surface. Figures adapted from Ref. [39] and reprinted with permission from AAAS.

After the initial experimental realization in the transition-metal monophosphides, many more Weyl semimetals have been realized in different inversion-symmetry breaking materials [34]. Because all these materials break inversion symmetry, they necessarily contain multiples of four cones. The quest for an 'ideal' Weyl semimetal with the minimum of two cones in a system with broken time-reversal symmetry has been on for a while. Experimental observations of such magnetic Weyl semimetals have been reported very recently in the material $EuCd_2As_2$ [45–47].[k]

1.1.8 Does solid-state physics offer more possibilities?

The game of finding quasiparticles that mimic fundamental particles from particle physics does not stop at quasiparticles that behave as if they were Weyl fermions. As Lorentz invariance is not a requirement in a solid-state material, there are many more possibilities for exotic quasiparticles.[l]

[k] For low temperatures this material is a ferromagnet, gapping out its Weyl cones. Above a certain temperature, the local magnetic moments are not ordered but do break TRS.

[l] In fact, there is a whole "zoo of lattice fermions", see Refs. [48, 49] for e.g. hourglass fermions, spin-1 fermions and nodal-line fermions.

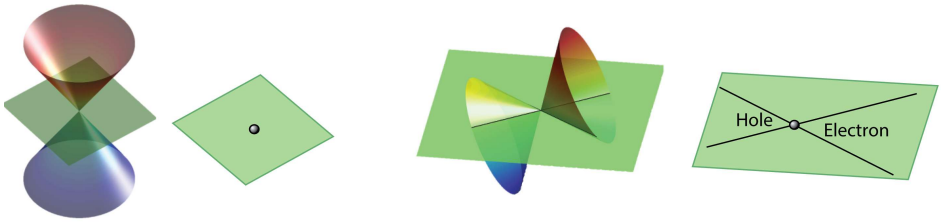

(a) type-I WSM (b) type-II WSM

Figure 1.4: Type-I and type-II Weyl semimetals. In (a) the Fermi surface is a point when the chemical potential is zero and an ellipse when it is non-zero. In (b) the cone is tilted over so much that there are electron and hole pockets. Reprinted (adapted) with permission from Ref. [31].

A simple generalization of Eq. (1.4) that breaks rotational invariance and has a tilted energy-dispersion is

$$\mathcal{H}_\chi(\boldsymbol{k}) = \hbar v_F(\boldsymbol{k}\cdot\boldsymbol{t})\sigma^0 + \chi\hbar v_F\boldsymbol{\sigma}\cdot\boldsymbol{k}, \tag{1.9}$$

with $\boldsymbol{t}$ the tilting direction. As rotational invariance is very often broken in a solid-state material, this Hamiltonian is in fact more natural than the isotropic, non-tilted one. Next to breaking rotational invariance, the tilting vector $\boldsymbol{t}$ breaks time-reversal symmetry. Moreover, when $|\boldsymbol{t}| > 1$ (type-II), the cone is tipped over and the density of states becomes metallic [50], whereas in the case $|\boldsymbol{t}| < 1$ (type-I) the density of state remains semimetallic. Chapters 2 and 3 are devoted to investigating the consequences of such a tilt $|\boldsymbol{t}| < 1$ on various transport phenomena.

1.2 Transport properties of Weyl metals

Now that we have introduced the protagonist of this thesis, (type-I tilted) Weyl metals, it is time to delve a bit deeper into the topics that are of relevance for the research presented in Chapters 2-5. We start by discussing the anomalous transport properties of Weyl metals in this section, which were for a large part the source of the recent excitement surrounding the discovery of Weyl metals. In Chapters 2 and 3 we use the machinery of quantum field theory to compute the response of Weyl cones to external perturbations. In

this section, instead, we apply *semiclassical chiral kinetic theory* to elucidate the main features of anomalous transport in Weyl metals.[m]

Kinetic theory describes the distribution of a large number of particles that frequently collide and obey Newton's laws of motion in between collisions [11]. Our line of approach is *semi*classical kinetic theory, meaning that we employ quantum mechanics in two ways: 1) we incorporate Fermi-Dirac statistics for the electrons and 2) include the effects of the monopole Berry curvature from Eq. (1.5). As the Berry curvature depends on the chirality χ, also the second adjective in the term 'semiclassical chiral kinetic theory' is explained. Thus, we consider Weyl fermions in the band n with position $\boldsymbol{x}$ and wavenumber $\boldsymbol{k}$. The corresponding particle distribution function $f_{n\chi}(\boldsymbol{x}, \boldsymbol{k}, t)$ obeys the Boltzmann transport equation

$$\left[\partial_t + \dot{\boldsymbol{k}} \cdot \partial_{\boldsymbol{k}} + \dot{\boldsymbol{x}} \cdot \partial_{\boldsymbol{x}}\right] f_{n\chi}(\boldsymbol{x}, \boldsymbol{k}, t) = \mathcal{I}_{\text{coll.}}[f_{n\chi}(\boldsymbol{x}, \boldsymbol{k}, t)], \tag{1.10}$$

where $\mathcal{I}_{\text{coll.}}$ is a collision integral that incorporates the effect of collisions among particles. The dynamics of the position and wavenumber is governed by [27]

$$\dot{\boldsymbol{x}}_{n\chi} = \frac{1}{\hbar}\frac{\partial \varepsilon_{n\boldsymbol{k}}}{\partial \boldsymbol{k}} - \dot{\boldsymbol{k}} \times \boldsymbol{\Omega}_{n\chi}(\boldsymbol{k}), \tag{1.11a}$$

$$\hbar\dot{\boldsymbol{k}}_{n\chi} = -e\mathbf{E} - e\dot{\boldsymbol{x}}_{n\chi} \times \mathbf{B}, \tag{1.11b}$$

where we explicitly denoted the band and chirality dependence and a dot stands for differentiation with respect to time. The second equation is simply the change in momentum due to the electric field $\mathbf{E}$ and the Lorentz force[n] due to the magnetic field $\mathbf{B}$, and the first term on the right-hand side of the first equation is the band velocity $\boldsymbol{v}_{n\boldsymbol{k}} \equiv \partial \varepsilon_{n\boldsymbol{k}}/\partial \hbar \boldsymbol{k}$.[o] The second term on the right-hand side in the first equation is called the *anomalous velocity* [52, 53]. Remembering the fact that for a Weyl node the Berry curvature is like a magnetic monopole in momentum space, this term can also be interpreted as a Lorentz force in momentum space, thereby endowing the coupled equations with a more symmetric look. The coupled equations in

[m] For this section the excellent expositions on chiral kinetic theory by Alberto Cortijo and Mikhail Stephanov were indispensable.

[n] The electric charge is defined as $-e$ such that $e > 0$.

[o] In fact, in the presence of a magnetic field the single-particle dispersion relation is modified to $\varepsilon_{n\boldsymbol{k}} - \boldsymbol{m}_{n\chi}(\boldsymbol{k}) \cdot \mathbf{B}$, with $\boldsymbol{m}_{n\chi}(\boldsymbol{k})$ the orbital magnetic moment [51]. We discuss the consequences of this term in more detail in Chapter 3 but ignore it here.

Eq. (1.11) can be decoupled into the form

$$\Delta_{n\chi}(\boldsymbol{k})\dot{\boldsymbol{x}}_{n\chi} = \boldsymbol{v}_{n\boldsymbol{k}} + \frac{e}{\hbar}\mathbf{E}\times\boldsymbol{\Omega}_{n\chi}(\boldsymbol{k}) + \frac{e}{\hbar}\big[\boldsymbol{v}_{n\boldsymbol{k}}\cdot\boldsymbol{\Omega}_{n\chi}(\boldsymbol{k})\big]\mathbf{B}, \tag{1.12a}$$

$$\Delta_{n\chi}(\boldsymbol{k})\hbar\dot{\boldsymbol{k}}_{n\chi} = -e\mathbf{E} - e(\boldsymbol{v}_{n\boldsymbol{k}}\times\mathbf{B}) - \frac{e^2}{\hbar}(\mathbf{E}\cdot\mathbf{B})\boldsymbol{\Omega}_{n\chi}(\boldsymbol{k}), \tag{1.12b}$$

with $\Delta_{n\chi}(\boldsymbol{k}) \equiv \big|1 + e\mathbf{B}\cdot\boldsymbol{\Omega}_{n\chi}(\boldsymbol{k})/\hbar\big|$ the modified density of states which is necessary to satisfy Liouville's theorem in phase space. For our purposes, it suffices to assume that all integrals over $\boldsymbol{k}$ have to be supplemented with this modified density of states. We now discuss the various transport phenomena that follow from Eqs. (1.12).

1.2.1 Anomalous Hall effect

First and foremost, the second term on the right-hand side of Eq. (1.12a) gives rise to the so-called *topological anomalous Hall effect*. To derive this, we consider a Weyl semimetal with broken TRS at the charge neutrality point, i.e., $\mu = 0$, with two nodes that have dispersions $\varepsilon_{n\chi\boldsymbol{k}} = n\hbar v_F|\boldsymbol{k} - \chi\mathbf{b}|$. In addition, we neglect collisions for now, such that up to zeroth order in the external electromagnetic fields, the solution to Eq. (1.10) is given by the Fermi-Dirac distribution. Integrating Eq. (1.12a) over the whole phase space and taking $\mathbf{B} = \mathbf{0}$, we find the current density [54, 55]

$$\begin{aligned}\boldsymbol{J} &= -e\sum_{n,\chi=\pm}\int\frac{\mathrm{d}^3\boldsymbol{k}}{(2\pi)^3}\,\Delta_{n\chi}(\boldsymbol{k})\dot{\boldsymbol{x}}_{n\chi}N_{\mathrm{F}}(\varepsilon_{n\chi\boldsymbol{k}})\\ &= -\frac{e^2}{\hbar}\mathbf{E}\times\sum_{n,\chi=\pm}\int\frac{\mathrm{d}^3\boldsymbol{k}}{(2\pi)^3}\,\boldsymbol{\Omega}_{n\chi}(\boldsymbol{k})N_{\mathrm{F}}(n\hbar v_F|\boldsymbol{k}-\chi\mathbf{b}|)\\ &= -\frac{e^2}{\hbar}\mathbf{E}\times\sum_{\chi=\pm}\chi\int\frac{\mathrm{d}^3\boldsymbol{k}}{(2\pi)^3}\,\frac{\boldsymbol{k}+\chi\mathbf{b}}{2|\boldsymbol{k}+\chi\mathbf{b}|^3} = \frac{e^2\mathbf{b}\times\mathbf{E}}{2\pi^2\hbar},\end{aligned} \tag{1.13}$$

where we took for simplicity $T = 0$, such that only the valence band contributed, and we shifted $\boldsymbol{k}\to\boldsymbol{k}+\chi\mathbf{b}$ in the second step. The computation of the integral in the last step is non-trivial because the integral is not convergent per cone. It only yields a finite answer upon adding the contributions from both cones[p], which is a situation we encounter more often in Chapters

[p] For a clear exposition of how to perform the integral in Eq. (1.13), see Ref. [56].

2 and 3. The found Hall effect is topological in the sense that it is strictly due to the separation of the Weyl nodes and universal because it does not depend on any other material parameters. In fact, we could have foreseen its presence from our discussion on the Fermi arc. As noted there, for every plane in between the Weyl nodes we have a Chern insulator which necessarily means there is a surface state and also an anomalous Hall conductivity.

1.2.2 Chiral magnetic effect and chiral anomaly

The two last terms on the right-hand sides of Eqs. (1.12) are unusual, because they lead to a current density that is in the direction of the magnetic field. To see this, we do a similar calculation as in the previous section, but now we consider a Weyl cone located at $\boldsymbol{k} = \mathbf{0}$ that is doped with a non-zero chemical potential μ_χ. Integrating the last term in Eq. (1.12a) over the whole phase space, we obtain for the current density $\boldsymbol{J}_\chi$ from a single cone

$$\begin{aligned}\boldsymbol{J}_\chi &= -e\sum_{n=\pm}\int\frac{\mathrm{d}^3\boldsymbol{k}}{(2\pi)^3}\,\Delta_{n\chi}(\boldsymbol{k})\dot{\boldsymbol{x}}_{n\chi}N_\mathrm{F}(\varepsilon_{n\chi\boldsymbol{k}}-\mu_\chi)\\ &= -\frac{e^2\mathbf{B}}{\hbar^2}\sum_{n=\pm}\int\frac{\mathrm{d}^3\boldsymbol{k}}{(2\pi)^3}\left[\partial_{\boldsymbol{k}}\varepsilon_{n\boldsymbol{k}}\cdot\boldsymbol{\Omega}_{n\chi}(\boldsymbol{k})\right]N_\mathrm{F}(n\hbar v_F|\boldsymbol{k}|-\mu_\chi)\\ &= \frac{e^2\chi(\mu_\chi-\Lambda)}{4\pi^2\hbar^2}\mathbf{B},\end{aligned}\tag{1.14}$$

where we used the isotropy to go from an integral over $\boldsymbol{k}$ to an integral over $|\boldsymbol{k}|$ and introduced an ultraviolet cut-off $|\boldsymbol{k}| < \Lambda/\hbar v_F$ to render the integral over the valence band finite.[q] We can learn two things from this result. First of all, again we only find a finite result by adding the contributions from both cones. Secondly, if the chemical potential of both cones is the same, the total current density is simply zero. There is, however, a way to give the two cones a different chemical potential.

Such an imbalance can be generated by the last term on the right-hand side of Eq. (1.12b), which is proportional to $\mathbf{E}\cdot\mathbf{B}$. To derive this, we assume spatial homogeneity and denote the corresponding distribution function by $f_{n\chi}(\boldsymbol{k}, t)$. Integrating the Boltzmann equation from Eq. (1.10) over the whole

[q] The integral in Eq. (1.14) can be performed for all temperatures because of the exact identity $\int_0^\infty \mathrm{d}k\left[N_F(k-\mu_\chi/\hbar v_F) - N_F(k+\mu_\chi/\hbar v_F)\right] = \mu_\chi/\hbar v_F$.

phase space, substituting the equation of motion in Eq. (1.12b) and summing over the bands, we find

$$\sum_{n=\pm}\int\frac{\mathrm{d}^3\boldsymbol{k}}{(2\pi)^3}\Delta_{n\chi}(\boldsymbol{k})\partial_t f_{n\chi}(\boldsymbol{k},t)$$
$$=\sum_{n=\pm}\int\frac{\mathrm{d}^3\boldsymbol{k}}{(2\pi)^3}\left[\frac{e}{\hbar}\mathbf{E}+\frac{e}{\hbar}\boldsymbol{v}_{n\boldsymbol{k}}\times\mathbf{B}+\frac{e^2}{\hbar^2}(\mathbf{E}\cdot\mathbf{B})\boldsymbol{\Omega}_{n\chi}(\boldsymbol{k})\right]\cdot\partial_{\boldsymbol{k}}f_{n\chi}(\boldsymbol{k},t), \quad (1.15)$$

where we ignored the collision integral for the time being. The term on the left-hand side is per definition the time-derivative of the density of particles with chirality χ, which we call ρ_χ. At zeroth order in the external electromagnetic fields, $f_{n\chi}(\boldsymbol{k},t)$ is a Fermi-Dirac distribution and thus at $T=0$ we have $\partial_{\boldsymbol{k}}f_{n\chi}(\boldsymbol{k},t)=-n\hat{\boldsymbol{k}}\delta(\mu_\chi/\hbar v_F-n|\boldsymbol{k}|)$. Using this, the first two terms on the second line vanish upon integration, while the third term yields [57, 58]

$$\partial_t\rho_\chi=\frac{\chi e^2(\mathbf{E}\cdot\mathbf{B})}{4\pi^2\hbar^2}. \quad (1.16)$$

This is a surprising result, as it dictates that in the presence of non-orthogonal electromagnetic fields, the number of Weyl fermions with chirality χ is not conserved. Naturally, the total number of particles is conserved, as follows from $\partial_t(\rho_+ + \rho_-)\equiv 0$. For the difference of densities, however, we find

$$\partial_t(\rho_+-\rho_-)=\frac{e^2(\mathbf{E}\cdot\mathbf{B})}{2\pi^2\hbar^2}. \quad (1.17)$$

This non-conservation of chiral particles in external electromagnetic fields is known in the context of high-energy physics as the *chiral anomaly*. It is referred to as an anomaly because the chiral symmetry of the Lagrangian in Eq. (1.6) is broken upon including quantum corrections [59]. In condensed-matter physics the interpretation is less mysterious. In a band structure Weyl cones of opposite chirality are connected. By applying non-orthogonal electric and magnetic fields, particles are 'pumped' from one Weyl cone to another, thereby switching their chirality. Because we ignored the collision integral in deriving Eq. (1.17), charge will accumulate indefinitely in one cone. In reality, particles will scatter from one cone to the other on a time scale τ_5. We phenomenologically include this intervalley scattering by

amending Eq. (1.17) to

$$\partial_t(\rho_+ - \rho_-) = \frac{e^2(\mathbf{E}\cdot\mathbf{B})}{2\pi^2\hbar^2} - \frac{\rho_+ - \rho_-}{\tau_5}, \tag{1.18}$$

which will eventually lead to a steady state where the cone with chirality $\pm$ has chemical potential $\mu_\pm = [\mu^3 \pm 3\hbar v_F^3 e^2 \tau_5 \mathbf{E}\cdot\mathbf{B}/2]^{1/3}$. Using this and going back to Eq. (1.14), we find the famous chiral magnetic effect, i.e.,

$$\boldsymbol{J} = \frac{e^2\mu_5}{2\pi^2\hbar^2}\mathbf{B} \equiv \sigma^{\mathrm{CME}}\mathbf{B}, \tag{1.19}$$

where we defined the so-called chiral chemical potential $\mu_5 \equiv (\mu_+ - \mu_-)/2$. The chiral magnetic effect is special for several reasons. Firstly, it is a current in the direction of the magnetic field, whereas Maxwell's equations only allow for currents and magnetic fields that are perpendicular. Secondly, the chiral magnetic effect constitutes a *dissipationless* current which does not contribute to the entropy production [60].[r] This can be seen from Eq. (1.19) by noting that both the current density and the magnetic field are odd under time-reversal. This means that the conductivity σ^{CME} is even under time-reversal and thus cannot be due to dissipative processes. Finally, note that the current density is odd under inversion, whereas the magnetic field is even. Hence, Eq. (1.19) is only possible because the conductivity is proportional to the chiral chemical potential, which is itself odd under inversion.

An important consequence of the chiral magnetic effect and the chiral anomaly is the phenomenon of Negative Longitudinal MagnetoResistance (NLMR), which is a longitudinal current density of the form $J_z = \sigma_{zz}^{\mathrm{NLMR}} E_z$. For a magnetic field in the z-direction, the corresponding conductivity reads $\sigma_{zz}^{\mathrm{NLMR}} \simeq e^4\tau_5 v_F^3 B_z^2/4\pi^2\hbar\mu^2$ under the assumptions $\mu/k_BT, \mu\tau_5/\hbar \gg 1$ [61]. Hence, this effect constitutes a positive magneto*conductivity*, as the current increases when the magnitude of the externally applied magnetic field is increased. There have been several experimental reports in which negative longitudinal magnetoresistance has been observed in materials hosting Weyl nodes [62–64]. It is tempting to conclude that these experiments are verifications of the chiral anomaly. There are, however, other phenomena that can lead to NLMR. Examples include long-range disorder [65] and *current*

[r] Bart van Wees is gratefully acknowledged for stimulating remarks on this subject.

name	current	conductivity
chiral magnetic effect	$\boldsymbol{J} = \sigma^{\mathrm{CME}}\mathbf{B}$	$\frac{e^2\mu_5}{2\pi^2\hbar^2}$
chiral magnetic energy effect	$\boldsymbol{J}_\varepsilon = \sigma_\varepsilon^{\mathrm{CME}}\mathbf{B}$	$-\frac{e\mu\mu_5}{2\pi^2\hbar^2}$
chiral magnetic separation effect	$\boldsymbol{J}_5 = \sigma_5^{\mathrm{CME}}\mathbf{B}$	$\frac{e^2\mu}{2\pi^2\hbar^2}$
chiral vortical effect	$\boldsymbol{J} = 2\sigma^{\mathrm{CVE}}\boldsymbol{\omega}$	$-\frac{e\mu\mu_5}{2\pi^2\hbar^2 v_F^2}$
chiral vortical energy effect	$\boldsymbol{J}_\varepsilon = 2\sigma_\varepsilon^{\mathrm{CVE}}\boldsymbol{\omega}$	$\frac{\mu_5(3\mu^2+\mu_5^2+\pi^2k_B^2T^2)}{6\pi^2\hbar^2v_F^2}$
chiral vortical separation effect	$\boldsymbol{J}_5 = 2\sigma_5^{\mathrm{CVE}}\boldsymbol{\omega}$	$-\frac{e(3\mu^2+3\mu_5^2+\pi^2k_B^2T^2)}{12\pi^2\hbar^2v_F^2}$

Table 1.1: Table summarizing different dissipationless transport phenomena present in a gas of chiral fermions with temperature T and dispersion relation $\varepsilon_{\boldsymbol{k}} = \hbar v_F|\boldsymbol{k}|$ that flows with a velocity profile $\boldsymbol{v}$ containing vorticity $\boldsymbol{\omega} = (\boldsymbol{\nabla}\times\boldsymbol{v})/2$, and is subjected to an external magnetic field $\mathbf{B}$ [68]. All conductivities displayed here are only valid in the static limit, as we discuss in detail in Chapter 3.

jetting, which is the tendency of a strong magnetic field to focus a current along the field direction [34, 66, 67].

1.2.3 Magnetovortical response

In addition to the chiral magnetic effect, there is in fact a plethora of dissipationless transport phenomena present in a gas of chiral fermions, which we summarize in Table 1.1. First of all, the chiral anomaly also manifests itself in the energy current density $\boldsymbol{J}_\varepsilon$, leading to the so-called *chiral magnetic energy effect*. In addition, rotation of a fluid of chiral fermions leads to a vorticity $\boldsymbol{\omega}$, that also induces a current. This is referred to as the *chiral vortical effect* and again there is a corresponding effect in the energy current. Finally, there are similar effects present in the response of the axial electric current density $\boldsymbol{J}_5$, which is the difference, instead of the sum of the electric currents densities of two cones with opposite chiralities. Interestingly, these dissipationless transport phenomena have played an important role in the study of the quark-gluon plasma at the Large Hadron Collider [68, 69].

In Chapters 2 and 3 we revisit the effects from Table 1.1 in the context

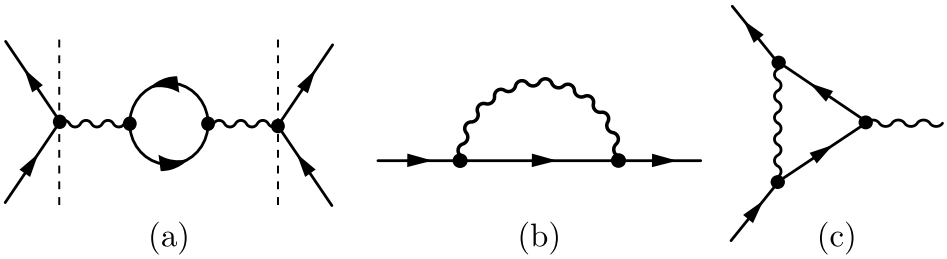

Figure 1.5: One-loop Feynman diagrams for electrons (straight lines) coupling to propagating bosons (whiggly lines). The bosons of interest are photons in Chapter 4 and phonons in Chapter 5. (a) Electron-electron scattering mediated by the one-loop boson propagator, which is the diagram in between the vertical dashed lines. (b) Electronic self-energy. (c) Vertex correction to the electron-boson scattering vertex.

of condensed-matter realizations of Weyl semimetals. We investigate how the tilting of the cones, c.f. Eq. (1.9), affects the dissipationless transport phenomena and discuss the long-wavelength behavior of the corresponding conductivities.

1.3 Interaction effects in Weyl metals

Up to now we have discussed the intriguing properties of noninteracting Weyl metals. In the last part of this chapter we switch gears and focus on interaction effects in Weyl metals, thereby providing the prerequisites for Chapters 4 and 5.

When considering interactions among electrons mediated by propagating bosons, the machinery of quantum field theory tells us that there are three one-loop Feynman diagrams that are of particular interest. These diagrams are displayed in Fig. 1.5. In Chapter 4 we consider the interaction between electrons and photons in Weyl metals and combine the diagrams in Figs. 1.5(a) and (c). In Chapter 5, on the other hand, we discuss the interaction between electrons and phonons and focus on the diagram in Fig. 1.5(b). We proceed by introducing both lines of research in the next two sections.

1.3.1 Screening, plasmons and anomalous magnetic moment

From classical electromagnetism we know that the repulsive force between two electrons in vacuum at a distance $|\boldsymbol{x}|$ is given by Coulomb's law: $\mathbf{F}_e(\boldsymbol{x}) = -\boldsymbol{\nabla} V_c(|\boldsymbol{x}|)$, with $V_c(|\boldsymbol{x}|) = e^2/4\pi\varepsilon_0|\boldsymbol{x}|$ the Coulomb potential in terms of the vacuum permittivity ε_0. In a medium the permittivity is typically enhanced by a dimensionless factor ε_r, which is called the relative permittivity.

With the development of quantum field theory came the realization that the repulsive force between electrons is in fact mediated by photons. As photons are quantum-mechanical propagating degrees of freedom themselves, they are influenced by their coupling to the electrons. To calculate the effect of the electrons on the photons we need to calculate the Feynman diagram depicted in between dashed vertical lines in Fig. 1.5(a). Of particular interest to us is the influence of a non-zero density of electrons, like in a Weyl metal, on the photons.[s] This is captured by the so-called density-density correlator $\Pi^{00}(\omega, |\boldsymbol{q}|)$, which depends on the frequency ω and wavenumber $|\boldsymbol{q}|$ of the photons. A non-zero density-density correlator leads to a complex-valued relative permitivity $\varepsilon_r(\omega, |\boldsymbol{q}|)$ that depends on the frequency and wavenumber. In the so-called Random Phase Approximation (RPA), it is given by[t]

$$\varepsilon_r(\omega, |\boldsymbol{q}|) = 1 - V_c(|\boldsymbol{q}|)\Pi^{00}(\omega, |\boldsymbol{q}|), \tag{1.20}$$

where $V_c(|\boldsymbol{q}|) = e^2/\varepsilon_0|\boldsymbol{q}|^2$ is the Fourier-transformed Coulomb potential. We thus find that the Coulomb potential is modified to

$$V_{\mathrm{sc}}(\omega, |\boldsymbol{q}|) = \frac{V_c(|\boldsymbol{q}|)}{\varepsilon_r(\omega, |\boldsymbol{q}|)} \overset{\substack{|\boldsymbol{q}|\to 0\\ \omega\to 0}}{=} \frac{e^2}{\varepsilon_0}\frac{1}{|\boldsymbol{q}|^2 + \xi^{-2}}, \tag{1.21}$$

where we used that $\Pi^{00}(0, |\boldsymbol{q}| \to 0) = -\varepsilon_0/e^2\xi^2$ in the long-wavelength limit[u], with ξ the *screening length*, which is only non-zero when the chem-

[s] The one-loop correction to the photon propagator is given by the symmetric two-tensor $\Pi^{\mu\nu}(\omega, \boldsymbol{q})$. We focus on the 00-th component because the components $\Pi^{i0}(\omega, \boldsymbol{q})$ are surpressed by a factor of $v_F/c \simeq 1/300$ and the components $\Pi^{ij}(\omega, \boldsymbol{q})$ even by a factor of $(v_F/c)^2$ [70].

[t] In the random phase approximation all bubble diagrams are summed up. This approximation becomes exact in the high-density limit.

[u] As we shall see more often in this thesis, the limits $\omega \to 0$ and $|\boldsymbol{q}| \to 0$ do not commute when considering many-body correlation functions. Here the appropriate limit is to first take the zero-frequency limit.

ical potential of the fermions is non-zero. The modified Coulomb potential $V_{\mathrm{sc}}(\omega, |\boldsymbol{q}|)$ is referred to as the *screened* Coulomb potential, because Fourier transformation back to real space of the long-wavelength limit result in Eq. (1.21) yields $V_{\mathrm{sc}}(|\boldsymbol{x}|) = (e^2/4\pi\varepsilon_0|\boldsymbol{x}|)e^{-|\boldsymbol{x}|/\xi}$. The non-zero density of electrons thus screens the photons on the length scale ξ, thereby endowing them with an effective mass $m_{\mathrm{ph}} \equiv \hbar/\xi c$.

As a side remark, we note that in the limit $\omega \gg v_F|\boldsymbol{q}|$, we find $\Pi^{00}(\omega, |\boldsymbol{q}|) \to \varepsilon_0\omega_p^2/e^2\omega^2$ with ω_p the so-called *plasma frequency*.[v] From Eq. (1.20) we thus see that the relative permittivity contains a real-valued zero at the plasma frequency. As a zero of the relative permittivity corresponds to a pole in the screened Coulomb potential, this frequency corresponds to a bonafide collective, bosonic excitation, which is the *plasmon* that we alluded to at the beginning of this chapter.

The next piece of the puzzle is given by the vertex correction depicted in Fig. 1.5(c). Among other things, the vertex correction gives a contribution to the magnetic moment $\boldsymbol{\mu}$ of the electron. The magnetic moment of the electron determines the amount of torque $\boldsymbol{\tau} = \boldsymbol{\mu} \times \mathbf{B}$ an electron experiences in an external magnetic field. In free space the spin contribution $\boldsymbol{\mu}_s$ to the magnetic moment is given by[w]

$$\boldsymbol{\mu}_s = -g_m \frac{e\hbar}{2m_e}\mathbf{S}, \tag{1.22}$$

with $\mathbf{S} = \hbar\boldsymbol{\sigma}/2$ the spin of the electron. The dimensionless constant g_m follows in the non-interacting case from the Dirac equation in Eq. (1.1), yielding $g_m = 2$. Calculating the contribution from the vertex correction in Fig. 1.5(c) shows that g_m is in fact given by $g_m = 2 + \alpha/\pi$, with $\alpha = e^2/4\pi\varepsilon_0\hbar c \simeq 1/137$ the fine-structure constant. This result was first obtained by the American physicist Julian Schwinger and was very important in the history of quantum electrodynamics (QED).[x] Currently, the value for g_m predicted by advanced QED-calculations and experimental measurements agrees up to nine decimals [73]! This puts QED among the most precise theories ever devised by mankind.

[v] The specific value of the plasma frequency depends on the dispersion relation of the electrons under consideration and the dimensionality of the system, see e.g. Ref. [71].

[w] The total magnetic moment also contains a contribution from the orbital angular momentum $\mathbf{L}$.

[x] For a wonderful account of the history of quantum field theory, see Ref. [72].

In the context of Weyl metals it is interesting to ask how the relation Eq. (1.22) is modified when the electrons are effectively massless. Taking the limit $m_e \to 0$ in Eq. (1.22) leads to a divergence, which is ultimately due to an infrared divergence in the vertex correction in Fig. 1.5(c) when considering massless electrons and photons. A way around this conundrum is by noting that in the presence of a non-zero density of electrons, the photons attain an effective mass m_{ph} as we noted when discussing the screened Coulomb potential in Eq. (1.21). This is the main idea behind Chapter 4, where we calculate the transverse vertex corrections in doped Weyl metals.

1.3.2 Electron-phonon interactions

Another interesting type of interaction to investigate in Weyl metals is the coupling between electrons and phonons. Electron-phonon coupling can have far-reaching consequences. The most prominent example can be found in superconductors, in which the electron-phonon coupling is responsible for the Cooper instability that makes an attractive interaction between electrons possible [74]. There is however, a slightly different type of electron-phonon coupling possible in materials with massless quasiparticles. The reason for this is the fact that Dirac and Weyl semimetals respond to strain as if electromagnetic fields were applied.

A simple way to see this is by comparing the minimal Hamiltonian for a TRS-breaking Weyl semimetal, i.e., $\mathcal{H}(\boldsymbol{k}) = v_F\chi(\hbar\boldsymbol{k} + \chi\hbar\boldsymbol{b})\cdot\boldsymbol{\sigma}$, c.f. Eq. (1.7), to the Hamiltonian of a minimally coupled Weyl node located at $\boldsymbol{k} = \mathbf{0}$, i.e., $\mathcal{H}(\boldsymbol{k}) = v_F\chi(\hbar\boldsymbol{k} + e\mathbf{A})$, with $\mathbf{A}$ the external vector potential. Clearly, the time-reversal symmetry-breaking vector $\boldsymbol{b}$ acts like an axial vector potential that couples with a different sign to the two Weyl nodes with opposite chirality [75]. This analogy becomes more satisfactory if the time-reversal symmetry breaking vector varies smoothly in space and contains a curl, such that we can define an emergent, fictitious pseudo-magnetic field $\mathbf{B}_5 \equiv \hbar(\boldsymbol{\nabla}\times\boldsymbol{b})/e$ [76]. Similarly, we can define a pseudo-electric field $\mathbf{E}_5 = \hbar(\partial_t\boldsymbol{b} - v_F\boldsymbol{\nabla}b_0)/e$.[y]

In order to have pseudo-magnetic fields present, b_μ needs to depend on the position (we omit time dependence from here on). This position dependence can be achieved by applying strain. To illustrate this, we consider a toy-

[y] The pseudo-magnetic field has the same discrete symmetries as the ordinary magnetic field. The pseudo-electric field is odd under both TRS and IS symmetry, whereas the ordinary electric field is only odd under the latter [76].

model for a Weyl semimetal on a cubic lattic, given by the Hamiltonian [75, 76]

$$\mathcal{H}(\boldsymbol{k}) = t_1 \sin(k_x a)\sigma^x + t_1 \sin(k_y a)\sigma^y + t_2\big[\cos(k_z a) - m\big]\sigma^z, \tag{1.23}$$

with $t_{1,2}$ hopping amplitudes and a the lattice spacing. This Hamiltonian has low-energy Weyl nodes when $|m| < 1$, which are located at $\boldsymbol{k}_\pm = (0, 0, \pm \arccos(m)/a)$. The corresponding anisotropic Fermi velocities are $v_x = v_y = at_1/\hbar$ and $v_z = at_2\sqrt{1-m^2}/\hbar$, and the separation between the two nodes is given by $2b_z = 2\arccos(m)/a$.

Applying strain to a material changes the relative orientation and distance between atomic orbitals. In a tight-binding model like the Hamiltonian in Eq. (1.23), this leads to a change in the hopping amplitudes $t_{1,2}$, which are simply a measure for the amount of overlap between atomic orbitals. Applying strain in the z-direction can be accounted for by the replacement [77] $t_2\sigma^z \to t_2(1-u_{zz})\sigma^z$ in Eq. (1.23).[z] In this expression $u_{ij} \equiv (\partial_i u_j + \partial_j u_i)/2$ is the linearized strain tensor in terms of the lattice displacement u_i. In the simple case of a displacement $u_z = z(\Delta L/L)\hat{z}$, corresponding to an elongation or shrinking of the crystal by $\Delta L/L$, we find that the change in distance between the Weyl nodes is $\Delta b_z/b_z \approx -\Delta L/La^2b_z^2$, assuming that $\Delta L/L \ll 1$. This simple example illustrates how applying more intricate types of strain can lead to a non-zero value for $\boldsymbol{\nabla} \times \boldsymbol{b}$.

Having understood how pseudo-electromagnetic fields can emerge in materials hosting massless quasiparticles, we may wonder what their (observable) consequences are. One interesting consequence is the fact that the chiral anomaly from Eq. (1.18) attains a contribution proportional to $\mathbf{E}_5 \cdot \mathbf{B}_5$ [75, 78]. In addition, pseudo-electromagnetic fields lead to Landau levels that are distinct from Landau levels resulting from ordinary electromagnetic fields. In graphene, for instance, a pseudo-magnetic field with a magnitude equivalent to 300 Tesla has been observed by direct observation of its corresponding Landau levels [79].

How does all of this connect to the self-energy diagram in Fig. 1.5(b)? The pseudomagnetic fields can be expressed in terms of the strain tensor

[z] There is in principle also a change in the hopping amplitudes due to torsional strain, which changes the relative orientation of orbitals and is not diagonal in pseudospin space [75]. For simplicity we omit this contribution here, but we do include it in Chapter 5.

u_{ij}, which in turn can be written in terms of the displacement u_i. Quantization of the latter leads to phonons, which in this particular case lead to a different type of coupling between the electrons and the phonons than the usual electron-phonon coupling. By computing the self-energy diagram in Fig. 1.5(b) that results from this unusual coupling, we show in Chapter 5 that it leads to interesting fermionic satellite peaks in Weyl metals.

1.4 Outline

The research in the remainder of this thesis is divided into two parts. The first part focusses on the transport properties of non-interacting Weyl metals under the influence of external perturbations. The second part, on the other hand, centers around interaction effects in Weyl metals.

We start in Chapter 2 by investigating the influence of tilting the Weyl cones on the transport properties due to an externally applied electric and magnetic field. We find that the famous chiral anomaly remains unmodified, whereas transport measurements should reveal a renormalization of the chiral magnetic conductivity due to the tilting of the cones. Moreover, we show that the tilting direction forms a time-reversal symmetry-breaking vector, such that an additional anomalous Hall effect manifests itself.

Next, building upon the work from Chapter 2, we investigate in Chapter 3 how the thermoelectric and magnetovortical transport properties of a Weyl metal are affected by the tilting of the cones. In the case of the off-diagonal thermoelectric response matrix we find that next to an anomalous Hall effect, also an anomalous Nernst and a thermal Hall effect emerge due to the tilting of the cones. For the magnetovortical response matrix, we find that the chiral vortical effects become anisotropic, attaining a component longitudinal and transverse to the tilting direction. The chiral magnetic effects, however, remain isotropic and in the static limit even universal.

Hereafter we switch from non-interacting Weyl fermions to interacting Weyl fermions in the second part of this thesis. In Chapter 4 we calculate the transverse vertex correction in Weyl metals with Coulomb interactions. We show that the screening due to the Coulomb interactions introduces an infrared cut-off that is necessary to avoid a divergence stemming from the massless character of the Weyl quasiparticles. In addition, we show that the resulting magnetic moments are relatively large and discuss a set-up in

which the possible consequences might be detected.

Finally, in Chapter 5 we discuss how straining a Weyl metal leads to an unusual electron-phonon coupling. To investigate its observable consequences, we calculate the electronic self-energy following from this coupling. From this self-energy we compute the corresponding spectral function, which shows the emergence of interesting satellite peaks.

2 Anisotropic chiral magnetic effect from tilted Weyl cones

We determine the antisymmetric current-current response for a pair of (type-I) tilted Weyl cones with opposite chirality. We find that the dynamical chiral magnetic effect depends on the magnitude of the tilt and on the angle between the tilting direction and the wave vector of the magnetic field. Additionally, the chiral magnetic effect is shown to be closely related to the presence of an intrinsic anomalous Hall effect with a current perpendicular to the tilting direction and the electric field. We investigate the nonanalytic long-wavelength limit of the corresponding transport coefficients.[a]

2.1 Introduction

In classical electrodynamics, magnetic fields always induce currents that are perpendicular to the magnetic field direction due to the Lorentz force. However, in quantum electrodynamics, a current can also be generated in the same direction as the magnetic field. This was first realized for massless fermions in particle physics [80, 81]. It is a consequence of the fact that quantum mechanically a magnetic field quenches the kinetic energy perpendicular to its direction and also spin polarizes the lowest Landau level. As a result massless fermions only obtain a drift velocity along the magnetic field with an opposite sign for opposite chiralities. Inducing an imbalance between the two chiral species then gives a net current along the magnetic field direction known now as the chiral magnetic effect (CME).

Massless chiral fermions also occur as low-energy quasiparticles in the recently discovered Weyl (semi)metals [39, 40, 42, 43, 82]. These quasipar-

[a] This chapter is directly based on "E.C.I. van der Wurff and H.T.C. Stoof, *Anisotropic chiral magnetic effect from tilted Weyl cones*, Physical Review B **96**, 121116 (R) (2017)".

ticles do not move at the speed of light, as in elementary-particle physics, but rather at the Fermi velocity. Additionally, the effective Weyl cones with different chirality are in a real material always connected by the full band-structure and hence electrons can be transported from one cone to another by applying both an electric and a magnetic field [55]. In particle physics the same phenomenon occurs due to the breaking of chiral symmetry by quantum corrections. This breaking of chiral symmetry due to the renormalization of ultraviolet divergencies is called a chiral anomaly and causes the difference between the numbers of particles with positive and negative chirality to be no longer conserved [83–85].

The main difference with particle physics is that Lorentz invariance is not enforced in a condensed-matter material. This gives, besides a velocity that is smaller than the speed of light, also the possibility that Weyl nodes are separated in energy-momentum space. Splitting them in the momentum direction gives rise to a topological anomalous Hall effect [55], whereas splitting them in the energy direction is exactly the situation of most interest for the CME [54, 80]. Indirect measurements of the chiral magnetic effect have recently been made by the observation of a negative magnetoresistance [61, 65, 86, 87]. Another interesting possibility is tilting the Weyl cones, meaning that the slope of the dispersion relation is not the same in opposite directions [88, 89]. Materials that exhibit such tilted Weyl cones are of type I if the tilt is relatively small and of type II if the cones are overtilted such that the electron and hole dispersions intersect the energy plane of the Weyl node itself [90–92]. Moreover, the tilt is affected and can even be generated by disorder and interaction effects [1, 93, 94]. It is thus of considerable interest to investigate what such a tilt does to the chiral magnetic conductivity of a Weyl (semi)metal. The chiral magnetic conductivity is in principle a function of the wavenumber and frequency of the applied magnetic field.[b] When calculating the long-wavelength limit, the order of limits is crucial and we need to distinguish the case in which the Weyl nodes are located at the same energy and the case in which they are not [95–98]. Only when the chiral imbalance of the two Weyl nodes is exactly opposite to their energy separation, is there a vanishing current in the static limit [54, 99, 100].

Here, we reconsider these subtleties for a pair of type-I tilted Weyl cones. We first illustrate the short-wavelength physics involved by calculating the

[b] We do not consider a time-dependent chiral imbalance.

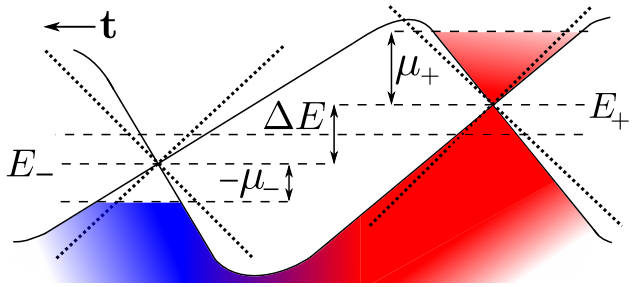

Figure 2.1: Illustration of a band structure with two imbalanced Weyl cones at chiral chemical potentials $\mu_\pm$ and node energies $E_\pm$, both tilted in the same direction $\boldsymbol{t}$.

full frequency and wave-number dependence of the effective CME for a transverse electromagnetic wave propagating along the tilting direction. For arbitrary magnetic field directions we focus on the long-wavelength response. We find that the chiral magnetic conductivity is anisotropic and in general nonuniversal, even though the chiral anomaly is unmodified by the tilt. Our results for the homogeneous and static limit are summarized in Fig. 2.4.

2.2 Current-current response function

We consider a pair of Weyl cones with opposite chiralites $\chi = \pm$ that are doped with chemical potentials $\mu_\pm \equiv \mu \pm \mu_5$, defined with respect to the Weyl nodes, as depicted in Fig. 2.1. The chiral chemical potential μ_5 indicates a chiral population imbalance that can be created by applying an electric field pulse with a component parallel to an already present magnetic field. We also allow the Weyl nodes to be split up in energy, which we denote by $\Delta E \equiv E_+ - E_-$, and we comment on the effect of this later on. The topological anomalous Hall effect, however, is well understood and therefore not discussed throughout the following. Furthermore, we consider for simplicity cones with an isotropic Fermi velocity v_F, which is straightforwardly generalized to the anisotropic case.

Tilting the cones in a direction $\boldsymbol{t}$ can be achieved in two distinct ways. Either we introduce a momentum-dependent chiral chemical potential $\mu_5(\boldsymbol{k}) \equiv \mu_5 - \hbar v_F \boldsymbol{k}\cdot\boldsymbol{t}$, where $\hbar\boldsymbol{k}$ is the momentum, or a momentum-dependent chem-

ical potential $\mu(\boldsymbol{k}) \equiv \mu - \hbar v_F \boldsymbol{k}\cdot\boldsymbol{t}$. Only the latter replacement breaks inversion symmetry [101]. Physically, breaking inversion symmetry corresponds to tilting the two cones in the same direction (c.f. Fig. 2.1), while inversion symmetry is preserved upon tilting the two cones in opposite directions. In this chapter we perform all calculations explicitly in the case that inversion symmetry is broken, and we comment on the other case in our discussion. Hence, the appropriate Hamiltonian reads ($\hbar = 1$)

$$\mathcal{H}(\boldsymbol{k}) = (v_F \boldsymbol{k}\cdot\boldsymbol{\sigma} - \mu_5\sigma^0)\tau^z + (v_F\boldsymbol{k}\cdot\boldsymbol{t} - \mu)\tau^0\sigma^0, \tag{2.1}$$

where $\boldsymbol{\tau}$ are the Pauli matrices acting in orbital space and $\boldsymbol{\sigma}$ in spin space, complemented by the 2×2 unit matrices τ^0 and σ^0. The Hamiltonian has four distinct eigenvalues $\pm\varepsilon_{\boldsymbol{k}} + v_F\boldsymbol{k}\cdot\boldsymbol{t} - \mu_\chi$, with $\varepsilon_{\boldsymbol{k}} \equiv v_F|\boldsymbol{k}|$ the dispersion relation of the massless fermions. Here, we consider type-I (semi)metals, meaning that we restrict ourselves to $0 < t < 1$ for $t = |\boldsymbol{t}|$. For simplicity we consider the two cones to have the same absolute value for the tilt t, but also this is easily generalized.

In order to calculate the response to an externally applied magnetic or electric field, we couple the fermions with charge $-e$ to an external vector potential $\mathbf{A}$ via the minimal coupling prescription $\boldsymbol{k} \to \boldsymbol{k} + e\mathbf{A}$. Next, we perform second-order perturbation theory in the external gauge field to obtain the current-current response function $\Pi^{ij}(\boldsymbol{q},\omega;\boldsymbol{t})$. In the process the subtraction of the two Dirac seas of the cones leads to the elimination of a logarithmic ultra-violet divergence. In terms of the frequency $\omega^+ = \omega + i0$, the antisymmetric part of the retarded current-current response function $\Pi_l(\boldsymbol{q},\omega;\boldsymbol{t}) = \epsilon_{ijl}\Pi^{ij}(\boldsymbol{q},\omega;\boldsymbol{t})/2$ reads[c]

$$\begin{aligned} i\Pi_l(\boldsymbol{q},\omega;\boldsymbol{t}) = \frac{e^2 v_F^2}{2}\sum_{\chi,\sigma,\sigma'=\pm}\chi\int\frac{\mathrm{d}^3\boldsymbol{k}}{(2\pi)^3}F_l^{\sigma\sigma'}(\boldsymbol{k},\boldsymbol{q};\boldsymbol{t}) \\ \times\left[\frac{N_{\mathrm{F}}(\varepsilon_{\boldsymbol{k}} - \sigma\mu_\chi(\boldsymbol{k})) - \sigma\sigma' N_{\mathrm{F}}(\varepsilon_{\boldsymbol{k}+\boldsymbol{q}} - \sigma\mu_\chi(\boldsymbol{k}+\boldsymbol{q}))}{\omega^+ - v_F\boldsymbol{q}\cdot\boldsymbol{t} + \sigma\varepsilon_{\boldsymbol{k}} - \sigma'\varepsilon_{\boldsymbol{k}+\boldsymbol{q}}}\right], \end{aligned} \tag{2.2}$$

[c] The derivation of the antisymmetric part of the current-current response function can be found in Appendix 2.A.1.

where we defined a structure factor $F_l^{\sigma\sigma'}(\boldsymbol{k},\boldsymbol{q};\boldsymbol{t})$ by

$$\boldsymbol{F}^{\sigma\sigma'}(\boldsymbol{k},\boldsymbol{q};\boldsymbol{t}) \equiv \frac{\boldsymbol{k}}{|\boldsymbol{k}|} - \sigma\sigma' \frac{\boldsymbol{k}+\boldsymbol{q}}{|\boldsymbol{k}+\boldsymbol{q}|} - \sigma' \frac{\boldsymbol{q}(\boldsymbol{k}\cdot\boldsymbol{t}) - (\boldsymbol{q}\cdot\boldsymbol{t})\boldsymbol{k}}{|\boldsymbol{k}+\boldsymbol{q}||\boldsymbol{k}|}. \tag{2.3}$$

In Eq. (2.2) we denoted the Fermi-Dirac distribution by $N_{\mathrm{F}}(x) \equiv (e^{\beta x}+1)^{-1}$ with $\beta = (k_B T)^{-1}$. Physically, the sum over χ accounts for the two cones with opposite chirality, whereas the sums over σ and σ' account for the four possibilities for particle-hole pairs in a chiral cone consisting of two touching bands. In the limit $\boldsymbol{t} = \boldsymbol{0}$ the expression in Eq. (2.2) reduces to the well-known result for a three-dimensional chirally doped Weyl semimetal [102]. Including a tilt alters the energy-dispersion relation and yields an additional term in the interaction vertex, resulting in the last term in the structure factor in Eq. (2.3).

The antisymmetric part of the current-current response function in Eq. (2.2) is in general spanned by a linear combination of the vectors $\boldsymbol{q}$ and $\boldsymbol{t}$, i.e., we can decompose it as[d]

$$i\Pi_l(\boldsymbol{q},\omega^+;\boldsymbol{t}) = \sigma^{\mathrm{CME}}(\boldsymbol{q},\omega)q_l + \sigma^{\mathrm{AHE}}(\boldsymbol{q},\omega)\omega t_l. \tag{2.4}$$

As explicitly indicated this gives rise to two distinct effects: a chiral magnetic effect and a tilt-induced planar intrinsic anomalous Hall effect (AHE) [103–105]. The corresponding currents read

$$\boldsymbol{J}^{\mathrm{CME}}(\boldsymbol{q},\omega) = \sigma^{\mathrm{CME}}(\boldsymbol{q},\omega)\mathbf{B}(\boldsymbol{q},\omega), \tag{2.5}$$

$$\boldsymbol{J}^{\mathrm{AHE}}(\boldsymbol{q},\omega) = \sigma^{\mathrm{AHE}}(\boldsymbol{q},\omega)\boldsymbol{t}\times\mathbf{E}(\boldsymbol{q},\omega), \tag{2.6}$$

in terms of the chiral magnetic and anomalous Hall conductivities $\sigma^{\mathrm{CME}}(\boldsymbol{q},\omega)$ and $\sigma^{\mathrm{AHE}}(\boldsymbol{q},\omega)$, respectively. The intimate relation between these two effects is even more clear in relativistic notation, where we have that $\Pi^{\kappa\nu} = i\epsilon^{\kappa\lambda\mu\nu}P_\lambda q_\mu$ and thus $J^\kappa = \Pi^{\kappa\nu}A_\nu = \epsilon^{\kappa\lambda\mu\nu}P_\lambda F_{\mu\nu}/2$, where $F_{\mu\nu}$ is the Faraday tensor and $P^\lambda = (\sigma^{\mathrm{CME}}, \sigma^{\mathrm{AHE}}\boldsymbol{t})$ elegantly combines the two conductivities. Note that the gauge invariance of the result is then also manifest.

In the following, we discuss the tilt dependence of both effects separately.

[d] One could also think of a term of the form $\gamma(\boldsymbol{q},\omega;\boldsymbol{t})(\boldsymbol{q}\times\boldsymbol{t})^l$. However, from Eq. (2.2) we deduce the identity $\Pi_l(\boldsymbol{q},\omega;\boldsymbol{t}) = -\Pi_l(-\boldsymbol{q},\omega;-\boldsymbol{t})$, implying that $\gamma(\boldsymbol{q},\omega;\boldsymbol{t}) = -\gamma(-\boldsymbol{q},\omega;-\boldsymbol{t})$. As $\gamma(\boldsymbol{q},\omega;\boldsymbol{t})$ is a scalar, it must therefore be zero.

In principle, both $\sigma^{\mathrm{CME}}(\boldsymbol{q},\omega)$ and $\sigma^{\mathrm{AHE}}(\boldsymbol{q},\omega)$ depend on the angle between $\boldsymbol{q}$ and $\boldsymbol{t}$. In order to make analytic progress, however, we specialize to zero temperature and first consider as an illustrative example the propagation of a purely transverse electromagnetic wave (light) with $\boldsymbol{q} \parallel \boldsymbol{t}$ for arbitrary wavenumbers and frequencies. This case corresponds to $\mathbf{B} \perp \boldsymbol{t}$, $\mathbf{E} \perp \boldsymbol{t}$, and $\mathbf{B} \perp \mathbf{E}$, as the magnetic field is given in momentum space by $\mathbf{B}(\boldsymbol{q},\omega) = i\boldsymbol{q} \times \mathbf{A}(\boldsymbol{q},\omega) = \boldsymbol{q} \times \mathbf{E}(\boldsymbol{q},\omega)/\omega$, and gives an effective CME response that, interestingly, is a combination of the chiral magnetic and anomalous Hall effects.

2.3 Effective chiral magnetic effect for a transverse wave

In the above case the total current along the magnetic field is determined by the effective CME conductivity

$$\sigma_{\perp}^{\mathrm{CME}}(\boldsymbol{q},\omega) \equiv \frac{iq^{l}\Pi_{l}(\boldsymbol{q},\omega^{+};\boldsymbol{t})}{q^{2}} = \sigma^{\mathrm{CME}}(\boldsymbol{q},\omega) + \sigma^{\mathrm{AHE}}(\boldsymbol{q},\omega)\frac{\omega t}{q}, \tag{2.7}$$

with $q = |\boldsymbol{q}|$. Ultimately we find for the effective chiral magnetic conductivity

$$\sigma_{\perp}^{\mathrm{CME}}(q,\omega) = \frac{e^{2}}{4\pi^{2}} \sum_{\chi=\pm} \chi\mu_{\chi}\mathcal{S}_{\perp}^{\mathrm{CME}}\left(\frac{\omega^{+}}{v_{F}q} - t, \frac{\mu_{\chi}}{v_{F}q}; t\right). \tag{2.8}$$

The dimensionless function $\mathcal{S}_{\perp}^{\mathrm{CME}}(x,y;t)$ captures all frequency, wavenumber and tilt-dependence of the conductivity. It is given by

$$\mathcal{S}_{\perp}^{\mathrm{CME}}(x,y;t) = \frac{1-x^{2}}{2(1+xt)} - \sum_{\sigma,\sigma'=\pm} \sigma\, K_{\sigma'}(x,y;t) H_{\sigma\sigma'}(x,y;t), \tag{2.9}$$

in terms of the dimensionless functions

$$K_{\sigma}(x,y;t) \equiv \left(\frac{1-x^{2}}{16y}\right)\left[\left(\frac{2\sigma y + t + x}{1+xt}\right)^{2} - 1\right], \tag{2.10}$$

$$H_{\sigma\sigma'}(x,y;t) \equiv \log\left(1 + \frac{2y}{(1-\sigma\sigma' t)(\sigma' x - \sigma)}\right). \tag{2.11}$$

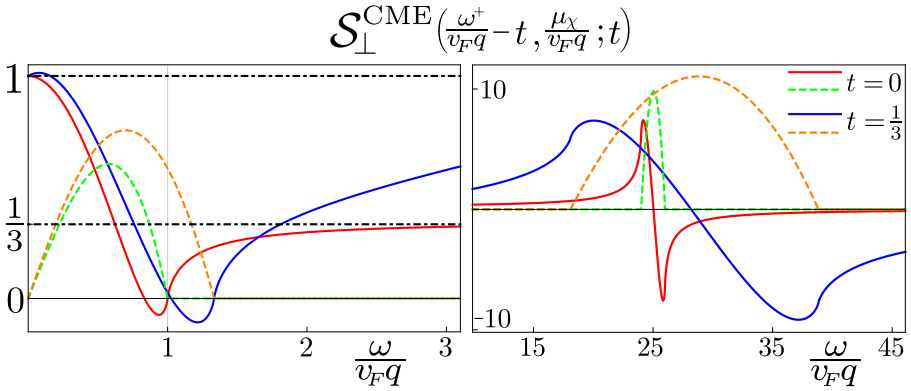

Figure 2.2: Plot of the real (solid lines) and imaginary (dashed lines) part of $\mathcal{S}_\perp^{\mathrm{CME}}$ for $2\mu_\chi/v_F q = 25$ and for $t = 0$ (red, green) and $t = 1/3$ (blue, orange). The left plot shows the behavior for small $\omega/v_F q$, whereas the right plot shows the resonance for larger values of $\omega/v_F q$. The black dotted-dashed lines indicate the static and homogeneous limit for $t = 0$.

The expression for the conductivity in Eq. (2.8) has a nontrivial dependence on the wavenumber q and frequency ω of the externally applied field. In fact, it is a function of the fraction $\omega/v_F q$, giving a different result in the homogeneous limit and the static limit. Indeed, in the static limit ($\omega/v_F q \to 0$), we find the well-known [55, 90] universal result $e^2\mu_5/2\pi^2$, whereas in the homogeneous limit ($\omega/v_F q \to \infty$), we find the tilt-dependent result

$$\lim_{\substack{q\to 0\\ \omega\to 0}} \sigma_\perp^{\mathrm{CME}}(q,\omega) \to \left[1 - 2l(t) + tl(t)\frac{\omega}{v_F q}\right]\frac{e^2\mu_5}{2\pi^2}, \tag{2.12}$$

in terms of the function

$$l(t) \equiv \frac{1}{2t^3}\log\left(\frac{1+t}{1-t}\right) - \frac{1}{t^2} \overset{t\to 0}{=} \frac{1}{3}. \tag{2.13}$$

We thus obtain the result $e^2\mu_5/6\pi^2$ for the homogeneous limit of Eq. (2.12) if $t = 0$ [98]. The function $l(t)$ diverges upon taking the limit $t \to 1$. The physical reason for this divergence is that then the cones are tilted up to the point that the density of states becomes infinite, thus resulting in an

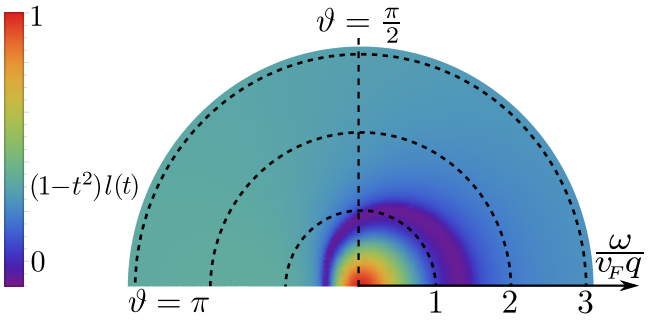

Figure 2.3: Anisotropic behavior of $\mathrm{Re}[\mathcal{S}^{\mathrm{CME}}]$ for $t = 1/2$ as a function of the angle ϑ and the radial coordinate $\omega/v_F q$. In the static (small radius) and homogeneous (large radius) limit, we obtain the isotropic results 1 and $(1-t^2)l(t) \simeq 0.3$.

infinite conductivity. In fact, the conductivity in Eq. (2.12) is due to the presence of the in-plane anomalous Hall effect formally always infinite in the homogeneous limit $\omega/v_F q \to \infty$. Note, however, that for light propagation we have that ω/q is equal to the speed of light in the material.

We plot the real and imaginary part of $\mathcal{S}_{\perp}^{\mathrm{CME}}\left(\omega^{+}/v_F q - t, \mu_\chi/v_F q, t\right)$ as a function of $\omega/v_F q$, but for a fixed value of $\mu_\chi/v_F q$ and different values of the tilt t in Fig. 2.2. When $t = 0$, the real part interpolates between the value 1 in the static limit and 1/3 in the homogeneous limit [102, 106]. Additionally, there is a resonance at $\omega = 2\mu_\chi$, after which the conductivity goes to zero as $1/\omega$. This resonance is effectively shifted to infinity in the homogeneous limit. For a non-zero tilt t, the static limit remains unchanged and in the homogeneous limit the real part of the conductivity diverges as $tl(t)\omega/v_F q$, rather than becoming constant as in the case of zero tilt. The resonance at $\omega = 2\mu_\chi$ remains present at non-zero tilt but becomes broader, as its width is now set by $2\mu_\chi/(1 \pm t)$. Note that the conductivity $\sigma_{\perp}^{\mathrm{CME}}(q, \omega)$ depends in a highly nonlinear way on the chiral imbalance μ_5. Theoretically this implies that the CME is not fully determined by the triangle diagram of the chiral anomaly. This is only true in the long-wavelength limit [28, 29].

At this point it is important to discuss why the conductivity is finite in the static limit in equilibrium. In deriving Eq. (2.2) a logarithmic divergence was avoided by a cancellation of the Dirac-sea contributions of the two cones.[e]

[e] The details can be found in Appendix 2.A.1.

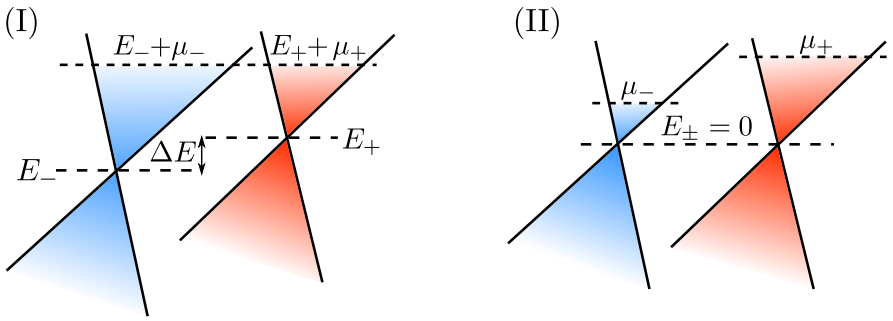

$\sigma^{\mathrm{CME}}(q,\omega)$	$2\mu_5 = -\Delta E$ (I)	$\Delta E = 0$ (II)
$\lim_{q\to 0}\lim_{\omega\to 0}$	0	$\frac{e^2\mu_5}{2\pi^2}$
$\lim_{\omega\to 0}\lim_{q\to 0}$	$\left[1-(1-t^2)l(t)\right]\frac{e^2\Delta E}{4\pi^2}$	$(1-t^2)l(t)\frac{e^2\mu_5}{2\pi^2}$

Figure 2.4: Results for the long-wavelength limit of the chiral magnetic conductivity. We show the cases (I) where $2\mu_5 = -\Delta E$ and (II) where the Weyl node separation is zero, i.e., $\Delta E = 0$. The zero-tilt results are [97, 98] (bottom, left) $e^2\Delta E/6\pi^2$, and (bottom, right) $e^2\mu_5/6\pi^2$. The response in the second row is sometimes referred to as gyrotropy.

This cancellation is correct up to a constant, which is proportional to the energy separation $\Delta E = E_+ - E_-$ of the Weyl nodes [107–109]. Hence, our answers for the static limit and Eq. (2.12) only apply when the energy separation between the nodes is zero. If that is not the case, then the true equilibrium situation corresponds to the situation where the chiral imbalance is exactly canceled by the energy separation between the Weyl nodes, i.e., $2\mu_5 = \mu_+ - \mu_- = -\Delta E$. Using this renormalization condition, we find that the chiral magnetic conductivity is zero in equilibrium, as expected. We will follow the same procedure when we consider a general angle between the externally applied magnetic field and the tilt direction.

2.4 Angle dependence chiral magnetic effect

We define ϑ to be the angle between $\mathbf{q}$ and $\boldsymbol{t}$, such that $\mathbf{q}\cdot\boldsymbol{t} = qt\cos\vartheta \equiv qt_\parallel$. For arbitrary angles ϑ we cannot perform the necessary integrals analytically

for all wavenumbers q and frequencies ω. However, we can investigate the tilt dependence of the long-wavelength limit of the conductivity for arbitrary angles. To do so, we take the limit $q \to 0$ in the integrand of Eq. (2.2), while keeping $\omega/v_F q$ fixed. Keeping in mind that we are not considering a possible topological contribution to the anomalous Hall effect, we find in general the interesting relation $\sigma^{\mathrm{AHE}}(\boldsymbol{q},\omega) = \sigma^{\mathrm{CME}}(\boldsymbol{q},\omega)/v_F(1-t^2)$ with

$$\sigma^{\mathrm{CME}}(\boldsymbol{q},\omega) = \frac{e^2\mu_5}{2\pi^2}\mathcal{S}^{\mathrm{CME}}\left(\frac{\omega^+}{v_F q} - t_\parallel; \boldsymbol{t}\right). \tag{2.14}$$

The dimensionless function $\mathcal{S}^{\mathrm{CME}}(x;\boldsymbol{t})$ is given by

$$\mathcal{S}^{\mathrm{CME}}(x;\boldsymbol{t}) = \frac{(1-t^2)(1-x^2)}{N^2(x;\boldsymbol{t})}\left[1 + \frac{(x+t_\parallel)H(x;\boldsymbol{t})}{2N(x;\boldsymbol{t})}\right], \tag{2.15}$$

in terms of the functions[f]

$$N(x;\boldsymbol{t}) \equiv \sqrt{(1-t^2)(1-x^2) + (x+t_\parallel)^2} \tag{2.16a}$$

$$H(x;\boldsymbol{t}) \equiv \sum_{\sigma=\pm} \sigma \log[(x-\sigma)M_\sigma(x;\boldsymbol{t})] \tag{2.16b}$$

$$M_\sigma(x;\boldsymbol{t}) \equiv (1 + N(x;\boldsymbol{t}) + t_\parallel x)(1-\sigma t_\parallel) - (t^2 - t_\parallel^2)(1+\sigma x). \tag{2.16c}$$

In Fig. 2.3 we show the resulting angular dependence of the conductivities. In the static limit we have that the chiral magnetic conductivity is equal to $e^2\mu_5/2\pi^2$ and is independent of the tilt [90]. In the homogeneous limit we find the result $(1-t^2)l(t)e^2\mu_5/2\pi^2$ for all angles.[g] Again, we need to add an appropriate renormalization constant for $\Delta E \neq 0$ such that the chiral magnetic current is zero in equilibrium. Using this subtraction procedure, which in particle physics amounts to adding a Bardeen counterterm [109], we find a general answer that depends on μ_5 and ΔE and modifies the results in the homogeneous limit. We displayed the final results for the special cases of equilibrium and zero energy separation between the cones in Fig. 2.4.

[f] The derivation is presented in more detail in Appendix 2.A.2.

[g] Note that Eq. (2.12) can be rederived from Eq. (2.8) by expanding $[1 + \omega t/v_F q(1-t^2)]S^{\mathrm{CME}}(\omega/v_F q - t;\boldsymbol{t})$ up to first order in $\omega/v_F q$. It is thus important to take into accound the terms of $\mathcal{O}(v_F q/\omega)$ in the homogeneous limit of $S^{\mathrm{CME}}(\omega/v_F q - t;\boldsymbol{t})$.

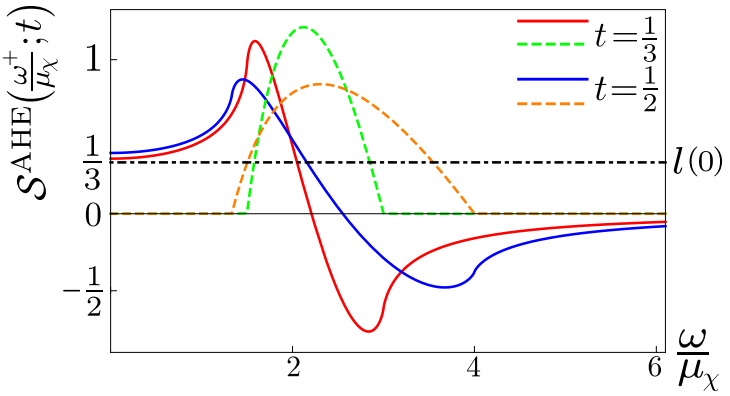

Figure 2.5: Plot of the real (solid lines) and imaginary (dashed lines) parts of the function $\mathcal{S}^{\mathrm{AHE}}(\omega^+/\mu_\chi;t)$ for $t = 1/3$ (red, green), and $t = 1/2$ (blue, orange) [103]. The black dotted-dashed line indicates the tilt-independent limit.

2.5 Frequency dependence anomalous Hall effect

As advertized the tilt induces another interesting effect, namely a planar intrinsic anomalous Hall effect with a current given by Eq. (2.6) that is perpendicular to both the external electric field and the tilting direction. Apart from the long-wavelength limit following from Eq. (2.8), we are also able to obtain the full frequency dependence of the homogeneous anomalous Hall conductivity as[h]

$$\sigma^{\mathrm{AHE}}(\mathbf{0},\omega) = \frac{e^2}{4\pi^2 v_F}\sum_{\chi=\pm}\chi\mu_\chi\mathcal{S}^{\mathrm{AHE}}\Big(\frac{\omega^+}{\mu_\chi};t\Big), \tag{2.17}$$

in terms of the dimensionless function

$$\mathcal{S}^{\mathrm{AHE}}(y;t) = -\frac{1}{2t^2} + \sum_{\sigma,\sigma'=\pm}\sigma' L_\sigma(y;t)H_{\sigma\sigma'}(0,1/y;t), \tag{2.18}$$

[h] The derivation can be found in Appendix 2.A.3.

where $L_\sigma(y;t) \equiv \left[y^2t^2 - (2-\sigma y)^2\right]/16yt^3$ and again we encounter the functions $H_{\sigma\sigma'}(x,y;t)$ from Eq. (2.11). This result was recently obtained in a different way both analytically [103, 104] and numerically [105]. In the zero-frequency limit the conductivity reduces to $\sigma^{\mathrm{AHE}}(\mathbf{0},0) = l(t)e^2\mu_5/2\pi^2 v_F$, which corresponds exactly to the slope of the linear divergence in Eq. (2.12). We plot the dependence of the real and imaginary part of $\mathcal{S}^{\mathrm{AHE}}(\omega^+/\mu_\chi;t)$ on ω/μ_χ in Fig. 2.5 for several magnitudes of the tilt. Again, we observe a resonance behavior around $\omega = 2\mu_\chi$, similar to the one in Fig. 2.2, because the current response in that figure is dominated by the AHE at large frequencies.

2.6 Discussion

We have shown that the electric and magnetic response of a pair of tilted Weyl cones is in general non-universal and depends on the magnitude of the tilt and on the angle between the tilt direction and the wave vector of the magnetic field. However, the chiral anomaly is due to the lowest Landau level, which only obtains a change of slope due to a tilting of the cones [80]. Hence, we expect the chiral anomaly to be unmodified and thus isotropic. Using the relation between the current-current correlation function and the triangle diagram in the static (adiabatic) limit, we find for the time derivative of the chiral number density $n_5 \equiv n_+ - n_-$,

$$\frac{\mathrm{d}n_5}{\mathrm{d}t} = \lim_{\omega\to 0} \frac{e^2}{2\pi^2}\, \mathcal{S}^{\mathrm{CME}}\big(\omega^+/v_F q - t_\parallel; \boldsymbol{t}\big)\mathbf{E}\cdot\mathbf{B}. \tag{2.19}$$

In the static limit we have $\mathcal{S}^{\mathrm{CME}}(\omega^+/v_F q - t_\parallel;\boldsymbol{t}) \to 1$, such that we indeed find an unmodified chiral anomaly.

Additionally, we showed that the chiral magnetic effect is closely related to an in-plane tilt-induced anomalous Hall effect, for which we calculated the dynamical conductivity. We have also performed all these calculations in the case that inversion symmetry is not broken, corresponding to tilting the Weyl cones in opposite directions. An important consequence is that in the long-wavelength limit the anomalous Hall effect becomes proportional to 2μ, instead of $2\mu_5$, i.e., $\sigma^{\mathrm{AHE}}(\mathbf{0},0) = l(t)e^2\mu/2\pi^2 v_F$. The chiral magnetic effect, however, remains proportional to $2\mu_5$ due to Bloch's theorem [110].

Acknowledgements: It is our pleasure to thank Guido van Miert for useful discussions and a critical reading of the manuscript on which this chapter is based.

2.A Appendix: derivations

In this appendix we provide detailed derivations of some of the results presented in this chapter. We start by deriving the antisymmetric part of the electric current-current response function from Eq. (2.2). Furthermore, we discuss how to obtain the results of Section 2.4 for the long-wavelength limit of the chiral magnetic conductivity for arbitrary angles between the tilting direction and the wavenumber of the external field. Finally, we calculate the AC intrinsic anomalous Hall conductivity from Section 2.5.

2.A.1 Current-current response function

We describe two Weyl fermions with opposite chirality by a four-dimensional Dirac spinor ψ and denote the corresponding chiral imbalance by μ_5. Setting $v_F = \hbar = 1$ for the moment, the Hamiltonian in Eq. (2.1) in Section 2.2 corresponds to the following quadratic action in Fourier space

$$S_0[\bar{\psi},\psi] = \int \frac{\mathrm{d}^4k}{(2\pi)^4}\bar{\psi}(k)\big[k_\mu\Gamma^\mu - \mu\gamma^0 - \mu_5\gamma^0\gamma^5\big]\psi(k), \tag{2.20}$$

where γ^μ and γ^5 are the Dirac gamma matrices[i], $\Gamma^\mu \equiv \gamma^\mu + \gamma^0 t^\mu$ with $t^\mu = (0,\boldsymbol{t})$ and $k^\mu = (\omega,\boldsymbol{k})$ is the four-momentum. Minimal coupling yields the electric current $J^\mu(k) = e\bar{\psi}(k)\Gamma^\mu\psi(k)$ with $-e$ the electron charge. The Feynman propagator $S_F(k)$ following from the action in Eq. (2.20) is

$$S_F(k) \equiv i\big(k_\mu\Gamma^\mu - \mu\gamma^0 - \mu_5\gamma^0\gamma^5\big)^{-1} = i\begin{pmatrix} G_-(k) & 0 \\ 0 & G_+(k)\end{pmatrix}\gamma^0, \tag{2.21}$$

where we introduced the propagator $G_\pm(k)$ for a single cone with chirality $\pm$. The Matsubara Green's function associated with the latter is given by

$$G_\chi(i\omega_n,\boldsymbol{k}) = \frac{(i\omega_n + \mu_\chi - \boldsymbol{k}\cdot\boldsymbol{t})\sigma^0 + \chi\boldsymbol{k}\cdot\boldsymbol{\sigma}}{(i\omega_n + \mu_\chi - \boldsymbol{k}\cdot\boldsymbol{t})^2 - |\boldsymbol{k}|^2} = \frac{1}{2}\sum_{u=\pm}\frac{\sigma^0 + \chi u\hat{\boldsymbol{k}}\cdot\boldsymbol{\sigma}}{i\omega_n + \mu_\chi - \varepsilon_{u\boldsymbol{k}}}, \tag{2.22}$$

[i] We use the metric $\eta_{\mu\nu} = \mathrm{diag}(-,+,+,+)$. For the gamma matrices we use the representation $\gamma^0 = i\sigma^y\otimes\mathbb{1}_2$, $\gamma^j = \sigma^x\otimes\sigma^j$ and $\gamma^5 = -\sigma^z\otimes\mathbb{1}_2$, such that $(\gamma^0)^2 = -\mathbb{1}_4$, $(\gamma^i)^2 = \mathbb{1}_4$ and γ^5 anti-commutes with all other gamma matrices.

in terms of the fermionic Matsubara frequencies $\omega_n = (2n+1)\pi/\beta$ with $\beta \equiv 1/k_B T$ and the single-particle energies $\varepsilon_{u\boldsymbol{k}} = u|\boldsymbol{k}| + \boldsymbol{k}\cdot\boldsymbol{t}$ of the conduction ($u = +$) and valence ($u = -$) band.[j] By integrating out the fermions, the polarization tensor, or current-current correlator, $\Pi^{\mu\nu}_{ee}(q)$ is found to be

$$\Pi^{\mu\nu}_{ee}(q) = -e^2 \int \frac{\mathrm{d}^4 k}{(2\pi)^4} \mathrm{Tr}\big[\Gamma^\mu S_F(k+q)\Gamma^\nu S_F(k)\big]. \tag{2.23}$$

Using the expression for the single-cone Green's function in Eq. (2.22) and considering spatial indices, the current-current correlator can be expressed in terms of the bosonic Matsubara frequency $i\omega_m$ as

$$\begin{aligned}&\Pi^{ij}_{ee}(\boldsymbol{q}, i\omega_m) \\ &= \frac{ie^2}{4\beta} \sum_{\substack{i\omega_n, \\ \chi,u,v=\pm}} \int_{\boldsymbol{k}} \frac{\mathrm{Tr}\big[\big(\sigma^i + \chi t^i\big)\big(\sigma^0 + \chi u \hat{\boldsymbol{p}}\cdot\boldsymbol{\sigma}\big)\big(\sigma^j + \chi t^j\big)\big(\sigma^0 + \chi v \hat{\boldsymbol{k}}\cdot\boldsymbol{\sigma}\big)\big]}{\big(i\omega_{m+n} + \mu_\chi - \varepsilon_{u\boldsymbol{k}+\boldsymbol{q}}\big)\big(i\omega_n + \mu_\chi - \varepsilon_{v\boldsymbol{k}}\big)},\end{aligned} \tag{2.24}$$

where we defined $\hat{p}^i \equiv (k+q)^i/|\boldsymbol{k}+\boldsymbol{q}|$ and $\int_{\boldsymbol{k}} \equiv \int \mathrm{d}^3\boldsymbol{k}/(2\pi)^3$. The Matsubara sum is readily evaluated by going to the complex plane [111], yielding

$$\begin{aligned}N^\chi_{uv}(i\omega_m, \boldsymbol{q}, \boldsymbol{t}, \boldsymbol{k}) &\equiv \frac{1}{\beta}\sum_{i\omega_n} \frac{1}{\big(i\omega_{m+n} + \mu_\chi - \varepsilon_{u\boldsymbol{k}+\boldsymbol{q}}\big)\big(i\omega_n + \mu_\chi - \varepsilon_{v\boldsymbol{k}}\big)} \\ &= \frac{N_\mathrm{F}(\varepsilon_{v\boldsymbol{k}} - \mu_\chi) - N_\mathrm{F}(\varepsilon_{u\boldsymbol{k}+\boldsymbol{q}} - \mu_\chi)}{i\omega_m - \varepsilon_{u\boldsymbol{k}+\boldsymbol{q}} + \varepsilon_{v\boldsymbol{k}}},\end{aligned} \tag{2.25}$$

in terms of the Fermi-Dirac distribution $N_\mathrm{FD}(x) \equiv (e^{\beta x}+1)^{-1}$. We now analytically continue to real frequencies by writing $i\omega_m \to \omega^+ \equiv \omega + i\eta$ with $\eta \to 0$ in Eq. (2.25). Performing the trace in Eq. (2.24) and taking the antisymmetric part by writing $\Pi^k_{ee}(\boldsymbol{q}, \omega; \boldsymbol{t}) = \varepsilon^{ijk}\Pi^{ij}_{ee}(\boldsymbol{q}, \omega; \boldsymbol{t})/2$, where we

[j] Note that here we include the tilt in the single-particle energies, whereas in Section 2.2 we absorb them in the chemical potential by writing $\mu_\chi(\boldsymbol{k}) = \mu_\chi - \hbar v_F \boldsymbol{k}\cdot\boldsymbol{t}$ and use $\varepsilon_{\boldsymbol{k}}$ for the untilted single-particle energies.

explicitly indicated the dependence on $\boldsymbol{t}$, we find

$$i\Pi^k_{ee}(\boldsymbol{q},\omega;\boldsymbol{t}) = -\frac{e^2}{2}\sum_{\chi,u,v=\pm}\chi\int_{\boldsymbol{k}} vF^{uv}_k(\boldsymbol{k},\boldsymbol{q};\boldsymbol{t})N^{\chi}_{uv}(\omega,\boldsymbol{q},\boldsymbol{t},\boldsymbol{k}), \tag{2.26}$$

where we used the definition of the structure factor $F^{uv}_k(\boldsymbol{k},\boldsymbol{q};\boldsymbol{t})$ from Eq. (2.3). This expression can be brought into the form of Eq. (2.2) by reinstating units and by using the identity $N_F(-x) = 1 - N_F(x)$ several times. The ultraviolet divergence coming from the '1' is cancelled by performing the sum over the chirality χ in Eq. (2.26).

Using the fact that the function $N^{\chi}_{uv}(\omega,\boldsymbol{q},\boldsymbol{t},\boldsymbol{k})$ has the useful properties

$$N^{\chi}_{uv}(\omega,\boldsymbol{q},\boldsymbol{t},\boldsymbol{k}) = N^{\chi}_{uv}(\omega,-\boldsymbol{q},-\boldsymbol{t},-\boldsymbol{k}) = \big[N^{\chi}_{vu}(-\omega,-\boldsymbol{q},\boldsymbol{t},\boldsymbol{k}+\boldsymbol{q})\big]^*, \tag{2.27}$$

it follows that the the antisymmetric part of the response function obeys

$$\Pi^k_{ee}(\omega,\boldsymbol{q};\boldsymbol{t}) = -\Pi^k_{ee}(\omega,-\boldsymbol{q};-\boldsymbol{t}) = -\big[\Pi^k_{ee}(-\omega,-\boldsymbol{q};\boldsymbol{t})\big]^*. \tag{2.28}$$

Because of these symmetries a term of the form $\gamma(\boldsymbol{q},\omega;\boldsymbol{t})(\boldsymbol{q}\times\boldsymbol{t})^k$ is not allowed and the decomposition of $\Pi^k_{ee}(\omega,\boldsymbol{q};\boldsymbol{t})$ in Eq. (2.4) is appropriate. The current density due to the antisymmetric part of the current-current correlator is given by $J^i = \varepsilon_{ijk}\Pi^k_{ee}A^j$. Hence, if we use the decomposition Eq. (2.4), we obtain the chiral magnetic and anomalous Hall contributions to the current:

$$\boldsymbol{J}(\boldsymbol{q},\omega) = \sigma^{\mathrm{CME}}(\boldsymbol{q},\omega)\mathbf{B}(\boldsymbol{q},\omega) + \sigma^{\mathrm{AHE}}(\boldsymbol{q},\omega)\boldsymbol{t}\times\mathbf{E}(\boldsymbol{q},\omega), \tag{2.29}$$

and the conductivities follow by taking the following projections

$$\sigma^{\mathrm{CME}}(\boldsymbol{q},\omega) = \frac{\big[|\boldsymbol{t}|^2 q_l - (\boldsymbol{q}\cdot\boldsymbol{t})t_l\big]\,i\Pi^l_{ee}(\boldsymbol{q},\omega^+;\boldsymbol{t})}{|\boldsymbol{q}|^2|\boldsymbol{t}|^2 - (\boldsymbol{q}\cdot\boldsymbol{t})^2}, \tag{2.30a}$$

$$\sigma^{\mathrm{AHE}}(\boldsymbol{q},\omega) = \frac{1}{\omega}\frac{\big[|\boldsymbol{q}|^2 t_l - (\boldsymbol{q}\cdot\boldsymbol{t})q_l\big]\,i\Pi^l_{ee}(\boldsymbol{q},\omega^+;\boldsymbol{t})}{|\boldsymbol{q}|^2|\boldsymbol{t}|^2 - (\boldsymbol{q}\cdot\boldsymbol{t})^2}. \tag{2.30b}$$

Physically there is no reason for a pole at $|\boldsymbol{q}|^2|\boldsymbol{t}|^2 - (\boldsymbol{q}\cdot\boldsymbol{t})^2 = 0$ and we therefore expect the denominator to exactly drop out once we form the linear combinations in the numerator to find the conductivities.

2.A.2 Long-wavelength limit chiral magnetic conductivity

In order to obtain the long-wavelength limit of the conductivities in Eq. (2.30), we take the limit $q \to 0$ while keeping $x \equiv z/v_F q$ fixed. The homogeneous limit then corresponds to $x \to \infty$, whereas the static limit correponds to $x \to 0$. To find the two conductivities separately, we need to calculate the projection of the current-current response function onto $\boldsymbol{t}$ and $\boldsymbol{q}$ and subsequently form the linear combinations as written down in Eq. (2.30). To calculate the necessary integrals we choose $\boldsymbol{q}$ along the z-axes without loss of generality and we denote $\boldsymbol{q}\cdot\boldsymbol{t} = qt_\parallel$. Furthermore, we can put $\boldsymbol{t}$ in the xz-plane. Hence, when going to spherical coordinates (ϕ, θ, k), we have $\boldsymbol{q}\cdot\boldsymbol{k} = kq\cos\theta$ and $\boldsymbol{k}\cdot\boldsymbol{t} = k\big(t_\perp \cos\phi \sin\theta + t_\parallel \cos\theta\big)$. Performing all remaining integrals explicitly at $T = 0$, we find for the two projections

$$
\begin{aligned}
iq_l\Pi^l(\boldsymbol{q},\omega;\boldsymbol{t}) &= q^2(1 + t_\parallel x' - t_\perp^2)\left[\frac{\mathcal{S}^{\mathrm{CME}}(\omega^+/v_F q - t_\parallel;\boldsymbol{t})}{1-t^2}\right]\frac{e^2\mu_5}{2\pi^2},\\
it_l\Pi^l(\boldsymbol{q},\omega;\boldsymbol{t}) &= q(t_\parallel + t_\parallel^2 x' + t_\perp^2 x')\left[\frac{\mathcal{S}^{\mathrm{CME}}(\omega^+/v_F q - t_\parallel;\boldsymbol{t})}{1-t^2}\right]\frac{e^2\mu_5}{2\pi^2},
\end{aligned}
\tag{2.31}
$$

where we denoted $x' = \omega^+/v_F q - t_\parallel$ and used $\mathcal{S}^{\mathrm{CME}}(x';\boldsymbol{t})$, which was defined in Eq. (2.15). Forming the linear combinations from Eq. (2.30), we find, as claimed,

$$
\sigma^{\mathrm{AHE}}(\boldsymbol{q},\omega) = \frac{e^2\mu_5}{2\pi^2 v_F(1-t^2)} S^{\mathrm{CME}}\left(\frac{\omega^+}{v_F q} - t_\parallel;\boldsymbol{t}\right) = \frac{\sigma^{\mathrm{CME}}(\boldsymbol{q},\omega)}{v_F(1-t^2)}. \tag{2.32}
$$

Note that this identity only holds because we are not explicitly taking into account the topological contribution to the anomalous Hall effect due to the separation of the cones.

2.A.3 AC intrinsic anomalous Hall conductivity

Upon projecting the antisymmetric part of the response function in Eq. (2.4) onto $\boldsymbol{t}$ and considering $\boldsymbol{q} = \boldsymbol{0}$, the chiral magnetic conductivity drops out and we obtain the intrinsic anomalous Hall current density $\boldsymbol{J}^{\mathrm{AHE}}(\omega) = \sigma^{\mathrm{AHE}}(\omega)\boldsymbol{t}\times\mathbf{E}(\omega)$. The corresponding AC anomalous Hall conductivity

$\sigma^{\mathrm{AHE}}(\omega)$ is given at $T = 0$ by[k]

$$\begin{aligned}\sigma^{\mathrm{AHE}}(\omega) &= \frac{it^l \Pi_l(\mathbf{0}, \omega^+; \boldsymbol{t})}{\omega t^2} \\ &= 2\frac{e^2 v_F^2}{t^2} \sum_{\chi=\pm} \chi \int_{\boldsymbol{k}} \frac{\hat{\boldsymbol{k}} \cdot \boldsymbol{t}}{(\omega^+)^2 - 4v_F^2 |\boldsymbol{k}|^2} \vartheta(|\mu_\chi| - \varepsilon_{+\boldsymbol{k}}). \end{aligned} \tag{2.33}$$

To perform the integral we take spherical coordinates (φ, θ, k) along the axis defined by $\boldsymbol{t}$, such that $\boldsymbol{k} \cdot \boldsymbol{t} = kt\cos\theta$. The azimuthal integration over φ is trivial and yields 2π. After a change of integration variable to $x = \cos\theta$, we find

$$\begin{aligned}\sigma^{\mathrm{AHE}}(\omega) &= \sum_{\chi=\pm} \frac{e^2\chi}{(2\pi)^2 t} \int_{-1}^{1} \mathrm{d}x\, x \int_0^\infty \mathrm{d}k\, \frac{2(v_F k)^2 \vartheta(|\mu_\chi| - v_F k(1+xt))}{(\omega^+)^2 - (2v_F k)^2} \\ &= \sum_{\chi=\pm} \frac{2e^2\chi}{(2\pi)^2 v_F t} \int_{-1}^{1} \mathrm{d}x\, x \int_0^{\frac{|\mu_\chi|}{v_F(1+xt)}} \mathrm{d}\bar{k} \left[\frac{\bar{k}^2}{(\omega^+)^2 - 4\bar{k}^2}\right] \\ &= \sum_{\chi=\pm} \frac{e^2\chi\mu_\chi}{(2\pi)^2 v_F} \left[\sum_{u,v=\pm} v L_u\Big(\frac{\omega^+}{|\mu_\chi|}; t\Big) H_{uv}\Big(0, \frac{|\mu_\chi|}{\omega^+}; t\Big) - \frac{1}{2t^2}\right], \end{aligned} \tag{2.34}$$

where we used the definition of $H_{uv}(x, y; t)$ from Eq. (2.11) and in addition defined the rational function

$$L_u(y; t) \equiv \frac{y^2 t^2 - (2 - uy)^2}{16 y t^3}. \tag{2.35}$$

[k] From the antisymmetric contribution to the current-current response function one can deduce that the contributions for $\mu_\chi < 0$ and $\mu_\chi > 0$ are the same. We therefore use $|\mu_\chi|$ here.

3 Magnetovortical and thermoelectric transport in tilted Weyl metals

We investigate how tilting affects the off-diagonal, dissipationless response of a pair of chirally imbalanced Weyl cones to various external perturbations. The pair of chirally imbalanced Weyl cones can be described as a chiral electron fluid, that can flow with a velocity field that contains vorticity. Upon applying an external magnetic field, we obtain the so-called magnetovortical linear-response matrix that relates electric and heat currents to the magnetic field (chiral magnetic effect) and the vorticity (chiral vortical effect). We show how this reponse matrix becomes anisotropic upon tilting the cones and determine its non-analytic long-wavelength behavior, as well as the corresponding AC response. In addition, we discuss how the tilt dependence of the electronic (or density-density) susceptibility introduces anisotropy in the dispersion relation of the sound-like excitations in the fluid of chiral fermions, which are known as chiral magnetic waves. In the case of an externally applied electric field and a temperature gradient, we find a Hall-like response in the electric and heat current density that is perpendicular to both the tilting direction and the perturbations. As the tilting direction forms a time-reversal symmetry breaking vector, a non-zero (heat) orbital magnetization manifests itself. We calculate the magnetization currents microscopically and elucidate how to subtract these contributions to obtain the transport currents.[a]

[a] This chapter is directly based on "E.C.I. van der Wurff and H.T.C. Stoof, *Magnetovortical and thermoelectric transport in type-I Weyl metals*, arXiv:1903.10985 (2019)".

3.1 Introduction

The most important symmetry principle of particle physics is Lorentz invariance. Indeed, requiring invariance under Lorentz transformations yields a powerful restriction on which equations are eligible to describe the particles we encounter in Nature. For instance, it was Lorentz invariance, together with the wish for a counterpart to the Schrödinger equation that was first order in time derivatives, that allowed Paul Dirac to derive his famous equation describing massive spin-1/2 particles in 1928 [16]. The price that Dirac had to pay for finding an equation that obeyed these two requirements was that the spin-1/2 particle had to be described in terms of a four-component spinor, instead of the expected two-component wavefunction. It was only one year later when Hermann Weyl realized that Dirac's equation simplified greatly when considering massless spin-1/2 particles [17]. Instead of one equation involving a four-component spinor, Weyl obtained two decoupled equations, each for a two-component spinor with a definite chirality. Weyl fermions were, at least theoretically, born.

Contrastingly, not even translational symmetry is fully preserved in the presence of the atomic lattice out of which any ordinary solid is built up. Invariance under the even bigger Lorentz group thus seems too much to ask for in condensed matter. However, in certain cases Lorentz invariance can emerge at low energies in solid-state materials. One example of such a case occurs in the recently discovered Weyl semimetals [36, 38–40, 42, 43, 82]. These materials host quasiparticles in their low-energy bandstructure that obey the aforementioned Weyl equation. This leads to a conical dispersion relation just like the light cone for massless particles known from particle physics, albeit with the speed of light replaced by the, typically much smaller, Fermi velocity.

These so-called Weyl cones are topological: depending on the chirality of the cone, they acts as a sink or drain of Berry curvature in momentum space [25]. Only when the distance in energy-momentum space between two Weyl nodes with opposite chirality becomes zero, the monopoles annihilate, yielding a doubly-degenerate Dirac cone. Reversely, a pair [26] of non-degenerate Weyl cones can emerge from a doubly-degenerate Dirac cone in two distinct ways. Breaking time-reversal symmetry yields two Weyl cones separated in momentum space, whereas breaking of inversion symmetry yields two Weyl cones separated in energy space [35, 54].

Interestingly, the emergent Lorentz symmetry in Weyl semimetals is not enforced by any crystal symmetries and thus generically it will be broken. The simplest way for this to happen is when the cones are tilted [88, 89]. This is achieved mathematically by adding a term to the low-energy Hamiltonian that is proportional to the unit matrix in spin space and linear in momentum. Cones that are only slightly tilted are referred to as type-I Weyl cones, whereas cones that are tipped over are called type-II Weyl cones [90, 112]. The existence of such tilted Weyl cones raises many interesting questions. For instance, we can ask how the diagonal optical response to an electric field is altered by the tilt [101, 113], how the magnetoconductivity depends on the tilt [114], how the renormalization-group flow equations change [115], what happens to the Landau level structure [116], how do tilted Weyl cones respond to disorder [93, 94] and finally we can even show that vertex corrections due to Coulomb interactions naturally tilt the cone in the presence of a magnetic field [1].

In this chapter we discuss how tilting the cones affects the electric and thermal transport of a Weyl metal. More specifically, we focus on the off-diagonal, dissipationless transport. It is important to note that the tilting direction of the Weyl cones forms another time-reversal symmetry breaking vector, besides the displacement vector in momentum space connecting the two Weyl cones. The thermoelectric response driven by an external electric field $\mathbf{E}$ and a thermal gradient $\boldsymbol{\nabla} T$ therefore contains a Hall part, describing currents that are perpendicular to the tilting direction [2, 103, 117]. Besides this novel thermoelectric response, we show that the magnetovortical response to an externally applied magnetic field $\mathbf{B}$ and a vorticity $\boldsymbol{\omega} = (\boldsymbol{\nabla} \times \boldsymbol{v})/2$, due to the fermion fluid flowing with a spatial velocity profile $\boldsymbol{v}$, becomes anisotropic due to the tilting of the cones. Furthermore, we discuss the nonanalytic frequency-momentum behavior of the various transport coefficients in detail.

This chapter is organized as follows. We introduce the minimal model for a chirally imbalanced Weyl metal with tilted cones in Section 3.2. Subsequently we discuss the magnetovortical and thermoelectric response of a material that is described by such a Hamiltonian and give a summary of the main results we have obtained. The rest of the chapter is devoted to a more in-depth discussion of the various properties of the transport coefficients. We explain how to use linear-response theory to calculate the transport coefficients due to the perturbations $\mathbf{B}$, $\mathbf{E}$, $\boldsymbol{\nabla} T$ and $\boldsymbol{\omega}$ in Section 3.3. Next, we

calculate and discuss the tilt-dependent, anisotropic magnetovortical effects in Section 3.4 in three different regimes: the long-wavelength limit (Section 3.4.1), the static and homogeneous limit (Section 3.4.2) and finally the AC frequency response (Section 3.4.3). In Section 3.5 we obtain the thermoelectric response due to tilted cones by explicitly calculating the magnetization contributions to the currents and subtracting them. Finally, we discuss our results in Section 4.5.

3.2 Dissipationless transport

In this section we start by introducing a minimal model for a chirally imbalanced Weyl metal with tilted cones. Subsequently, we discuss the magnetovortical and thermoelectric response and highlight what changes upon tilting the cones, thereby summarizing the main results of the rest of the chapter.

3.2.1 Model for tilted Weyl cones

We consider a doped time-reversal symmetry breaking Weyl metal. Because we focus on the off-diagonal response due to the tilting of the cones, we do not take an explicit separation between the Weyl nodes into account. Then, the simplest continuum two-band, grand-canonical Hamiltonian describing a tilted Weyl cone with chirality $\chi = \pm$ and isotropic[b] Fermi velocity v_F is given by

$$\mathcal{H}_\chi(\boldsymbol{k}) = \chi\hbar v_F \boldsymbol{k}\cdot\boldsymbol{\sigma} + \big(\hbar v_F \boldsymbol{k}\cdot\boldsymbol{t}_\chi - \mu_\chi\big)\sigma^0, \tag{3.1}$$

with $\sigma^\mu = (\mathbb{1}_2, \boldsymbol{\sigma})$ the four-vector of Pauli matrices and $\mu_\pm \equiv \mu \pm \mu_5$ the chemical potential of the Weyl node with chirality $\pm$, in terms of the chemical potential $\mu \equiv (\mu_+ + \mu_-)/2$ and the chiral, or axial, chemical potential $\mu_5 \equiv (\mu_+ - \mu_-)/2$. Note that we have defined the chemical potentials with respect to the energy of the corresponding Weyl node. In what follows we will consider mostly the case that the energy difference between the Weyl nodes $\Delta E = 0$. In addition, we note that a typical experimental value for the Fermi velocity is $v_F \simeq c/300 \simeq 10^6$ m/s, with c the speed of light.

[b] In principle, there can be different Fermi velocities in all three directions. This anisotropy can however always be transformed away by an appropriate scaling of the momenta.

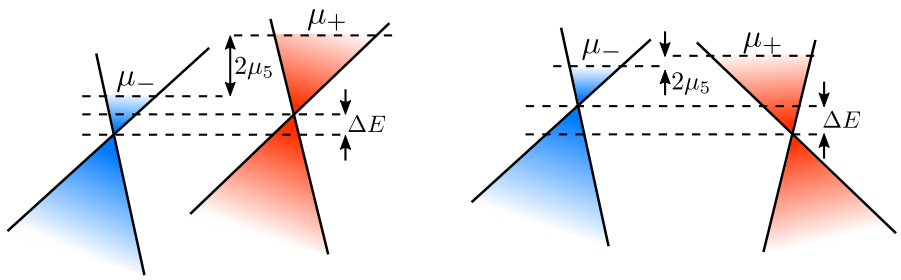

(a) $\mathbf{t}_+ = \mathbf{t}_-$ (b) $\mathbf{t}_+ = -\mathbf{t}_-$

Figure 3.1: Schematic depiction of a pair of tilted Weyl cones with negative (positive) chirality in blue (red) and corresponding chemical potential μ_- (μ_+). The chiral imbalance is $\mu_5 = (\mu_+ - \mu_-)/2$ and the nodes are separated by an energy difference ΔE. In this chapter we mostly discuss the case $\Delta E = 0$. (a) Inversion-symmetry breaking tilt: Weyl cones are tilted by the same amount in one direction. (b) Inversion-symmetry retaining tilt: Weyl cones are tilted by the same amount in opposite directions. Note that we defined the tilting direction such that the associated energy contribution in Eq. (3.1) increases for momenta in the direction of the tilt.

The tilting direction of each cone is indicated by $\boldsymbol{t}_\chi$ in Eq. (3.1). For simplicity we take $0 \leq |\boldsymbol{t}_\chi| = t < 1$, meaning that we consider type-I Weyl cones that are tilted by the same amount. The latter requirement is easily generalized if necessary. Next to the magnitude, each cone can also have a different tilting direction. Indeed, $\boldsymbol{t}_\chi = \chi \boldsymbol{t}$ is the inversion-symmetric case and $\boldsymbol{t}_\chi = \boldsymbol{t}$ when inversion symmetry is broken. Physically, the inversion-symmetric case corresponds to the situation where the two Weyl cones are tilted in opposite directions by exactly the same amount. This is pictorially displayed in Fig. 3.1. For later reference, we note that the eigenvalues of the Hamiltonian in Eq. (3.1) are given by

$$\varepsilon_{n\chi\boldsymbol{k}} - \mu_\chi = n\hbar v_F |\boldsymbol{k}| + \hbar v_F \boldsymbol{k} \cdot \boldsymbol{t}_\chi - \mu_\chi, \tag{3.2}$$

with $n = \pm$ indicating the conduction (+) and valence (-) band, respectively.

The presence of a chiral imbalance $\mu_+ \neq \mu_-$ (for $\Delta E = 0$), is a non-equilibrium property. One way to generate a chiral imbalance is by irredi-

ating a Weyl semimetal with circularly polarized light, thereby transferring chirality from the light to the electrons [118]. Another way is to apply strain to the Weyl semimetal [119]. We instead focus on the possibility to pump charge from one cone to the other by applying non-orthogonal electric and magnetic fields, which we discuss in the next section. Whatever the pumping mechanism is, it will be counterbalanced by an intervalley scattering time τ_5 that inevitably is present. In the end, a steady state develops, which we took as a starting point in Eq. (3.1).

3.2.2 Magnetovortical response

An interesting property of the quantum theory of Weyl fermions is that the amount of left-handed and right-handed Weyl fermions is not separately conserved when subjected to externally applied magnetic and electric fields that are non-orthogonal. In vacuum this leads to an interesting paradox: particles of one chirality seem to disappear, whereas particles with the opposite chirality appear out of nothing. This phenomenon is called the chiral anomaly and it is proportional to $\mathbf{E} \cdot \mathbf{B}$ [83, 84]. In a condensed-matter system hosting Weyl cones the explanation of the chiral anomaly is straightforward. Namely, in a bandstructure the Weyl cones always come in pairs that are connected via the rest of the bandstructure [26]. Applying external electric and magnetic fields will subsequently transfer population from one cone to the other, thereby converting the quasiparticles from one type of chirality into the other. The result is a chiral imbalance, which is signaled by a distinct chemical potential $\mu_\pm$ for the cone with chirality $\pm$, which we already used in Eq. (3.1).

It is exactly this chiral imbalance that gives rise to interesting transport properties in the presence of an external magnetic field $\mathbf{B}$ and a vorticity $\boldsymbol{\omega} = (\boldsymbol{\nabla} \times \boldsymbol{v})/2$ due to a non-zero local velocity $\boldsymbol{v}$ of the fermion fluid [120]. The vorticity $\boldsymbol{\omega}$ is quantized in superfluids and superconductors, but we consider it here as a classical quantity that can be assigned to a flowing fermion fluid. Interestingly, very recently the electrons in graphene have been shown experimentally to act as a viscuous fluid that flows with a velocity profile that contains vorticity [121]. In addition, the quark-gluon plasma produced at the Large Hadron Collider is surmised to contain vorticity as well [68].

The most famous of these magnetovortical effects is the chiral magnetic

effect (CME) [54, 80, 81, 102], which constitutes an electric current density in the direction of an externally applied magnetic field: $\langle \boldsymbol{J}_e \rangle = \sigma^{\mathrm{CME}} \mathbf{B}$. The coupled magnetovortical response for the electric and energy current densities $\langle \boldsymbol{J}_e \rangle$ and $\langle \boldsymbol{J}_\varepsilon \rangle$ is neatly summarized in the response matrix

$$\begin{pmatrix} \langle \boldsymbol{J}_e \rangle \\ \langle \boldsymbol{J}_\varepsilon \rangle \end{pmatrix} = \begin{pmatrix} \sigma^{\mathrm{CME}} & \sigma^{\mathrm{CVE}} \\ \sigma_\varepsilon^{\mathrm{CME}} & \sigma_\varepsilon^{\mathrm{CVE}} \end{pmatrix} \begin{pmatrix} \mathbf{B} \\ 2\boldsymbol{\omega}/v_F^2 \end{pmatrix}, \tag{3.3}$$

with σ^{CVE}, $\sigma_\varepsilon^{\mathrm{CME}}$ and $\sigma_\varepsilon^{\mathrm{CVE}}$ the linear-response transport coefficients of the magnetovortical effects (CME/CVE) [122, 123]. This response matrix clarifies why the magnetovortical response is dissipationless. The pseudovectors $\mathbf{B}$ and $\boldsymbol{\omega}$ are odd under time reversal, just like the electric and energy current densities. The real part of the corresponding conductivities is therefore necessarily even under time reversal, signaling that the conductivities cannot be due to dissipation and hence warrant the name dissipationless.

The response matrix in Eq. (3.3) is written in terms of the electric and energy current density. In condensed matter, however, the natural reference energy for the carriers of charge and energy is the chemical potential. It is therefore customary to define the heat current density

$$\langle \boldsymbol{J}_Q \rangle \equiv \sum_{\chi=\pm} \left[\langle \boldsymbol{J}_\varepsilon^\chi \rangle + \frac{\mu_\chi}{e} \langle \boldsymbol{J}_e^\chi \rangle \right], \tag{3.4}$$

with $-e$ the electron charge and $\boldsymbol{J}_{e,\varepsilon}^\chi$ the currents per cone. The associated response matrix reads

$$\begin{pmatrix} \langle \boldsymbol{J}_e \rangle \\ \langle \boldsymbol{J}_Q \rangle \end{pmatrix} = \begin{pmatrix} \sigma^{\mathrm{CME}} & \sigma^{\mathrm{CVE}} \\ \sigma_Q^{\mathrm{CME}} & \sigma_Q^{\mathrm{CVE}} \end{pmatrix} \begin{pmatrix} \mathbf{B} \\ 2\boldsymbol{\omega}/v_F^2 \end{pmatrix}, \tag{3.5}$$

with

$$\sigma_Q^{\mathrm{CME}} \equiv \sum_{\chi=\pm} \left[\sigma_{\varepsilon,\chi}^{\mathrm{CME}} + \frac{\mu_\chi}{e} \sigma_\chi^{\mathrm{CME}} \right], \tag{3.6a}$$

$$\sigma_Q^{\mathrm{CVE}} \equiv \sum_{\chi=\pm} \left[\sigma_{\varepsilon,\chi}^{\mathrm{CVE}} + \frac{\mu_\chi}{e} \sigma_\chi^{\mathrm{CVE}} \right], \tag{3.6b}$$

where we used $\sigma^{\mathrm{CME}} = \sum_{\chi=\pm} \sigma_\chi^{\mathrm{CME}}$ and likewise for the other conductiv-

ities. All magnetovortical effects are only non-zero in the presence of a non-zero chiral imbalance and the off-diagonal elements of Eq. (3.5) also require a non-zero chemical potential, as we show later. There is a similar response matrix for the axial currents [124], which are defined as the difference between, instead of the sum of, the currents coming from the separate Weyl cones. In this case the corresponding transport coefficients all require a non-zero chemical potential μ and the off-diagonal components in Eq. (3.5) again require a non-zero chiral imbalance μ_5 as well. We, however, do not pursue this direction here, although our methods can easily be used in this case as well because the response is diagonal in the chirality [125].

We instead investigate how the magnetovortical transport changes upon tilting the cones. Due to the fact that the tilting direction breaks rotational symmetry, the response matrix from Eq. (3.5) is generalized to

$$\begin{pmatrix} \langle J_e^i \rangle \\ \langle J_Q^i \rangle \end{pmatrix} = \begin{pmatrix} \sigma_{ij}^{\mathrm{CME}} & \sigma_{ij}^{\mathrm{CVE}} \\ \sigma_{Q,ij}^{\mathrm{CME}} & \sigma_{Q,ij}^{\mathrm{CVE}} \end{pmatrix} \begin{pmatrix} B^j \\ 2\omega^j/v_F^2 \end{pmatrix}. \tag{3.7}$$

As it turns out the chiral magnetic conductivities remain isotropic, i.e., $\sigma_{ij}^{\mathrm{CME}} = \sigma^{\mathrm{CME}}\delta^{ij}$ and $\sigma_{Q,ij}^{\mathrm{CME}} = \sigma_Q^{\mathrm{CME}}\delta^{ij}$, which is a property that is ultimately enforced by the chiral anomaly. The vortical conductivities, on the other hand, become anisotropic and can be decomposed in a transverse and longitudinal part with respect to the tilting direction $\hat{t}^i = t^i/t$ as follows

$$\sigma_{ij}^{\mathrm{CVE}} = \sigma_{\perp}^{\mathrm{CVE}}\big(\delta_{ij} - \hat{t}_i\hat{t}_j\big) + \sigma_{\parallel}^{\mathrm{CVE}}\hat{t}_i\hat{t}_j, \tag{3.8}$$

and analogous expressions hold for the chiral vortical heat or energy conductivities.

We calculate all the magnetovortical transport coefficients in Section 3.4 in the long-wavelength limit and in addition obtain their frequency dependence. For the static and homogeneous limit we summarize all results obtained in Table 3.1. In Section 3.4.2 we comprehensively discuss all results presented there and give physical arguments to clarify them.

3.2.3 Thermoelectric transport

As alluded to before, Weyl cones also respond interestingly in the presence of an electric field $\mathbf{E}$ and a temperature gradient $\boldsymbol{\nabla} T$, even in the absence of

a chiral imbalance. In the case of a time-reversal symmetry breaking Weyl semimetal with two Weyl cones separated in momentum space, there is a topological off-diagonal response. Most famously, for non-tilted Weyl cones the associated intrinsic topological anomalous Hall effect (AHE) is given by [35]

$$\langle \boldsymbol{J}_e \rangle = \frac{e^2}{4\pi^2\hbar} \Delta \boldsymbol{k} \times \mathbf{E}, \tag{3.9}$$

with $\Delta \boldsymbol{k}$ the momentum-space separation between the Weyl nodes. Furthermore, the breaking of time-reversal symmetry allows for a topological thermal Hall effect (THE), which is the flow of a transverse heat current as a response to a temperature gradient in the absence of an electric current [126], i.e.,

$$\langle \boldsymbol{J}_Q \rangle = -\frac{k_B^2 T}{12\hbar} \Delta \boldsymbol{k} \times \boldsymbol{\nabla} T. \tag{3.10}$$

Due to the existence of thermoelectricity, we may also expect a transverse electric current due to a temperature gradient. Such an anomalous Nernst effect (ANE) is however absent in a simple, linear continuum model of the Weyl cones [127], but present in a more realistic two-band model [128]. Furthermore, we note that besides the intrinsic, topological contributions presented in Eqs. (3.9) and (3.10), extrinsic contributions due to skew and side-jump scattering of electrons off impurities may also be present [27]. From now on, however, we only consider the intrinsic, non-topological contributions to the thermoelectric response coefficients.

What happens to the thermoelectric response upon tilting the cones? Firstly, the transport coefficients are renormalized by the tilt [113, 128]. Secondly, the tilt introduces another time-reversal symmetry-breaking vector, thereby allowing for a different contribution to the anomalous Hall effect [2, 103, 105, 129] in Eq. (3.9), and to the thermal Hall effect [117] in Eq. (3.10). Additionally, the anomalous Nernst effect becomes non-zero, even in a linear model [117, 130–132]. The off-diagonal, explicitly tilt-dependent part of the response matrix for the total electric and heat current densities can then be written as

$$\begin{pmatrix} \langle \boldsymbol{J}_e \rangle \\ \langle \boldsymbol{J}_Q \rangle \end{pmatrix} = \begin{pmatrix} \sigma^{\mathrm{AHE}} & \alpha^{\mathrm{ANE}} T \\ \alpha^{\mathrm{ANE}} T & \bar{\kappa}^{\mathrm{THE}} T \end{pmatrix} \begin{pmatrix} \boldsymbol{t} \times \mathbf{E} \\ \boldsymbol{t} \times \boldsymbol{\nabla} T/T \end{pmatrix}, \tag{3.11}$$

with $\boldsymbol{t}$ the tilting direction. Onsager reciprocity forces the off-diagonal elements of the response matrix to be the same, so $\sigma_Q^{\mathrm{ANE}} \equiv \alpha^{\mathrm{ANE}} T$. In Eq. (3.11), we have defined the anomalous Nernst conductivity as by Niu *et al.* [133]. The anomalous Nernst coefficient can, however, also be defined as the steady-state constant of proportionality between the voltage difference due to the redistribution of charge caused by an applied temperature gradient in a sample without leads. The anomalous Nernst coefficient is then given by $\vartheta^{\mathrm{ANE}} \equiv -\alpha^{\mathrm{ANE}}/\sigma^{\mathrm{AHE}}$.

Thermal conductivity is defined as a heat current in the absence of a charge current, i.e. $\langle \boldsymbol{J}_Q \rangle = \kappa^{\mathrm{THE}} \boldsymbol{t} \times \boldsymbol{\nabla} T\big|_{\langle \boldsymbol{J}_e \rangle = \boldsymbol{0}}$. In this manner, the thermal Hall coefficient is found from Eq. (3.11) to be

$$\kappa^{\mathrm{THE}} = \bar{\kappa}^{\mathrm{THE}} - \frac{T(\alpha^{\mathrm{ANE}})^2}{\sigma^{\mathrm{AHE}}}, \tag{3.12}$$

where we only took off-diagonal contributions into account. In principle the linear-response coefficients σ^{AHE}, α^{ANE} and $\bar{\kappa}^{\mathrm{THE}}$ can be calculated by extracting from the off-diagonal part of the appropriate current-current correlators the contribution that is proportional to $\boldsymbol{t}$. However, when calculating the thermal transport coefficients α^{ANE} and $\bar{\kappa}^{\mathrm{THE}}$ a problem arises: they contain terms that are dependent on the chemical potential μ, but independent of the temperature T. From the response matrix in Eq. (3.11) it is clear that such a term renders the zero-temperature limit ill-defined. The physical explanation is that tilting the cones generates a non-zero magnetization density $\boldsymbol{M}$ in the direction of the tilt $\boldsymbol{t}$. Such a magnetization density in turn yields a circulating current of the form $\boldsymbol{\nabla} \times \boldsymbol{M}$, that gives a contribution to the transport coefficients coming from the Kubo formulas, but is unobservable with a transport measurement [51, 133, 134]. In order to calculate the transport current that can be measured in experiment, this superfluous term should therefore be subtracted. How this can be achieved is discussed in Section 3.5.1.

Having discussed the most important differences that occur in the magnetovortical and thermoelectric response due to tilting the Weyl cones, we now turn to a more in-depth discussion of how to calculate all the corresponding transport coefficients.

3.3 Linear-response theory

In this section we set up the linear-response theory necessary to derive all the transport coefficients that we discussed in the previous sections. Note that within linear response the magnetic field is small compared to the separation $|\Delta \boldsymbol{k}|$ between the Weyl nodes in momentum space, i.e., $\sqrt{e|\mathbf{B}|/\hbar} \ll |\Delta \boldsymbol{k}|$. The Weyl nodes are therefore not gapped out by the magnetic field in this regime [135].

We start by writing the action corresponding to the Hamiltonian Eq. (3.1) and giving the corresponding Green's function or propagator. We proceed by deriving the electric, momentum and energy currents using the Hamiltonian and the corresponding action. Subsequently, we discuss how these three currents give rise to nine different current-current correlation functions, of which six are relevant for the response matrices in Eqs. (3.3), (3.5) and (3.11) we set out to calculate. Finally, we derive and give explicit expressions for the antisymmetric part of the current-current correlation functions and discuss how they can be appropriately decomposed. In what follows we take $\hbar \equiv 1$ and $v_F \equiv 1$, only reinstating v_F in our final results.

3.3.1 Electronic action and Green's functions

For calculational purposes it is convenient to combine the two copies of the Hamiltonian from Eq. (3.1) for the two cones with opposite chirality into a Dirac-like action in terms of the four-component spinor ψ, i.e.,

$$S_0[\psi, \bar{\psi}] = \int \mathrm{d}^4x\, \bar{\psi}\big[-i\Gamma^\mu \partial_\mu - \mu\gamma^0 - \mu_5\gamma^0\gamma^5\big]\psi, \tag{3.13}$$

where γ^μ are the usual gamma matrices[c], $\bar{\psi} = \psi^\dagger\gamma^0$ and $\Gamma^\mu \equiv \gamma^\mu + \gamma^0 t^\mu$ with $t^\mu = (0, \boldsymbol{t})$ in the inversion-symmetry breaking case and $\Gamma^\mu \equiv \gamma^\mu + \gamma^0\gamma^5 t^\mu$ in the inversion-symmetric case. The Feynman propagator defined by Eq. (4.3) is given in momentum space by

$$S_F(k) \equiv i\big(k_\mu\Gamma^\mu - \mu\gamma^0 - \mu_5\gamma^0\gamma^5\big)^{-1} = i\begin{pmatrix} G_-(k) & 0 \\ 0 & G_+(k)\end{pmatrix}\gamma^0, \tag{3.14}$$

[c]For the gamma matrices we use the representation $\gamma^0 = i\sigma^y \otimes \mathbb{1}_2$, $\gamma^j = \sigma^x \otimes \sigma^j$ and $\gamma^5 = -\sigma^z \otimes \mathbb{1}_2$, such that they obey a Clifford algebra $\{\gamma^\mu, \gamma^\nu\} = 2\eta^{\mu\nu}$, with $\eta_{\mu\nu} = \mathrm{diag}(-,+,+,+)$ the mostly-plus Minkowski metric.

where we used the four-vector notation $k^\mu = (\omega, \boldsymbol{k})$ and introduced the propagator $G_\pm(k)$ for a single cone with chirality $\pm$. The Matsubara Green's function associated with the latter is given by

$$G_\chi(i\omega_n, \boldsymbol{k}) = \frac{1}{2}\sum_{u=\pm} \frac{\sigma^0 + \chi u \hat{\boldsymbol{k}}\cdot\boldsymbol{\sigma}}{i\omega_n + \mu_\chi - \varepsilon_{u\chi\boldsymbol{k}}}, \tag{3.15}$$

in terms of the fermionic Matsubara frequencies $\omega_n = (2n+1)\pi/\beta$ with $\beta \equiv 1/k_B T$ and $\hat{\boldsymbol{k}} = \boldsymbol{k}/|\boldsymbol{k}|$.

3.3.2 Electric current, energy current and momentum density

In order to calculate the coupled response matrices of the Weyl cones, we need to couple the electrons i) to an external gauge field A_μ; ii) to a temperature gradient $\boldsymbol{\nabla} T$ and iii) to the vorticity $\boldsymbol{\omega}$. The first of these three is achieved by applying the minimal-coupling procedure $\partial_\mu \psi \to \partial_\mu \psi + ieA_\mu \psi$ to the action in Eq. (4.3). This yields a coupling of the form $J_e^\mu A_\mu$, with $J_e^\mu \equiv e\bar{\psi}\Gamma^\mu\psi$ the electric current density in terms of the previously defined tilt-dependent vertex Γ^μ.

Secondly, we couple the fermions to a temperature gradient. This was pioneered by Luttinger [136] using a fictitious gravitational potential. Assuming a homogeneous temperature T, perturbed by small spatial variations $\delta T(\boldsymbol{x})$, the temperature profile can be written as

$$T(\boldsymbol{x}, t) = T + \delta T(\boldsymbol{x}) e^{-i\omega t}. \tag{3.16}$$

Such an inhomogeneous temperature can be shown to act as a perturbation on the Minkowski metric $\eta_{\mu\nu}$ [137]. In linear response the modified metric $g_{\mu\nu}$ is found to be

$$\mathrm{d}s^2 = \eta_{\mu\nu}\mathrm{d}x^\mu \mathrm{d}x^\nu - 2\frac{e^{-i\omega t}}{i\omega}\frac{\partial_j T}{T}\mathrm{d}x^j \mathrm{d}t, \tag{3.17}$$

such that the change in metric is $\delta g_{j0} = -e^{-i\omega t}\partial_j T/i\omega T$. Such metric fluctuations couple to the energy-momentum tensor $T^{\mu\nu}$ in the action as $\delta g_{\mu\nu} T^{\mu\nu}$, meaning that they act as a source for the energy-momentum tensor. The off-diagonal part of the metric in Eq. (3.17) thus couples to the energy current density $J_\varepsilon^\mu \equiv T^{\mu 0}$, which is defined by the conservation law of energy,

i.e.,

$$\partial_0 T^{00} + \partial_j T^{j0} \equiv \partial_t \mathcal{E} + \boldsymbol{\nabla} \cdot \boldsymbol{J}_\varepsilon = 0, \tag{3.18}$$

with $\mathcal{E}$ the canonical energy density. Physically, the energy current density is simply given by the hermitian, symmetrized expression of energy times the velocity. Using the action from Eq. (4.3), we find

$$T^{\mu 0} = \frac{i}{2}\Big[\partial_j \bar{\psi}\Gamma^j \gamma^0 \Gamma^\mu \psi - \bar{\psi}\Gamma^\mu \gamma^0 \Gamma^j \partial_j \psi\Big], \tag{3.19}$$

which depends on the tilt via Γ^μ. Note that we can also write an expression for $T^{\mu 0}$ in terms of only temporal derivatives by imposing the equations of motion. Our expression for $T^{\mu 0}$ obeys the conservation law Eq. (3.18) with the *canonical* energy density $\mathcal{E}(x) \equiv T^{00}$. Similarly, we could derive the heat current density $\boldsymbol{J}_Q$ by using the grand-canonical Hamiltonian density, that follows from Eq. (4.3), in the conservation law in Eq. (3.18).

Finally, we consider how to include a vorticity $\boldsymbol{\omega} = (\boldsymbol{\nabla} \times \boldsymbol{v})/2$. Giving the electron fluid a non-zero velocity $\boldsymbol{v}$ is achieved by performing a Galilean transformation on the Hamiltonian Eq. (3.1): $\mathcal{H}_\chi(\boldsymbol{k}) \to \mathcal{H}_\chi(\boldsymbol{k}) - \boldsymbol{k} \cdot \boldsymbol{v}$. Alternatively, to make the connection with the previous discussion, we can consider the velocity to be a perturbation on the metric, i.e., $\delta g_{0i} = v^i$. This part of the metric then couples to the momentum density $J_p^i \equiv T^{0i}$, which obeys the conservation law

$$\partial_0 T^{0i} + \partial_j \Pi^{ji} = 0, \tag{3.20}$$

with $\Pi^{ji} = i\big[\bar{\psi}\Gamma^j \partial^i \psi - \partial^i \bar{\psi}\Gamma^j \psi\big]/2$ the stress tensor. The momentum density is given explicitly by

$$J_p^\mu = T^{0\mu} = \frac{i}{2}\Big[\bar{\psi}\gamma^0 \partial^\mu \psi - \partial^\mu \bar{\psi}\gamma^0 \psi\Big], \tag{3.21}$$

from which the total (center-of-mass) momentum follows by averaging the spatial part over the whole space, i.e.,

$$\int \mathrm{d}\boldsymbol{x}\, \boldsymbol{J}_p(\boldsymbol{x}) = \sum_{\boldsymbol{k}} \psi_{\boldsymbol{k}}^\dagger \boldsymbol{k} \psi_{\boldsymbol{k}}, \tag{3.22}$$

as expected. As can be seen from Eqs. (3.19) and (3.21), the energy-momentum

tensor is not manifestly symmetric, which we discuss in more depth lateron. In principle it can be made symmetric by adding suitable boundary terms to the action. We, however, refrain from doing so because Eqs. (3.19) and (3.21) are the physical, conserved currents that are determined by the equations of motion for the Dirac field and the conservation laws in Eq. (3.18) and Eq. (3.20).

3.3.3 Current-current response functions and their decomposition

Having obtained the coupling between the fermions and the external perturbations, we can integrate out the fermions to arrive at the effective action for the external perturbations. This effective action is quadratic in the external gauge field A_μ and the fluctuation of the metric $\delta g_{\mu\nu}$. The electric (energy) current now follows in linear response from taking the functional derivative of the effective action with respect to the gauge field (metric fluctuation), leading to

$$\langle J^\mu_a(q)\rangle = \Pi^{\mu\nu}_{ae}(q)A_\nu(q) + \Pi^{\mu\nu}_{ap}(q)\delta g_{0\nu}(q) + \Pi^{\mu\nu}_{a\varepsilon}(q)\delta g_{\nu 0}(q), \tag{3.23}$$

with $a \in \{e, \varepsilon\}$. Note that in a similar manner we can compute the expectation value of the momentum density $\langle J^\mu_p(q)\rangle$, in which case the index a would be a 'p'. We focus here, however, on the experimentally more accessible electric and heat current densities.

To ensure causality the response functions $\Pi^{\mu\nu}_{ab}(q)$ are understood to be retarded. They can generically be written as

$$\begin{aligned} i\Pi^{\mu\nu}_{ab}(q) &\equiv -\int \mathrm{d}^4(x-y)\langle J^\mu_a(x)J^\nu_b(y)\rangle e^{-iq_\mu(x-y)^\mu} \\ &= \int \frac{d^4k}{(2\pi)^4}\mathrm{Tr}\big[\Lambda^\mu_a(k,q)S_F(k+q)\Lambda^\nu_b(k,q)S_F(k)\big], \end{aligned} \tag{3.24}$$

where we omitted disconnected contributions and contributions from the (energy) magnetization, to which we return later. The electric, momentum

and energy vertices are given by

$$\Lambda_e^\mu = e\Gamma^\mu, \tag{3.25a}$$

$$\Lambda_p^\mu(k,q) = -\frac{1}{2}\big(2k^\mu + q^\mu\big)\gamma^0, \tag{3.25b}$$

$$\Lambda_\varepsilon^\mu(k,q) = \frac{1}{2}\big(k_j + q_j\big)\Gamma^j\gamma^0\Gamma^\mu + \frac{1}{2}k_j\Gamma^\mu\gamma^0\Gamma^j. \tag{3.25c}$$

From the vertices and Eq. (3.24) it follows that $\Pi_{\varepsilon e}^{\mu\nu}(q) = \Pi_{e\varepsilon}^{\nu\mu}(-q)$, and similarly for other mixed current-current correlators.

The response matrices from Eqs. (3.3), (3.5) and (3.11) can now be derived by focussing on the antisymmetric part of the current-current response functions. Writing out the dependence on $\boldsymbol{q}$ and $\boldsymbol{t}$ explicitly, their antisymmetric part is given by $\Pi_{ab}^k(\omega,\boldsymbol{q};\boldsymbol{t}) \equiv \varepsilon^{ijk}\Pi_{ab}^{ij}(\omega,\boldsymbol{q};\boldsymbol{t})/2$. This antisymmetric part is a vector itself that is spanned by $\boldsymbol{t}$ and $\boldsymbol{q}$ [2]. We can therefore decompose the relevant current-current response functions as follows

$$i\Pi_{ee}^k(\omega,\boldsymbol{q};\boldsymbol{t}) = \sigma^{\mathrm{CME}}q^k + \sigma^{\mathrm{AHE}}\omega t^k, \tag{3.26a}$$

$$i\Pi_{\varepsilon e}^k(\omega,\boldsymbol{q};\boldsymbol{t}) = \sigma_\varepsilon^{\mathrm{CME}}q^k + \alpha_\varepsilon^{\mathrm{ANE}}T\omega t^k, \tag{3.26b}$$

$$i\Pi_{\varepsilon\varepsilon}^k(\omega,\boldsymbol{q};\boldsymbol{t}) = C_{\varepsilon\varepsilon}q^k + \bar{\kappa}_\varepsilon^{\mathrm{THE}}T\omega t^k, \tag{3.26c}$$

$$i\Pi_{ep}^k(\omega,\boldsymbol{q};\boldsymbol{t}) = \sigma_\parallel^{\mathrm{CVE}}q^k + 2\big(\sigma_\perp^{\mathrm{CVE}} - \sigma_\parallel^{\mathrm{CVE}}\big)(\boldsymbol{q}\cdot\hat{\boldsymbol{t}})\hat{t}^k, \tag{3.26d}$$

$$i\Pi_{\varepsilon p}^k(\omega,\boldsymbol{q};\boldsymbol{t}) = \sigma_{\varepsilon,\parallel}^{\mathrm{CVE}}q^k + 2\big(\sigma_{\varepsilon,\perp}^{\mathrm{CVE}} - \sigma_{\varepsilon,\parallel}^{\mathrm{CVE}}\big)(\boldsymbol{q}\cdot\hat{\boldsymbol{t}})\hat{t}^k, \tag{3.26e}$$

where all transport coefficients are a function of ω and $\boldsymbol{q}$. A few remarks are in order about these decompositions:

1) In principle there could be terms proportional to $(\boldsymbol{q}\times\boldsymbol{t})^k$ present in the decompositions as well. For $a,b \in \{e,\varepsilon\}$ we have $\Pi_{ab}^k(\omega,\boldsymbol{q};\boldsymbol{t}) = -\Pi_{ab}^k(\omega,-\boldsymbol{q};-\boldsymbol{t})$, meaning that such terms are not allowed. The other two correlators do not obey this symmetry and such terms are thus allowed. However, they can be shown to vanish in the long-wavelength limit and we therefore do not consider them here.

2) The last two decompositions do not contain a term proportional to ωt^k like the first three because $i\Pi_{ep}^k(\omega,\boldsymbol{0};\boldsymbol{t}) = i\Pi_{\varepsilon p}^k(\omega,\boldsymbol{0};\boldsymbol{t}) = 0$.

3) The first two decompositions do not contain a term proportional to $(\boldsymbol{q}\cdot\hat{\boldsymbol{t}})\hat{t}^k$ because such a term would violate the residual invariance under

time-independent gauge transformations that are consistent with our gauge choice $A_0 = 0$, which we use throughout this chapter.

4) The term proportional to $C_{\varepsilon\varepsilon}$ is of no interest to us because it yields zero upon contracting it with $\epsilon_{ijk}q^jT/i\omega$ to compute the energy current.

Using the decompositions in Eqs. (3.26a)-(3.26e), the resulting current densities can easily be derived in linear response from Eq. (3.23). As the magnetic field is given in momentum space by $B^i = i\varepsilon^{ijk}q^jA^k$ and the velocity can be written in terms of the vorticity as $v^i = \varepsilon^{ijk}\omega^jx^k$, we find, for instance, for the magnetovortical response in the electric current density

$$\begin{aligned}\langle J_e^i\rangle &= \Pi_{ee}^{ij}A^j + \Pi_{ep}^{ij}v^j \\ &= \sigma^{\mathrm{CME}}B^i + 2\sigma_{\parallel}^{\mathrm{CVE}}\omega^i - 2\varepsilon^{ijk}\big(\sigma_{\perp}^{\mathrm{CVE}} - \sigma_{\parallel}^{\mathrm{CVE}}\big)\hat{t}^l\hat{t}^k\partial^l v^j \\ &= \sigma^{\mathrm{CME}}B^i + 2\sigma_{\perp}^{\mathrm{CVE}}\big(\delta^{ij} - \hat{t}^i\hat{t}^j\big)\omega^j + 2\sigma_{\parallel}^{\mathrm{CVE}}\hat{t}^i\hat{t}^j\omega^j. \end{aligned} \tag{3.27}$$

Similarly, $\sigma_{Q,\perp}^{\mathrm{CVE}}$ and $\sigma_{Q,\parallel}^{\mathrm{CVE}}$ can be derived such that the full magnetovortical response matrix from Eq. (3.5) is obtained once all coefficients in the decompositions in Eqs. (3.26a), (3.26d) and (3.26e) have been calculated.

Using the same procedure we can derive the thermoelectric response matric in Eq. (3.11) from the decompositions in Eqs. (3.26a), (3.26b) and (3.26c). However, as explained in the previous section, the coefficients $\alpha_{\varepsilon}^{\mathrm{ANE}}$ and $\bar{\kappa}_{\varepsilon}^{\mathrm{THE}}$ do not yet constitute the actual anomalous Nernst and thermal Hall transport coefficients. To obtain α^{ANE} and $\bar{\kappa}^{\mathrm{THE}}$ we need to consider the response of the heat current and not the energy current. In order to calculate the transport coefficients associated with the heat current, we need to obtain the current-current correlators $\langle J_Q^i(x)J_b^j(y)\rangle$ with $b \in \{e, p\}$. Using Eq. (3.4) the corresponding response functions $\Pi_{Qb}^{ij}(q)$ are given by linear combinations of the decompositions in Eqs. (3.26a)-(3.26e), i.e.,

$$\Pi_{Qb}^{ij}(q) = \Pi_{\varepsilon b}^{ij}(q) + \sum_{\chi=\pm}\frac{\mu_\chi}{e}\Pi_{eb}^{ij,\chi}(q), \tag{3.28}$$

where $\Pi_{eb}^{ij,\chi}(q)$ is the contribution of the cone with chirality χ to $\Pi_{eb}^{ij}(q)$.

Besides making this linear combination, for the thermoelectric coefficients we also need to subtract the superfluous contribution coming from the ro-

tating currents due to the electric and heat orbital magnetizations M_e^{orb} and M_Q^{orb}, respectively. We show in Section 3.5.1 how these contributions naturally occur as diamagnetic-like contributions to the effective action and compute them explicitly.

3.3.4 Explicit expressions for the current-current response functions

As an example, let us consider the computation of $i\Pi^k_{ep}(\omega, \boldsymbol{q}; \boldsymbol{t})$ in some more detail. All other current-current correlators can be computed in a similar manner, albeit in terms of lengthier expressions. Upon restricting to spatial indices and going from real to imaginary time, we find, using Eq. (3.24) and the vertices in Eq. (3.25a) and Eq. (3.25b),

$$i\Pi^{ij}_{ep}(i\omega_b, \boldsymbol{q}; \boldsymbol{t}) = -\frac{ie}{2\beta}\sum_{\chi, i\omega_n}\chi\int_{\boldsymbol{k}}(2k^j + q^j) \\ \times \mathrm{Tr}\big[(\sigma^i + \chi t^i_\chi)G_\chi(i\omega_n + i\omega_b, \boldsymbol{k}+\boldsymbol{q})G_\chi(i\omega_n, \boldsymbol{k})\big], \quad (3.29)$$

with $i\omega_b$ an external bosonic Matsubara frequency and $\int_{\boldsymbol{k}} \equiv \int \mathrm{d}^3\boldsymbol{k}/(2\pi)^3$. Substituting the Matsubara Green's function from Eq. (4.4), we perform the trace and Matsubara sum [111] and Wick rotate back to real frequencies to find for the retarded current-current correlator

$$i\Pi^{ij}_{ep}(\omega, \boldsymbol{q}; \boldsymbol{t}) = -\frac{ie}{4}\sum_{\chi,u,v=\pm}u\int_{\boldsymbol{k}}\frac{N^\chi_{uv}(\omega, \boldsymbol{q}, \boldsymbol{t}, \boldsymbol{k})}{|\boldsymbol{k}+\boldsymbol{q}|}\Big[iv\chi(\boldsymbol{q}\times\hat{\boldsymbol{k}})^i \\ + uv|\boldsymbol{k}+\boldsymbol{q}|\hat{k}^i + k^i + q^i + v(|\boldsymbol{k}| + \hat{\boldsymbol{k}}\cdot\boldsymbol{q})t^i_\chi\Big](2k^j + q^j), \quad (3.30)$$

where we defined the function [102]

$$N^\chi_{uv}(\omega, \boldsymbol{q}, \boldsymbol{t}, \boldsymbol{k}) \equiv \frac{N_{\mathrm{FD}}(\varepsilon_{v\chi\boldsymbol{k}} - \mu_\chi) - N_{\mathrm{FD}}(\varepsilon_{u\chi\boldsymbol{k}+\boldsymbol{q}} - \mu_\chi)}{\omega^+ + \varepsilon_{v\chi\boldsymbol{k}} - \varepsilon_{u\chi\boldsymbol{k}+\boldsymbol{q}}} \\ = \frac{vN_{\mathrm{FD}}(v\varepsilon_{v\chi\boldsymbol{k}} - v\mu_\chi) - uN_{\mathrm{FD}}(u\varepsilon_{u\chi\boldsymbol{k}+\boldsymbol{q}} - u\mu_\chi) + \frac{1}{2}(u-v)}{\omega^+ + \varepsilon_{v\chi\boldsymbol{k}} - \varepsilon_{u\chi\boldsymbol{k}+\boldsymbol{q}}}, \quad (3.31)$$

with $N_{\mathrm{FD}}(x) \equiv (e^{\beta x}+1)^{-1}$ the Fermi-Dirac distribution and $\varepsilon_{n\chi\boldsymbol{k}}$ the dispersion relation defined in Eq. (3.2). In the second step we used the identity

$N_{\mathrm{FD}}(x) = 1 - N_{\mathrm{FD}}(-x)$, such that the terms proportional to $(u-v)/2$ explicitly represent the contribution from the Dirac sea that yields an ultraviolet divergence when integrated in Eq. (3.30) over all $\boldsymbol{k}$. For the first term in Eq. (3.30), which is proportional to χ, this divergence is exactly cancelled upon carrying out the sum over the two cones. In fact, the first term proportional to χ in Eq. (3.30) is the only one of interest to us, because the other terms do not contribute to the antisymmetric part of the current-current correlation function in the long-wavelength limit. This can be shown by realizing that

$$\begin{aligned} N^{\chi}_{uv}(\omega, \boldsymbol{q}, \boldsymbol{t}, \boldsymbol{k}) &= N^{\chi}_{uv}(\omega, -\boldsymbol{q}, -\boldsymbol{t}, -\boldsymbol{k}) \\ &= \left[N^{\chi}_{vu}(-\omega, -\boldsymbol{q}, \boldsymbol{t}, \boldsymbol{k}+\boldsymbol{q})\right]^{*}. \end{aligned} \tag{3.32}$$

Using these relations to explicitly symmetrize the integrand in Eq. (3.30) and subsequently going to the long-wavelength limit shows that the last four terms do not contribute in this limit. Therefore we focus on the antisymmetric part of the first term in Eq. (3.30). In the end, we can write the remaining result as

$$i\Pi^{k}_{ab}(\omega, \boldsymbol{q}; \boldsymbol{t}) = \frac{1}{4} \sum_{\chi,u,v=\pm} \chi \int_{\boldsymbol{k}} N^{\chi}_{uv}(\omega, \boldsymbol{q}, \boldsymbol{t}, \boldsymbol{k}) f^{k,uv}_{ab}(\boldsymbol{q}, \boldsymbol{t}_{\chi}, \boldsymbol{k}), \tag{3.33}$$

with

$$f^{k,uv}_{ep}(\boldsymbol{q}, \boldsymbol{t}, \boldsymbol{k}) = \frac{euv(2\boldsymbol{k}+\boldsymbol{q}) \cdot \left(\boldsymbol{q}\, k^{k} - \boldsymbol{k}\, q^{k}\right)}{2|\boldsymbol{k}||\boldsymbol{k}+\boldsymbol{q}|}. \tag{3.34}$$

In a similar fashion we obtain $f^{k,uv}_{ab}(\boldsymbol{q}, \boldsymbol{t}, \boldsymbol{k})$ for the other current-current correlators. As they are rather lengthy, we present them in Appendix 3.A. The most important point to note is that $f^{k,uv}_{ee}(\boldsymbol{q}, \boldsymbol{t}, \boldsymbol{k})$, $f^{k,uv}_{e\varepsilon}(\boldsymbol{q}, \boldsymbol{t}, \boldsymbol{k})$ and $f^{k,uv}_{\varepsilon\varepsilon}(\boldsymbol{q}, \boldsymbol{t}, \boldsymbol{k})$ contain terms that do not vanish at $\boldsymbol{q} = \boldsymbol{0}$. It is exactly these terms that lead to σ^{AHE}, $\alpha^{\mathrm{ANE}}_{\varepsilon}$ and $\bar{\kappa}^{\mathrm{THE}}_{\varepsilon}$ in the decompositions in Eqs. (3.26a), (3.26b) and (3.26c).

Now that we have explained how to obtain and decompose the relevant current-current correlation function, we use them in the next section to calculate the magnetovortical response in several cases of interest.

3.4 Anisotropic magnetovortical transport

In order to calculate the magnetovortical effects, we thus need to calculate the contributions in Eqs. (3.26a)-(3.26e) that are linear in q^k. From, e.g., Eq. (3.34) we see that the current-current response functions contain terms in their integrands that are already explicitly proportional to q^k, but also terms proportional to k^k. The latter types of term give, upon integration, terms proportional to q^k and t^k. By forming linear combinations of the projections of $\Pi^k_{ab}(\omega, \boldsymbol{q}; \boldsymbol{t})$ onto q^k and t^k we can extract the part that is proportional to q^k. For instance,

$$\sigma^{\mathrm{CME}}(\omega, \boldsymbol{q}) = \left[\frac{|\boldsymbol{t}|^2 q_k - (\boldsymbol{q}\cdot\boldsymbol{t})t_k}{|\boldsymbol{q}|^2|\boldsymbol{t}|^2 - (\boldsymbol{q}\cdot\boldsymbol{t})^2}\right] i\Pi^k_{ee}(\omega, \boldsymbol{q}; \boldsymbol{t}), \tag{3.35}$$

and similarly for the other transport coefficients. We will calculate the magnetovortical transport coefficients both in the long-wavelength limit and compute their frequency dependence, starting with the former. It turns out that the magnetovortical transport coefficients are invariant under $\boldsymbol{t} \to -\boldsymbol{t}$ in the static and homogeneous limit. The same is true for the frequency-dependent conductivities. It thus does not matter in these cases if we consider inversion-symmetry breaking or retaining tilt. We therefore focus on the inversion-symmetry breaking case and use $\boldsymbol{t}_\chi = \boldsymbol{t}$ in this section.

3.4.1 Long-wavelength limit

It is well-known that the long-wavelength limit of current-current response functions depends on the order of limits [138]. Therefore, we expand the expressions for the current-current response functions for small $|\boldsymbol{q}|$ and ω, but keep the fraction $x \equiv \omega/v_F|\boldsymbol{q}|$ fixed, such that $x \to 0$ corresponds to the static limit and $x \to \infty$ to the homogeneous, or transport limit. Using this procedure on $N^\chi_{uv}(\omega, \boldsymbol{q}, \boldsymbol{t}, \boldsymbol{k})$ yields a Fermi sea (interband) contribution when $uv = -1$, i.e., at $T = 0$ we find

$$N^\chi_{-+}(\omega, \boldsymbol{q}, \boldsymbol{t}, \boldsymbol{k}) \approx \left[1 - \frac{\omega}{2v_F|\boldsymbol{k}|} + \frac{\boldsymbol{q}\cdot\boldsymbol{t}}{2|\boldsymbol{k}|} - \frac{\boldsymbol{k}\cdot\boldsymbol{q}}{2|\boldsymbol{k}|^2}\right] \frac{N_{\mathrm{FD}}(\varepsilon_{+\chi\boldsymbol{k}} - \mu_\chi)}{2v_F|\boldsymbol{k}|}, \tag{3.36}$$

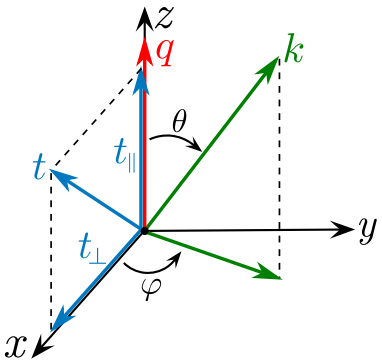

Figure 3.2: Coordinate system used to calculate the tilt-dependent magnetovortical transport coefficients in the long-wavelength limit. We choose the coordinate system such that the vector $\boldsymbol{q}$ (depicted in red) lies along the z-axis and the vector $\boldsymbol{t}$ (depicted in blue) in the xz-plane. Therefore: $\boldsymbol{k}\cdot\boldsymbol{q} = |\boldsymbol{k}||\boldsymbol{q}|\cos\theta$, $\boldsymbol{q}\cdot\boldsymbol{t} = qt_{\parallel}$ and $\boldsymbol{k}\cdot\boldsymbol{t} = k(t_{\perp}\cos\varphi\sin\theta + t_{\parallel}\cos\theta)$ with $\varphi \in [0, 2\pi)$ and $\theta \in [0, \pi]$.

from which $N_{+-}(\omega, \boldsymbol{q}, \boldsymbol{t}, \boldsymbol{k})$ follows by using Eq. (3.32). When $u = v = +1$ we find a Fermi surface (intraband) contribution given by

$$N^{\chi}_{++}(\omega, \boldsymbol{q}, \boldsymbol{t}, \boldsymbol{k}) \overset{|\boldsymbol{q}|\to 0}{=} -\frac{\big(\hat{\boldsymbol{q}}\cdot\boldsymbol{t} + \hat{\boldsymbol{k}}\cdot\hat{\boldsymbol{q}}\big)N'_{\mathrm{F}}(\varepsilon_{+\chi\boldsymbol{k}} - \mu_{\chi})}{\omega/v_F|\boldsymbol{q}| - \hat{\boldsymbol{q}}\cdot\boldsymbol{t} - \hat{\boldsymbol{k}}\cdot\hat{\boldsymbol{q}}}, \tag{3.37}$$

with $N'_{\mathrm{F}}(x)$ the derivative of the Fermi-Dirac distribution. We thus observe that in the homogeneous limit this last term does not contribute, whereas in the static limit it does contribute. Finally, we note that at $T = 0$ the term with $u, v = -$ yields zero.

Armed with these expansions we calculate the magnetovortical response in the long-wavelength limit. Using the coordinate system illustrated in Fig. 3.2, we find for the chiral magnetic conductivities

$$\sigma^{\mathrm{CME}}(\omega/v_F|\boldsymbol{q}|) = \frac{e^2\mu_5}{2\pi^2}(1-t^2)W(\omega/v_F|\boldsymbol{q}|;\boldsymbol{t}), \tag{3.38a}$$

$$\sigma^{\mathrm{CME}}_{\varepsilon}(\omega/v_F|\boldsymbol{q}|) = -\frac{e\mu\mu_5}{2\pi^2}\big[2(1-t^2)W(\omega/v_F|\boldsymbol{q}|;\boldsymbol{t}) - 1\big], \tag{3.38b}$$

and similar, but lengthier, expressions for the vortical effects. The function

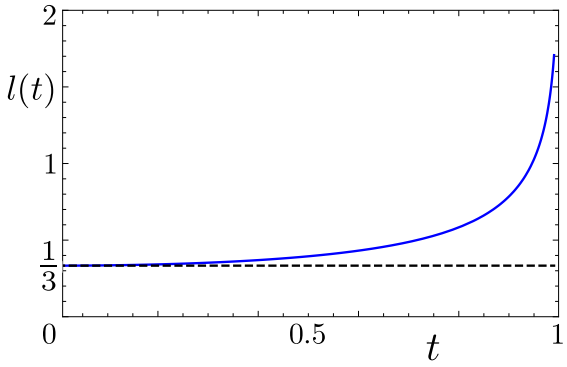

Figure 3.3: Plot of the function $l(t)$ from Eq. (3.40). It goes to the constant value of $1/3$ for small t (indicated by the dashed black line) and diverges when $t \to 1$, which signals the Lifshitz transition from a type-I to a type-II Weyl cone.

$W(\omega/v_F|\boldsymbol{q}|;\boldsymbol{t})$ is given explicitly in Appendix 3.A. In general it depends on the angle between $\boldsymbol{q}$ and $\boldsymbol{t}$, but in the static and homogeneous limit it reduces to an angle-independent result given by

$$W(\omega/v_F|\boldsymbol{q}|;\boldsymbol{t}) = \begin{cases} (1-t^2)^{-1} & \text{for} \quad \omega/v_F|\boldsymbol{q}| \to 0, \\ l(t) & \text{for} \quad \omega/v_F|\boldsymbol{q}| \to \infty, \end{cases} \tag{3.39}$$

in terms of the function, c.f. Fig. 3.3,

$$l(t) \equiv \frac{1}{2t^3} \log\left(\frac{1+t}{1-t}\right) - \frac{1}{t^2} \overset{t\to 0}{=} \frac{1}{3}. \tag{3.40}$$

To illustrate its angle-dependence, we show a polar plot of the function $W(\omega/v_F|\boldsymbol{q}|;\boldsymbol{t})$ in Fig.3.4. The fact that in the long-wavelength limit the transport properties depend on the tilting direction in a non-trivial way, is of importance for, for instance, the phenomenon of chiral magnetic waves [139, 140]. These are massless sound-like excitations in a fluid of chiral fermions. To understand how such excitations occur, we consider local fluctuations of the number densities $\delta n_\pm$ pertaining to the cone with chirality $\pm$. Assuming the fluctuations to be small, we may write $\delta\mu_\pm = \delta n_\pm/\chi^\pm_{nn}$ in the current due to the chiral magnetic effect, with $\chi^\pm_{nn} = \partial n_\pm/\partial\mu_\pm$ the corresponding susceptibilities. Considering the case of zero electric field, there is no chiral

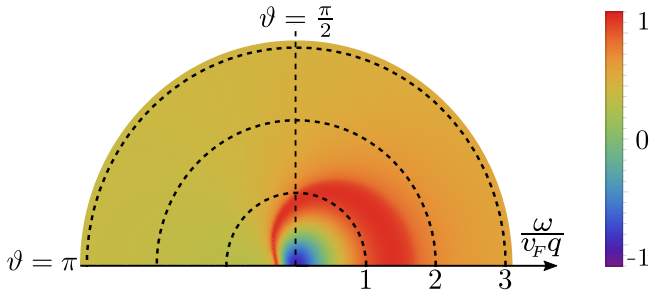

Figure 3.4: Polar plot of the function $W(x, \boldsymbol{t})$ from Eq. (3.39) for $t = 7/10$. The radial coordinate is $x = \omega/v_F q$ and the angle ϑ is defined by $\boldsymbol{q} \cdot \boldsymbol{t} = |\boldsymbol{q}||\boldsymbol{t}| \cos\vartheta$. The homogeneous limit is obtained for large radii and becomes angle-independent. Likewise, the static limit is reached for vanishing radii and also becomes angle-independent.

anomaly and we find from current conservation that

$$\left(\partial_t \pm \frac{eB_z}{4\pi^2 \chi^{\pm}_{nn}} \partial_z\right) \delta n_{\pm} = 0, \tag{3.41}$$

where we took for simplicity a magnetic field in the z-direction. If the susceptibilities were constant and isotropic, the dispersion relations following from Eq. (3.41) would read $\omega^{\pm}_{\boldsymbol{q}} = \pm v^{\pm}_{\mathrm{CMW}} q_z$, with $v^{\pm}_{\mathrm{CMW}} = eB_z/4\pi^2 \chi^{\pm}_{nn}$. The susceptibilities, however, are anisotropic due to the tilting of the cones and in addition have a non-trivial frequency and wavenumber dependence. From the density-density response function $\Pi^{00}_{ee}(\omega, \boldsymbol{q}; \boldsymbol{t})/e^2$, we find for the susceptibilities

$$\begin{aligned} \chi^{\chi}_{nn}(\omega, \boldsymbol{q}; \boldsymbol{t}) &= -\frac{1}{2} \sum_{u,v=\pm} \int_{\boldsymbol{k}} \left(1 + uv \frac{|\boldsymbol{k}|^2 + \boldsymbol{k} \cdot \boldsymbol{q}}{|\boldsymbol{k}||\boldsymbol{k} + \boldsymbol{q}|}\right) N^{\chi}_{uv}(\omega, \boldsymbol{q}, \boldsymbol{t}, \boldsymbol{k}) \\ &\overset{|\boldsymbol{q}|\to 0}{=} \int_{\boldsymbol{k}} \frac{(\hat{\boldsymbol{k}} \cdot \hat{\boldsymbol{q}} + \hat{\boldsymbol{q}} \cdot \boldsymbol{t}) N'_{\mathrm{F}}(\varepsilon_{+\chi \boldsymbol{k}} - \mu_{\chi})}{\omega/v_F |\boldsymbol{q}| - \hat{\boldsymbol{q}} \cdot \boldsymbol{t} - \hat{\boldsymbol{k}} \cdot \hat{\boldsymbol{q}}}, \end{aligned} \tag{3.42}$$

where we used Eq. (3.37) and reinstated v_F. The remaining integral can be performed exactly by using the coordinate system of Fig. 3.2 and yields an analytical result, c.f. Appendix 3.A, in terms of the function $W(x; \boldsymbol{t})$. At

zero frequency the obtained expression reduces to

$$\chi^{\pm}_{nn}(0,\mathbf{0};\boldsymbol{t}) = \frac{\mu_{\pm}^2}{2\pi^2(1-t^2)^2 v_F^3} = \frac{\partial n_{\pm}}{\partial \mu_{\pm}}, \tag{3.43}$$

as it should. Fourier transforming Eq. (3.41) and using the result we obtained for $\chi^{\pm}_{nn}(0,\mathbf{0};\mathbf{0})$ to make the resulting equation dimensionless, we find

$$2\left(\frac{\omega}{v_F q_z}\right)\frac{\chi^{\pm}_{nn}(\omega,\boldsymbol{q};\boldsymbol{t})}{\chi^{\pm}_{nn}(0,\mathbf{0};\mathbf{0})} = \pm\frac{eB_z v_F^2}{\mu_{\pm}^2}, \tag{3.44}$$

from which the dispersion relation $\omega_{\boldsymbol{q}}$ can be found by solving the equation self-consistently. In our discussion we focus on the wave that propagates in the direction of the magnetic field, which corresponds to the plus sign in Eq. (3.44). To find the dispersion relation, we resort to numerics. For $t = 0$, there are two solutions: one with a relatively high velocity that is highly damped and another solution with a lower velocity and corresponding lower damping. At a critical value for the dimensionless parameter $eB_z v_F^2/\mu_+^2$ these two solutions meet and above this value there are no solutions with a real part. We plot these solutions as a function of $eB_z v_F^2/\mu_+^2$ in Fig. 3.5(a), together with the result that is obtained by simply using the static-limit result for $\chi^{+}_{nn}(\omega,\boldsymbol{q};\boldsymbol{t})$. This plot shows that it is a rather good approximation to neglect the wavenumber dependence of the susceptibility, as only for relatively large values of $eB_z v_F^2/\mu_+^2$ the solutions start to deviate. In addition, we note that the expression for the susceptibility itself in Eq. (3.42) is only valid for weak magnetic fields.

The situation changes drastically upon tilting the cones. Firstly, the tilt renormalizes the magnitude of the susceptibility in Eq. (3.42). As can be seen most clearly from the static-limit result in Eq. (3.43), the susceptibility becomes ever larger as $t \to 1$, signaling the Lifschitz transition from a type-I to a type-II Weyl cone. From Eq. (3.44) we see that this causes the velocity of the (least-damped) chiral wave to become significantly smaller as t increases. We illustrate this behavior in Fig. 3.5(a). Another interesting consequence of tilting the cones is the fact that the dispersion relation becomes dependent on the angle ϑ between the magnetic field and the tilting direction. This is what we illustrate in Fig. 3.5(b) for one value of the dimensionless parameter $eB_z v_F^2/\mu_+^2$ and several values of t.

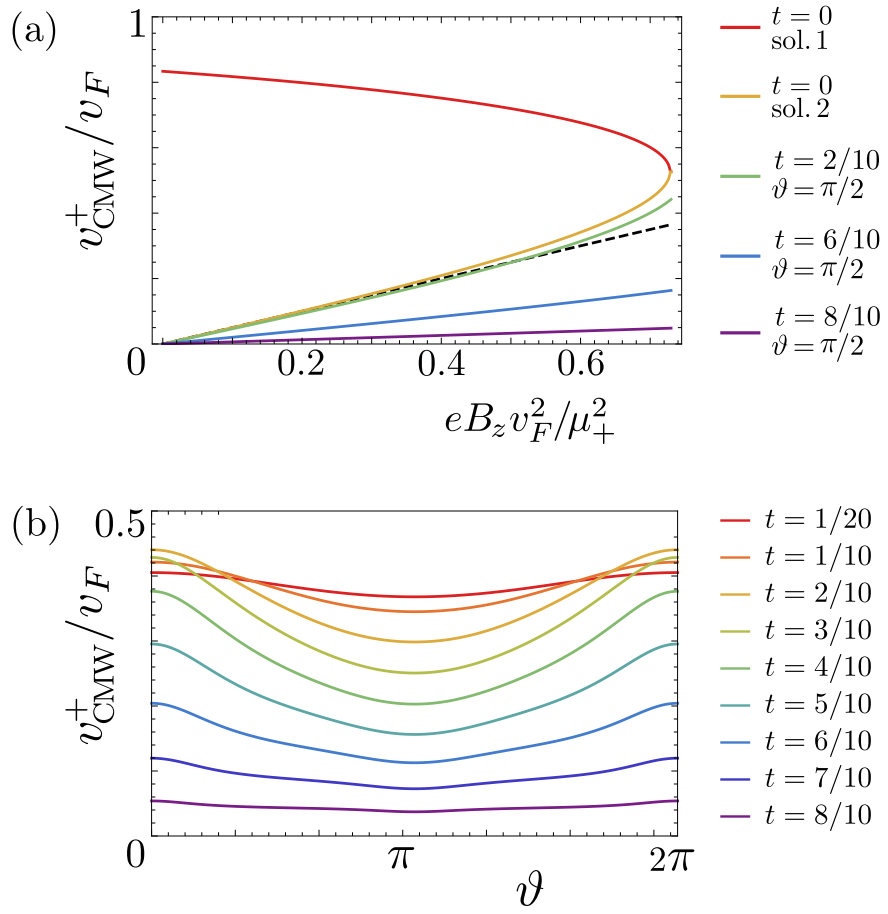

Figure 3.5: (a) Plot of the chiral magnetic wave velocity (for a positive chirality) as a function of the dimensionless parameter $eB_z v_F^2/\mu_+^2$. The black dashed line indicates the result obtained by using the static-limit result for the susceptibility, which simply yields a linear function with a slope of 1/2. The (from top to bottom) first and second curve give the highly damped and less-damped solutions at $t = 0$, obtained by including the wavenumber and frequency dependence of the susceptibility in the long-wavelength limit. The last three plots show the least damped solution for several values of t and $\mathbf{B} \cdot \boldsymbol{t} = 0$. (b) Plot of the chiral magnetic wave velocity as a function of the angle ϑ between the magnetic field and the tilting direction. Here, we took $eB_z v_F^2/\mu_+^2 = 0.65$ and show the angle-dependence for several values of t. For small t, the velocity goes to a non-zero value and becomes angle-independent, whereas for $t \to 1$ its magnitude goes to zero.

From the plots we observe again that as t grows, the velocity of the chiral magnetic wave goes to zero. Moreover, Fig. 3.5(b) shows that there is a quantitative difference between the case in which $\mathbf{B}$ is pointing in the same direction as $\boldsymbol{t}$ ($\vartheta = 0$) and the case in which they are pointing in opposite directions ($\vartheta = \pi$). This is not surprising as the tilt breaks rotational invariance and introduces a preferred direction, which is also observable in Fig. 3.4.

To conclude this discussion of the anisotropic chiral magnetic wave, it is important to remark that in a material with a non-zero density of electrons, the dispersion of the chiral magnetic wave will inevitably be pushed up to the plasma frequency due to the fact that these chiral magnetic waves necessarily involve charge density fluctuations [141–143]. A way around this is by considering not a single pair but rather two pairs of Weyl cones, yielding a total of four cones. We can then tune the chemical potentials such that the total chemical potential is zero, whereas the two pairs of cones have opposite chiral chemical potential. In this scenario, one of the chiral magnetic wave remains gapless because it does not involve fluctuations of the charge density.

3.4.2 Static and homogeneous limit

Having studied the tilt-induced anisotropic behavior in the long-wavelength limit, we now specialize to two special cases of the long-wavelength limit: the static and the homogeneous limit. We summarize the results obtained for the various current-current correlators in the static and homogenous limit in Table 3.1 and proceed by discussing the results presented in this table in detail.

The first thing to note from Table 3.1 is that the transport coefficients are non-zero in the static limit. In the case of the chiral magnetic conductivity this initially led to the believe that this constituted an equilibrium magnetic-field-driven current [35], which appears to be unphysical as there can be no currents in equilibrium due to the Kohn theorem. The solution to this conundrum lies in the fact that the results in Table 3.1 only hold for an energy difference $\Delta E = 0$ between the Weyl nodes [98, 109]. Taking ΔE into account amounts to the replacement $\mu_5 \to \mu_5 + \Delta E/2$, leading to the vanishing of the currents in equilibrium since the system is in equilibrium when $2\mu_5 = -\Delta E$.

Secondly, we note that our results for the vortical effects differ in the static

and homogeneous limit from earlier obtained results for $t = 0$ by Landsteiner *et al.* [120, 124]. The reason is that the authors of these references use a different set of currents. We derived the momentum density in Eq. (3.21) and energy current in Eq. (3.19) directly from the conservation laws that they obey and the equations of motion of the Dirac field. Landsteiner *et al.*, instead, use the symmetrized energy-momentum tensor as the energy current. This coincides with $(J_p^i + J_\varepsilon^i)/2$ in our definitions. Due to this symmetric definition they find that the chiral vortical conductivity σ^{CVE} and chiral magnetic energy conductivity $\sigma_\varepsilon^{\mathrm{CME}}$ are the same in the static limit. In Table 3.2 we show that upon taking the appropriate linear combinations, our results coincide at $t = 0$ in both the static and the homogeneous limit with those of Landsteiner *et al.*

Thirdly, it is interesting to note that the chiral magnetic conductivities are universal in the static limit, i.e., they do not dependent on the tilt of the Weyl cones. The other magnetovortical effects are, however, not universal in the static limit. The former can be understood by considering the Landau levels originating from a tilted Weyl cone. For a magnetic field in the z-direction, the dispersion relation of the chiral lowest Landau level is given by [91]

$$E_0^\chi(k_z) = \chi v_F \Big(t_z - \sqrt{1 - t_x^2 - t_y^2}\Big) k_z, \tag{3.45}$$

under the assumption $t_x^2 + t_y^2 + t_z^2 < 1$. The lowest Landau level is thus still dispersing along the direction of the magnetic field, albeit with a renormalized slope. The higher Landau levels originating from the conduction and valence band each yield a zero net current and the Landau level degeneracy $eB/2\pi$ is not affected by the tilt. We can therefore obtain the charge current in the static limit from a one-dimensional integral along the k_z-direction, i.e.,

$$\begin{aligned}\langle \boldsymbol{J}_e \rangle &= -\frac{e^2 \mathbf{B}}{2\pi} \sum_{\chi,u=\pm} \int_0^\infty \frac{\mathrm{d}k_z}{2\pi} \frac{\mathrm{d}E_0^\chi(k_z)}{\mathrm{d}k_z} N_{\mathrm{FD}}(E_0^\chi(k_z) - u\mu_\chi) \\ &= \frac{e^2 \mathbf{B}}{4\pi^2} \sum_{\chi,u=\pm} \chi u \int_0^\infty \mathrm{d}\varepsilon \, N_{\mathrm{FD}}(\varepsilon - u\mu_\chi) = \frac{e^2 \mu_5}{2\pi^2} \mathbf{B},\end{aligned} \tag{3.46}$$

which yields a universal answer because the density of states exactly cancels the slope of the lowest Landau level that determines the velocity. This also explains why the chiral magnetic energy current density is universal. Indeed,

			static limit		homogeneous limit	
conductivity (correlator)	type	units	$t \neq 0$	$t = 0$	$t \neq 0$	$t = 0$
$\sigma^{\mathrm{CME}}\left(i\Pi^k_{ee}\right)$	isotr.	$e^2\mu_5/2\pi^2$	1	1	$(1-t^2)l(t)$	1/3
$\sigma^{\mathrm{CME}}_{\varepsilon}\left(i\Pi^k_{\varepsilon e}\right)$	isotr.	$e\mu\mu_5/2\pi^2$	-1	-1	$1-2(1-t^2)l(t)$	1/3
$\sigma^{\mathrm{CME}}_{Q}\left(i\Pi^k_{Qe}\right)$	isotr.	$e\mu\mu_5/2\pi^2$	1	1	1	1
$\sigma^{\mathrm{CVE}}_{\parallel}\left(i\Pi^k_{ep}\right)$	long.	$e\mu\mu_5/2\pi^2$	$-\frac{1}{(1-t^2)^2}$	-1	$-\frac{1}{2}\left(\frac{1}{1-t^2}-l(t)\right)$	$-1/3$
$\sigma^{\mathrm{CVE}}_{\perp}\left(i\Pi^k_{ep}\right)$	transv.	$e\mu\mu_5/2\pi^2$	$-\frac{2-t^2}{2(1-t^2)^2}$	-1	$-\frac{1}{4}\left(\frac{1}{1-t^2}+l(t)\right)$	$-1/3$
$\sigma^{\mathrm{CVE}}_{\varepsilon,\parallel}\left(i\Pi^k_{\varepsilon p}\right)$	long.	$\mu_5(3\mu^2+\mu_5^2)/6\pi^2$	$\frac{1}{(1-t^2)^2}$	1	$\frac{1}{4}\left(\frac{1-3t^2}{(1-t^2)^2}-3l(t)\right)$	0
$\sigma^{\mathrm{CVE}}_{\varepsilon,\perp}\left(i\Pi^k_{\varepsilon p}\right)$	transv.	$\mu_5(3\mu^2+\mu_5^2)/6\pi^2$	$\frac{2-t^2}{2(1-t^2)^2}$	1	$-\frac{1}{8}\left(\frac{1+t^2}{(1-t^2)^2}-3l(t)\right)$	0
$\sigma^{\mathrm{CVE}}_{Q,\parallel}\left(i\Pi^k_{Qp}\right)$	long.	$\mu_5(3\mu^2+\mu_5^2)/6\pi^2$	$-\frac{1}{2(1-t^2)^2}$	$-1/2$	$-\frac{1}{2(1-t^2)^2}$	$-1/2$
$\sigma^{\mathrm{CVE}}_{Q,\perp}\left(i\Pi^k_{Qp}\right)$	transv.	$\mu_5(3\mu^2+\mu_5^2)/6\pi^2$	$-\frac{2-t^2}{4(1-t^2)^2}$	$-1/2$	$-\frac{2-t^2}{4(1-t^2)^2}$	$-1/2$

Table 3.1: Table summarizing the results for the magnetovortical conductivities in the static and homogeneous limit. Note that the chiral magnetic conductivity has equal longitudinal and transverse parts in both limits, meaning that it is isotropic. All results presented here are at $T = 0$ and for equal tilt of both cones. As all the tilt-dependend functions used here are invariant under $t \to -t$, these results hold for both inversion-symmetry breaking and inversion-symmetry retaining tilts.

Result Ref. [144]	units	stat. lim.	hom. lim.
CME	$e^2\mu_5/2\pi^2$	1	1/3
CME-ε	$e\mu\mu_5/2\pi^2$	-1	0
CVE	$e\mu\mu_5/2\pi^2$	-1	0
CVE-ε	$\mu_5(3\mu^2+\mu_5^2)/2\pi^2$	1/3	0

Table 3.2: Table displaying the results from Landsteiner *et al.* for the chiral magnetic, chiral vortical and chiral vortical energy conductivity in the static and homogeneous limit [144]. We have $t = 0$ and $T = 0$ here. We reproduce these results by using the symmetrized energy-momentum tensor, resulting in the linear combination $i\big(\Pi^k_{e\varepsilon} + \Pi^k_{ep}\big)/2$ for the chiral vortical conductivity and $i\big(\Pi^k_{\varepsilon\varepsilon} + 2\Pi^k_{\varepsilon p}\big)/4$ for the chiral vortical energy conductivity. The latter does not contain a contribution from Π^k_{pp} because its antisymmetric part vanishes. Note that with the symmetric definition of the energy-momentum tensor the chiral magnetic energy conductivity and chiral vortical conductivity necessarily coincide.

doing a similar calculation as in Eq. (3.46), we find

$$\begin{aligned}\langle \boldsymbol{J}_\varepsilon \rangle &= -\frac{e\mathbf{B}}{4\pi^2}\sum_{\chi,u=\pm}\chi\int_0^\infty \mathrm{d}\varepsilon\,\varepsilon N_{\mathrm{FD}}(\varepsilon - u\mu_\chi)\\ &= -\frac{e\mu\mu_5}{2\pi^2}\mathbf{B},\end{aligned} \tag{3.47}$$

which reproduces the corresponding result in Table 3.1. The overall minus sign in Eq. (3.47) as compared to Eq. (3.46) is due to the fact that the energy and charge current density differ by a factor of $-e$. The previous argument likewise clarifies why the chiral vortical conductivity σ^{CVE} and the chiral vortical energy conductivity $\sigma_\varepsilon^{\mathrm{CVE}}$ depend in the same way on the tilt and only differ a factor of $-e$ in the static limit.

Another convenient framework to understand the universality of the chiral magnetic conductivities, as well as the non-universality and angle-dependence of the chiral vortical conductivity, is the semiclassical chiral kinetic theory [57, 58, 145]. In kinetic theory the semiclassical equation of motion for the velocity of a wavepacket in the band n attains a correction in the direction of the magnetic field when the band has a non-zero Berry curvature [27]. This so-called anomalous velocity results in the following simple expression

for the chiral magnetic current density, i.e.,

$$\langle \boldsymbol{J}_e \rangle = -e^2 \sum_{n,\chi=\pm} \int_{\boldsymbol{k}} \left[\boldsymbol{\Omega}_{n\chi}(\boldsymbol{k}) \cdot \partial_{\boldsymbol{k}} \varepsilon_{n\chi\boldsymbol{k}} \right] N_{\mathrm{F}}(\varepsilon_{n\chi\boldsymbol{k}} - \mu_\chi) \mathbf{B}, \tag{3.48}$$

where the Berry curvature is given by

$$\boldsymbol{\Omega}_{n\chi}(\boldsymbol{k}) \equiv \boldsymbol{\nabla}_{\boldsymbol{k}} \times \langle u_{n\chi\boldsymbol{k}} | i \boldsymbol{\nabla}_{\boldsymbol{k}} | u_{n\chi\boldsymbol{k}} \rangle = -\frac{n\chi \boldsymbol{k}}{2|\boldsymbol{k}|^3}, \tag{3.49}$$

in terms of the Bloch states $|u_{n\chi\boldsymbol{k}}\rangle$ associated with Eq. (3.1). Performing the integral in Eq. (3.48) then simply yields the universal result in Eq. (3.46). Note that the divergence due to the Dirac sea cancels because of the sum over chiralities.

For the vortical conductivity a similar argument holds. By comparing the minimally-coupled Hamiltonian corresponding to Eq. (3.1), i.e., $\mathcal{H}_\chi(\boldsymbol{k}+e\mathbf{A})$, to the Hamiltonian $\mathcal{H}_\chi(\boldsymbol{k}) - \boldsymbol{k} \cdot \boldsymbol{v}$, it becomes clear that in the isotropic case the velocity $\boldsymbol{v}$ acts as an effective vector potential that is given by $\mathbf{A}_{\text{eff}} = -\varepsilon_{n\chi\boldsymbol{k}} \boldsymbol{v}/ev_F^2$. Taking the rotation on both sides of this relation results in a vorticity that can be described by an effective magnetic field $\mathbf{B}_{\text{eff}} = -2\varepsilon_{n\chi\boldsymbol{k}} \boldsymbol{\omega}/ev_F^2$. In the case of an isotropic single-particle energy, simply substituting this effective magnetic field into Eq. (3.48) yields

$$\begin{aligned} \langle \boldsymbol{J}_e \rangle &= \frac{2e}{v_F^2} \sum_{n,\chi=\pm} \int_{\boldsymbol{k}} \left[\boldsymbol{\Omega}_{n\chi}(\boldsymbol{k}) \cdot \partial_{\boldsymbol{k}} \varepsilon_{n\chi\boldsymbol{k}} \right] \varepsilon_{n\chi\boldsymbol{k}} N_{\mathrm{F}}(\varepsilon_{n\chi\boldsymbol{k}} - \mu_\chi) \boldsymbol{\omega} \\ &= -\frac{e\mu\mu_5}{2\pi^2} \frac{2\boldsymbol{\omega}}{v_F^2}, \end{aligned} \tag{3.50}$$

where again the Dirac sea cancelled due to the sum over chiralities. The only question that remains to be answered is how the relation $\mathbf{A}_{\text{eff}} = -\varepsilon_{n\chi\boldsymbol{k}} \boldsymbol{v}/ev_F^2$ changes when the dispersion relation is modified by a tilting of the cones. It is clear that in this case the effective gauge field and velocity can be decomposed into components pointing along and perpendicular to the tilting direction. This ultimately leads to a chiral vortical conductivity that has a longitudinal and transverse component, as can also be seen in Table 3.1. Unfortunately, we have not yet been able to find a simple argument for the appropriate effective magnetic field to reproduce the tilt-dependent longitu-

dinal and transversal chiral vortical conductivities obtained from the Kubo formula.

Finally, we note that the results presented in Table 3.1 have all been calculated at $T = 0$ because the integrals otherwise cannot be performed exactly for non-zero tilt. In the case of zero tilt, the transport coefficients can be calculated exactly at $T \neq 0$ in the static and homogeneous limit. The result is that σ^{CME}, $\sigma_{\varepsilon}^{\mathrm{CME}}$ and $\sigma_{e}^{\mathrm{CVE}}$ do not change at non-zero temperature, whereas $\sigma_{\varepsilon}^{\mathrm{CVE}}$ attains an additional term proportional to T^2 that can be attributed to the mixed gauge-gravitional anomaly [109, 120]. It stands to reason that similar behavior will be found when doing a numerical calculation at non-zero temperature that includes tilt of the cones.

3.4.3 AC response

Having discussed the long-wavelength response in detail, we now turn our attention to the AC magnetovortical response. In order to obtain the non-zero-frequency response of the chiral magnetovortical effects, we extract the parts of the current-current correlators that are proportional to q^k and subsequently evaluate the rest in the local limit $\boldsymbol{q} = \boldsymbol{0}$ while keeping ω non-zero. In this limit the contribution from the Fermi surface (intraband) vanishes, as can be seen from Eq. (3.37), and only the Fermi sea (interband) contribution remains. Note that upon taking the zero-frequency limit in the AC conductivities we obtain in this section, the answers reduce to the homogeneous-limit results presented in Table 3.1.

We start with the frequency dependence of the chiral magnetic effect. Using the procedure outlined above, we find

$$\sigma^{\mathrm{CME}}(\omega) = -2e^2 v_F^3 \sum_{\chi=\pm} \chi \int_{\boldsymbol{k}} \frac{\vartheta(\mu_\chi - \varepsilon_{+\chi\boldsymbol{k}})}{(\omega^+)^2 - 4v_F^2|\boldsymbol{k}|^2} \times \left[1 + \hat{\boldsymbol{k}} \cdot \boldsymbol{t} + 4v_F^2 \frac{|\boldsymbol{k}|^2 - (\boldsymbol{k} \cdot \hat{\boldsymbol{t}})^2}{(\omega^+)^2 - 4v_F^2|\boldsymbol{k}|^2}\right]. \tag{3.51}$$

The first term in this expression is proportional to $[(\omega^+)^2 - v_F^2|\boldsymbol{k}|^2]^{-1}$, which can be split into two first-order poles. The second term, however, contains second-order poles. These appear due to the fact that the electric charge current-current correlator, as can be seen from Eq. (3.24), is not automatically proportional to q^k after performing the trace. To obtain the part that

is linear in the external wavenumber, the propagator $S_F(k+q)$ has to be expanded in q, thereby yielding an additional propagator in the integrand. The chiral magnetic conductivity is thus obtained from the trace over three propagators, which is in fact a triangle diagram. This explains the occurence of double poles in Eq. (3.51). The chiral vortical conductivities, contrastingly, are already linear in q^k, as can be seen from e.g. Eq. (3.34), and therefore in this case no expansion of the propagator is necessary. The vortical conductivities therefore only contain single poles and are not due to a triangle diagram, but rather the more conventional bubble diagram.

Although the integral in Eq. (3.51) can be performed analytically for nonzero tilt, it is illustrative to first consider the case of zero tilt, for which we find for the real and imaginary parts of the chiral magnetic conductivity [102, 144]

$$\mathrm{Re}\big[\sigma^{\mathrm{CME}}(\omega)\big] = \sum_{\chi,u=\pm} \frac{\chi e^2 \mu_\chi}{12\pi^2} \frac{\mu_\chi}{2\mu_\chi - u\omega} \tag{3.52a}$$

$$\mathrm{Im}\big[\sigma^{\mathrm{CME}}(\omega)\big] = \sum_{\chi,u=\pm} \frac{\chi e^2 \omega^2}{48\pi} u\delta(\omega - 2u\mu_\chi), \tag{3.52b}$$

which displays resonances around $\omega = \pm 2\mu_\chi$. Physically, this is due to the creation of an electron-hole pair by the excitation of a valence electron to the conduction band. Because of Pauli blocking this is for a single cone only possible when the externally applied frequency ω obeys $|\omega| > 2\mu_+$. Upon subtracting the contributions from both cones, however, the transitions from deep in the Dirac sea, i.e., for $|\omega| > 2\mu_+$ when $\mu_+ > \mu_-$, destructively interfere. The fact that the imaginary part in Eq. (3.52b) contains delta functions, instead of the more conventional heaviside step functions, is precisely due to the fact that Eq. (3.51) contains second-order poles, so that the answer is proportional to the derivative of these heaviside functions instead.

Tilting the cones yields four frequency intervals, rather than the four single frequencies $\omega = \pm 2\mu_\chi$, given by

$$\omega_{\mathrm{min}}(\mu_\chi) \equiv \frac{2\mu_\chi}{1+t} < \omega < \frac{2\mu_\chi}{1-t} \equiv \omega_{\mathrm{max}}(\mu_\chi), \tag{3.53}$$

and similarly for negative ω. In what follows we always use values for $\mu_\pm$ and t such that $\omega_{\mathrm{min}}(\mu_+) > \omega_{\mathrm{max}}(\mu_-)$. We thus expect the imaginary part

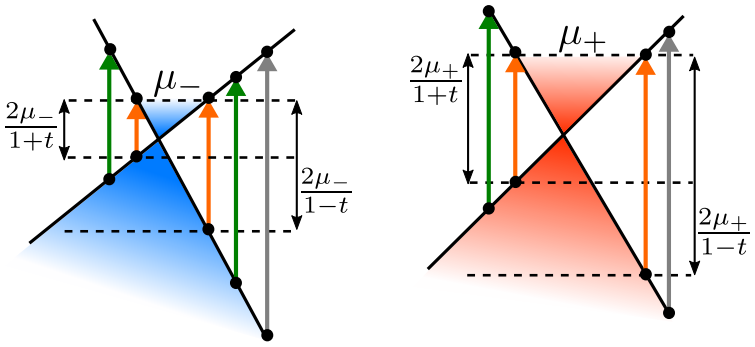

Figure 3.6: Schematic representation of the optical absorption processes (i.e. with $\boldsymbol{q} = \boldsymbol{0}$) that are allowed for a pair of tilted Weyl cones (the tilt is chosen in the opposite direction of the momentum direction that defines the cones here). Orange arrows indicate the border of the frequency ranges defined by $\omega_{\mathrm{min/max}}$ and green arrows transitions that are allowed within such a frequency range. rey arrows indicate processes from deep in the Dirac sea that in principle are allowed, but destructively interfere upon subtracting the contributions from both cones.

of the chiral magnetic conductivity to be non-zero and finite within the two intervals defined by Eq. (3.53). Additionally, the real part should still show a resonance, albeit less pronounced than in Eq. (3.52a). In Fig. 3.6 we present a graphical illustration of the allowed excitation processes for a pair of tilted cones.

We perform the integral in Eq. (3.51) by choosing spherical coordinates (φ, θ, k) along the direction of $\boldsymbol{t}$, such that $\boldsymbol{k} \cdot \boldsymbol{t} = kt\cos\theta$. This renders the integral over φ trivial. The integral over k can be written as an integral over the energy by employing the changes of variables $y = \cos\theta$ and $\varepsilon = (1 + ty)v_F k$. The double integral can then be written as a product of an integral over y and one over ε. The former integral is easily performed, whereas the latter can be performed analytically only at $T = 0$ for non-zero frequencies. Doing so, we find for the tilt and frequency-dependent chiral magnetic conductivity

$$\sigma^{\mathrm{CME}}(\omega) = -\sum_{\chi=\pm} \frac{\chi e^2 \mu_\chi (1-t^2)}{16\pi^2 t^3} \left[2t - L_1(\omega) + \frac{(1-t^2)\omega^2 + 4\mu_\chi^2}{4\omega\mu_\chi} L_2(\omega) \right], \tag{3.54}$$

where we defined the functions [103]

$$L_1(\omega) = \log\left(\frac{(\omega^+)^2 - \omega_{\max}^2}{(\omega^+)^2 - \omega_{\min}^2}\right), \tag{3.55a}$$

$$L_2(\omega) = \log\left(\frac{(\omega^+ - \omega_{\max})(\omega^+ + \omega_{\min})}{(\omega^+ + \omega_{\max})(\omega^+ - \omega_{\min})}\right), \tag{3.55b}$$

$$L_3(\omega) = \log\left(1 - \frac{\omega_{\min}^2}{(\omega^+)^2}\right) + \log\left(1 - \frac{\omega_{\max}^2}{(\omega^+)^2}\right), \tag{3.55c}$$

and omitted the dependence of $\omega_{\min/\max}$ on the chemical potential for brevity.

We plot the real and imaginary part of $\sigma^{\mathrm{CME}}(\omega)$ as a function of ω/μ_- in Fig. 3.7. For a tilt of $t = 3/10$ we observe the expected behavior in Fig. 3.7 (a): in between $\omega_{\min}(\mu_\pm)$ and $\omega_{\max}(\mu_\pm)$ the chiral magnetic conductivity has an imaginary part, whereas the real part has a resonance that is broader and less steep than for the zero-tilt case. It is interesting to note that the imaginary part goes to zero exactly at $\omega_{\min}(\mu_\pm)$ and $\omega_{\max}(\mu_\pm)$ and is zero in between $\omega_{\max}(\mu_-)$ and $\omega_{\min}(\mu_+)$. The reason can be deduced from Eq. (3.54): both the function $L_1(\omega)$ and $L_2(\omega)$ contribute to the imaginary part, but exactly at $\omega_{\min}(\mu_\chi)$ and $\omega_{\max}(\mu_\chi)$ the function multiplying $L_2(\omega)$ becomes equal to 1, thereby cancelling the contribution from $L_1(\omega)$, which simply comes with a factor of minus one. Hence, tilting the cone renders the chiral magnetic conductivity non-zero and finite, even around $\omega = \pm 2\mu_\chi$. In Fig. 3.7 (b) we show that upon decreasing the tilt to $t = 3/100$, a very narrow resonance reappears. Clearly the results of Eq. (3.52) are reproduced as t goes to zero.

It is also interesting to note that a very similar calculation for the anomalous Hall effect shows that

$$\sigma^{\mathrm{AHE}}(\omega) = \frac{\sigma^{\mathrm{CME}}(\omega)}{v_F(1-t^2)}, \tag{3.56}$$

which only holds if we do not take the topological contribution due to the separation between the Weyl nodes into account and if the cones are tilted in the same direction. As the chiral magnetic conductivity remains non-zero when $t \to 0$, the above equation seems to imply that the anomalous Hall conductivity also remains non-zero in this limit. However, the anomalous

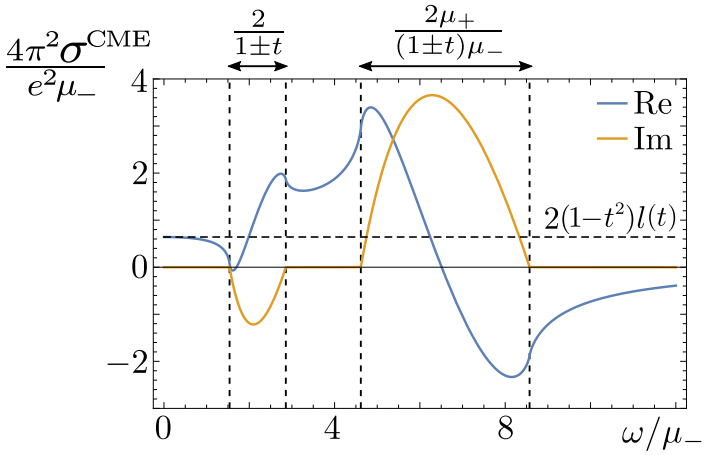

(a) $t = 3/10$

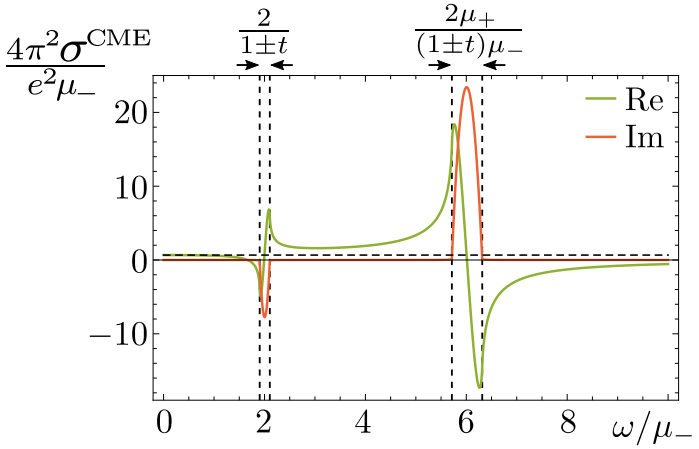

(b) $t = 5/100$

Figure 3.7: Plots of the chiral magnetic conductivity from Eq. (3.54) as a function of ω/μ_-, normalized on $e^2\mu_-/4\pi^2$, and for $\mu_+/\mu_- = 3$. In (a) we used $t = 3/10$ to illustrate the tilt dependence and in (b) $t = 5/100$ to illustrate the convergence to the tilt-independent result from Eq. (3.52a) and (3.52b). In (a) it is clear that the imaginary part is only non-zero between $2\mu_\chi/(1 \pm t)$, which is indicated by the vertical dashed lines in both figures. The limiting value for $\omega/\mu_- \to 0$ is given by $(\mu_+/\mu_- - 1)(1 - t^2)l(t)$ and is indicated by the horizontal dashed line in both figures.

Hall current density does vanish because we defined it proportional to t: $\boldsymbol{J}^{\mathrm{AHE}}(\omega,\boldsymbol{q}) = \sigma^{\mathrm{AHE}}(\omega,\boldsymbol{q})\boldsymbol{t}\times\mathbf{E}$.

We now turn to the frequency dependence of the vortical effects. Following the same procedure, we find for instance for the electric charge current-momentum density correlator

$$i\Pi^{k}_{ep}(\omega,\boldsymbol{q};\boldsymbol{t}) \approx \frac{ev_F q^l}{4}\sum_{\chi=\pm}\chi\int_{\boldsymbol{k}}\vartheta(\mu_\chi-\varepsilon_{+\chi\boldsymbol{k}})\left[\delta^{kl}-\hat{k}^k\hat{k}^l\right] \times\left[\frac{1}{\omega^+-2v_F|\boldsymbol{k}|}-\frac{1}{\omega^++2v_F|\boldsymbol{k}|}\right]. \tag{3.57}$$

From this expression we firstly observe one important difference with the chiral magnetic conductivity that we already alluded to before: there are no double poles present. We therefore expect a non-zero imaginary part in between $\omega_{\mathrm{max}}(\mu_-)$ and $\omega_{\mathrm{min}}(\mu_+)$. Furthermore, from Eq. (3.57) it becomes clear that the vortical conductivity is anisotropic. The reason is that the integral over the term proportional to $\hat{k}^k\hat{k}^l$ can either yield a contribution proportional to δ^{kl}, or a contribution proportional to $\hat{t}^k\hat{t}^l$, because these are the only symmetric tensors left after taking $|\boldsymbol{q}|\to 0$.

The longitudinal and transverse vortical conductivities can also be expressed in terms of the functions $L_i(\omega)$ defined in Eq. (3.55) and we list the explicit, but lengthy expressions in Appendix 3.A.2. Here, we instead plot the frequency dependence of the longitudinal and transversal chiral vortical conductivity for $t = 6/10$ in Fig. 3.8(a) $t = 3/100$ in Fig. 3.8(b). We do the same for the chiral vortical energy conductivity in Fig. 3.9.

As expected, we observe in both figures a non-zero imaginary part on the whole frequency range defined by $\omega_{\mathrm{min}}(\mu_-) < \omega < \omega_{\mathrm{max}}(\mu_+)$. In addition, both the real and imaginary parts of the longitudinal conductivities are always larger than the transverse counterparts. This can be understood from the integrand in Eq. (3.57), which contains the transverse projection operator $\delta^{kl}-\hat{k}^k\hat{k}^l$. Because of the relative minus sign in this operator, the contribution of the term proportional to $\hat{k}^l\hat{k}^k$ to the transverse conductivity is negative.

Furthermore, from Fig. 3.9(b) we note that in the limit of small tilt, the chiral vortical energy conductivity displays a resonance similar to the one for the chiral magnetic effect in Fig. 3.7(b). Its magnitude, however, is sig-

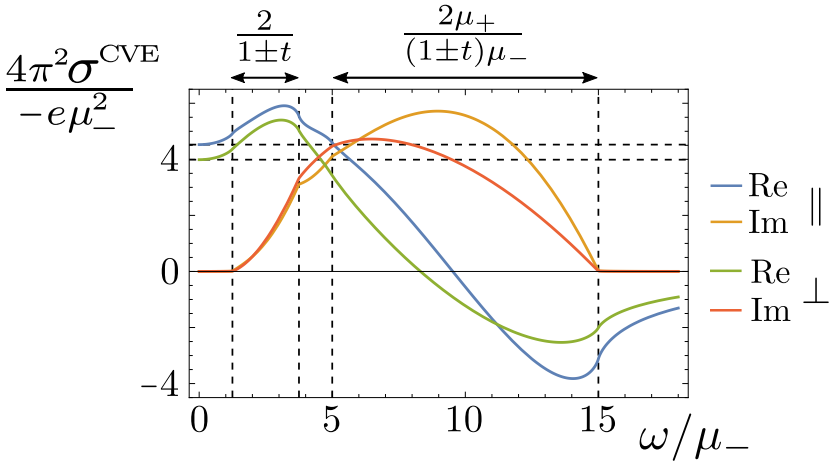

(a) $t = 6/10$

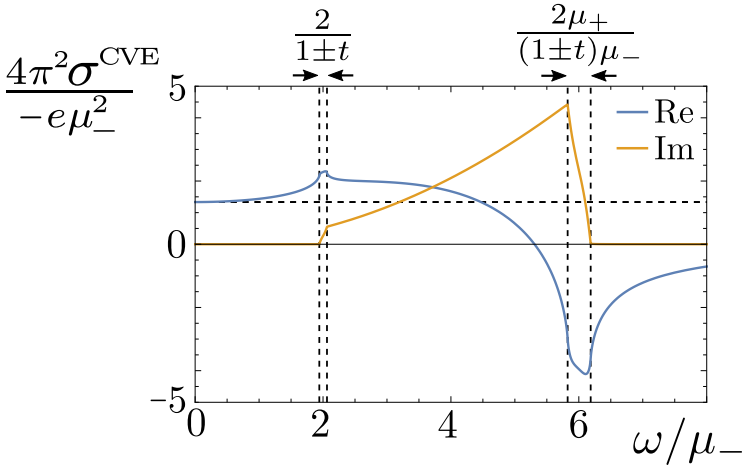

(b) $t = 3/100$

Figure 3.8: Plot of the anisotropic chiral vortical conductivity, normalized on $-e\mu_-^2/4\pi^2$ and as a function of ω/μ_-. In (a) we plot both $\sigma_\perp^{\mathrm{CVE}}$ and $\sigma_\parallel^{\mathrm{CVE}}$ for $t = 6/10$ and $\mu_+/\mu_- = 3$. The vertical dashed lines indicate the positions of $\omega_{\min}(\mu_\pm)$ and $\omega_{\max}(\mu_\pm)$. The horizontal dashed lines indicate the zero-frequency limiting values, given by the values listed in Table 3.1, multiplied by an additional factor of $(\mu_+^2/\mu_-^2 - 1)$, which is due to the normalization used in these plots. In (b) we plot only $\sigma_\parallel^{\mathrm{CVE}}$ for $t = 3/100$ because the difference with $\sigma_\perp^{\mathrm{CVE}}$ is very small.

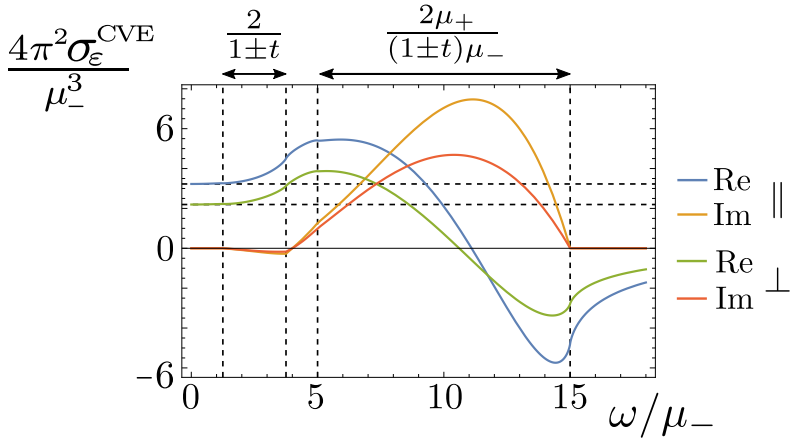

(a) $t = 6/10$

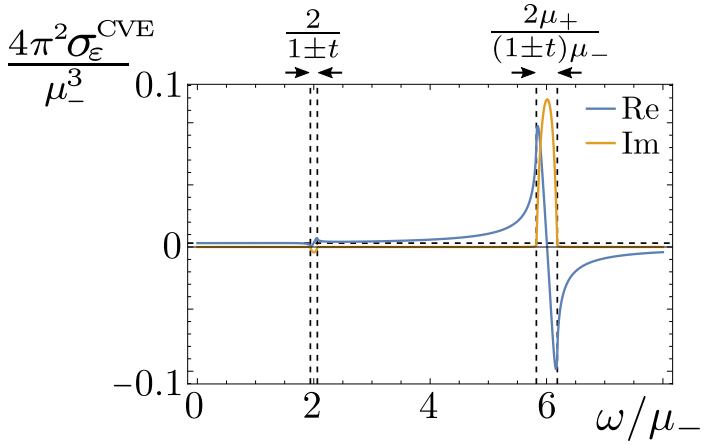

(b) $t = 3/100$

Figure 3.9: Plot of the anisotropic chiral vortical energy conductivity, normalized on $\mu_-^3/4\pi^2$ and as a function of ω/μ_-. In (a) we plot both $\sigma_\perp^{\mathrm{CVE}}$ and $\sigma_\parallel^{\mathrm{CVE}}$ for $t = 6/10$ and $\mu_+/\mu_- = 3$. The vertical dashed lines indicate the positions of $\omega_{\min}(\mu_\pm)$ and $\omega_{\max}(\mu_\pm)$. The horizontal dashed lines indicate the zero-frequency limiting values, given by the values listed in Table 3.1, multiplied by an additional factor of $(\mu_+^3/\mu_-^3 - 1)$ for the chiral vortical energy conductivity, which is due to the normalization used in these plots. In (b) we plot only $\sigma_{\varepsilon,\parallel}^{\mathrm{CVE}}$ for $t = 3/100$ because the difference with $\sigma_{\varepsilon,\perp}^{\mathrm{CVE}}$ is very small.

nificantly smaller and upon taking the tilt to zero the chiral vortical energy conductivity vanishes. This is consistent with the result obtained in the homogeneous limit in Table 3.1. On the other hand, the small-tilt behavior of the chiral vortical conductivity in Fig. 3.8(b) is rather different. We observe that for small tilt it saturates to two peaks around $\omega = 2\mu_{\pm}$, with a non-zero imaginary part in between. Upon inspecting the frequency behavior of the chiral magnetic energy conductivity, we find exactly the same behavior, but with an opposite sign. Adding both contributions, which is equivalent to using a symmetrized version of the energy-momentum tensor, thus yields zero for all frequencies, except at $\omega = 0$. This result is consistent with previous work by Landsteiner *et al.* [144]. These authors use the symmetric energy-momentum tensor, a combination of Ward identities and rotational symmetry to show that only at $\omega = 0$ there is a non-zero vortical response in the electric current. Physically, this means that all interband transitions are forbidden in their case. The situation in our case is different for two reasons: 1) we use a different set of currents and 2) rotational symmetry is broken by the tilting of the cones. We therefore have non-trivial frequency dependence for the magnetovortical conductivities.

Before we turn our attention to the thermoelectric transport of tilted Weyl cones, let us summarize the main findings of this section. We started by calculating the long-wavelength response of the magnetovortical conductivities. The anisotropy introduced by the tilting of the cones led to an anisotropic velocity of the chiral magnetic waves. Subsequently we considered two specific cases of the long-wavelength limit: the static and the homogeneous limit, and listed all magnetovortical conductivities in Table 3.1. We found that the chiral magnetic conductivities remains isotropic, whereas the vortical conductivitities attain a transverse and longitudinal part. Moreover, the chiral magnetic conductivities turned out to be tilt-independent, or universal, in the static limit, which we managed to explain based on exact quantum and semiclassical arguments. Finally, we focussed on the AC magnetovortical response, finding rather different behavior for the vortical and magnetic conductivities. We explained how this ultimately is due to the fact that the chiral magnetic effect is determined by a triangle diagram, whereas the chiral vortical conductivities follow from a bubble diagram.

3.5 Electronic and thermal transport

We now turn to the coupled off-diagonal thermoelectric transport from tilted Weyl cones as described by Eq. (3.11). Some of the results we discuss have already been presented by Bardarson *et al.* [117]. These authors circumvent the need to subtract the superfluous contributions coming from unobservable, circulating currents of the form $\nabla \times \boldsymbol{M}_{e/Q}^{\mathrm{orb}}$, with $\boldsymbol{M}_{e}^{\mathrm{orb}}$ ($\boldsymbol{M}_{Q}^{\mathrm{orb}}$) the electric (heat) orbital magnetization density. In order to do this, they first calculate the anomalous Hall conductivity σ^{AHE}, which does not require any subtractions. Subsequently they use the Mott relation and Wiedemann-Franz law to calculate α^{ANE} and κ^{THE} from σ^{AHE}.

Instead, we discuss here how these orbital magnetizations arise naturally as diamagnetic-like terms when performing linear response theory in the presence of a temperature gradient. We then calculate $\boldsymbol{M}_{e}^{\mathrm{orb}}$ and $\boldsymbol{M}_{Q}^{\mathrm{orb}}$ microscopically and explicitly subtract them from the currents coming from the Kubo formula to yield the transport currents [128]. Finally, we discuss how the answers for the transport coefficients differ when considering inversion-symmetric or inversion-symmetry breaking tilt and discuss the consequences of a non-zero chiral chemical potential μ_5.

3.5.1 Magnetization contributions

To see that magnetization contributions occur as diamagnetic-like terms when performing linear-response theory in the presence of a temperature gradient, consider an imaginary time action that contains a coupling between the electric current density $J_e^i(\boldsymbol{x},\tau)$ and an external vector potential $A^i(\boldsymbol{x},\tau)$, i.e.,

$$S_{\mathrm{coup.}} = \int \mathrm{d}\boldsymbol{x} \int_0^{\hbar\beta} \mathrm{d}\tau A_i(\boldsymbol{x},\tau) J_e^i(\boldsymbol{x},\tau), \tag{3.58}$$

with $\beta = 1/k_B T$ in terms of the temperature T. Performing linear-response theory with this action shows that the first order contribution to the effective action for the gauge potential vanishes, because in equilibrium we have $\langle J_e^i(\boldsymbol{x},\tau)\rangle_0 = 0$. The contribution at second order, on the other hand, is non-zero and yields the current-current response functions we discussed in Section 3.3.3.

The situation changes if we now include temperature variations by writing $T(\boldsymbol{x}) = T + \delta T(\boldsymbol{x})$. This causes the upper boundary of the integral over

imaginary time in Eq. (3.58) to depend on the position. We can remove this position-dependence from the integration boundary by introducing a new imaginary time coordinate with the transformation $\tau \to \tau/(1+\delta T(\boldsymbol{x})/T)$. Assuming small temperature variations, we find

$$S_{\text{coup.}} \simeq \int \mathrm{d}\boldsymbol{x} \int_0^{\hbar\beta} \mathrm{d}\tau \left(1 - \frac{\delta T(\boldsymbol{x})}{T}\right) A_i(\boldsymbol{x},\tau) J_e^i(\boldsymbol{x},\tau), \tag{3.59}$$

where we expanded in $\delta T(\boldsymbol{x})/T$. Writing $\delta T(\boldsymbol{x}) = x^j \partial_j T(\boldsymbol{x})$ and using from Eq. (3.17) that $\delta g_{j0} = -e^{-i\omega\tau}\partial_j T/i\omega T$, we can write the second term in Eq. (3.59) as

$$\delta S_{\text{coup.}} \simeq \int \mathrm{d}\boldsymbol{x} \int_0^{\hbar\beta} \mathrm{d}\tau A_i(\boldsymbol{x},\tau) J_e^i(\boldsymbol{x},\tau) x^j \delta\dot{g}_{j0}(\boldsymbol{x},\tau), \tag{3.60}$$

where the dot on δg_{j0} denotes an imaginary time derivative. If we now use Eq. (3.60) to calculate the effective action of the gauge field in linear-response theory, we obtain a quadratic contribution already at first order. This diamagnetic-like term exactly constitutes a contribution due to the orbital magnetization, as can be seen from the definition for the magnetization density due to a current density $\boldsymbol{J}_e(\boldsymbol{x})$, i.e.,

$$\boldsymbol{M}_e^{\text{orb}} = \frac{1}{2V} \int \mathrm{d}\boldsymbol{x} \, \langle \boldsymbol{x} \times \boldsymbol{J}_e(\boldsymbol{x}) \rangle_0, \tag{3.61}$$

which implies that $\langle J_e^i(\boldsymbol{x},\tau) x^j \rangle_0 \propto \varepsilon^{ijk} M_{e,k}^{\text{orb}}$. A similar line of reasoning can be followed when starting from an action like Eq. (3.58) with the coupling $J_\varepsilon^i \delta g_{i0}$. We find

$$\delta S_{\text{coup.}} \simeq \int \mathrm{d}\boldsymbol{x} \int_0^{\hbar\beta} \mathrm{d}\tau \, \delta g_{i0}(\boldsymbol{x},\tau) J_\varepsilon^i(\boldsymbol{x},\tau) x^j \delta\dot{g}_{j0}(\boldsymbol{x},\tau), \tag{3.62}$$

which can be recognized as a contribution coming from the so-called energy magnetization density, that is defined by replacing the electric current density in Eq. (3.63) by the energy current density, i.e.,

$$\boldsymbol{M}_\varepsilon^{\text{orb}} = \frac{1}{2V} \int \mathrm{d}\boldsymbol{x} \, \langle \boldsymbol{x} \times \boldsymbol{J}_\varepsilon(\boldsymbol{x}) \rangle_0. \tag{3.63}$$

As we only considered the contributions to the currents due to the current-current correlators in Section 3.3.3, we need to add the diamagnetic-like contributions coming from the (heat) orbital magnetization. These contributions are only non-zero in the case of broken time-reversal symmetry. In our case this is provided for by the tilting direction $\boldsymbol{t}$. As we shall see, the magnetization densities point in the opposite direction of the tilt.

3.5.2 Orbital magnetization due to tilted cones

A convenient way to calculate the (heat) orbital magnetization is by expressing them in terms of Bloch wavefunctions [146]. This follows from the semiclassical theory of Bloch electron dynamics, in which electrons can be described as wave packets that are constructed by forming a superposition of the Bloch states of a band [27]. Such a wave packet has a non-zero spread in real space, such that it can rotate around its center of mass, leading to an orbital magnetic moment. For a band with Bloch wavefunction $|u_{n\boldsymbol{k}}\rangle$ and energy $\varepsilon_{n\boldsymbol{k}}$, the orbital magnetic moment is given by $e\boldsymbol{m}_n^{(1)}(\boldsymbol{k})$, with [147]

$$\boldsymbol{m}_n^{(p)}(\boldsymbol{k}) = -\frac{i}{2}\langle\partial_{\boldsymbol{k}}u_{n\boldsymbol{k}}| \times (\mathcal{H}(\boldsymbol{k}) - \varepsilon_{n\boldsymbol{k}})^p|\partial_{\boldsymbol{k}}u_{n\boldsymbol{k}}\rangle. \tag{3.64}$$

An explicit calculation for the two-band model from Eq. (3.1) yields for a cone with chirality χ: $e\boldsymbol{m}_{n\chi}^{(1)}(\boldsymbol{k}) = -ev_F\chi\boldsymbol{k}/2|\boldsymbol{k}|^2$. Similar to the way in which microscopic spins add up to form a macroscopic magnetization of a material, the orbital magnetic moment contributes to the macroscopic orbital magnetization $\boldsymbol{M}_e^{\mathrm{orb}}$. However, besides the contribution of the orbital magnetic moment, there is also a contribution from the center-of-mass motion of the wave packet. The total temperature-dependent orbital magnetization density can therefore be expressed as [27]

$$\begin{aligned}\boldsymbol{M}_e^{\mathrm{orb}} = \sum_{n,\chi=\pm}\int_{\boldsymbol{k}}\Big[&e\boldsymbol{m}_{n\chi}^{(1)}(\boldsymbol{k})N_{\mathrm{FD}}(\varepsilon_{n\chi\boldsymbol{k}} - \mu_\chi) \\ &+ ek_BT\boldsymbol{\Omega}_{n\chi}(\boldsymbol{k})\log\left(1 + e^{-\beta(\varepsilon_{n\chi\boldsymbol{k}}-\mu_\chi)}\right)\Big],\end{aligned} \tag{3.65}$$

In this expression the first term is simply a thermodynamic average over the orbital magnetic moments and thus ultimately due to the self-rotation of the

wave packet, whereas the second term is due to the center-of-mass motion of the wave packet.

Recall that the Weyl nodes in our model are located at the same position in momentum space, because we are interested in intrinsic contributions to the various conductivities, as opposed to topological contributions. Therefore, the only vector that contributes to $\boldsymbol{M}_e^{\mathrm{orb}}$ is the tilting direction $\boldsymbol{t}$, such that we can write $\boldsymbol{M}_e^{\mathrm{orb}} = M_e^{\mathrm{orb}}\boldsymbol{t}$. We perform the integral in Eq. (3.65) by going to spherical coordinates and subtract the Dirac sea, yielding

$$M_e^{\mathrm{orb}} = -\frac{e}{8\pi^2 v_F}\sum_{\chi=\pm}\frac{\chi t_\chi}{(1-t^2)t}\left[\mu_\chi^2 + \frac{\pi^2 k_B^2 T^2}{3}\right] \equiv \sum_{\chi=\pm} M_{e,\chi}^{\mathrm{orb}}. \tag{3.66}$$

In a completely similar fashion we calculate the circulating contribution in the heat current. Analogously to the electric orbital magnetization, the heat orbital magnetization can be expressed as [51]

$$\begin{aligned}\boldsymbol{M}_Q^{\mathrm{orb}} = &\sum_{n,\chi=\pm}\int_{\boldsymbol{k}} \boldsymbol{\Omega}_{n\chi}(\boldsymbol{k})\int_0^{\varepsilon_{n\chi\boldsymbol{k}}-\mu_\chi} \mathrm{d}x\, x N_{\mathrm{FD}}(x)\\ &-\sum_{n,\chi=\pm}\int_{\boldsymbol{k}}\left[(\varepsilon_{n\chi\boldsymbol{k}}-\mu_\chi)\boldsymbol{m}_{n\chi}^{(1)}(\boldsymbol{k}) + \boldsymbol{m}_{n\chi}^{(2)}(\boldsymbol{k})/4\right]N_{\mathrm{FD}}(\varepsilon_{n\chi\boldsymbol{k}}-\mu_\chi).\end{aligned} \tag{3.67}$$

Using Eq. (3.64) we find $\boldsymbol{m}_{n\chi}^{(2)}(\boldsymbol{k}) = n\chi v_F^2 \boldsymbol{k}/|\boldsymbol{k}|$. Again writing $\boldsymbol{M}_Q^{\mathrm{orb}} = M_Q^{\mathrm{orb}}\boldsymbol{t}$ we then find for the finite contribution to the heat orbital magnetization density

$$M_Q^{\mathrm{orb}} = -\sum_{\chi=\pm}\frac{\chi\mu_\chi\left[(2-t^2)\mu_\chi^2 + t^2\pi^2 k_B^2 T^2\right]}{24\pi^2(1-t^2)^2 v_F} \equiv \sum_{\chi=\pm} M_{Q,\chi}^{\mathrm{orb}}. \tag{3.68}$$

Now that we have explicitly calculated the diamagnetic-like orbital magnetization contributions due to the tilting of the cones, we calculate the contributions to the current coming from the current-current response functions.

3.5.3 Electric, energy and mixed current-current correlators

We start by considering the current-current response functions $\Pi^k_{ee}(\omega, \boldsymbol{q}; \boldsymbol{t})$, $\Pi^k_{e\varepsilon}(\omega, \boldsymbol{q}; \boldsymbol{t})$ and $\Pi^k_{\varepsilon\varepsilon}(\omega, \boldsymbol{q}; \boldsymbol{t})$ that describe the linear response of the electric and energy current densities. Once we have the corresponding transport coefficients, the response for the electric and heat current density can then be obtained by using the relation $\langle \boldsymbol{J}_Q \rangle = \sum_\chi \left[\langle \boldsymbol{J}^\chi_\varepsilon \rangle + (\mu_\chi/e) \langle \boldsymbol{J}^\chi_e \rangle \right]$.

In the local, i.e., $\boldsymbol{q} = \boldsymbol{0}$, limit, we find using Eq. (3.33) together with Eq. (3.81), Eq. (3.79), and Eq. (3.80),

$$i\Pi^k_{ab}(\omega^+, \boldsymbol{0}; \boldsymbol{t}) = 2\omega v_F^2 \sum_{\chi, u=\pm} \chi \int_{\boldsymbol{k}} \frac{h^k_{ab}(\boldsymbol{k}, \boldsymbol{t}_\chi) N_{\mathrm{FD}}(u\varepsilon_{u\chi\boldsymbol{k}} + u\mu_\chi)}{(\omega^+)^2 - 4v_F^2 |\boldsymbol{k}|^2}, \tag{3.69}$$

with $h^k_{ee}(\boldsymbol{k}, \boldsymbol{t}) = e^2 \hat{k}^k$, $h^k_{e\varepsilon}(\boldsymbol{k}, \boldsymbol{t}) = -ev_F(\boldsymbol{k} \cdot \boldsymbol{t})\hat{k}^k$ and $h^k_{\varepsilon\varepsilon}(\boldsymbol{k}, \boldsymbol{t}) = v_F^2(\boldsymbol{k} \cdot \boldsymbol{t})^2 \hat{k}^k$. The integrals above have to be proportional to $\boldsymbol{t}$, as there is no other vector left. The anomalous Hall conductivity thus follows from $\sigma^{\mathrm{AHE}}(\omega) = i\Pi^k_{ee}(\omega^+, \boldsymbol{0}; \boldsymbol{t}) t_k/\omega t^2$. Similarly we define $\alpha^{\mathrm{ANE}}_\varepsilon(\omega) \equiv i\Pi^k_{e\varepsilon}(\omega^+, \boldsymbol{0}; \boldsymbol{t}) t_k/\omega t^2$ and $\bar{\kappa}^{\mathrm{THE}}_\varepsilon(\omega) = i\Pi^k_{\varepsilon\varepsilon}(\omega^+, \boldsymbol{0}; \boldsymbol{t}) t_k/\omega t^2$, where the subscript '$\varepsilon$' refers to the fact that these linear-response coefficients are for the coupled electric and energy current response and do not contain the magnetization subtractions yet.

To obtain the coefficients σ^{AHE}, $\alpha^{\mathrm{ANE}}_\varepsilon$ and $\bar{\kappa}^{\mathrm{THE}}_\varepsilon$, we simplify the remaining integral by again choosing spherical coordinates along the direction of $\boldsymbol{t}$ like we did to obtain Eq. (3.54). The angular integrals are then easily performed, whereas the integral over $|\boldsymbol{k}|$ can only be performed analytically in two specific cases: 1) at $T = 0$ for all ω and 2) at $\omega = 0$ for all T. Here, we focus on the second case because we have only obtained the magnetizations at zero frequency in the previous section. Defining the integrals

$$I_n(\mu_\chi) \equiv \int_0^\infty \mathrm{d}\varepsilon\, \varepsilon^{n-1} \left[N_{\mathrm{FD}}(\varepsilon + \mu_\chi) + (-1)^n N_{\mathrm{FD}}(\varepsilon - \mu_\chi) \right], \tag{3.70a}$$

$$J_n(t) \equiv \int_{-1}^1 \mathrm{d}y \frac{y^n}{(1+ty)^n}, \tag{3.70b}$$

we find for the anomalous Hall conductivity

$$\sigma^{\mathrm{AHE}} = \sum_{\chi=\pm} \frac{\chi e^2 t_\chi}{8\pi^2 t^2 v_F} J_1(t) I_1(\mu_\chi) = \frac{e^2 l(t)}{4\pi^2 v_F} \sum_{\chi=\pm} \frac{\chi \mu_\chi t_\chi}{t} \equiv \sum_{\chi=\pm} \sigma^{\mathrm{AHE}}_\chi. \tag{3.71}$$

Furthermore we find for $\alpha_{\varepsilon}^{\mathrm{ANE}}$

$$\begin{aligned}\alpha_{\varepsilon}^{\mathrm{ANE}} &= \sum_{\chi=\pm} \frac{e\chi t_\chi}{8\pi^2 T t v_F} J_2(t) I_2(\mu_\chi) \\ &= \sum_{\chi=\pm} \frac{e\chi t_\chi}{8\pi^2 v_F T t}\left[\frac{1}{1-t^2} - 2l(t)\right]\left[\mu_\chi^2 + \frac{\pi^2 k_B^2 T^2}{3}\right] \equiv \sum_{\chi=\pm} \alpha_{\varepsilon,\chi}^{\mathrm{ANE}}, \quad (3.72)\end{aligned}$$

and finally for $\bar{\kappa}_{\varepsilon}^{\mathrm{THE}}$

$$\begin{aligned}\bar{\kappa}_{\varepsilon}^{\mathrm{THE}} &= \sum_{\chi=\pm} \frac{\chi t_\chi}{8\pi^2 T v_F} J_3(t) I_3(\mu_\chi) \\ &= \sum_{\chi=\pm} \frac{\chi t_\chi \mu_\chi\left(\mu_\chi^2 + \pi^2 k_B^2 T^2\right)}{4\pi^2 v_F T t}\left[l(t) - \frac{1-2t^2}{3(1-t^2)^2}\right] \equiv \sum_{\chi=\pm} \bar{\kappa}_{\varepsilon,\chi}^{\mathrm{THE}}. \quad (3.73)\end{aligned}$$

Upon performing the sum over the two cones with opposite chirality, we find for the anomalous Hall effect $e^2\mu_5 l(t)/2\pi^2$ in the case of inversion-symmetry breaking tilt ($t_\chi = t$) and $e^2\mu l(t)/2\pi^2$ when inversion symmetry is retained ($t_\chi = \chi t$). Furthermore, we note that the anomalous Nernst conductivity is only dependent on temperature in the case of inversion-symmetric tilt. The term proportional to μ_χ^2 in the expression for the anomalous Nernst effect is ill-defined in the low-temperature limit and should be compensated for when we subtract the orbital magnetization density.

3.5.4 Thermoelectric transport coefficients by subtraction

Now that we have obtained explicit expressions for the orbital magnetizations, we can compute the transport coefficients. For the anomalous Nernst effect we find,

$$\begin{aligned}\alpha^{\mathrm{ANE}} T &= \sum_{\chi=\pm}\left[\alpha_{\varepsilon,\chi}^{\mathrm{ANE}} T + \frac{\mu_\chi}{e}\sigma_\chi^{\mathrm{AHE}} + M_{e,\chi}^{\mathrm{orb}}\right] \\ &= -\frac{e k_B^2 T^2 l(t)}{12 v_F \hbar^2}\sum_{\chi=\pm}\frac{\chi t_\chi}{t}, \quad (3.74)\end{aligned}$$

where we reinstated $\hbar$. For small t this result coincides with results obtained elsewhere [117]. Due to the subtraction of the orbital magnetization the

anomalous Nernst coefficient is now well-behaved in the limit $T \to 0$. Additionally, we note that in the case of a tilt that breaks inversion symmetry, i.e., $t_\chi = t$, the contributions from the two cones with opposite chirality subtract, yielding zero. In the case of inversion-symmetry preserving tilt and no chiral imbalance, it is easy to see from Eq. (3.71) and Eq. (3.74) that the Mott-like rule

$$\alpha^{\mathrm{ANE}} = -\frac{\pi^2 k_B^2 T}{3e} \frac{\mathrm{d}\sigma^{\mathrm{AHE}}(\mu)}{\mathrm{d}\mu}, \tag{3.75}$$

which was derived by Niu *et al.*, is satisfied [133]. Note that there is a relative sign in Eq. (3.75) because we have defined the anomalous Nernst current as $\langle \boldsymbol{J}_e \rangle = \alpha^{\mathrm{ANE}} \boldsymbol{t} \times \boldsymbol{\nabla} T$, i.e., with the same overall sign as the anomalous Hall current $\langle \boldsymbol{J}_e \rangle = \sigma^{\mathrm{AHE}} \boldsymbol{t} \times \mathbf{E}$.

Similarly, we compute the coefficient $\bar{\kappa}^{\mathrm{THE}}$ by combining the results from the current-current correlators and the heat orbital magnetization, finding

$$\begin{aligned} \bar{\kappa}^{\mathrm{THE}} T &= \sum_{\chi=\pm} \left[\kappa_\chi T + 2\frac{\mu_\chi}{e} \alpha_\chi T + \frac{\mu_\chi^2}{e^2} \sigma_\chi^{\mathrm{AHE}} + 2M_{Q,\chi}^{\mathrm{orb}} \right] \\ &= \frac{l(t) k_B^2 T^2}{12 v_F \hbar^2} \sum_{\chi=\pm} \frac{\chi \mu_\chi t_\chi}{t}, \end{aligned} \tag{3.76}$$

where we also reinstated $\hbar$. From the expression above it is clear that $\bar{\kappa}^{\mathrm{THE}}$ is only non-zero within our simple model when either inversion symmetry is broken and there is a chiral imbalance μ_5, or when inversion symmetry is retained and there is a non-zero chemical potential μ. In the latter case we find for the thermal Hall coefficient from Eq. (3.12),

$$\kappa^{\mathrm{THE}} = \frac{l(t) \mu k_B^2 T}{6 v_F \hbar^2} \left[1 - \frac{1}{3} \frac{k_B^2 T^2}{\mu^2} \right]. \tag{3.77}$$

In the low-temperature limit $k_B T/\mu \ll 1$ the second term is negligible and κ^{THE} reduces to previously obtained results[117]. Additionally, we observe that in this limit the Wiedemann-Franz law

$$\kappa^{\mathrm{THE}} = \frac{\pi^2 k_B^2}{3e^2} T \sigma^{\mathrm{AHE}}, \tag{3.78}$$

for the off-diagonal transport coefficients, is obeyed.

3.6 Conclusion and discussion

In this chapter we have investigated the off-diagonal linear response of a pair of tilted Weyl cones, when subjected to a temperature gradient, electric field, magnetic field and vorticity. We focussed on the electronic contributions to the electric and heat current densities and neglected contributions from e.g. phonons. As the off-diagonal response is inherently dissipationless, we considered a clean system without disorder. In addition, we neglected the influence of Coulomb interactions among the Weyl fermions. Finally, to preserve clarity, we concentrated on the tilt dependence and did not take the well-known topological contribution to the anomalous Hall and thermal Hall effect into account by taking the the momentum-space separation between the Weyl nodes equal to zero. Under these assumptions, we performed linear-response theory and calculated the appropriate current-current response functions. As the off-diagonal response is determined by their antisymmetric part, we explicitly showed how this part of the current-current response functions can be decomposed in terms of the tilting direction and the external wavenumber.

In the case of the chiral magnetic conductivities, we found that the response remains isotropic when considering tilted cones. In the static limit these conductivities even remain universal, which can be attributed to the chiral anomaly. In the homogeneous or transport limit, on the other hand, the conductivities are renormalized. The situation turned out to be very different for the vortical conductivities: these are generically anisotropic and can be decomposed into a component longitudinal and transverse to the tilting direction. The corresponding longitudinal and transverse chiral vortical conductivities have different values in the static and homogeneous limit as well, but are always tilt-dependent and thus never universal.

To verify our results coming from the Kubo formalism, we used a combination of exact quantum and semiclassical arguments, thereby explaining the universality of the chiral magnetic conductivities. In the case of the anisotropic vortical conductivities we argued that already simple integrals over the anomalous velocity due to a non-zero Berry curvature, necessarily become anisotropic when including a tilting direction. We were, however, not able to simply explain the appropriate expressions for the effective magnetic field due to vorticity in the case of non-zero tilt and plan to investigate this in future work.

Moreover, we calculated the magnetovortical transport coefficients and the susceptibility not only in the static and homogeneous limit, but also in the more general long-wavelength limit. This turned out to be another source of anisotropy, as the results depend on the angle between the tilting direction and the external wavenumber. To illustrate the effect of this anisotropy we computed the dispersion relation of the chiral magnetic wave using the long-wavelength result for the susceptibility. Interestingly, we found that there is a significant dependence of the chiral wave velocity on the angle between the external magnetic field and the tilting direction. Next to this angle-dependence, we showed that the wave becomes soft when the tilt of the cone becomes too large, signaling the Lifshitz transition from a type-I to a type-II Weyl cone. For zero tilt, however, we found that using simply the static-limit result for the susceptibility is a rather good approximation.

In addition, we showed that also the frequency dependence of the chiral magnetic and the chiral vortical conductivities is very different indeed. The AC chiral magnetic conductivity is unusual in the sense that at zero tilt, its imaginary part is given by delta functions centered around $\omega = \pm 2\mu_{\pm}$. Ultimately this is due to the fact that in order to obtain the part of the electric current-current response function that is linear in the external wavenumber, we needed to expand a propagator, thereby turning the bubble diagram into a triangle diagram. For a non-zero tilt, however, the imaginary part attains a finite height and width. The behavior of the AC vortical conductivities was rather different, as the appurtenant current-current response functions were already linear in the external wavenumber. The imaginary part is therefore determined by the more usual Heaviside step functions and is finite both for zero and non-zero tilt.

In the last part of this chapter we concentrated on the off-diagonal thermoelectric transport and elucidated how magnetization contributions to the current occur as diamagnetic-like contributions. Subsequently, we obtained the contribution from the magnetization explicitly by performing a microscopic calculation. As it turns out, the magnetizations are always pointing in the opposite direction of the tilting direction. Having obtained the magnetizations explicitly, we subtracted them to find the transport linear-response coefficients. We found it an illustrative exercise to do this explicitly and it would be interesting to investigate how this scheme can be extended to non-zero frequencies. An important difference with the magnetovortical coefficients turned out to be that the thermoelectric coefficients are odd func-

tions of the tilting direction, whereas the former are even functions of the tilting direction. The magnetovortical coefficients therefore do not depend on whether the tilt breaks inversion symmetry or not. Contrastingly, in the case of the thermoelectric coefficients, the anomalous Hall and thermal Hall effect are only non-zero in the case of broken inversion symmetry if there is a chiral imbalance. The anomalous Nernst effect is only non-zero when inversion symmetry is retained.

It is insightful to estimate the size of some of the conductivities, and corresponding conductances, that we calculated in this chapter. By virtue of the chiral anomaly, a chiral imbalance on the order of $\mu_5 \simeq 10$ meV can be achieved by applying a magnetic field of 1 mT and an electric field of 10^4 V/m [85]. If we then consider the chiral magnetic effect in the homogeneous limit with Weyl cones that are not tilted, we find a resulting current density $|\boldsymbol{J}^{\mathrm{CME}}|_{t=0} \simeq 6 \cdot 10^4$ A/m^2. Alternatively, the corresponding dimensionless conductance for a cubic Weyl semimetal of volume L^3 is given by $G^{\mathrm{CME}}/G_0 = hL\sigma^{\mathrm{CME}}/2v_F e^2 \simeq (8 \cdot 10^5\ \mathrm{m}^{-1})L$, with $G_0 = 2e^2/h$ the conductance quantum. Using the results of Table 3.1, we find that upon tilting the cones to the value $t = 7/10$, the current density and conductance decrease by approximately 25%. This drop in conductance, if measured, could serve as a way to verify the bandstructure details deduced from ARPES-measurements. Similarly, considering two cones that are tilted by the same amount $t = 7/10$ in the same direction, we estimate from Eq. (3.71) the current density coming from the anomalous Hall effect to be $|\boldsymbol{J}^{\mathrm{AHE}}|_{t=7/10} \simeq 6 \cdot 10^5$ A/m^2. The corresponding dimensionless conductance is given by $G^{\mathrm{AHE}}/G_0 = hL\sigma^{\mathrm{AHE}}/2e^2 \simeq (1 \cdot 10^6\ \mathrm{m}^{-1})L$.

Finally, for future research it would interestering to investigate the influence of disorder and Coulomb interactions on the magnetovortical conductivities, which has already been explored for the chiral magnetic conductivity [106].

3.A Appendix: explicit expressions

In this appendix we give some explicit expressions that were too lengthy to put in the main body of this chapter. In the first section we list some result related to the long-wavelength limit and in the second section we list the full frequency and tilt dependence of all magnetovortical conductivities that we used to make the plots in Section 3.4.3.

3.A.1 Long-wavelength limit

We start by giving the functions $f_{ab}^{k,uv}(\boldsymbol{q},\boldsymbol{t},\boldsymbol{k})$ that we introduced in Eq. (3.33). The leading-order expressions for $f_{\varepsilon e}^{k,uv}(\boldsymbol{q},\boldsymbol{t},\boldsymbol{k})$ and $f_{\varepsilon\varepsilon}^{k,uv}(\boldsymbol{q},\boldsymbol{t},\boldsymbol{k})$ are

$$\begin{aligned} f_{\varepsilon e}^{k,uv}(\boldsymbol{q},\boldsymbol{t},\boldsymbol{k}) = -e\Bigg[&2\left(\frac{u}{|\boldsymbol{k}+\boldsymbol{q}|}-\frac{v}{|\boldsymbol{k}|}\right)(\boldsymbol{k}\cdot\boldsymbol{t})k^k + (3u+v)(\hat{\boldsymbol{k}}\cdot\boldsymbol{t})q^k \\ &- 2v(\boldsymbol{q}\cdot\boldsymbol{t})\hat{k}^k + (1+uv)q^k - 2uv(\hat{\boldsymbol{k}}\cdot\boldsymbol{q})\hat{k}^k \\ &- 2uv(\hat{\boldsymbol{k}}\cdot\boldsymbol{t})(\boldsymbol{q}\cdot\boldsymbol{t})\hat{k}^k + 2uv(\hat{\boldsymbol{k}}\cdot\boldsymbol{t})^2 q^k\Bigg] + \mathcal{O}(|\boldsymbol{q}|^2), \end{aligned} \tag{3.79}$$

and

$$\begin{aligned} f_{\varepsilon\varepsilon}^{k,uv}(\boldsymbol{q},\boldsymbol{t},\boldsymbol{k}) = &-2\left(\frac{u}{|\boldsymbol{k}+\boldsymbol{q}|}-\frac{v}{|\boldsymbol{k}|}\right)(\boldsymbol{k}\cdot\boldsymbol{t})^2 k^k - 2uv(\hat{\boldsymbol{k}}\cdot\boldsymbol{t})^2(\boldsymbol{q}\cdot\boldsymbol{t})k^k \\ &+ (1+uv)\big[(\boldsymbol{k}\cdot\boldsymbol{t})q^k - (\boldsymbol{q}\cdot\boldsymbol{t})k^k\big] + 2(2u+v)(\hat{\boldsymbol{k}}\cdot\boldsymbol{t})^2|\boldsymbol{k}|q^k \\ &+ (u+v)\big(|\boldsymbol{k}|q^k + (\boldsymbol{k}\cdot\boldsymbol{q})\hat{k}^k\big) - 4v(\boldsymbol{k}\cdot\boldsymbol{t})(\boldsymbol{q}\cdot\boldsymbol{t})\hat{k}^k \\ &- 4uv(\hat{\boldsymbol{k}}\cdot\boldsymbol{q})(\hat{\boldsymbol{k}}\cdot\boldsymbol{t})k^k + 2uv|\boldsymbol{k}|(\hat{\boldsymbol{k}}\cdot\boldsymbol{t})^3 q^k + \mathcal{O}(|\boldsymbol{q}|^2). \end{aligned} \tag{3.80}$$

From these expressions it becomes clear which terms contribute to the thermoelectric transport coefficients. Indeed, the first two terms in $f_{ee}^{k,uv}(\boldsymbol{q},\boldsymbol{t},\boldsymbol{k})$, $f_{\varepsilon e}^{k,uv}(\boldsymbol{q},\boldsymbol{t},\boldsymbol{k})$ and $f_{\varepsilon\varepsilon}^{k,uv}(\boldsymbol{q},\boldsymbol{t},\boldsymbol{k})$ are the only terms that are non-zero when $|\boldsymbol{q}|=0$. An expansion of $N_{uv}^{\chi}(\omega,\boldsymbol{q},\boldsymbol{t},\boldsymbol{k})$ with $uv=-1$ for small $|\boldsymbol{q}|$ gives a term proportional to ω, as can be seen in Eq. (3.36), thereby leading to the terms proportional to ωt^k in Eqs. (3.26a)-(3.26c).

For $f_{\varepsilon p}^{k,uv}(\boldsymbol{q},\boldsymbol{t},\boldsymbol{k})$ and $f_{ee}^{k,uv}(\boldsymbol{q},\boldsymbol{t},\boldsymbol{k})$ the full dependence on $\boldsymbol{q}$ is tractable.

The latter is given by

$$f_{ee}^{k,uv}(\boldsymbol{q},\boldsymbol{t},\boldsymbol{k}) = \frac{2ue^2}{|\boldsymbol{k}+\boldsymbol{q}|}\Big[k^k - uv|\boldsymbol{k}+\boldsymbol{q}|\hat{k}^k + q^k + v(\hat{\boldsymbol{k}}\cdot\boldsymbol{t})q^k - v(\boldsymbol{q}\cdot\boldsymbol{t})\hat{k}^k\Big], \quad (3.81)$$

and the former by

$$f_{\varepsilon p}^{k,uv}(\boldsymbol{q},\boldsymbol{t},\boldsymbol{k}) = -u\frac{\big[2(\hat{\boldsymbol{k}}\cdot\boldsymbol{q})k^k - 2|\boldsymbol{k}|q^k + |\boldsymbol{q}|^2\hat{k}^k - (\hat{\boldsymbol{k}}\cdot\boldsymbol{q})q^k\big]}{4|\boldsymbol{k}+\boldsymbol{q}|} \times\Big[|\boldsymbol{k}| + uv|\boldsymbol{k}+\boldsymbol{q}| + 2v(\boldsymbol{k}\cdot\boldsymbol{t}) + v(\boldsymbol{q}\cdot\boldsymbol{t})\Big]. \quad (3.82)$$

Furthermore, the function $W(x;\boldsymbol{t})$ that we used in the expressions for the chiral magnetic conductivities Eq. (3.38b) and Eq. (3.38a), is defined by

$$W(x;\boldsymbol{t}) \equiv \frac{1-(x-t_\parallel)^2}{Z(x;\boldsymbol{t})^2}\left[1+\frac{x}{2}Y(x;\boldsymbol{t})\right] = \begin{cases}(1-t^2)^{-1} & \text{for } x\to 0,\\ l(t) & \text{for } x\to\infty,\end{cases} \quad (3.83)$$

in terms of

$$Y(x;\boldsymbol{t}) \equiv \frac{1}{Z}\log\left(\frac{[x'-1][1-t_\parallel+t_\parallel x - t^2(1+x') + (1-t_\parallel)Z]}{[x'+1][1+t_\parallel+t_\parallel x - t^2(1-x') + (1+t_\parallel)Z]}\right), \quad (3.84a)$$

$$Z(x;\boldsymbol{t}) \equiv \sqrt{1+2t_\parallel x - t_\parallel^2 - t^2 + t^2(x-t_\parallel)^2}, \quad (3.84b)$$

where we denoted $x' \equiv x - t_\parallel$ and omitted the dependence of $Z(x;\boldsymbol{t})$ on $x,\boldsymbol{t}$ in the definition of $Y(x;\boldsymbol{t})$.

Finally, the explicit expression for the susceptibility in the long-wavelength limit from Eq. (3.42) can also be expressed in terms of $W(x;\boldsymbol{t})$ in the following way

$$\chi_{nn}^{\pm}(x,\boldsymbol{0};\boldsymbol{t}) = \frac{\mu_\pm^2}{4\pi^2 v_F^3 Z(x;\boldsymbol{t})^2}\left[\frac{t_\parallel^2 - t^2}{1-t^2} + \left(2+t^2-3t_\parallel^2+\frac{2x^2}{1-(x-t_\parallel)^2}\right)W(x;\boldsymbol{t})\right]. \quad (3.85)$$

Two useful limiting cases for $\chi^{\pm}_{nn}(x,\mathbf{0};\boldsymbol{t})$ are

$$\lim_{x\to 0}\chi^{\pm}_{nn}(x,\mathbf{0};\boldsymbol{t})=\frac{\mu_{\pm}^2}{2\pi^2(1-t^2)^2v_F^3}, \tag{3.86}$$

which we used in Eq. (3.43), and

$$\lim_{\boldsymbol{t}\to\mathbf{0}}\chi^{\pm}_{nn}(x,\mathbf{0};\boldsymbol{t})=\frac{\mu_{\pm}^2}{2\pi^2v_F^3}\left[1-\frac{x}{2}\log\left(\frac{x+1}{x-1}\right)\right]. \tag{3.87}$$

3.A.2 Frequency dependence magnetovortical conductivities

Here we list the full frequency dependence of the chiral magnetic and chiral vortical conductivities. They can all be expressed in terms of the functions $L_i(\omega)$ defined in Eqs.(3.55a), (3.55b) and (3.55c). We find for chiral magnetic energy conductivity

$$\begin{aligned}\sigma_{\varepsilon}^{\mathrm{CME}}(\omega)=-\sum_{\chi=\pm}\frac{\chi\mu_\chi^2(1-t^2)}{24\pi^2t^3}\Bigg[&\frac{(t^2-4)t}{1-t^2}+\frac{\omega^2+12\mu_\chi^2}{8\mu_\chi^2}L_1(\omega)\\&-\frac{3\omega^2+4\mu_\chi^2}{4\omega\mu_\chi}L_2(\omega)-\frac{\omega^2t^3}{8\mu_\chi^2}L_3(\omega)\Bigg].\end{aligned} \tag{3.88}$$

For the longitudinal and transverse chiral vortical conductivities we have

$$\begin{aligned}\sigma_{\parallel}^{\mathrm{CVE}}(\omega)=-\sum_{\chi=\pm}\frac{\chi\mu_\chi^2}{48\pi^2t^3}\Bigg[&\frac{(2+t^2)t}{1-t^2}-\frac{(1+3t^2)\omega^2+12\mu_\chi^2}{16\mu_\chi^2}L_1(\omega)\\&+\frac{3(1+t^2)\omega^2+4\mu_\chi^2}{8\omega\mu_\chi}L_2(\omega)+\frac{\omega^2t^3}{4\mu_\chi^2}L_3(\omega)\Bigg],\end{aligned} \tag{3.89}$$

and

$$\begin{aligned}\sigma_{\perp}^{\mathrm{CVE}}(\omega)=\sum_{\chi=\pm}\frac{\chi\mu_\chi^2}{96\pi^2t^3}\Bigg[&\frac{(2-5t^2)t}{1-t^2}-\frac{(1-9t^2)\omega^2+12\mu_\chi^2}{16\mu_\chi^2}L_1(\omega)\\&+\frac{3(1-3t^2)\omega^2+4\mu_\chi^2}{8\omega\mu_\chi}L_2(\omega)-\frac{\omega^2t^3}{2\mu_\chi^2}L_3(\omega)\Bigg].\end{aligned} \tag{3.90}$$

The longitudinal chiral vortical energy conductivity reads

$$\sigma^{\mathrm{CVE}}_{\varepsilon,\parallel}(\omega) = -\sum_{\chi=\pm} \frac{\chi\mu_\chi^3}{64\pi^2 t^3}\Bigg[\frac{(3t^4+14t^2-9)t}{3(1-t^2)^2} - \frac{(1+3t^2)t\omega^2}{4\mu_\chi^2} - \frac{(1+2t^2-3t^4)\omega^4 + 8(3+t^2)\omega^2\mu_\chi^2 + 16\mu_\chi^4}{32\omega\mu_\chi^3} L_2(\omega) + \frac{(1+t^2)\omega^2 + 4\mu_\chi^2}{4\mu_\chi^2} L_1(\omega)\Bigg], \tag{3.91}$$

and, finally, the transversal chiral vortical energy conductivity

$$\sigma^{\mathrm{CVE}}_{\varepsilon,\perp}(\omega) = -\sum_{\chi=\pm} \frac{\chi\mu_\chi^3}{128\pi^2 t^3}\Bigg[\frac{(9-14t^2+13t^4)t}{3(1-t^2)^2} + \frac{(1-5t^2)t\omega^2}{4\mu_\chi^2} + \frac{(1-6t^2+5t^4)\omega^4 + 24(1-t^2)\omega^2\mu_\chi^2 + 16\mu_\chi^4}{32\omega\mu_\chi^3} L_2(\omega) - \frac{(1-3t^2)\omega^2 + 4\mu_\chi^2}{4\mu_\chi^2} L_1(\omega)\Bigg]. \tag{3.92}$$

4 Large anomalous magnetic moment in doped three-dimensional semimetals

We investigate the effect of Coulomb interactions on the electromagnetic response of three-dimensional Dirac and Weyl semimetals. In a calculation reminiscent of Schwinger's seminal work on quantum electrodynamics, we find three physically distinct effects for the anomalous magnetic moment of the relativistic-like quasiparticles in the semimetal. In the case of non-zero doping, the anomalous magnetic moment is finite at long wavelengths and typically orders of magnitude larger than Schwinger's result. We also find interesting effects of one of the three new Hamiltonian terms on the topological surface states at the interface between vacuum and a Weyl semimetal. We conclude that observation of these effects should be within experimental reach.[a]

4.1 Introduction

Two breakthroughs in the history of quantum mechanics were the discovery of spin by Stern and Gerlach in 1922 and the formulation of the Schrödinger equation in 1926 [148, 149]. These two concepts were combined in 1927, when Pauli generalized Schrödinger's equation to take into account the Zeeman interaction of an electron's spin with an external magnetic field, assuming the value $g_m = 2$ for its dimensionless magnetic moment [150]. This theory was subsequently put on a firm footing by Dirac in 1928 when he derived the fully relativistic wave equation that now carries his name [16]. A natural result

[a] This chapter is directly based on "E.C.I. van der Wurff and H.T.C. Stoof, *Large anomalous magnetic moment in three-dimensional Dirac and Weyl semimetals*, Physical Review B **94**, 155118 (2016)".

in his derivation of Pauli's theory was a dimensionless magnetic moment of precisely $g_m = 2$ for the electron. However, in 1947 a slight deviation from $g_m = 2$ was measured [151, 152]. It took only a year before this discrepancy was resolved, when Schwinger used the powerful tools of the newly developed quantum field theory to calculate the anomalous magnetic moment of the electron due to its coupling to the photon [153].

One important consequence of the anomalous magnetic moment becomes clear when it is added to the Dirac equation for an electron in an external magnetic field. In its absence, the energy spectrum consists of Landau levels that are all doubly degenerate, except for the spin-polarized zero-energy Landau level. However, this spin degeneracy is removed when an anomalous magnetic moment is present [154]. This spin splitting is reminiscent of the situation that occurs when spin degeneracy is removed in a Dirac semimetal by breaking time-reversal or inversion symmetry, which splits the Dirac cone into two Weyl cones. The resulting material is nowadays referred to as a Weyl semimetal.

Recently, Dirac and Weyl physics has been discovered in materials such as Cd_3As_2 and Na_3Bi, and TaAs, respectively [36, 155–159]. The last material has also been proposed to exhibit anomalous transport properties due to its topological nature such as an anomalous Hall effect and a chiral anomaly [54, 55, 83, 84, 99]. In view of these rapid developments it is of interest to take a closer look at the anomalous magnetic moment of the electrons in these materials. However, there is now a fundamental difference with Schwinger's calculation: he considered the case of *massive* electrons in the vacuum, whereas the electrons in a Weyl semimetal are described by *massless* electrons around the band-touching points. In the case of massless electrons in a vacuum, one would find that the anomalous magnetic moment contains an infrared divergence. Luckily, there is a way around this conundrum. Due to their coupling to a non-zero density of electrons, photons acquire an effective mass at long wavelengths. This results in a screened Coulomb potential between the electrons in the material, providing an infrared cutoff that renders the anomalous magnetic moment finite.

There have been previous investigations on the role of *unscreened* Coulomb interactions between the electrons in a Weyl semimetal, including the effect on charge transport [160], the Berry curvature [161] and the thermodynamic stability [162]. Additionally, vertex corrections were investigated both numerically [163] and using the renormalization group [164]. Here we instead

include the effects of screening and provide an analytical calculation of the anomalous magnetic moment resulting from the transversal part of the vertex correction.

We start our discussion by deriving the screened Coulomb potential in doped Weyl semimetals in Section 4.2. Subsequently, we investigate how the coupling of the electrons to an external electromagnetic field is changed by including these screened electron-electron interactions. By calculating the so-called transverse vertex corrections in Section 4.3 we find that the anomalous magnetic moment of a Weyl fermion generates three distinct Hamiltonian terms, one of which constitutes a Rashba spin-orbit coupling, whereas the other two form a Zeeman-like effect. Due to the large ratio of the free electron mass and the effective mass of the photon, both effects are non-negligible. To illustrate that these effects can have observable consequences, we consider the influence of the anomalous Rashba spin-orbit coupling on the topological edge states of a Weyl semimetal in Section 4.4. Finally, we discuss our results in Section 4.5.

4.2 Screening in Dirac and Weyl semimetals

We start by considering a three-dimensional semimetal with Dirac dispersion $\varepsilon_{\boldsymbol{k}} = \hbar v_F |\boldsymbol{k}|$, in terms of its Fermi velocity v_F, which we always assume to be much less then the speed of light c so that we are allowed to neglect retardation effects and current-current interactions. Moreover, throughout the following we will ignore logarithmic interaction corrections. For instance, the Fermi velocity will be taken constant, independent of the doping of the material. To preserve generality we consider a system with g degenerate Dirac cones that split up into $g/2$ pairs of Weyl cones when time-reversal symmetry is broken. In principle, each of these pairs of cones can be separated in momentum space with its own time-reversal symmetry breaking vector $\boldsymbol{b}$ that acts as an internal Zeeman field.

The dielectric function for such a material has been studied extensively and is known analytically in the random-phase approximation [165–169]. This is a good approximation because the number of Weyl nodes g is typically large and higher-order corrections are surpressed in powers of $1/g$ [170]. In terms of its complex frequency z and wavenumber q the dielectric function equals $\varepsilon(q, z) = 1 - V(q)\Pi(q, z)$, with the Coulomb potential $V(q) = e^2/\varepsilon_0 q^2$. The

polarizability at zero temperature can be written as

$$\Pi(q,z) = \frac{-g}{24\pi^2\hbar v_F}\left[8k_F^2 + q^2\log\left(\frac{v_F^2\Lambda^2}{v_F^2q^2-z^2}\right) - q^2\sum_{\sigma,\sigma'=\pm} G\left(\frac{\sigma' z + 2v_F k_F}{\sigma v_F q}\right) H\left(\frac{\sigma' z - \sigma v_F q}{2v_F k_F}\right)\right], \tag{4.1}$$

where k_F is the Fermi wavenumber and we defined the dimensionless functions $H(x) \equiv \ln(1+1/x)$ and $G(x) \equiv \left(x^3-3x+2\right)/4$. Here, Λ is an ultraviolet cutoff scale. Its physical origin lies in the fact that in a real material, the linear Dirac dispersion is only an approximation that holds up to a certain energy scale.

The screened Coulomb potential follows from the static retarded dielectric function $\varepsilon(q,0^+)$ and reads, again up to logarithmic corrections,

$$V_{\mathrm{sc}}(q) = \frac{V(q)}{\varepsilon(q,0^+)} \overset{q\to 0}{=} \frac{e^2}{\varepsilon_0}\frac{1}{q^2+\xi^{-2}}, \tag{4.2}$$

with the screening length $\xi \equiv \sqrt{\pi/2g\bar{\alpha}k_F^2}$ in terms of the dimensionless effective fine-structure constant $\bar{\alpha} \equiv c\alpha/v_F = e^2/4\pi\varepsilon_0\hbar v_F$. This also defines an effective photon mass $m_{\mathrm{ph}} \equiv \hbar/\xi c$.

We note explicitly that, due to $v_F/c \ll 1$, this screened Coulomb potential does not depend on the separation in momentum space between a pair of Weyl cones. Furthermore, the screened Coulomb potential reduces to an ordinary one in the case of zero doping. Additionally, the numerically transformed Coulomb potential shows very small-amplitude Friedel oscillations at large distances, but as the exponential Yukawa-decay is dominant, we will neglect those here [169]. We also noted above that the effective photon mass in the screened Coulomb potential will act as an infrared cutoff. For the typical parameters $k_F = 0.04$ Å^{-1}, $g = 12$ and $v_F = c/300$ [36, 157], we have $k_F\xi \approx 0.24$ and a photon mass which is three orders of magnitude smaller than the free electron mass m_{el}. This implies that the Coulomb potential has a relatively large range and as a result vertex corrections can be of significant size, as we will show now.

4.3 Transversal vertex corrections in Weyl metals

We specialize to a Weyl semimetal with broken time-reversal symmetry characterized by a shift of $2\mathbf{b}$ between a pair of Weyl points in momentum space. Although we shall ultimately consider the zero-temperature limit, we set up our framework at a non-zero temperature T. The Weyl fermions are described by the spinor $\psi(\boldsymbol{x},\tau)$. Thus, the imaginary-time action for a single Weyl cone with chemical potential μ and chirality $\chi = \pm$ then reads

$$S_0[\psi,\psi^\dagger] = \hbar\int_0^{\hbar\beta} \mathrm{d}\tau \int \mathrm{d}\boldsymbol{x}\, \psi^\dagger(\boldsymbol{x},\tau)\Big[\partial_\tau - \frac{\mu}{\hbar} - v_F\boldsymbol{\sigma}\cdot\big(i\chi\boldsymbol{\nabla} + \boldsymbol{b}\big)\Big]\psi(\mathbf{x},\tau), \quad (4.3)$$

with $\beta = (k_B T)^{-1}$ and $\boldsymbol{\sigma}$ is the vector of Pauli matrices. The emergent Lorentz symmetry allows us to use a relativistic notation with unit metric. Using this notation, we couple the Weyl fermions with charge $-e$ to the external four-potential $A^\mu = (\phi/v_F, \mathbf{A})$ via the minimal substitution $\hbar\partial_\tau \to \hbar\partial_\tau - e\phi(\boldsymbol{x},\tau)$ and $-i\hbar\boldsymbol{\nabla} \to -i\hbar\boldsymbol{\nabla} + e\mathbf{A}(\boldsymbol{x},\tau)$. This way the coupling terms in the action can be written as $-ev_F A_\mu\gamma^\mu$, with $\gamma^\mu = (1, -\chi\boldsymbol{\sigma})$ the bare vertex. The final ingredient that we add to our theory is interactions between the fermions via the screened Coulomb potential $V_{\mathrm{sc}}(q)$ presented in Eq. (4.2).

We next perform perturbation theory in the bare vertex and the screened Coulomb interactions. The location of the Weyl cone can be absorbed into the wavenumber by defining $\boldsymbol{\sigma}\cdot(\chi\boldsymbol{k} - \boldsymbol{b}) \equiv \chi\boldsymbol{\sigma}\cdot\boldsymbol{p}$. Then the bare Matsubara propagator of the fermion is

$$G_0(i\omega_n,\boldsymbol{p}) = \frac{1}{i\omega_n + \mu/\hbar - \chi v_F\boldsymbol{\sigma}\cdot\boldsymbol{p}}, \quad (4.4)$$

and we find that the lowest-order vertex correction for a system of volume V reads

$$\hbar\beta V\Gamma^\mu(p,q) = -\sum_{\boldsymbol{p}',n'} G_0(p'+q)\gamma^\mu V_{\mathrm{sc}}(|\boldsymbol{p}'-\boldsymbol{p}|)G_0(p'), \quad (4.5)$$

where p^μ and q^μ are the incoming fermion and photon wavenumber. The vertex correction is depicted graphically in terms of a Feynman diagram in Fig. 4.1.

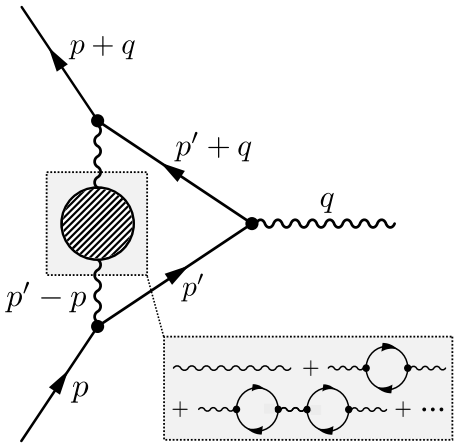

Figure 4.1: Feynman diagram for the vertex correction. Photons are denoted by whiggly lines and fermions by straight lines. The dashed circle and inset indicate that we are using the screened Coulomb interaction in the random-phase approximation.

The total vertex needs to preserve gauge invariance, which can be checked with the so-called Ward-Takahashi identity. For the bare vertex it is given by the relation $v_F q_\mu \gamma^\mu = G_0^{-1}(q+p) - G_0^{-1}(p)$, while for the vertex correction, the Ward-Takahashi identity reads [59]

$$v_F q_\mu \Gamma^\mu(p,q) = \Sigma(p) - \Sigma(q+p), \tag{4.6}$$

where

$$\hbar\beta V \Sigma(p) = -\sum_{\boldsymbol{p}',n'} G_0(p') V_{\mathrm{sc}}(|\boldsymbol{p}'-\boldsymbol{p}|) \tag{4.7}$$

is the self-energy in the so-called G_0W-approximation.

The vertex correction in Eq. (4.5) has longitudinal and transversal parts. The longitudinal part is divergent in the ultraviolet and upon regularization it ultimately leads to a renormalization of the Fermi velocity as a function of the doping. This has been investigated thoroughly in Ref.[171]. Since the renormalization is only logarithmic in μ, it is for our purposes allowed to not consider it here. Instead, we aim to investigate the transversal part of the vertex correction. Besides using the Ward-Takahashi identity, we fix the decomposition of the vertex correction in its transversal and longitudinal parts

uniquely by demanding that both the longitudinal and the transversal vertex are hermitian. To make analytic progress we specialize to zero temperature and perform perturbation theory in the external photon momentum up to first order. This is valid if we consider external electric and magnetic fields that vary slowly in space and time. Finally, gauge invariance enures that everything can be written in terms of the external electric and magnetic fields $\mathbf{E}$ and $\mathbf{B}$. The details of this calculation can be found in Appendix 4.A. In the end we find that the correction to the action in Eq. (4.3) reads

$$-ev_F A_\mu \Gamma^\mu_{\text{transv.}}(\boldsymbol{p}) = -\big[\boldsymbol{\mu}_1(\boldsymbol{p}) \times \boldsymbol{\sigma}\big] \cdot \frac{\mathbf{E}}{v_F} - \big[\boldsymbol{\mu}_2(p) - \chi \boldsymbol{\mu}_1(\boldsymbol{p})\big] \cdot \mathbf{B}, \tag{4.8}$$

in terms of the (magnetic) moments $\boldsymbol{\mu}_1(\boldsymbol{p}) \equiv \mu_1(p)\boldsymbol{p}$ and $\boldsymbol{\mu}_2(p) \equiv \mu_2(p)\boldsymbol{\sigma}$. The first term constitutes a Rashba-spin-orbit coupling, while the second and third term together form a Zeeman-like effect. Note that the third term is proportional to χ, indicating that its sign depends on the chirality of the Weyl cone under consideration.

The magnitudes $\mu_i(p)$, scaled by the Bohr magneton $\mu_B = e\hbar/2m_{\text{el}}$, are given by

$$\begin{aligned}\frac{\mu_1(p)}{\mu_B} = \frac{ec\alpha}{2\pi\mu_B \xi p^3}\Big\{ & 2p\xi - \arctan\big(\xi[k_F + p]\big) \\ & + \arctan\big(\xi[k_F - p]\big) - \frac{k_F \xi f(p\xi)}{2}\Big\},\end{aligned} \tag{4.9a}$$

$$\frac{\mu_2(p)}{\mu_B} = \frac{ec\alpha f(p\xi)}{8\pi\mu_B p}, \tag{4.9b}$$

in terms of the function

$$f(x) \equiv \ln\left(\frac{1 + (k_F\xi + x)^2}{1 + (k_F\xi - x)^2}\right). \tag{4.10}$$

In the long-wavelength limit we obtain

$$\frac{\mu_1(p)}{\mu_B} \overset{p\to 0}{=} \frac{\alpha}{2\pi}\frac{m_{\text{el}}}{m_{\text{ph}}}\left(\frac{2[1 - (k_F\xi)^2]}{3[1 + (k_F\xi)^2]^2}\right)\xi, \tag{4.11a}$$

$$\frac{\mu_2(p)}{\mu_B} \overset{p\to 0}{=} \frac{\alpha}{2\pi}\frac{m_{\text{el}}}{m_{\text{ph}}}\left(\frac{2k_F\xi}{1 + (k_F\xi)^2}\right), \tag{4.11b}$$

where $\alpha/2\pi$ is Schwinger's result in terms of the fine-structure constant α and $m_{\mathrm{el}}/m_{\mathrm{ph}} \gg 1$, as discussed previously. Eqs. (4.8), (4.9a) and (4.9b) form the central result of this chapter. We stress that although $\alpha/2\pi \approx 1.2 \cdot 10^{-3}$ is small, it is multiplied by the large fraction $m_{\mathrm{el}}/m_{\mathrm{ph}} \approx 1.6 \cdot 10^{3}$, indicating that our results are between two and three orders of magnitude larger than those of Schwinger. Indeed, we find for $k_F\xi \approx 0.24$ in the long-wavelength limit $\mu_1 k_F/\mu_B \approx 0.25$ and $\mu_2/\mu_B \approx 0.85$. Hence, these anomalous effects are substantial.

One interesting property is that both the magnetic moment $\boldsymbol{\mu}_1$ and the linear combination $\boldsymbol{\mu}_2 - \chi\boldsymbol{\mu}_1$ can change sign for small p and $k_F\xi < 1$. As $k_F\xi = \sqrt{\pi/2g\bar{\alpha}}$, this means that the strength of the effective fine-structure constant determines the sign of the Zeeman or Rashba effect. We have plotted the two moments for a range of different values[b] for $k_F\xi$ in Fig. 4.2.

Yet another important property is that the two magnetic moments are finite in the long-wavelength limit. The crucial ingredient for obtaining this finite long-wavelength behavior is a non-zero doping. This causes the Coulomb potential to be screened, yielding an infrared cutoff for the loop-integral in the vertex correction. Indeed, in the limit $k_F \to 0$, or $\xi \to \infty$, we obtain the infrared divergence $\mu_i(p) \sim p^{-2}$. Exactly the same behavior was recently found in a holographic calculation at the critical Dirac point [172].

4.4 Rashba-modified topological surface states

To consider observable effects of the anomalous magnetic moment, we now investigate how the Rashba spin-orbit coupling due to a constant external electric field $\mathbf{E}$ influences the topological surface states of a Weyl semimetal. The effect of the Zeeman-like anomalous terms will be discussed in future work. We would like to stress that the Rashba spin-orbit coupling we derived in Eq. (4.8) does not follow from a Peierls substitution in the Weyl Hamiltonian. Its true origin lies in the Coulomb interactions between the electrons.

We consider a simple model system inspired by Refs. [126, 173]. We consider an interface at $x = 0$ of a Dirac vacuum with mass m for $x < 0$ and

[b] In Ref. [1], the published version of this Chapter, we only plotted the magnetic moments for $k_F\xi = 1/4$ and $k_F\xi = 2$. Here we plot the magnetic moments for a broader range of values of $k_F\xi$.

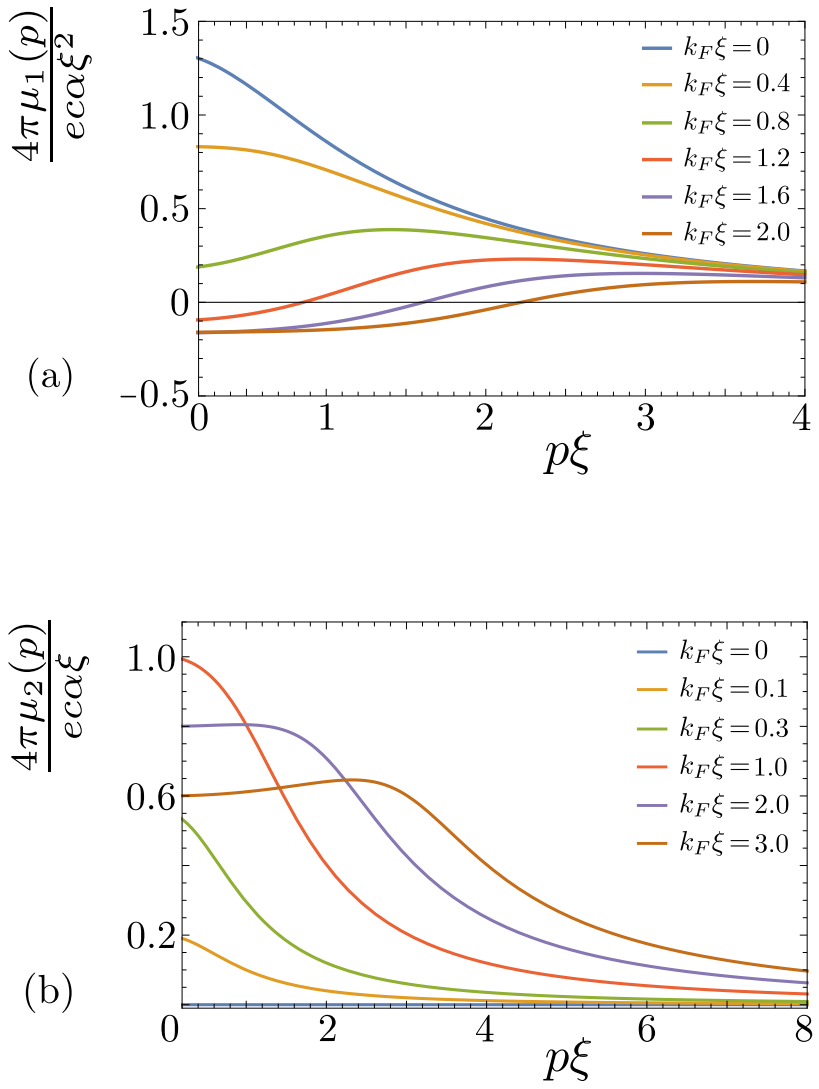

Figure 4.2: Plot of the dimensionless magnetic moments $4\pi\mu_1(p)/ec\alpha\xi^2$ in (a) and $4\pi\mu_2(p)/ec\alpha\xi$ in (b) as a function of $p\xi$ and for several values of $k_F\xi$. Note that $\mu_1(p)$ changes sign for small p when $k_F\xi < 1$ and that $\mu_2(p)$ is zero for $k_F\xi = 0$.

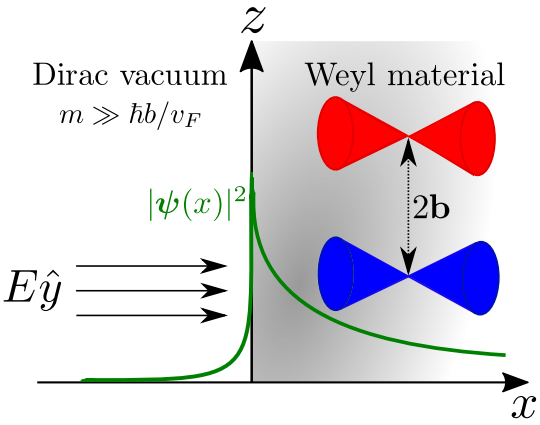

Figure 4.3: Schematic illustration of the proposed experimental set-up. A plane at $x = 0$ separates the vacuum ($x < 0$) from the Weyl semimetal ($x > 0$) with a time-reversal symmetry breaking vector $\boldsymbol{b} = b\hat{z}$. In this case the electric field is perpendicular to the surface, in the y-direction.

a massless Weyl semimetal with a time-reversal symmetry breaking vector $\boldsymbol{b} = b\hat{z}$ for $x > 0$, with $b > 0$. The mass $m \gg \hbar b/v_F$ acts as the equivalent of a work function for the electrons to leave the Weyl semimetal into the Dirac vacuum. Such a system has a surface state localized around $x = 0$ that propagates in the yz-plane. This state is chiral because it only admits the dispersion $\omega_{\boldsymbol{k}} = -v_F k_y$, whereas the dispersion with the other sign is not a solution. Additionally, it only exists for $|k_z| < b$, which leads to the so-called Fermi arc of the system [36]. A schematic image of this set-up is presented in Fig. 4.3.

Now we ask how these properties change when we turn on a constant external electric field which induces the anomalous Rashba spin-orbit coupling. For $x > 0$ the Hamiltonian is block diagonal with its constituent blocks $H_\pm$ corresponding to the different chiralities $\chi = \pm$. In the long-wavelength limit it reads

$$\frac{H_\pm(\boldsymbol{k})}{\hbar v_F} = \pm\big[\boldsymbol{k} \mp \boldsymbol{b}\big] \cdot \boldsymbol{\sigma} - \big[\bar{\mathbf{E}} \times (\boldsymbol{k} \mp \boldsymbol{b})\big] \cdot \boldsymbol{\sigma}, \tag{4.12}$$

where we introduced the dimensionless electric field $\bar{\mathbf{E}} \equiv \mu_1(0)\mathbf{E}/\hbar v_F^2$ and we reintroduced the time-reversal symmetry breaking vector by setting $\boldsymbol{p} = \boldsymbol{k} \mp \boldsymbol{b}$. The wavenumbers along the y and z-direction are good quantum

numbers, such that the eigenvalue problem becomes one-dimensional in the x-coordinate

We proceed by solving the eigenvalue problems of the Dirac and Weyl Hamiltonian for $x < 0$ and $x > 0$ separately and demand continuity of the spinors at $x = 0$. This yields a four-by-four matching matrix, which should have a vanishing determinant to support a bound state located around $x = 0$. There are three physically distinct situations. An electric field in the y-direction yields the same dispersion relation and Fermi arc as in the case of zero electric field. In the case of an electric field in the z-direction, we find a modified dispersion $\omega_{\boldsymbol{k}} = -v_F\sqrt{1+\bar{E}^2}k_y$, while the Fermi arc is still given by $|k_z| < b$. Finally, the most interesting situation is the one where the electric field is in the x-direction, perpendicular to the surface. In this case we find a dispersion relation that reads

$$\omega_{\boldsymbol{k}} = -v_F \frac{(1-\bar{E}^2)bk_y + \bar{E}(k_y^2 + k_z^2 - b^2)}{\sqrt{(b+\bar{E}k_y)^2 + \bar{E}^2 k_z^2}}, \tag{4.13}$$

which only is a solution in the exterior of the two circles defined by

$$\left[k_y + \frac{b}{\bar{E}}\right]^2 + \left[k_z \pm \frac{b}{2}\left(1 + \frac{1}{\bar{E}^2}\right)\right]^2 = \frac{b^2}{4}\left[1 + \frac{1}{\bar{E}^2}\right]^2. \tag{4.14}$$

Hence, there are no bound states with wavenumbers in the interior of these circles because the one-dimensional problem then corresponds to a topologically trivial band insulator. This is drastically different from the condition $|k_z| > b$ for zero electric field. Furthermore, by demanding $\omega_{\boldsymbol{k}} = v_F k_F$ we find that the Fermi arc is a part of a circle that increases in size for larger values of the electric field. This should be contrasted to the case of zero electric field, where the Fermi arc is just a straight line. We show a density plot of the dispersion relation and Fermi arc for two values of $\bar{E}$ in Fig. 4.4.

This dramatic change in the Fermi arc when an external electric field is applied could be an experimental signature to detect the anomalous Rashba spin-orbit coupling. Additionally, we deduce from Figs. 4.4(a) and (b) that there are bound states with a certain wavenumber which seize to be a bound state when a critical value for the externally applied electric field is reached. This could be another experimental signature of the presence of the anomalous Rashba spin-orbit coupling. To make quantitative predictions for a

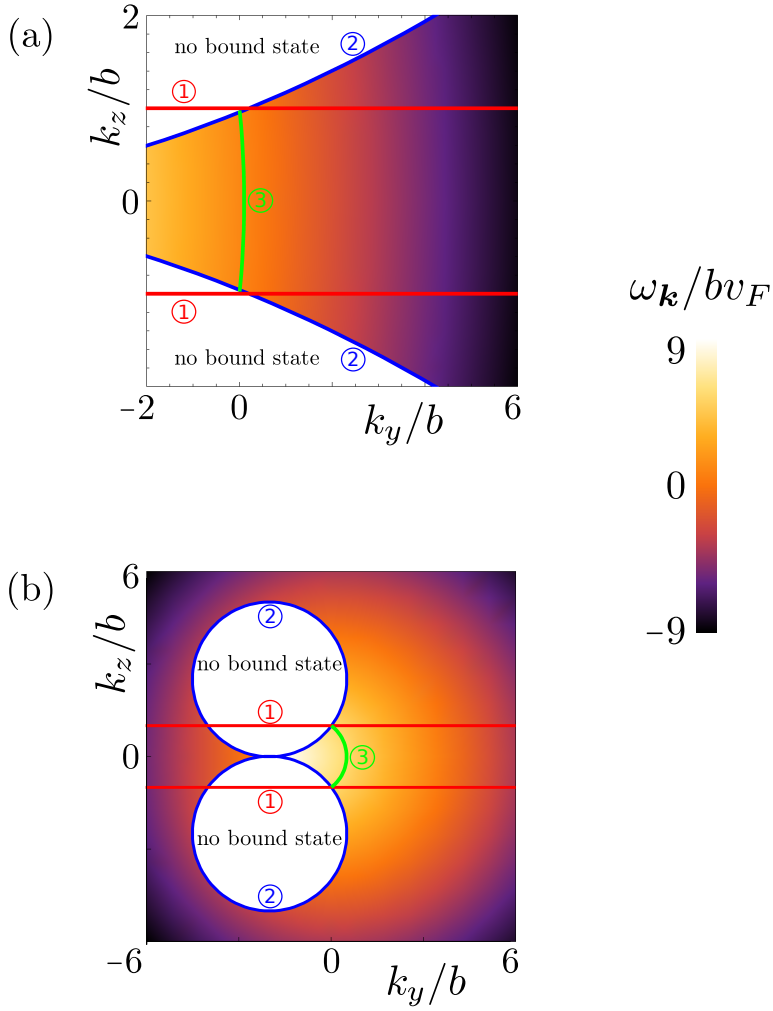

Figure 4.4: a) Density plot of the dimensionless dispersion $\omega_{\boldsymbol{k}}/bv_F$ as a function of k_y/b and k_z/b for an electric field in the y-direction with dimensionless magnitude $\bar{E} = 1/10$. b) Same as in a), but for $\bar{E} = 1/2$. The white regions cannot support a bound state. In both figures the red lines [and ①] indicate the boundary of the area where there are bound states for zero electric field, wheres the blue lines [and ②] do the same in the case of a non-zero electric field. The green lines [and ③] indicate the Fermi arc for a non-zero electric field.

specific material, one needs to consider a more detailed model of the surface. However, we stress that the qualitative behavior obtained above is determined by topology and will remain the same.

4.5 Conclusion and discussion

In conclusion, we have calculated the first-order vertex correction for a three-dimensional Weyl semimetal in which the massless electrons interact via a screened Coulomb potential. We have shown that the correction is orders of magnitude larger than Schwinger's result for the anomalous magnetic moment for massive electrons in quantum electrodynamics. Finally, we have demonstrated that the anomalous Rashba spin-orbit coupling has an observable effect on the surface states located between a Weyl semimetal and vacuum, as well as on the corresponding Fermi arcs. A surface Rashba effect due to the inevitable breaking of inversion symmetry at the surface of the material does not modify these latter observations [174]. Indeed, the mere existence of the surface states is determined by the topological nature of the band structure in the bulk, which is characterized by the bulk Hamiltonian that includes the Rashba-like spin-orbit coupling coming from the transversal vertex correction. Hence, a Rashba effect on the surface changes the dispersion relation in Eq. (4.13), but will not change the boundaries of the regions in the (k_y, k_z)-plane that determine whether or not there is a surface state.

In future work we plan to investigate the influence of the Zeeman-like term on the bound surface states of a Weyl semimetal.[c] It would also be interesting to explore if the anomalous effects derived in this chapter leave a distinct signature in the quasiparticle interference pattern of a Weyl semimetal [175–177].

Acknowledgements: It is our pleasure to thank Vivian Jacobs, Panos Betzios, Umut Gürsoy, Guido van Miert and Lars Fritz for useful discussions and the latter two also for reading the manuscript that led to the publication on which this chapter is based.

[c] This was studied in the master theses of Casper van Langen and Thijs van Gogh.

4.A Appendix: derivation transversal vertex correction

In this appendix we discuss the various details of the calculations that led to the results presented Section 4.3. We start by deriving the vertex correction and subsequently obtain an integral expression for its transverse part. Finally, we evaluate the corresponding magnetic moments in the long-wavelength limit.

4.A.1 Vertex correction

As discussed in Section 4.3, the imaginary time action describing a Weyl fermion coupled to an external magnetic field and experiencing Coulomb interactions can be written as $S[\psi,\psi^\dagger,A] = S_0[\psi,\psi^\dagger] + S_{\text{coup}}[\psi,\psi^\dagger,A] + S_{\text{int}}[\psi,\psi^\dagger]$. The free action $S_0[\psi,\psi^\dagger]$ is given by Eq. (4.3), while the coupling action $S_{\text{coup}}[\psi,\psi^\dagger,A]$ and the interaction action $S_{\text{int}}[\psi,\psi^\dagger]$ are given by

$$S_{\text{coup}} = -ev_F \int_{\tau,\boldsymbol{x}} \psi^\dagger_\alpha(\boldsymbol{x},\tau)\gamma^\mu_{0,\alpha\beta}\psi_\beta(\boldsymbol{x},\tau)A_\mu(\boldsymbol{x},\tau), \tag{4.15a}$$

$$S_{\text{int}} = \frac{1}{2}\int_{\tau,\boldsymbol{x},\boldsymbol{x}'} \psi^\dagger_\alpha(\mathbf{x},\tau)\psi^\dagger_\beta(\boldsymbol{x}',\tau)V_{\text{sc}}(|\boldsymbol{x}-\boldsymbol{x}'|)\psi_\beta(\boldsymbol{x}',\tau)\psi_\alpha(\boldsymbol{x},\tau), \tag{4.15b}$$

where we abbreviated $\int_{\tau,\boldsymbol{x}} \equiv \int_0^\beta \mathrm{d}\tau \int \mathrm{d}\boldsymbol{x}$ and took $\hbar \equiv 1$. The screened Coulomb interaction $V_{\text{sc}}(|\boldsymbol{x}-\boldsymbol{x}'|)$ can be calculated by considering the self-energy of a non-zero density of electrons due to a coupling to photons as is explained in Section 4.2. In real space the interaction potential $V_{\text{sc}}(|\boldsymbol{x}|)$ follows from the Fourier transform of Eq. (4.2) and is given by

$$V_{\text{sc}}(|\boldsymbol{x}|) = \int \frac{\mathrm{d}^3\boldsymbol{q}}{(2\pi)^3} V_{\text{sc}}(|\boldsymbol{q}|)e^{i\boldsymbol{q}\cdot\boldsymbol{x}} = \frac{e^2}{4\pi\varepsilon_0}\frac{e^{-|\boldsymbol{x}|/\xi}}{|\boldsymbol{x}|}, \tag{4.16}$$

i.e., it is of the Yukawa type with ξ the screening length that we defined underneath Eq. (4.2).

The vertex correction can now be derived by considering the diagram depicted in Fig. 4.1 and using the Feynman rules following from Eqs. (4.15a) and (4.15b). Equivalently, it can be obtained by performing perturbation theory in the coupling to the external gauge field and the screened Coulomb potential. Upon re-exponentiating, we find that the effective action reads in

Fourier space

$$S^{\text{eff}} = -\sum_{\boldsymbol{k},n} \psi^{\dagger}_{\boldsymbol{k},n} G_0^{-1}(\boldsymbol{k}, i\omega_n)\psi_{\boldsymbol{k},n} + \frac{e}{\sqrt{\beta V}} \sum_{\boldsymbol{p},\boldsymbol{p}',n,n'} \psi^{\dagger}_{\boldsymbol{p}+\boldsymbol{p}',n+n'} \Big[\gamma_0^{\mu} + \Gamma^{\mu}(\boldsymbol{p},\boldsymbol{p}', i\omega_n)\Big]\psi_{\boldsymbol{p}',n'} A_{\mu,\boldsymbol{p},n}, \quad (4.17)$$

with V the volume and $\Gamma^{\mu}(\boldsymbol{p},\boldsymbol{p}';i\omega_n)$ the vertex correction. The electronic Green's function $G_0(\boldsymbol{k}, i\omega_n)$ follows from the non-interacting action and is given in Eq. (4.4). The vertex correction reads

$$\Gamma^{\mu}(\boldsymbol{p},\boldsymbol{p}', i\omega_n) = -\frac{1}{\beta V}\sum_{\boldsymbol{k},i\omega_m} G_0(\boldsymbol{p}+\boldsymbol{k}, i\omega_n + i\omega_m)\gamma_0^{\mu} G_0(\boldsymbol{k}, i\omega_m) V_{\text{sc}}(|\boldsymbol{k}-\boldsymbol{p}'|). \quad (4.18)$$

As discussed in Section 4.3, the Ward identity is an exact identity relating the full interacting vertex and the interacting Green's function. Verifying if the Ward identity is obeyed is a powerful, non-trivial check. In our case the Ward identity for the bare vertex reads

$$v_F p_{\mu}\gamma_0^{\mu} = i\omega_n\gamma_0^0 + v_F p_i \gamma_0^i = G_0^{-1}(\boldsymbol{p}+\boldsymbol{k}, i\omega_n + i\omega_m) - G_0^{-1}(\boldsymbol{k}, i\omega_m), \quad (4.19)$$

which is easily verified using the expression in Eq. (4.4) for the fermionic propagator. Going one order higher, the Ward identity reads[d]

$$v_F p_{\mu}\Gamma^{\mu}(\boldsymbol{p},\boldsymbol{p}', i\omega_n) = \Sigma(\boldsymbol{k}, i\omega_m) - \Sigma(\boldsymbol{p}+\boldsymbol{k}, i\omega_n + i\omega_m), \quad (4.20)$$

where we used the self-energy

$$\Sigma(\boldsymbol{p}, i\omega_n) = -\frac{1}{\hbar\beta V}\sum_{\boldsymbol{k},i\omega_m} V_{\text{sc}}(|\boldsymbol{k}-\boldsymbol{p}|) G_0(\boldsymbol{k}, i\omega_m), \quad (4.21)$$

which coincides with Eq. (4.7). Using the expression in Eq. (4.18) for the vertex correction and the expression and yet again Eq. (4.4) for the fermionic

[d] The minus sign different between the right-hand side of Eq. (4.19) and Eq. (4.20) is due to the fact that in Dyson's equation for the interacting propagator $G(\boldsymbol{k}, i\omega_n)$ there is a relative minus sign between the propagator and self-energy: $G^{-1}(\boldsymbol{k}, i\omega_m) = G_0^{-1}(\boldsymbol{k}, i\omega_m) - \Sigma(\boldsymbol{k}, i\omega_m)$.

propagator, it is a straightforward but lengthy calculation to verify the Ward identity also up to first order.

4.A.2 Transversal vertex correction

We now split up the vertex function in a longitudinal and transversal part. There is some ambiguity in this decomposition, because a transversal term can always be added to the longitudinal term, leaving it longitudinal. We therefore constrain our decomposition by demanding that both the transversal and the longitudinal vertex are *indepedently* hermitian. From the action in Eq. (4.17) we find that hermiticity implies that

$$\Gamma^{\mu}_{\alpha\beta}(\boldsymbol{p},\boldsymbol{p}',i\omega_n) = \left[\Gamma^{\mu}_{\beta\alpha}(-\boldsymbol{p},\boldsymbol{p}+\boldsymbol{p}',-i\omega_n)\right]^*. \tag{4.22}$$

Using this to find the hermitian, transversal vertex correction, we find for the temporal part

$$\begin{aligned}&\Gamma^0_{\text{trans}}(\boldsymbol{p},\boldsymbol{p}',i\omega_n)\\ &= \sum_{\boldsymbol{k},i\omega_m} \frac{V_{\text{sc}}(|\boldsymbol{k}-\boldsymbol{p}'|)}{\beta V} \frac{-iv_F^2\varepsilon^{ijk}p^ik^j\sigma^k}{\left[(i\omega_{m+n}+\mu)^2-\varepsilon^2_{\boldsymbol{p}+\boldsymbol{k}}\right]\left[(i\omega_m+\mu)^2-\varepsilon^2_{\boldsymbol{k}}\right]},\end{aligned} \tag{4.23}$$

with $i\omega_{m+n} \equiv i\omega_n + i\omega_m = i[2(n+m)+1]\pi/\beta$ a fermionic Matsubara frequency and $\varepsilon_{\boldsymbol{k}} = v_F|\boldsymbol{k}|$ the single-particle dispersion relation. For the spatial part of the vertex correction we find

$$\begin{aligned}&\Gamma^i_{\text{trans}}(\boldsymbol{p},\boldsymbol{p}',i\omega_n)\\ &= \sum_{\boldsymbol{k},i\omega_m} \frac{v_F V_{\text{sc}}(|\boldsymbol{k}-\boldsymbol{p}'|)}{\beta V} \frac{i\varepsilon^{ijk}\left[v_F\chi p^jk^k + i\omega_n k^j\sigma^k - (i\omega_m+\mu)p^j\sigma^k\right]}{\left[(i\omega_{m+n}+\mu)^2-\varepsilon^2_{\boldsymbol{p}+\boldsymbol{k}}\right]\left[(i\omega_m+\mu)^2-\varepsilon^2_{\boldsymbol{k}}\right]}.\end{aligned} \tag{4.24}$$

Note that when calculating $v_F p_\mu \Gamma^\mu_{\text{trans}}(\boldsymbol{p},\boldsymbol{p}',i\omega_n) = i\omega_n\Gamma^0_{\text{trans}}(\boldsymbol{p},\boldsymbol{p}',i\omega_n) + v_F p_i \Gamma^i_{\text{trans}}(\boldsymbol{p},\boldsymbol{p}',i\omega_n)$, which should yield zero, the contribution coming from Eq. (4.23) and the contribution coming from the second term on the right-hand side in Eq. (4.24) drop out against one another. Furthermore, the first term and the last group of terms on the right-hand side in Eq. (4.24) are perpendicular to $\boldsymbol{p}$ and thus each vanish separately upon contracting with the external photon wavenumber.

Contracting the vertex correction with the external gauge field $A^\mu =$

$(\phi/v_F, \mathbf{A})$ should yield a gauge invariant result, i.e., it should be expressable in electric $\mathbf{E} = -\boldsymbol{\nabla}\phi - \partial_t \mathbf{A}$ and magnetic fields $\mathbf{B} = \boldsymbol{\nabla} \times \mathbf{A}$ only. Indeed we find

$$-ev_F A_\mu(i\omega_n, \boldsymbol{p})\Gamma^\mu(\boldsymbol{p}, \boldsymbol{p}', i\omega_n) = \frac{ev_F^2}{V}\sum_{\boldsymbol{k}} V_{\mathrm{sc}}(|\boldsymbol{k}-\boldsymbol{p}'|)\Big[(\boldsymbol{\sigma}\cdot\mathbf{B})N_1(\boldsymbol{p},\boldsymbol{k},i\omega_n) + \Big(\mathbf{E}\cdot(\boldsymbol{k}\times\boldsymbol{\sigma}) - \chi v_F(\boldsymbol{k}\cdot\mathbf{B})\Big)N_0(\boldsymbol{p},\boldsymbol{k},i\omega_n)\Big], \tag{4.25}$$

where we defined

$$N_a(\boldsymbol{p},\boldsymbol{k},i\omega_n) = \frac{1}{\beta}\sum_{i\omega_m}\frac{(i\omega_m+\mu)^a}{\big[(i\omega_{m+n}+\mu)^2-\varepsilon^2_{\boldsymbol{p}+\boldsymbol{k}}\big]\big[(i\omega_m+\mu)^2-\varepsilon^2_{\boldsymbol{k}}\big]}, \tag{4.26}$$

with a an integer. In the next section we consider Eq. (4.25) and Eq. (4.26) in the long-wavelength limit to derive the main result of Section 4.3. Additionally, we explicitly compute the magnetic moments $\mu_i(\boldsymbol{p}')$.

4.A.3 Magnetic moments

In order to calculate the magnetic moments $\mu_i(\boldsymbol{p}')$, we need to perform the Matsubara sum in Eq. (4.26). Splitting the fractions we find for $a = 1$

$$\begin{aligned} N_1(\boldsymbol{p},\boldsymbol{k},i\omega_n) &= \frac{k_BT}{4\varepsilon_{\boldsymbol{p}+\boldsymbol{k}}}\sum_{u,v=\pm}\sum_{i\omega_m}\frac{u}{\big[i\omega_{m+n}+\mu-u\varepsilon_{\boldsymbol{p}+\boldsymbol{k}}\big]\big[i\omega_m+\mu-v\varepsilon_{\boldsymbol{k}}\big]} \\ &= \frac{1}{4\varepsilon_{\boldsymbol{p}+\boldsymbol{k}}}\sum_{u,v=\pm} u\frac{N_{\mathrm{F}}(v\varepsilon_{\boldsymbol{k}}-\mu)-N_{\mathrm{F}}(u\varepsilon_{\boldsymbol{p}+\boldsymbol{k}}-\mu)}{i\omega_n-u\varepsilon_{\boldsymbol{p}+\boldsymbol{k}}+v\varepsilon_{\boldsymbol{k}}}, \end{aligned} \tag{4.27}$$

where in the second step we converted the Matsubara sum to an integral in the complex plane [111] and $N_{\mathrm{F}}(x) \equiv (e^{\beta x}+1)^{-1}$ is the Fermi-Dirac distribution. Similarly, we obtain for $a = 0$,

$$\begin{aligned} N_0(\boldsymbol{p},\boldsymbol{k},i\omega_n) &= \frac{k_BT}{4\varepsilon_{\boldsymbol{p}+\boldsymbol{k}}\varepsilon_{\boldsymbol{k}}}\sum_{u,v=\pm}\sum_{i\omega_m}\frac{uv}{\big[i\omega_{m+n}+\mu-u\varepsilon_{\boldsymbol{p}+\boldsymbol{k}}\big]\big[i\omega_m+\mu-v\varepsilon_{\boldsymbol{k}}\big]} \\ &= \frac{1}{4\varepsilon_{\boldsymbol{p}+\boldsymbol{k}}\varepsilon_{\boldsymbol{k}}}\sum_{u,v=\pm} uv\frac{N_{\mathrm{F}}(v\varepsilon_{\boldsymbol{k}}-\mu)-N_{\mathrm{F}}(u\varepsilon_{\boldsymbol{p}+\boldsymbol{k}}-\mu)}{i\omega_n-u\varepsilon_{\boldsymbol{p}+\boldsymbol{k}}+v\varepsilon_{\boldsymbol{k}}}. \end{aligned} \tag{4.28}$$

We now Wick rotate back to real frequency, i.e., $i\omega_n \to \omega + i\eta$ with $\eta \to 0$ and consider the long-wavelength limit of Eqs. (4.27) and (4.28). The limits $\boldsymbol{p} \to \boldsymbol{0}$ and $\omega \to 0$ do not commute [138] and we will consider the *static* limit, in which we first send $\omega \to 0$ and subsequently $\boldsymbol{p} \to \boldsymbol{0}$. Care must be taken when $u = v = +1$, because then both the numerator and the denominator in Eq. (4.27) go to zero in the static limit.[e] Taking the limit carefully yields the derivative of the Fermi-Dirac distribution. Ultimately we find

$$\lim_{\boldsymbol{p}\to\boldsymbol{0}} \lim_{\omega\to 0} N_1(\boldsymbol{p}, \boldsymbol{k}, \omega^+) = \frac{N_{\mathrm{F}}'(\varepsilon_{\boldsymbol{k}} - \mu)}{4v_F|\boldsymbol{k}|}, \tag{4.29a}$$

$$\lim_{\boldsymbol{p}\to\boldsymbol{0}} \lim_{\omega\to 0} N_0(\boldsymbol{p}, \boldsymbol{k}, \omega^+) = \frac{1 - N_{\mathrm{F}}(\varepsilon_{\boldsymbol{k}} - \mu) + v_F|\boldsymbol{k}|N_{\mathrm{F}}'(\varepsilon_{\boldsymbol{k}} - \mu)}{4v_F^3|\boldsymbol{k}|^3} + \frac{N_{\mathrm{F}}(\varepsilon_{\boldsymbol{k}} + \mu)}{4v_F^3|\boldsymbol{k}|^3}. \tag{4.29b}$$

For simplicity, we consider the zero-temperature limit $T = 0$, in which the last term in Eq. (4.29b) vanishes, $N_{\mathrm{F}}(\varepsilon_{\boldsymbol{k}} - \mu) = \vartheta(\mu - \varepsilon_{\boldsymbol{k}})$ and $N_{\mathrm{F}}'(\varepsilon_{\boldsymbol{k}} - \mu) = -\delta(\mu - \varepsilon_{\boldsymbol{k}})$. Considering Eq. (4.25) in the long-wavelength limit and at $T = 0$, we use Eqs.(4.29a) and (4.29b) to obtain Eq. (4.8), the main result from Section 4.3. The magnetic moments read

$$\mu_1(\boldsymbol{p}') = e \int_{\boldsymbol{k}} \frac{(\boldsymbol{k}\cdot\boldsymbol{p}')V_{\mathrm{sc}}(|\boldsymbol{k} - \boldsymbol{p}'|)}{4|\boldsymbol{k}|^3|\boldsymbol{p}'|^2} \big[\vartheta(|\boldsymbol{k}| - k_F) - |\boldsymbol{k}|\delta(k_F - |\boldsymbol{k}|)\big], \tag{4.30a}$$

$$\mu_2(\boldsymbol{p}') = -e \int_{\boldsymbol{k}} \frac{V_{\mathrm{sc}}(|\boldsymbol{k} - \boldsymbol{p}'|)}{4|\boldsymbol{k}|} \delta(k_F - |\boldsymbol{k}|), \tag{4.30b}$$

where we used $k_F \equiv \mu/v_F$ and took the continuum limit by replacing $V^{-1}\sum_{\boldsymbol{k}} \to \int_{\boldsymbol{k}} \equiv \int \mathrm{d}^3\boldsymbol{k}/(2\pi)^3$. In deriving Eq. (4.30a) we used the fact that for any function $f(\boldsymbol{k}, \boldsymbol{p}')$ we have that $\int_{\boldsymbol{k}} k^i f(\boldsymbol{k}, \boldsymbol{p}') = \hat{p}'^i \int_{\boldsymbol{k}} (\boldsymbol{k}\cdot\hat{\boldsymbol{p}}') f(\boldsymbol{k}, \boldsymbol{p}')$. Going to spherical coordinates with $k = |\boldsymbol{k}|$ and $p' = |\boldsymbol{p}'|$, and using Eq. (4.2)

[e] In the homogeneous limit, i.e. first sending $\boldsymbol{p} \to \boldsymbol{0}$ and subsequently $\omega \to 0$, this term vanishes.

for $V_{\mathrm{sc}}(|\boldsymbol{k}|)$, we find that $\mu_2(\boldsymbol{p}') = \mu_2(p')$ with

$$\begin{aligned}\mu_2(p') &= -\frac{e^3}{16\varepsilon_0\pi^2}\int_{-1}^{1}\mathrm{d}y\int_0^{\infty}\mathrm{d}k\,\frac{k\delta(k_F-k)}{k^2-2p'ky+p'^2+\xi^{-2}}\\ &= \frac{e^3}{32\pi^2\varepsilon_0 p'}\ln\left(\frac{1+\xi^2(p'+k_F)^2}{1+\xi^2(p'-k_F)^2}\right)\\ &\equiv \frac{e^3}{32\pi^2\varepsilon_0}\frac{f(\xi p')}{p'},\end{aligned} \tag{4.31}$$

which agrees with the result in Eq. (4.9b) upon reintroducing $\hbar$ and scaling on the Bohr magneton. Note that the function $f(x)$, defined in Eq. (4.10), can be expanded as $f(x) \approx 4k_F\xi x/[1+(k_F\xi)^2]$ for small x. The fraction $f(\xi p')/p'$ in Eq. (4.31) is therefore well-defined in the infrared. Following the same procedure, we find $\mu_1(\boldsymbol{p}') = \mu_1(p')$, with

$$\begin{aligned}\mu_1(p') &= \frac{e^3}{16\pi^2\varepsilon_0 p'}\int_{-1}^{1}\mathrm{d}y\int_0^{\infty}\mathrm{d}k\,\frac{\vartheta(k-k_F)-k\delta(k_F-k)}{k^2-2kp'y+p'^2+\xi^{-2}}\\ &= \frac{e^3}{16\pi^2\varepsilon_0 p'}\int_0^{\infty}\mathrm{d}k\left[\vartheta(k-k_F)-k\delta(k_F-k)\right]\\ &\quad\times\left[\left(\frac{1+\xi^2(k^2+p'^2)}{4k^2p'^2\xi^2}\right)\ln\left(\frac{1+\xi^2(k+p')^2}{1+\xi^2(k-p')^2}\right)-\frac{1}{kp'}\right]\\ &= \frac{e^3}{16\pi^2\varepsilon_0 p'^3\xi}\Bigg[2p'\xi-\arctan[(k_F+p')\xi]+\arctan[(k_F-p')\xi]\\ &\qquad\qquad-\frac{k_F\xi}{2}f(p'\xi)\Bigg],\end{aligned} \tag{4.32}$$

which coincides with the result in Eq. (4.9a) upon reintroducing $\hbar$ and scaling on the Bohr magneton.

4.B Appendix: derivation surface states

In this appendix we explicitly derive the aspects of the surface states that were discussed in Section 4.4. We start by discussing the model that is pictorially displayed in Fig. 4.3 in some more mathematical detail. Subsequently, we consider the case of a vanishing electric field and reproduce the well-known chiral surface dispersion relation $\omega_{\boldsymbol{k}} = -v_F k_y$ [126]. We proceed by doing a similar calculation with an electric field perpendicular to the surface, thereby deriving Eq. (4.13) and Eq. (4.14), which differ widely from the case of a vanishing electric field. Finally, we finish by doing the same calculation for an electric field parallel to the surface and find minor differences with the case of a vanishing electric field.

4.B.1 Set-up

We consider the Hamiltonian for a single Weyl cone with chirality χ, in the presence of an externally applied electric field, but vanishing magnetic field. We derived in Section 4.18 that upon including the vertex correction the Hamiltonian reads

$$H = \chi \hbar v_F \sum_{\boldsymbol{k}} \psi^\dagger_{\boldsymbol{k}} (\boldsymbol{\sigma} \cdot \boldsymbol{k}) \psi_{\boldsymbol{k}} - \sum_{\boldsymbol{k}} \psi^\dagger_{\boldsymbol{k}} \left[\frac{\mu_1(|\boldsymbol{k}|)}{v_F} \mathbf{E} \cdot (\boldsymbol{k} \times \boldsymbol{\sigma}) \right] \psi_{\boldsymbol{k}}, \tag{4.33}$$

with $\psi^\dagger_{\boldsymbol{k}}$ ($\psi_{\boldsymbol{k}}$) the fermionic creation (annihilation) operator. We will work in the long-wavelength limit for simplicity and thus take $\mu_1(|\boldsymbol{k}| \to 0)$. Furthermore, we introduce the dimensionless electric field $\bar{\mathbf{E}} \equiv \mu_1(0)\mathbf{E}/\hbar v_F^2$ and explicitly reintroduce the time-reversal symmetry breaking vector $\mathbf{b}$. Then the Bloch Hamiltonian that corresponds to two copies of Eq. (4.33) with opposite chirality reads in matrix form

$$\mathcal{H}_{\mathrm{W}}(\boldsymbol{k}) = \hbar v_F \begin{pmatrix} -\boldsymbol{\sigma} \cdot \boldsymbol{k}_+ + \boldsymbol{\sigma} \cdot (\bar{\mathbf{E}} \times \boldsymbol{k}_+) & 0 \\ 0 & \boldsymbol{\sigma} \cdot \boldsymbol{k}_- + \boldsymbol{\sigma} \cdot (\bar{\mathbf{E}} \times \boldsymbol{k}_-) \end{pmatrix}, \tag{4.34}$$

where we defined $\boldsymbol{k}_\pm \equiv \boldsymbol{k} \pm \boldsymbol{b}$. We now proceed by discussing the set-up displayed in Fig. 4.3. For $x < 0$ we consider a vacuum that is described by a Dirac Hamiltonian with mass m and velocity c, whereas for $x > 0$ we consider a slab of material described by the Hamiltonian in Eq. (4.34). We study the case $\boldsymbol{b} = (0, 0, b)$ and take a large mass $m \gg \hbar b / v_F$ that acts as

a work function for the electrons to leave the material in the region $x > 0$. The vacuum is described by the Dirac Hamiltonian

$$\mathcal{H}_{\mathrm{D}}(\boldsymbol{k}) = \hbar c \begin{pmatrix} -\boldsymbol{\sigma}\cdot\boldsymbol{k} & -i\tilde{m} \\ i\tilde{m} & \boldsymbol{\sigma}\cdot\boldsymbol{k} \end{pmatrix}, \tag{4.35}$$

where we defined $\tilde{m} = mc/\hbar$. As translation invariance is only broken in the x-direction, k_y and k_z are still good quantum numbers and we perform separation of variables in the y and z-direction. We thus decompose the full eigenspinor $\Psi(\boldsymbol{x})$ that enters the Schrödinger equation $H\Psi(\boldsymbol{x}) = \hbar\omega\Psi(\boldsymbol{x})$ as $\Psi(\boldsymbol{x}) = e^{ik_y y + ik_z z}\psi(x)$. In what follows we denote the wavefunction for $x < 0$ by $\psi_<(x)$ and by $\psi_>(x)$ for $x > 0$. Using Eq. (4.35), we find that $\psi_<(x)$ obeys the Schrödinger equation

$$\hbar c \begin{pmatrix} i\sigma^x\partial_x - \sigma^y k_y - \sigma^z k_z & -i\tilde{m} \\ i\tilde{m} & -i\sigma^x\partial_x + \sigma^y k_y + \sigma^z k_z \end{pmatrix} \psi_<(x) = \hbar\omega \mathbb{1}_4 \psi_<(x). \tag{4.36}$$

By multiplying the equation above with $i\sigma^z \otimes \sigma^y$, we obtain

$$\mathbb{1}_4 \partial_x \psi_<(x) = \begin{pmatrix} \sigma^z k_y - \sigma^y k_z - i\sigma^x\omega/c & \tilde{m}\sigma^x \\ \tilde{m}\sigma^x & \sigma^z k_y - \sigma^y k_z + i\sigma^x\omega/c \end{pmatrix} \psi_<(x). \tag{4.37}$$

The solutions to this matrix differential equation are of the form

$$\psi_<(x) = \sum_i A_i e^{\lambda_i x}\mathbf{u}_i, \tag{4.38}$$

where λ_i and $\mathbf{u}_i$ are the eigenvalues and eigenvectors of the matrix in Eq. (4.37). The matrix has two doubly degenerate eigenvalues with opposite sign. As we are considering the case $x < 0$ and we want normalizable solutions, we take the positive eigenvalue $\lambda_< \equiv \sqrt{k_y^2 + k_z^2 + \tilde{m}^2 - (\omega/c)^2}$ and set the remaining A_i to zero. The eigenvectors corresponding to $\lambda_<$ are

$$\mathbf{u}_1 = \left(\frac{k_y + \lambda_<}{\tilde{m}}, -\frac{i(k_z + \omega/c)}{\tilde{m}}, 0, 1 \right)^T, \tag{4.39a}$$

$$\mathbf{u}_2 = \left(\frac{i(k_z - \omega/c)}{\tilde{m}}, \frac{\lambda_< - k_y}{\tilde{m}}, 1, 0 \right)^T. \tag{4.39b}$$

In the limit $\tilde{m} \gg \omega/c, k_y, k_z$ these eigenvectors reduce to $\mathbf{u}_1 = (1,0,0,1)^T$ and $\mathbf{u}_2 = (0,1,1,0)^T$.

Now that we have obtained the solution for the wavefunction for $x < 0$, we will look for the solutions for $x > 0$ and match the two solutions at the surface $x = 0$ by demanding continuity. This matching procedure will only work when ω and (k_x, k_y) obey a certain relation, which is exactly the dispersion relation of the surface state we want to obtain. We will first perform this matching procedure in the easiest case of a vanishing electric field in the next Section.[f] This will give us some insight into how to handle the case of a non-zero electric field, which we will consider thereafter.

4.B.2 Vanishing electric field

The Schrödinger equation in the Weyl slab following from Eq. (4.34) for a vanishing electric field can be cast into the form

$$\mathbb{1}_4 \partial_x \psi_>(x) = \begin{pmatrix} \sigma^z k_y - k_{z,+}\sigma^y - i\sigma^x\tilde{\omega} & 0 \\ 0 & \sigma^z k_y - \sigma^y k_{z,-} + i\sigma^x\tilde{\omega} \end{pmatrix} \psi_>(x), \tag{4.40}$$

in terms of $k_{z,\pm} = k_z \pm b$ and $\tilde{\omega} \equiv \omega/v_F$. The solutions to this matrix differential equation are again of the form shown in Eq. (4.38). The matrix on the right-hand side of Eq. (4.40) has four different eigenvalues given by

$$\pm\lambda_>^{\pm} = \pm\sqrt{(k_z \pm b)^2 + k_y^2 - \tilde{\omega}^2}. \tag{4.41}$$

To obtain a normalizable solution, we choose the two negative eigenvalues which have corresponding eigenvectors

$$\mathbf{u}_3 = \left(\frac{i(k_y - \lambda_>^+)}{b + k_z + \tilde{\omega}}, 1, 0, 0\right)^T, \tag{4.42a}$$

$$\mathbf{u}_4 = \left(0, 0, \frac{-i(k_y - \lambda_>^-)}{b - k_z + \tilde{\omega}}, 1\right)^T. \tag{4.42b}$$

[f] This specific case was discussed in detail in Ref. [56], which in turn was an adaptation of Ref. [126]. All other calculations in this appendix are based on the procedure outlined in these references.

Using these eigenvectors and the eigenvectors $\mathbf{u}_{1,2}$ from Eqs.(4.39a) and (4.39b) for the region $x < 0$, the full wave function can be written as

$$\psi(x) = \vartheta(-x)\big[C\mathbf{u}_1 + D\mathbf{u}_2\big]e^{\lambda_< x} + \vartheta(x)\Big[Ae^{-\lambda_>^+ x}\mathbf{u}_3 + Be^{-\lambda_>^- x}\mathbf{u}_4\Big], \quad (4.43)$$

with A, B, C and D constants. Demanding continuity of the wavefunction at the surface, i.e., $\psi_<(0) = \psi_>(0)$, yields the matching condition[g]

$$\begin{pmatrix} \frac{i(k_y-\lambda_>^+)}{b+k_z+\tilde{\omega}} & 0 & -1 & 0 \\ 1 & 0 & 0 & -1 \\ 0 & \frac{-i(k_y-\lambda_>^-)}{b-k_z+\tilde{\omega}} & 0 & -1 \\ 0 & 1 & -1 & 0 \end{pmatrix} \begin{pmatrix} A \\ B \\ C \\ D \end{pmatrix} = 0. \quad (4.44)$$

To find a nontrivial solution we demand that the determinant of the matrix above vanishes, which results in the dispersion relation $\omega_{\boldsymbol{k}} = -v_F k_y$ [126].

Next, we turn to the more interesting case of a non-zero electric field that is directed perpendicular to the surface.

4.B.3 Electric field perpendicular to the surface

For simplicity we take $\bar{\mathbf{E}} = (\bar{E}, 0, 0)$, such that the electric field only has a component perpendicular to the surface. Similarly to before, we recast the Schrödinger equation with the Hamiltonian in Eq. (4.34) into the form

$$\mathbb{1}_4 \partial_x \psi_>(x) = \begin{pmatrix} \boldsymbol{\sigma}\cdot\mathbf{m}_+^\perp & 0 \\ 0 & \boldsymbol{\sigma}\cdot\mathbf{m}_-^\perp \end{pmatrix} \psi_>(x), \quad (4.45)$$

with

$$\mathbf{m}_\pm^\perp = (\mp i\tilde{\omega}, -k_{z,\pm} \pm \bar{E}k_y, k_y \pm \bar{E}k_{z,\pm}). \quad (4.46)$$

The eigenvalues of the matrix on the right-hand side of Eq. (4.45) are

$$\pm\lambda_\pm^\perp = \pm\sqrt{(b \pm k_z)^2(1+\bar{E}^2) + k_y^2(1+\bar{E}^2) - \tilde{\omega}^2}. \quad (4.47)$$

[g] To find the dispersion relation we need to demand that the determinant of the matching matrix M vanishes. It therefore suffices to consider the unnormalized eigenvectors $\mathbf{u}_i$, as normalizing them would simply give $C\det M = 0$, with C the product of the four normalization constants. To obtain the coefficients for the wavefunction in Eq. (4.43), we would need to solve the system of equations following from the normalized eigenvectors.

Calculating the eigenvectors corresponding to these eigenvalues yields the matching condition

$$\det \begin{pmatrix} 0 & \frac{i(b\bar{E}+k_y+\bar{E}k_z-\lambda_+^\perp)}{b-\bar{E}k_y+k_z+\tilde{\omega}} & -1 & 0 \\ 0 & 1 & 0 & -1 \\ \frac{i(-b\bar{E}-k_y+\bar{E}k_z+\lambda_-^\perp)}{b-\bar{E}k_y-k_z+\tilde{\omega}} & 0 & 0 & -1 \\ 1 & 0 & -1 & 0 \end{pmatrix} = 0, \tag{4.48}$$

which has a solution only outside the circles defined by Eq. (4.14). In this region the dispersion relation reads

$$\omega_{\boldsymbol{k}} = -v_F \frac{bk_y + (b^2 - k_y^2 - k_z^2)\bar{E} - b\bar{E}^2 k_y}{\sqrt{(b-\bar{E}k_y)^2 + \bar{E}^2 k_z^2}}, \tag{4.49}$$

which coincides with the result presented in Eq. (4.13). Note that upon taking $\bar{E} \to 0$ in Eq. (4.49), we reobtain the dispersion relation $\omega_{\boldsymbol{k}} = -v_F k_y$, as we should.

Finally, we briefly discuss the case of an electric field parallel to the surface in the next Section.

4.B.4 Electric field parallel to the surface

For an electric field parallel to the surface, there are two distinct cases to consider: 1) $\bar{\mathbf{E}} = (0, 0, \bar{E})$ and 2) $\bar{\mathbf{E}} = (0, \bar{E}, 0)$. In both cases we again obtain an equation of the same form as Eq. (4.45), i.e.,

$$\mathbb{1}_4 \partial_x \psi_>(x) = \frac{1}{1+\bar{E}^2} \begin{pmatrix} \boldsymbol{\sigma} \cdot \mathbf{m}_+^{i,\parallel} & 0 \\ 0 & \boldsymbol{\sigma} \cdot \mathbf{m}_-^{i,\parallel} \end{pmatrix} \psi_>(x), \tag{4.50}$$

with $\mathbf{m}_\pm^{1,\parallel}$ for the first case and $\mathbf{m}_+^{2,\parallel}$ for the second. These vectors are given by

$$\mathbf{m}_\pm^{1,\parallel} \equiv (\mp i\tilde{\omega} \mp \bar{E}k_{z,\pm}, -k_{z,\pm} + i\bar{E}\tilde{\omega}, (1+\bar{E}^2)k_y), \tag{4.51a}$$

$$\mathbf{m}_\pm^{2,\parallel} \equiv (\mp i\tilde{\omega} \mp \bar{E}k_y, -(1+\bar{E}^2)k_z, k_y - i\bar{E}\tilde{\omega}). \tag{4.51b}$$

In the first case the eigenvalues of the matrix on the right-hand side of Eq. (4.50) are given by

$$\pm\lambda_{\pm}^{1,\parallel} = \pm\sqrt{\frac{(b \pm k_z)^2 + k_y^2(1+\bar{E}^2) - (\omega/v_F)^2}{1+\bar{E}^2}}. \tag{4.52}$$

The corresponding matching matrix has a vanishing determinant provided that $b > |k_z|$ and the dispersion relation is given by $\hbar\omega_{\boldsymbol{k}} = -\hbar v_F k_y \sqrt{1+\bar{E}^2}$. This is the same dispersion relation as the one we obtained for a vanishing electric field, albeit with a renormalized Fermi velocity.

Finally, in the second case the eigenvalues are given by

$$\pm\lambda_{\pm}^{2,\parallel} = \pm\sqrt{\frac{(b \pm k_z)^2(1+\bar{E}^2) + k_y^2 - (\omega/v_F)^2}{1+\bar{E}^2}} \tag{4.53}$$

and we find that the corresponding matching matrix has a vanishing determinant when $\omega_{\boldsymbol{k}} = -v_F k_y$, provided that $b > |k_z|$. In this case the electric field thus has no influence on the dispersion relation.

5 Fermionic many-body excitations in Weyl semimetals due to elastic gauge fields

We study the single-particle spectrum of three-dimensional Weyl semimetals taking into account electron-phonon interactions that are the result of straining the material. We find that a well-defined fermionic excitation appears in addition to the standard peak corresponding to quasiparticle states as suggested by Landau-Fermi liquid theory. Contrary to the case of Dirac systems interacting via the Coulomb interaction, these satellite peaks appear even at lowest order in perturbation theory. The new excitations are anisotropic, as opposed to the single-particle spectrum, and their behavior is dictated by the Debye frequency, which naturally regulates the electron-phonon coupling.[a]

5.1 Introduction

Quite generically, equilibrium and transport properties of many-body metallic systems are accounted for by the Landau theory of the Fermi liquid. This theory is based on the notion of *quasiparticles*: single-particle fermionic excitations that are in one-to-one correspondence to the non-interacting fermionic states. In this regard, the single-particle spectral function $\rho(\omega, \boldsymbol{k})$ provides information about how good the quasiparticle approximation is in an interacting system. For non-interacting fermions the spectral function is given by a Dirac delta function, $\rho^0(\omega, \boldsymbol{k}) = \delta(\hbar\omega + \mu - \varepsilon_{\boldsymbol{k}})$, where $\varepsilon_{\boldsymbol{k}}$ is the dispersion relation of the particle and μ the chemical potential. Upon including interactions, Landau's Fermi liquid theory states that, because the

[a] This chapter is directly based on "E.C.I. van der Wurff and A. Cortijo, *Many-body fermionic excitations in Weyl semimetals due to elastic gauge fields*, arXiv:1905.00908 (2019)".

damping rate of the quasiparticles scales quadratically with the energy at the Fermi level, the spectral function $\rho^0(\omega, \boldsymbol{k})$ becomes a Dirac delta function that is weighted by a parameter $0 < Z < 1$.

It was realized a long time ago [178, 179] that the actual spectral function of an interacting fermionic system is richer than the one suggested by Landau-Fermi liquid theory. Apart from the existence of a well-defined quasiparticle peak, extra weakly-damped, i.e. long-lived, fermionic satellite excitations appear due to the coupling of bare fermions with propagating bosonic degrees of freedom. Such satellite excitations, currently called *plasminos*, were theoretically reported in the context of the quark-gluon plasma [180, 181], and more generically in hot or dense relativistic plasmas [182–184]. In condensed matter physics, they are referred to as *plasmarons*, and they have been theoretically studied in graphene [185–188] and Bismuth [189]. Experimental evidence of these emergent modes has been found using angle-resolved photoemission spectroscopy (ARPES) and optical measurements in graphene [190] and Bismuth [191]. These satellite fermionic excitations are not just of purely theoretical interest. They modify the transport and optical properties of the electronic system [189, 192]: in the case of plasminos, it is well known that they have an opposite helicity-to-chirality ratio as compared to the quasiparticle excitations [193].

In the context of condensed-matter physics, Weyl semimetals are materials that host low-energy quasiparticles that linearly disperse [34]. These quasiparticles also have a chirality and have similar kinematics to chiral ultra-relativistic particles. It is therefore interesting to analyze the many-body fermionic spectrum in these systems and see how many-body quantum effects interfere with ultra-relativistic (or pseudo-relativistic) invariance in solid-state systems.

Despite their appealing similarities to ultra-relativistic systems, we have to keep in mind that Weyl semimetals are condensed matter systems in which the transverse electromagnetic degrees of freedom are not important compared to the collective plasmon mode [194]. Moreover, in three-dimensional systems, longitudinal and transverse plasmonic modes become gapped, with the gap set by the plasma frequency. Effects associated to electron-plasmon interactions are therefore weaker than in the two-dimensional counterpart [170, 171, 195]. Phonons, on the contrary, remain gapless even after including many-body effects in three dimensions. Besides, electron-phonon interactions appear in Weyl semimetals in the form of elastic gauge fields

[76, 196], so they become a promising alternative to study the physics of emergent fermionic degrees of freedom different from the quasiparticles, even at lowest order in perturbation theory [180, 182–184, 197, 198].

In the present work we show that novel fermionic excitations appear in Weyl semimetals due to electron-phonon couplings that can be expressed in terms of elastic gauge (vector) fields. A distinctive feature of the electron-phonon coupling is that extra energy/momentum scales appear in the problem. On the one hand there are the longitudinal/transverse phonon velocities, which are typically much smaller than the Fermi velocity of the electrons, and on the other hand there is the Debye frequency, which naturally acts as a cutoff for the electron-phonon interaction. Another interesting feature is that, as we will see, despite the isotropic nature of the original non-interacting electronic spectrum, the emergent fermionic modes will be anisotropic due the particular nature of the elastic vector fields in Weyl metals. Both the anisotropy and the presence of additional energy and momentum scales make the problem quite different from the situation in relativistic plasmas.

5.2 Strain in Weyl metals

We start by considering the minimal model for a time-reversal symmetry breaking Weyl metal. Setting $\hbar \equiv 1$, the Hamiltonian that describes two Weyl cones separated by $2b_z\hat{\boldsymbol{z}}$ reads

$$\mathcal{H}^W_{0,\chi}(\boldsymbol{k}) = v\boldsymbol{\sigma}_\perp \cdot \boldsymbol{k}_\perp - \chi v_z(k_z - \chi b_z \sigma_z), \tag{5.1}$$

with $\boldsymbol{k} = (\boldsymbol{k}_\perp, k_z)$, $\boldsymbol{\sigma} = (\boldsymbol{\sigma}_\perp, \sigma_z)$ Pauli matrices, $\chi = \pm$ the chirality of the cone and v and v_z Fermi velocities.

It was shown in Ref. [196] that when strain is considered, the lowest-order modification of the Hamiltonian in Eq. (5.1) due to strain is

$$\delta\mathcal{H}[u] = v\chi\boldsymbol{\sigma}_\perp \cdot \boldsymbol{A}^{\rm el}_\perp + v_z A^{\rm el}_z \sigma_z. \tag{5.2}$$

From this expression, we see that the presence of the chirality χ implies that the coupling between electrons and the strain tensor is through a chiral vector potential $\boldsymbol{A}^{\rm el} = (\boldsymbol{A}^{\rm el}_\perp, A^{\rm el}_z)$. That is, it couples with a different sign to the two Weyl nodes with opposite chirality. This so-called elastic gauge

field can be expressed in terms of the microscopic tight-binding parameters leading to the low-energy Hamiltonian in Eq. (5.1) and the linearized strain tensor $u_{ij} \equiv (\partial_i u_j + \partial_j u_i)/2$ that itself is defined in terms of the displacement vector u_i, which measures the deviation from the equilibrium situation [196, 199].

The influence of strain can also be derived from a more generic symmetry-based approach. In this line of approach, all possible scalars that can be constructed from the available scalars, vectors and tensors are added to the Hamiltonian for the unstrained material. At first order in the strain tensor, the strain-induced Hamiltonian $\delta\mathcal{H}[u]$ for one cone contains three possible terms [200], i.e.,

$$\delta\mathcal{H}[u] = vg_0\sigma_0 \mathrm{Tr}[u] + vg_1\sigma_i u_{ij} b_j + vg_2\sigma_i \delta_{ij} b_j \mathrm{Tr}[u], \tag{5.3}$$

with $g_{0,1,2}$ coupling constants. The first term, proportional to the identity matrix σ_0, is the standard electron-phonon coupling coming from the changes induced in the electronic density due to changes in the volume, $\delta V/V = \mathrm{Tr}[u]$. The Hamiltonian given by Eq. (5.3) gives rise to different types of electron-phonon coupling. These couplings can be derived by writing the strain tensor u_{ij} in terms of the displacement u_i and subsequently quantizing the latter to yield phonons. Phonons come in two types: longitudinal and transverse. By construction, only longitudinal phonons contribute to the trace in the first and third term of Eq. (5.3), whereas the second term receives contributions from both longitudinal and transverse phonons.

The coupling between transverse phononic degrees of freedom and electrons is similar to what happens in QED (quantum electrodynamics), where electrons couple to transverse gauge degrees of freedom. However, there is a crucial difference: in ultrarelativistic QED both the gauge and fermionic degrees of freedom have the same velocity, and the transverse modes are gapped as the longitudinal collective plasmonic mode [201]. In the case of phonons, in contrast, the phonon velocity is much smaller than the Fermi velocity, thereby resembling the case of sound modes in plasmas due to ionic collective modes. These modes do not develop a gap but they do attain a strong renormalization of the sound velocity. These observations place the vector electron-phonon coupling in Eq.(5.4) in an unique situation not addressed before in condensed matter, nor in relativistic plasmas.

We therefore proceed by focussing on the second term in Eq. (5.3). The

corresponding second-quantized continuum Hamiltonian $\delta\mathcal{H}_2[u]$ reads in momentum space

$$\delta\mathcal{H}_2[u] = \frac{iv_F g_1}{2}\int_{\boldsymbol{k},\boldsymbol{q}} \psi^\dagger_{\boldsymbol{k}+\boldsymbol{q}}\sigma_i b_j(q_i\delta_{jr} + q_j\delta_{ir})u_r(\boldsymbol{q})\psi_{\boldsymbol{k}}, \tag{5.4}$$

where $\int_{\boldsymbol{k}} \equiv \int \mathrm{d}^3\boldsymbol{k}/(2\pi)^3$, $\psi^\dagger_{\boldsymbol{k}}$ ($\psi_{\boldsymbol{k}}$) is the fermionic creation (annihilation) operator and we denoted the Fermi velocity by v_F. We wrote Eq. (5.4) explicitly in terms of the displacement field $u_r(\boldsymbol{q})$ using the definition of the strain tensor. Upon quantizing the displacement field, we find the electron-phonon vertex $g^\alpha_{\boldsymbol{q}}$, i.e.,

$$g^\alpha_{\boldsymbol{q}} = \frac{i}{2}\frac{v_F g_1}{\sqrt{2\rho\omega_\alpha(\boldsymbol{q})}}\sigma_i b_a(q_i\delta_{ar} + q_a\delta_{ir})\hat{e}^\alpha_r, \tag{5.5}$$

with ρ the mass density of the material under consideration, $\omega_\alpha(\boldsymbol{q}) = c_\alpha|\boldsymbol{q}|$ the dispersion relation of the longitudinal ($\alpha = L$) and transverse acoustic phonons ($\alpha = T$) and c_α the corresponding speeds of sound. Furthermore, the polarization vectors $\hat{e}^\alpha_r$ form a basis in momentum space and obey the identity $\sum_\alpha \hat{e}^\alpha_i\hat{e}^\alpha_j = \delta_{ij}$, with $\hat{e}^L_i = \hat{q}^i$.

It is important to stress that the electron-phonon coupling in Eq. (5.5) follows from very generic elasticity theory. It therefore holds in any Weyl semimetal. Contributions from optical phonons, in contrast, are rather material and model-dependent. Additionally, due to their defining energy-gap at the Γ-point, we expect the contributions from optical phonons to be negligible. We therefore do not consider the effect of optical phonons here and proceed with the computation of the self-energy due to the coupling of the electrons to the acoustic phonons.

5.3 Electronic self-energy

For simplicity we consider an isotropic Weyl cone with dispersion relation $\varepsilon_{\boldsymbol{k}} = v_F|\boldsymbol{k}|$. Furthermore, we treat the acoustic phonons within the Debye model such that upon crossing the Debye frequency ω_D, the phonon density of states becomes zero. The Matsubara Green's function for the acoustic

phonons therefore reads [202]

$$D_0^{\alpha\alpha'}(i\omega_m, \boldsymbol{q}) = \frac{2\omega_\alpha(\boldsymbol{q})}{(i\omega_m)^2 - \omega_\alpha^2(\boldsymbol{q})}\vartheta(k_D^\alpha - |\boldsymbol{q}|)\delta_{\alpha\alpha'}, \tag{5.6}$$

with $i\omega_m$ a bosonic Matsubara frequency and $k_D^\alpha = \omega_D/c_\alpha$ the Debye wavenumber. Upon integrating out the phonons[b], we obtain the one-loop electron self-energy [203]. At $T = 0$ the retarded self-energy reads [183]

$$\Sigma(\omega, \boldsymbol{k}) = \sum_{\substack{\alpha\in\{L,T\}\\ u=\pm}} \int_{k_D^\alpha > |\boldsymbol{q}|} g_{-\boldsymbol{q}}^\alpha \left[\frac{\Lambda_{-u}(\boldsymbol{k}-\boldsymbol{q})}{\omega^+ + u\varepsilon_{\boldsymbol{k}-\boldsymbol{q}} + u\omega_\alpha(\boldsymbol{q})}\right.$$
$$\left. + \frac{u\Lambda_+(\boldsymbol{k}-\boldsymbol{q})\vartheta(\mu - \varepsilon_{\boldsymbol{k}-\boldsymbol{q}})}{\omega^+ - \varepsilon_{\boldsymbol{k}-\boldsymbol{q}} + u\omega_\alpha(\boldsymbol{q})}\right] g_{\boldsymbol{q}}^\alpha, \tag{5.7}$$

with $\Lambda_\pm(\boldsymbol{k}) \equiv (\sigma^0 \pm \boldsymbol{\sigma}\cdot\hat{\boldsymbol{k}})/2$ and $\omega^+ = \omega + i0$. Note that we absorbed the chemical potential in the frequency ω and that the integral is rendered finite by the high-momentum cut-off provided for by the Debye wavenumber. The sum over the polarizations in Eq. (5.7) can be performed separately for the longitudinal and transverse phonons. The full self-energy is then given by the sum of the longitudinal and transverse contribution, i.e., $\Sigma(\omega, \boldsymbol{k}) \equiv \Sigma^L(\omega, \boldsymbol{k}) + \Sigma^T(\omega, \boldsymbol{k})$. For simplicity we will take $c_L = c_T \equiv c$ in the following.

Before we compute the self-energy, it is instructive to introduce dimensionless variables by scaling all parameters on $|\boldsymbol{b}|$, i.e., $\tilde{\omega} \equiv \omega/v_F|\boldsymbol{b}|$, $\tilde{k} \equiv |\boldsymbol{k}|/|\boldsymbol{b}|$, $\tilde{\mu} \equiv \mu/v_F|\boldsymbol{b}|$ and $\tilde{k}_D \equiv k_D/|\boldsymbol{b}|$. The ratio of the dimensionless chemical potential and Debye wavenumber is given by $\tilde{\mu}/\tilde{k}_D = c\mu/v_F\omega_D \equiv \varepsilon\mu/\omega_D$ in terms of the typically small parameter $\varepsilon \equiv c/v_F$. This is rather different from the situation in relativistic plasmas, where the constituent particles are photons and electrons, both moving at the speed of light. Another important difference between the case at hand and relativistic plasmas is that there is no natural Debye frequency scale for photons like we have here. It is therefore interesting to investigate the different possible regimes set by $\tilde{\mu}/\tilde{k}_D$.

From now on we use these dimensionless variables and omit tildes. The

[b] For an explicit derivation of the self-energy, see Appendix 5.A.1.

dimensionless self-energy can be decomposed as

$$\frac{\Sigma(\omega,\boldsymbol{k})}{v_F|\boldsymbol{b}|} = G_1\big[\Sigma_0(\omega,\boldsymbol{k})\sigma_0 + \Sigma_1(\omega,\boldsymbol{k})\boldsymbol{\sigma}\cdot\hat{\boldsymbol{k}}\big], \tag{5.8}$$

with $G_1 \equiv g_1^2|\boldsymbol{b}|^4/4\rho v_F\varepsilon$ a new dimensionless coupling constant. Interestingly, the original coupling constant g_1 is thus increased by a factor of $1/\varepsilon \gg 1$.

After the scaling on $|\boldsymbol{b}|$, the self-energy still depends on the direction $\hat{b}^i$, as can be seen from the vertex in Eq. (5.5). To illustrate the resulting anisotropy in the self-energy, we consider the contribution of the longitudinal phonons to $\Sigma_1(\omega,\boldsymbol{k})$ in some more detail. From Eq. (5.7) it can be expressed as

$$\Sigma_1^L(\omega,\boldsymbol{k}) = \hat{b}^i\hat{b}^j\int_{k_D>|\boldsymbol{q}|}\frac{\hat{q}^i\hat{q}^j}{|\boldsymbol{k}-\boldsymbol{q}|}H_-(\omega,\boldsymbol{k}-\boldsymbol{q},\boldsymbol{q}) \times\big[(2\boldsymbol{k}\cdot\boldsymbol{q}-|\boldsymbol{q}|^2)(\hat{\boldsymbol{k}}\cdot\hat{\boldsymbol{q}})-|\boldsymbol{k}||\boldsymbol{q}|\big], \tag{5.9}$$

with $H_-(\omega,\boldsymbol{k}-\boldsymbol{q},\boldsymbol{q})$ a scalar function that will be specified later. The tensorial structure in Eq. (5.9) can be simplified by noting that the integrand is symmetric under $i\leftrightarrow j$. The integral thus has to yield a linear combination of δ^{ij} and $\hat{k}^i\hat{k}^j$. The latter leads to a contribution proportional to $(\hat{\boldsymbol{b}}\cdot\hat{\boldsymbol{k}})^2$, whereas the former does not depend on the angle between $\boldsymbol{b}$ and $\boldsymbol{k}$. Clearly the resulting expression depends on the angle between $\boldsymbol{b}$ and $\boldsymbol{k}$ in a non-trivial way.

In what follows we investigate the anisotropy of the self-energy in two distinct cases: $\boldsymbol{\lambda}\perp\boldsymbol{k}$ and $\boldsymbol{\lambda}\parallel\boldsymbol{k}$. The corresponding self-energy contributions are $\Sigma_n^\theta(\omega,\boldsymbol{k})$, with $\theta=\perp,\parallel$ and $n=0,1$. They can be expressed as

$$\Sigma_n^\theta(\omega,\boldsymbol{k}) = \frac{1}{8}\int_{k_D>|\boldsymbol{k}+\boldsymbol{q}|}\frac{f_n^\theta(\boldsymbol{k},\boldsymbol{q})H_{\eta_n}(\omega,\boldsymbol{q},\boldsymbol{k}+\boldsymbol{q})}{|\boldsymbol{k}+\boldsymbol{q}|^{2n+1}}, \tag{5.10}$$

with $\eta_0=+,\eta_1=-$. The function $H_\pm(\omega,\boldsymbol{x},\boldsymbol{y})$ reads

$$H_\pm(\omega,\boldsymbol{x},\boldsymbol{y}) \equiv \frac{\vartheta(\mu-|\boldsymbol{x}|)}{\omega^+-|\boldsymbol{x}|+\varepsilon|\boldsymbol{y}|} - \frac{\vartheta(\mu-|\boldsymbol{x}|)}{\omega^+-|\boldsymbol{x}|-\varepsilon|\boldsymbol{y}|} + \frac{1}{\omega^+-|\boldsymbol{x}|-\varepsilon|\boldsymbol{y}|} \pm \frac{1}{\omega^++|\boldsymbol{x}|+\varepsilon|\boldsymbol{y}|}. \tag{5.11}$$

Finally, the functions $f_n^\theta(\boldsymbol{k},\boldsymbol{q})$ in Eq. (5.10) capture the angle-dependence and are functions of $|\boldsymbol{k}|$, $|\boldsymbol{q}|$ and $\boldsymbol{k}\cdot\boldsymbol{q}$. We give explicit derivations and expressions for them in Appendix 5.A.3.

5.4 Spectral functions

Using the expressions following from Eq. (5.10), we calculate the imaginary part of the self-energy analytically. Subsequently, we obtain the real part by numerically integrating the corresponding Kramers-Kronig relation. To investigate the many-body behavior resulting from the self-energy, we calculate the dimensionless spectral function $\rho^\theta(\omega,\boldsymbol{k}) \equiv \rho_+^\theta(\omega,\boldsymbol{k}) + \rho_-^\theta(\omega,\boldsymbol{k})$, with

$$\rho_\pm^\theta(\omega,\boldsymbol{k}) = -\frac{1}{\pi}\frac{G_1\mathrm{Im}[\Sigma_\pm^\theta(\omega,\boldsymbol{k})]}{\left(\omega \mp k - G_1\mathrm{Re}[\Sigma_\pm^\theta(\omega,\boldsymbol{k})]\right)^2 + \left(G_1\mathrm{Im}[\Sigma_\pm^\theta(\omega,\boldsymbol{k})]\right)^2}, \quad (5.12)$$

where $\Sigma_\pm^\theta(\omega,\boldsymbol{k}) \equiv \Sigma_0^\theta(\omega,\boldsymbol{k}) \pm \Sigma_1^\theta(\omega,\boldsymbol{k})$. The spectral function obeys the sum rule $\int_{-\infty}^{\infty} \mathrm{d}\omega\, \rho^\theta(\omega,\boldsymbol{k}) = 2$, as a Weyl fermion has two degrees of freedom. We checked that the sum rule is satisfied for all numerically obtained spectral functions within 1% accuracy. We plot the spectral function in Fig. 5.1 for several interesting cases and proceed to discuss the results presented there in detail.

We start with the case $\boldsymbol{b} \perp \boldsymbol{k}$. In Fig. 5.1(a) we show $\rho^\perp(\omega,\boldsymbol{k})$ for $k_D/\mu = 1/2$ and five different values of $|\boldsymbol{k}| \equiv |\boldsymbol{k}|/|\boldsymbol{b}|$, taking small enough values such that the linear approximation around the Weyl nodes remains justified. As expected, we observe high quasiparticle peaks centered around $\omega_{\boldsymbol{k}} = \tilde{v}_F|\boldsymbol{k}|$, with $\tilde{v}_F$ a renormalized Fermi velocity. There are however, no other satellite peaks present in this case. The situation changes when we increase the ratio k_D/μ. In Fig. 5.1(b) we show the case $k_D/\mu = 2$, for which a broad peak appears around the Debye frequency. As k_D/μ is increased even further, c.f. Fig. 5.1(c), the peak centers around the new value for k_D/μ and becomes narrower and higher, signaling the emergence of a well-defined excitation. Interestingly, the peak is split in two for small $|\boldsymbol{k}|/|\boldsymbol{b}|$ and is damped out upon increasing $|\boldsymbol{k}|/|\boldsymbol{b}|$.

The situation is more pronounced when $\boldsymbol{b} \parallel \boldsymbol{k}$. In this case, the behavior in the regime $k_D/\mu < 1$ is very similar to the behavior presented for the

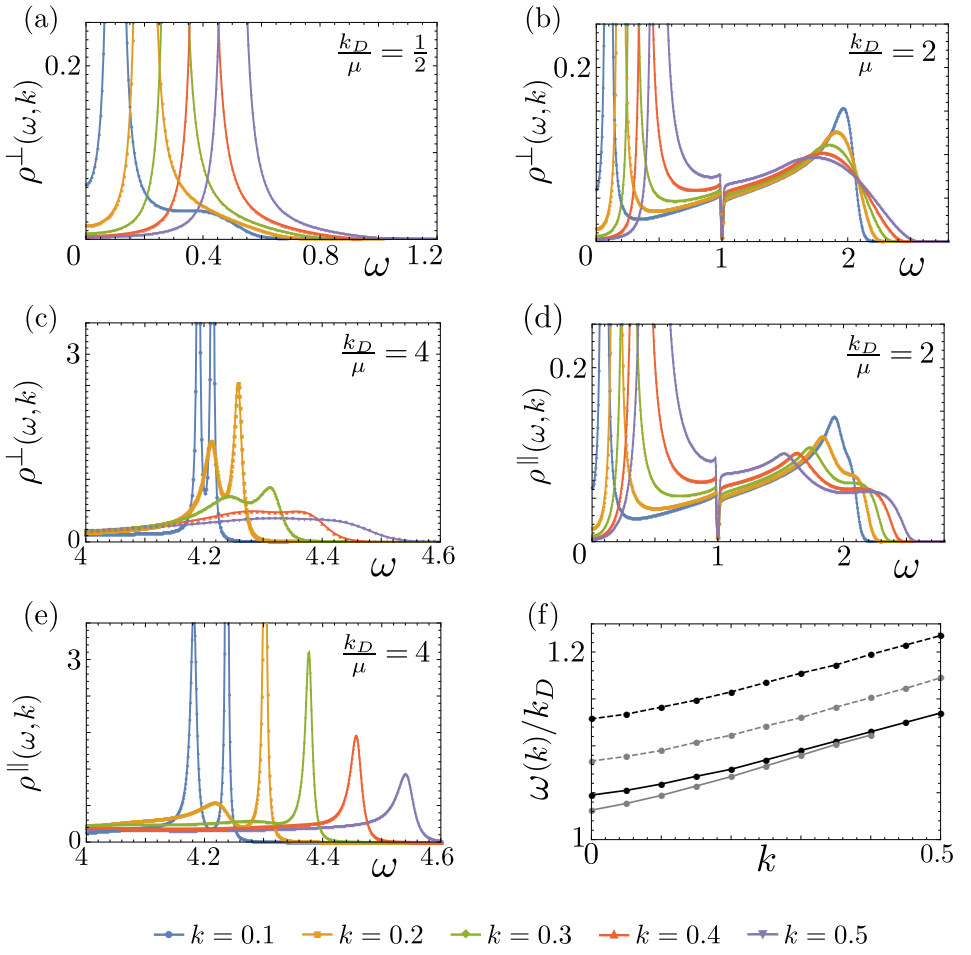

Figure 5.1: (a)-(e) Plots of the spectral function $\rho(\omega, \boldsymbol{k})$, as a function of $\omega \equiv \omega/v_F|\boldsymbol{b}|$ and for five different values of $k \equiv |\boldsymbol{k}|/|\boldsymbol{b}|$. Figs. (a)-(c) are for the case $\boldsymbol{b} \perp \boldsymbol{k}$ and (d), (e) for $\boldsymbol{b} \parallel \boldsymbol{k}$. In (c) and (e) we zoom in on frequencies around the Debye frequency, but the quasiparticle peaks for smaller frequencies remain present. For all spectral functions we used $\varepsilon = 1/100$ and $G_1 = 1.0$. Note that all spectral functions go to zero at $\omega \equiv \omega + \mu = 1$, as we absorbed the chemical potential in the frequency. This is generically the case in an interacting electron liquid because the imaginary part of the self-energy goes to zero for $\omega \to \mu$ [204]. (f) Dispersion relation following from the location of the emergent peaks in the spectral functions from (e). Used parameters in this plot are (from bottom to top): $k_D/\mu = 3.5$ and $\varepsilon = 1/100$ (gray), $k_D/\mu = 4.0$ and $\varepsilon = 1/100$ (black), $k_D/\mu = 4.0$ and $\varepsilon = 1/20$ (dashed gray), $k_D/\mu = 4.0$ and $\varepsilon = 1/10$ (dashed black).

perpendicular case in Fig. 5.1(a), so we refrain from showing a plot of it here. Upon increasing k_D/μ, a distinct behavior from the case $\boldsymbol{b} \perp \boldsymbol{k}$ becomes clear, as can be seen in Figs. 5.1(d) and (e). Especially in Fig. 5.1(e) it is clear that the peaks are even narrower and higher than in Fig. 5.1(c). Again the peaks are centered around the Debye frequency k_D and they disperse as $|\boldsymbol{k}|/|\boldsymbol{b}|$ is increased. In contrast to Fig. 5.1(c) the damping of the peaks as $|\boldsymbol{k}|/|\boldsymbol{b}|$ is increased is much smaller, leading to a well-defined satellite peak at higher wavenumbers. The height of the satellite peak is for a large part determined by the ratio between the phonon and electron velocity $\varepsilon \equiv c/v_F$. As ε is increased from, e.g., 1/100 to 1/10, the peaks become lower and broader, in addition to being located at higher frequencies. The corresponding plots are shown in the Supplemental Material.

In order to investigate the dispersive behavior, we collect the locations of the peaks for several values of $|\boldsymbol{k}|/|\boldsymbol{b}|$ and plot the corresponding dispersion relation $\omega_{\boldsymbol{k}}$, normalized on the Debye wavenumber k_D, in Fig. 5.1(f). We plot the dispersion relation for different values of the ratio between the phonon and electron velocity and the Debye wavenumber k_D. Clearly the dispersion is linear for larger wavenumbers, but it seems to slightly change slope as the wavenumber goes to zero. From Fig. 5.1(f) it is clear that the slope of the linear part of the dispersion is set by the phonon velocity via the dimensionless parameter ε. Upon closer inspection of the last two terms in Eq. (5.11), it appears that the slope is set by $v_F + c = v_F(1 + \varepsilon)$. Scaling the curves in Fig. 5.1(f) on $(1 + \varepsilon)$ does not lead to a perfect collapse due to numerical inaccuracies.

5.5 Conclusion

In summary, we have shown that gauge field-like electron-phonon coupling leads to novel satellite excitations in Weyl metals. The excitations have a rich phenomenology, depending on three parameters: i) the ratio between the Debye wavenumber and the chemical potential k_D/μ, ii) the ratio between the phonon and fermion velocity c/v_F and iii) the angle between the external wavenumber and the separation between the Weyl nodes, $\hat{\boldsymbol{b}} \cdot \hat{\boldsymbol{k}}$. It is also important to note that the transverse phonons contributed significantly to all the spectral functions in Fig. 5.1 and excluding them leads to very different results indeed.

Regarding the potential impact of higher orders in perturbation theory, we do not expect vertex corrections to significantly change the results presented here, as Migdal's theorem for massless fermions dictates that vertex corrections are surpressed by a factor of $c/v_F \ll 1$ [205]. Finally, we note that the emergent fermionic modes found in this work are well defined (the imaginary part of the self-energy becomes much smaller than the real part at small momenta) when $c/v_F \ll 1$, so in principle it is possible to implement schemes based on kinetic theory to compute the impact of these excitations on transport and optical properties [192, 206, 207]. A combination of optical, transport, and ARPES measurements could therefore be employed to show the existence of the new fermionic excitation experimentally.

Acknowledgements: It is a pleasure to thank M. A. H. Vozmediano, K. Landsteiner and H. T. C. Stoof for useful discussions.

5.A Appendix: derivation self-energies

In this appendix we first derive Eq. (5.7). Subsequently we derive the expression in Eq. (5.10) and the corresponding functions $f_n^\theta(\boldsymbol{k},\boldsymbol{q})$. Finally, as an illustrative example we calculate the self-energy at $\boldsymbol{k}=\boldsymbol{0}$, thereby explaining the numerical process that led to Fig. 5.1.

5.A.1 Matsubara sum

Upon integrating out the phonons, the full expression for the self-energy is given by

$$\Sigma(i\omega_m,\boldsymbol{k}) = -\frac{1}{\beta}\sum_{i\omega_n,\alpha,\alpha'}\int_{|\boldsymbol{q}|<k_D^\alpha} g^\alpha_{-\boldsymbol{q}} G_0(i\omega_m - i\omega_n, \boldsymbol{k}-\boldsymbol{q}) g^{\alpha'}_{\boldsymbol{q}} D_0^{\alpha\alpha'}(i\omega_n,\boldsymbol{q}). \tag{5.13}$$

The Matsubara Green's function for a Weyl fermion with an isotropic Weyl cone can be written as

$$G_0(i\omega_n,\boldsymbol{k}) = \frac{1}{2}\sum_{u=\pm}\frac{\sigma_0 + u\boldsymbol{\sigma}\cdot\hat{\boldsymbol{k}}}{i\omega_n+\mu-u\varepsilon_{\boldsymbol{k}}}. \tag{5.14}$$

Using this expression and the phonon propagator $D^0_{\alpha\alpha'}(i\omega_n,\boldsymbol{q})$ in Eq. (5.6), we rewrite the expression in Eq. (5.13) as

$$\Sigma(i\omega_m,\boldsymbol{k}) = \sum_{\alpha,a,b}\int_{|\boldsymbol{q}|<k_D^\alpha} g^\alpha_{-\boldsymbol{q}} b\Lambda_a(\boldsymbol{k}-\boldsymbol{q}) I^\alpha_{ab}(\boldsymbol{k},\boldsymbol{q},i\omega_m) g^\alpha_{\boldsymbol{q}}, \tag{5.15}$$

in terms of $\Lambda_\pm(\boldsymbol{k}) \equiv (\sigma^0 \pm \boldsymbol{\sigma}\cdot\hat{\boldsymbol{k}})/2$ and

$$\begin{aligned} I^\alpha_{ab}(\boldsymbol{k},\boldsymbol{q},i\omega_m) &\equiv -\frac{1}{\beta}\sum_{i\omega_n}\frac{1}{i\omega_m+\mu-i\omega_n-a\varepsilon_{\boldsymbol{k}-\boldsymbol{q}}}\cdot\frac{1}{i\omega_n - b\omega^\alpha_{\boldsymbol{q}}} \\ &= \frac{1}{2\pi i}\oint_C \mathrm{d}z \frac{N_\mathrm{B}(z)}{(i\omega_m+\mu-z-a\varepsilon_{\boldsymbol{k}-\boldsymbol{q}})(z-b\omega^\alpha_{\boldsymbol{q}})}, \end{aligned} \tag{5.16}$$

where we converted the Matsubara sum into a contour integral in the complex plane over the Bose distribution function $N_\mathrm{B}(z) \equiv (e^{\beta z}-1)^{-1}$. To make

the poles more explicit, we rewrite the integrand in Eq. (5.16) as

$$\frac{N_{\mathrm{B}}(z)}{(i\omega_m+\mu-z-a\varepsilon_{\boldsymbol{k}-\boldsymbol{q}})(z-b\omega^\alpha_{\boldsymbol{q}})} = \frac{N_{\mathrm{B}}(z)}{i\omega_m+\mu-(a\varepsilon_{\boldsymbol{k}-\boldsymbol{q}}+b\omega^\alpha_{\boldsymbol{q}})}\left(\frac{1}{z-b\omega^\alpha_{\boldsymbol{q}}}-\frac{1}{z-i\omega_m-\mu+a\varepsilon_{\boldsymbol{k}-\boldsymbol{q}}}\right).$$

The integrand in Eq. (5.16) thus has poles at $z_1 = b\omega^\alpha_{\boldsymbol{q}}$ and $z_2 = i\omega_m + \mu - a\varepsilon_{\boldsymbol{k}-\boldsymbol{q}}$. Performing the integral in Eq. (5.16) using the residue theorem, we find

$$I^\alpha_{ab}(\boldsymbol{k},\boldsymbol{q},i\omega_m) = \frac{N_{\mathrm{B}}(b\omega^\alpha_{\boldsymbol{q}}) - N_{\mathrm{B}}(i\omega_m+\mu-a\varepsilon_{\boldsymbol{k}-\boldsymbol{q}})}{i\omega_m+\mu-a\varepsilon_{\boldsymbol{k}-\boldsymbol{q}}-b\omega^\alpha_{\boldsymbol{q}}}. \tag{5.17}$$

As $i\omega_m$ is a fermionic Matsubara frequency, the second term can be simplified by noting that

$$N_{\mathrm{B}}(i\omega_m+\mu-a\varepsilon_{\boldsymbol{k}-\boldsymbol{q}}) = -N_{\mathrm{F}}(\mu-a\varepsilon_{\boldsymbol{k}-\boldsymbol{q}}), \tag{5.18}$$

where $N_{\mathrm{F}} \equiv (e^{\beta x}+1)^{-1}$ is the Fermi-Dirac distribution function. Furthermore, we have the identities

$$N_{\mathrm{B}}(-\omega^\alpha_{\boldsymbol{q}}) = -1 - N_{\mathrm{B}}(\omega^\alpha_{\boldsymbol{q}}), \tag{5.19a}$$
$$N_{\mathrm{F}}(\mu-\varepsilon_{\boldsymbol{k}}) = 1 - N_{\mathrm{F}}(\varepsilon_{\boldsymbol{k}}-\mu), \tag{5.19b}$$

such that the four terms defined by Eq. (5.17) read

$$I^\alpha_{++}(\boldsymbol{k},\boldsymbol{q},i\omega_m) = \frac{N_{\mathrm{B}}(\omega^\alpha_{\boldsymbol{q}}) - N_{\mathrm{F}}(\varepsilon_{\boldsymbol{k}-\boldsymbol{q}}-\mu)+1}{i\omega_m+\mu-\varepsilon_{\boldsymbol{k}-\boldsymbol{q}}-\omega^\alpha_{\boldsymbol{q}}}, \tag{5.20a}$$
$$I^\alpha_{+-}(\boldsymbol{k},\boldsymbol{q},i\omega_m) = \frac{N_{\mathrm{B}}(\omega^\alpha_{\boldsymbol{q}}) + N_{\mathrm{F}}(\varepsilon_{\boldsymbol{k}-\boldsymbol{q}}-\mu)}{i\omega_m+\mu-\varepsilon_{\boldsymbol{k}-\boldsymbol{q}}+\omega^\alpha_{\boldsymbol{q}}}, \tag{5.20b}$$
$$I^\alpha_{-+}(\boldsymbol{k},\boldsymbol{q},i\omega_m) = \frac{N_{\mathrm{B}}(\omega^\alpha_{\boldsymbol{q}}) + N_{\mathrm{F}}(\varepsilon_{\boldsymbol{k}-\boldsymbol{q}}+\mu)}{i\omega_m+\mu+\varepsilon_{\boldsymbol{k}-\boldsymbol{q}}-\omega^\alpha_{\boldsymbol{q}}}, \tag{5.20c}$$
$$I^\alpha_{--}(\boldsymbol{k},\boldsymbol{q},i\omega_m) = \frac{N_{\mathrm{B}}(\omega^\alpha_{\boldsymbol{q}}) - N_{\mathrm{F}}(\varepsilon_{\boldsymbol{k}-\boldsymbol{q}}+\mu)+1}{i\omega_m+\mu+\varepsilon_{\boldsymbol{k}-\boldsymbol{q}}+\omega^\alpha_{\boldsymbol{q}}}. \tag{5.20d}$$

We now proceed by going to the zero-temperature limit, $T = 0$, and we assume a positive chemical potential, $\mu > 0$. In this limit there are no

thermally activated phonons and fermions. Therefore $N_{\mathrm{B}}(\omega_{\boldsymbol{q}}^{\alpha}) = 0$ and $N_{\mathrm{F}}(\varepsilon_{\boldsymbol{k}-\boldsymbol{q}} + \mu) = 0$ such that $I_{-+}^{\alpha}(\boldsymbol{k}, \boldsymbol{q}, i\omega_m) = 0$. Performing the analytical continuation to real frequencies $i\omega_m \to \omega + i\eta$, with $\eta \to 0$, we obtain for the retarded self-energy

$$\Sigma(\omega, \boldsymbol{k}) = \sum_{\alpha} \int_{|\boldsymbol{q}|<k_D^{\alpha}} g_{-\boldsymbol{q}}^{\alpha} \Bigg[\frac{\Lambda_+(\boldsymbol{k}-\boldsymbol{q})\big[1-\vartheta(\mu-\varepsilon_{\boldsymbol{k}-\boldsymbol{q}})\big]}{\omega - \varepsilon_{\boldsymbol{k}-\boldsymbol{q}} - \omega_{\boldsymbol{q}}^{\alpha} + i\eta} + \frac{\Lambda_+(\boldsymbol{k}-\boldsymbol{q})\vartheta(\mu-\varepsilon_{\boldsymbol{k}-\boldsymbol{q}})}{\omega - \varepsilon_{\boldsymbol{k}-\boldsymbol{q}} + \omega_{\boldsymbol{q}}^{\alpha} + i\eta} + \frac{\Lambda_-(\boldsymbol{k}-\boldsymbol{q})}{\omega + \varepsilon_{\boldsymbol{k}-\boldsymbol{q}} + \omega_{\boldsymbol{q}}^{\alpha} + i\eta} \Bigg] g_{\boldsymbol{q}}^{\alpha}, \tag{5.21}$$

which is exactly Eq. (5.7). Note that we shifted $\omega + \mu \to \omega$ in Eq. (5.21), such that all frequencies are measured with respect to the chemical potential. The obtained expression for the self-energy contains four contributions: two proportional to $\vartheta(\mu - \varepsilon_{\boldsymbol{k}-\boldsymbol{q}})$ and two with just a 1 in the numerator. The former two are associated with the matter content and the latter two, being non-zero even at $\mu = 0$, are vacuum contributions.

5.A.2 Sum over polarizations

We now proceed by performing the sum over the polarizations by using the vertex from Eq. (5.5). For briefness we introduce $\hat{p}^l \equiv (k-q)^l/|\boldsymbol{k}-\boldsymbol{q}|$ and $\tilde{g}_1^2 \equiv v_F^2 g_1^2/4\rho$. For the longitudinal contribution to the self-energy we then find

$$\begin{aligned} & g_{-\boldsymbol{q}}^{L} \Lambda_{\pm}(\boldsymbol{k}-\boldsymbol{q}) g_{\boldsymbol{q}}^{L} \\ &\quad = \frac{\tilde{g}_1^2 \boldsymbol{q}^2}{4\omega_L(\boldsymbol{q})} b_a b_b \hat{e}_r^L \hat{e}_s^L \big(\hat{q}_i \delta_{ar} + \hat{q}_a \delta_{ir}\big)\big(\hat{q}_j \delta_{bs} + \hat{q}_b \delta_{js}\big) \sigma^i \big(\sigma^0 \pm \sigma^l \hat{p}_l\big) \sigma^j \\ &\quad = \frac{\tilde{g}_1^2 (\boldsymbol{b}\cdot\boldsymbol{q})^2}{\omega_L(\boldsymbol{q})} \left[\sigma^0 \pm \frac{\big[2\boldsymbol{k}\cdot\boldsymbol{q} - \boldsymbol{q}^2\big](\boldsymbol{q}\cdot\boldsymbol{\sigma})}{|\boldsymbol{k}-\boldsymbol{q}|\boldsymbol{q}^2} \mp \frac{(\boldsymbol{k}\cdot\boldsymbol{\sigma})}{|\boldsymbol{k}-\boldsymbol{q}|} \right], \end{aligned} \tag{5.22}$$

where we used $\hat{e}_i^L = \hat{q}_i$ and the identity $\sigma^i \sigma^j = \delta^{ij} + i\varepsilon^{ijk}\sigma_k$ several times. The first term in the expression above is proportional to σ^0 and leads to $\Sigma_0^L(\omega, \boldsymbol{k})$, whereas the other terms yield $\Sigma_{1,i}^L(\omega, \boldsymbol{k})\sigma^i$. Doing the same for

the sum over the transverse modes, we find

$$\begin{aligned}
&\sum_{\alpha=T_1,T_2} g^{\alpha}_{-\boldsymbol{q}}\Lambda_{\pm}(\boldsymbol{k}-\boldsymbol{q})g^{\alpha}_{\boldsymbol{q}} \\
&\quad= \frac{\tilde{g}_1^2|\boldsymbol{q}|^2}{4\omega_T(\boldsymbol{q})} b_a b_b(\delta_{rs}-\hat{q}_r\hat{q}_s)\big(\hat{q}_i\delta_{ar}+\hat{q}_a\delta_{ir}\big)\big(\hat{q}_j\delta_{bs}+\hat{q}_b\delta_{js}\big)\sigma^i\big(\sigma^0\pm\sigma^l\hat{p}_l\big)\sigma^j \\
&\quad= \frac{\tilde{g}_1^2}{4\omega_T(\boldsymbol{q})}\big[\boldsymbol{b}^2\boldsymbol{q}^2+(\boldsymbol{b}\cdot\boldsymbol{q})^2\big]\sigma^0 \pm \frac{\tilde{g}_1^2}{4\omega_T(\boldsymbol{q})|\boldsymbol{k}-\boldsymbol{q}|}\big[(\boldsymbol{b}\cdot\boldsymbol{q})^2-\boldsymbol{b}^2\boldsymbol{q}^2\big](\boldsymbol{k}\cdot\boldsymbol{\sigma}) \\
&\qquad\pm \frac{\tilde{g}_1^2}{4\omega_T(\boldsymbol{q})|\boldsymbol{k}-\boldsymbol{q}|}\Big\{2\big[\boldsymbol{b}^2-4(\boldsymbol{b}\cdot\hat{\boldsymbol{q}})^2\big](\boldsymbol{k}\cdot\boldsymbol{q})+2(\boldsymbol{b}\cdot\boldsymbol{q})(\boldsymbol{b}\cdot\boldsymbol{k}) \\
&\qquad+5(\boldsymbol{b}\cdot\boldsymbol{q})^2-\boldsymbol{b}^2\boldsymbol{q}^2\Big\}(\boldsymbol{q}\cdot\boldsymbol{\sigma}) \pm \frac{\tilde{g}_1^2(\boldsymbol{b}\cdot\boldsymbol{q})\big[\boldsymbol{k}\cdot\boldsymbol{q}-\boldsymbol{q}^2\big]}{2\omega_T(\boldsymbol{q})|\boldsymbol{k}-\boldsymbol{q}|}(\boldsymbol{b}\cdot\boldsymbol{\sigma}).
\end{aligned} \tag{5.23}$$

5.A.3 Tensorial decomposition

We now proceed with the computation of the self-energy that has been made dimensionless by scaling all parameters on $|\boldsymbol{b}|$, as discussed in Section 5.3. Additionally, we take for simplicity $\varepsilon_L = \varepsilon_T \equiv \varepsilon$ and $k_D^L = k_D^T \equiv k_D$ in the following. Using Eq. (5.22) and Eq. (5.21), we find for the longitudinal contributions to the dimensionless self-energy

$$\Sigma_0^L(\omega,\boldsymbol{k}) = \hat{b}^i\hat{b}^j\int_{k_D>|\boldsymbol{q}|}\frac{q^iq^j}{|\boldsymbol{q}|}H_+(\omega,\boldsymbol{k}-\boldsymbol{q},\boldsymbol{q}), \tag{5.24a}$$

$$\begin{aligned}
\Sigma_{1,i}^L(\omega,\boldsymbol{k})\sigma^i = \hat{b}^i\hat{b}^j\sigma^l\int_{k_D>|\boldsymbol{q}|}\frac{\hat{q}^i\hat{q}^j\hat{q}^l}{|\boldsymbol{k}-\boldsymbol{q}|}\big(2\boldsymbol{k}\cdot\boldsymbol{q}-|\boldsymbol{q}|^2\big)H_-(\omega,\boldsymbol{k}-\boldsymbol{q},\boldsymbol{q}) \\
-(\boldsymbol{\sigma}\cdot\boldsymbol{k})\hat{b}^i\hat{b}^j\int_{k_D>|\boldsymbol{q}|}\frac{q^iq^j}{|\boldsymbol{q}||\boldsymbol{k}-\boldsymbol{q}|}H_-(\omega,\boldsymbol{k}-\boldsymbol{q},\boldsymbol{q}),
\end{aligned} \tag{5.24b}$$

where we used $H_\pm(\boldsymbol{x},\boldsymbol{y})$, defined in Eq. (5.11). Note that $\Sigma_0(\omega,\boldsymbol{k})$ depends on $H_+(\omega,\boldsymbol{x},\boldsymbol{y})$, whereas $\Sigma_{1,i}(\omega,\boldsymbol{k})\sigma^i$ depends on $H_-(\omega,\boldsymbol{x},\boldsymbol{y})$. This is ultimately due to the fact that the last term in Eq. (5.21) is proportional to $\Lambda_-(\boldsymbol{k}-\boldsymbol{q})$, whereas the other terms are proportional $\Lambda_+(\boldsymbol{k}-\boldsymbol{q})$.

In order to simplify the expression Eq. (5.24a), we note that the integrand is symmetric in $i \leftrightarrow j$ and must therefore be a linear combination of δ^{ij} and $\hat{k}^i\hat{k}^j$. Making the ansatz $I^{ij}(k) = \alpha(k)\delta^{ij} + \beta(k)\hat{k}^i\hat{k}^j$ for the tensor resulting from the integral, one finds $\alpha(k) = \big(\delta_{ij}-\hat{k}_i\hat{k}_j\big)I^{ij}(k)/2$ and $\beta(k) =$

$\big(3\hat{k}_i\hat{k}_j - \delta_{ij}\big)I^{ij}(k)/2$. After shifting the integration variable $\boldsymbol{q} \to \boldsymbol{q} + \boldsymbol{k}$, we find

$$\Sigma_0^L(\omega, \boldsymbol{k}) = \frac{1}{2}\int_{k_D>|\boldsymbol{k}+\boldsymbol{q}|} \Big\{ \boldsymbol{q}^2 - (\hat{\boldsymbol{k}}\cdot\boldsymbol{q})^2 + (\hat{\boldsymbol{b}}\cdot\hat{\boldsymbol{k}})^2\big[3(\hat{\boldsymbol{k}}\cdot\boldsymbol{q})^2 + 2\boldsymbol{k}^2 - \boldsymbol{q}^2 + 4\boldsymbol{k}\cdot\boldsymbol{q}\big]\Big\}\frac{H_+(\omega, \boldsymbol{q}, \boldsymbol{k}+\boldsymbol{q})}{|\boldsymbol{k}+\boldsymbol{q}|}. \tag{5.25}$$

Only the terms on the second line depend on the angle between $\boldsymbol{b}$ and $\boldsymbol{k}$. In the special cases $\boldsymbol{b} \perp \boldsymbol{k}$ and $\boldsymbol{b} \parallel \boldsymbol{k}$, we denote the self-energy as $\Sigma_0^{L,\perp}(\omega, \boldsymbol{k})$ and $\Sigma_0^{L,\perp}(\omega, \boldsymbol{k})$ and find

$$\Sigma_0^{L,\perp}(\omega, \boldsymbol{k}) = \frac{1}{2}\int_{k_D>|\boldsymbol{k}+\boldsymbol{q}|} \big[\boldsymbol{q}^2 - (\hat{\boldsymbol{k}}\cdot\boldsymbol{q})^2\big]\frac{H_+(\omega, \boldsymbol{q}, \boldsymbol{k}+\boldsymbol{q})}{|\boldsymbol{k}+\boldsymbol{q}|}, \tag{5.26a}$$

$$\Sigma_0^{L,\parallel}(\omega, \boldsymbol{k}) = \int_{k_D>|\boldsymbol{k}+\boldsymbol{q}|} \big[\boldsymbol{k}^2 + (\hat{\boldsymbol{k}}\cdot\boldsymbol{q})^2 + 2(\boldsymbol{k}\cdot\boldsymbol{q})\big]\frac{H_+(\omega, \boldsymbol{q}, \boldsymbol{k}+\boldsymbol{q})}{|\boldsymbol{k}+\boldsymbol{q}|}. \tag{5.26b}$$

We follow a similar strategy for Eq. (5.24b). The integrand on the second line is of the same form as the integrand of Eq. (5.24a) and can thus be computed in the same way. For the integrand on the first line we note that it is symmetric in $i \leftrightarrow j \leftrightarrow l$. We can thus decompose the result of the integral as $I^{ijl}(k) = \alpha(k)\big(\delta^{ij}\hat{k}^l + \delta^{il}\hat{k}^j + \delta^{jl}\hat{k}^i\big) + \beta(k)\hat{k}^i\hat{k}^j\hat{k}^l$. The coefficients $\alpha(k)$ and $\beta(k)$ follow by contracting $I^{ijl}(k)$ with $\delta^{ij}\hat{k}^l$ and $\hat{k}^i\hat{k}^j\hat{k}^l$. They read $\alpha(k) = \big(\delta_{ij}\hat{k}_l - \hat{k}_i\hat{k}_j\hat{k}_l\big)I^{ijl}(k)/2$ and $\beta(k) = \big(5\hat{k}_i\hat{k}_j\hat{k}_l - 3\delta_{ij}\hat{k}_l\big)I^{ijl}(k)/2$. Combining all contributions we write $\Sigma_{1,i}^{L,\perp}(\omega, \boldsymbol{k})\sigma^i = \Sigma_1^{L,\perp}(\omega, \boldsymbol{k})(\hat{\boldsymbol{k}}\cdot\boldsymbol{\sigma})$ when $\boldsymbol{b} \perp \boldsymbol{k}$ and find

$$\Sigma_1^{L,\perp}(\omega, \boldsymbol{k}) = \frac{1}{2}\int_{k_D>|\boldsymbol{k}+\boldsymbol{q}|} \Big[\big(\boldsymbol{q}^2 + \boldsymbol{k}^2\big)(\hat{\boldsymbol{k}}\cdot\hat{\boldsymbol{q}})^3 + 2|\boldsymbol{k}||\boldsymbol{q}|(\hat{\boldsymbol{k}}\cdot\hat{\boldsymbol{q}})^2 - \big(\boldsymbol{q}^2 + \boldsymbol{k}^2\big)(\hat{\boldsymbol{k}}\cdot\hat{\boldsymbol{q}}) - 2|\boldsymbol{k}||\boldsymbol{q}|\Big]\frac{\boldsymbol{q}^2 H_-(\omega, \boldsymbol{q}, \boldsymbol{k}+\boldsymbol{q})}{|\boldsymbol{k}+\boldsymbol{q}|^3}, \tag{5.27}$$

In the case that $\boldsymbol{b} \parallel \boldsymbol{k}$, we write $\Sigma^{L,\parallel}_{1,i}(\omega,\boldsymbol{k})\sigma^i = \Sigma^{L,\parallel}_1(\omega,\boldsymbol{k})(\hat{\boldsymbol{k}}\cdot\boldsymbol{\sigma})$, with

$$\Sigma^{L,\parallel}_1(\omega,\boldsymbol{k}) = -\int_{k_D>|\boldsymbol{k}+\boldsymbol{q}|}\Big[\boldsymbol{q}^2(\boldsymbol{q}^2+\boldsymbol{k}^2)(\hat{\boldsymbol{k}}\cdot\hat{\boldsymbol{q}})^3 + 2|\boldsymbol{k}||\boldsymbol{q}|(2\boldsymbol{q}^2+\boldsymbol{k}^2)(\hat{\boldsymbol{k}}\cdot\hat{\boldsymbol{q}})^2 + \boldsymbol{k}^2(\boldsymbol{k}^2+5\boldsymbol{q}^2)(\hat{\boldsymbol{k}}\cdot\hat{\boldsymbol{q}}) + 2\boldsymbol{k}^3|\boldsymbol{q}|\Big]\frac{H_-(\omega,\boldsymbol{q},\boldsymbol{k}+\boldsymbol{q})}{|\boldsymbol{k}+\boldsymbol{q}|^3}. \tag{5.28}$$

Following the same procedure as for the longitudinal part, but starting from Eq.(5.23) instead of Eq.(5.22), we find the transverse contributions.

$$\Sigma^{T,\perp}_0(\omega,\boldsymbol{k}) = \int_{k_D>|\boldsymbol{k}+\boldsymbol{q}|}\Big[3\boldsymbol{q}^2+4\boldsymbol{k}\cdot\boldsymbol{q}+2\boldsymbol{k}^2-(\hat{\boldsymbol{k}}\cdot\boldsymbol{q})^2\Big]\frac{H_+(\omega,\boldsymbol{q},\boldsymbol{k}+\boldsymbol{q})}{8|\boldsymbol{k}+\boldsymbol{q}|}, \tag{5.29a}$$

$$\Sigma^{T,\parallel}_0(\omega,\boldsymbol{k}) = \int_{k_D>|\boldsymbol{k}+\boldsymbol{q}|}\Big[\boldsymbol{q}^2+4\boldsymbol{k}\cdot\boldsymbol{q}+2\boldsymbol{k}^2+(\hat{\boldsymbol{k}}\cdot\boldsymbol{q})^2\Big]\frac{H_+(\omega,\boldsymbol{q},\boldsymbol{k}+\boldsymbol{q})}{4|\boldsymbol{k}+\boldsymbol{q}|}. \tag{5.29b}$$

Additionally, in the perpendicular case $\boldsymbol{b} \perp \boldsymbol{k}$ we write similarly to the longitudinal case $\Sigma^{T,\perp}_{1,i}(\omega,\boldsymbol{k})\sigma^i = \Sigma^{T,\perp}_1(\omega,\boldsymbol{k})(\hat{\boldsymbol{k}}\cdot\boldsymbol{\sigma})$. Following the same steps that led to Eq. (5.27), we obtain

$$\Sigma^{T,\perp}_1(\omega,\boldsymbol{k}) = \int_{k_D>|\boldsymbol{k}+\boldsymbol{q}|}\Big[2|\boldsymbol{k}|\boldsymbol{q}^3 - 2|\boldsymbol{k}|\boldsymbol{q}^3(\hat{\boldsymbol{k}}\cdot\hat{\boldsymbol{q}})^4 - \boldsymbol{q}^2(5\boldsymbol{q}^2+\boldsymbol{k}^2)(\hat{\boldsymbol{k}}\cdot\hat{\boldsymbol{q}})^3 - 2|\boldsymbol{k}||\boldsymbol{q}|(\boldsymbol{k}^2+4\boldsymbol{q}^2)(\hat{\boldsymbol{k}}\cdot\hat{\boldsymbol{q}})^2 - 2\boldsymbol{k}^4(\hat{\boldsymbol{k}}\cdot\hat{\boldsymbol{q}}) - \boldsymbol{q}^2(11\boldsymbol{k}^2-3\boldsymbol{q}^2)(\hat{\boldsymbol{k}}\cdot\hat{\boldsymbol{q}})\Big]\frac{H_-(\omega,\boldsymbol{q},\boldsymbol{k}+\boldsymbol{q})}{8|\boldsymbol{k}+\boldsymbol{q}|^3}, \tag{5.30}$$

Finally, when $\boldsymbol{b} \parallel \boldsymbol{k}$ we denote $\Sigma^{T,\parallel}_{1,i}(\omega,\boldsymbol{k})\sigma^i = \Sigma^{T,\parallel}_1(\omega,\boldsymbol{k})(\hat{\boldsymbol{k}}\cdot\boldsymbol{\sigma})$ and find

$$\Sigma^{T,\parallel}_1(\omega,\boldsymbol{k}) = \int_{k_D>|\boldsymbol{k}+\boldsymbol{q}|}\Big[2|\boldsymbol{k}|\boldsymbol{q}^3(\hat{\boldsymbol{k}}\cdot\hat{\boldsymbol{q}})^4 + 5\boldsymbol{q}^2(\boldsymbol{k}^2+\boldsymbol{q}^2)(\hat{\boldsymbol{k}}\cdot\hat{\boldsymbol{q}})^3 + 2|\boldsymbol{k}||\boldsymbol{q}|(5\boldsymbol{q}^2+2\boldsymbol{k}^2)(\hat{\boldsymbol{k}}\cdot\hat{\boldsymbol{q}})^2 + (7\boldsymbol{k}^2\boldsymbol{q}^2+2\boldsymbol{k}^4-3\boldsymbol{q}^4)(\hat{\boldsymbol{k}}\cdot\hat{\boldsymbol{q}}) + 4|\boldsymbol{k}||\boldsymbol{q}|(\boldsymbol{k}^2-\boldsymbol{q}^2)\Big]\frac{H_-(\omega,\boldsymbol{q},\boldsymbol{k}+\boldsymbol{q})}{4|\boldsymbol{k}+\boldsymbol{q}|^3}. \tag{5.31}$$

We have now obtained all longitudinal and transverse contributions to the

self-energy in the distinct cases $\boldsymbol{b} \perp \boldsymbol{k}$ and $\boldsymbol{b} \parallel \boldsymbol{k}$. Because we took $\varepsilon_L = \varepsilon_T \equiv \varepsilon$ we can simplify the full expression for the self-energy by adding the longitudinal and transverse contributions and arrive at Eq. (5.9). Using Eqs. (5.26a), (5.26b), (5.29a) and (5.29b) we obtain the functions $f_0^{\perp,\parallel}(\boldsymbol{k},\boldsymbol{q})$. They are given by

$$f_0^{\perp}(\boldsymbol{k},\boldsymbol{q}) = 7\boldsymbol{q}^2 - 5(\hat{\boldsymbol{k}}\cdot\boldsymbol{q})^2 + 4(\boldsymbol{k}\cdot\boldsymbol{q}) + 2\boldsymbol{k}^2, \tag{5.32a}$$

$$f_0^{\parallel}(\boldsymbol{k},\boldsymbol{q}) = 2\boldsymbol{q}^2 + 10(\hat{\boldsymbol{k}}\cdot\boldsymbol{q})^2 + 24(\boldsymbol{k}\cdot\boldsymbol{q}) + 12\boldsymbol{k}^2. \tag{5.32b}$$

Similarly, we obtain from Eqs. (5.27), (5.28), (5.30) and (5.31) the functions $f_1^{\perp,\parallel}(\boldsymbol{k},\boldsymbol{q})$. They are given by

$$\begin{aligned} f_1^{\perp}(\boldsymbol{k},\boldsymbol{q}) = {} & 3k^2q^2x(x^2-5) - 2k^4x - 2k^3q(x^2+3) \\ & - 2kq^3(x^4+3) - q^4x(x^2+1), \end{aligned} \tag{5.33a}$$

$$\begin{aligned} f_1^{\parallel}(\boldsymbol{k},\boldsymbol{q}) = {} & 2k^2q^2x(x^2-13) - 4k^4x - 8k^3q(x^2+1) \\ & + 4kq^3(x^4-3x^2-2) + 2q^4x(x^2-3), \end{aligned} \tag{5.33b}$$

where we abbreviated $x \equiv \hat{\boldsymbol{k}}\cdot\hat{\boldsymbol{q}}$, $k \equiv |\boldsymbol{k}|$ and $q \equiv |\boldsymbol{q}|$. Next, we calculate the self-energy in the simplest case: when $\boldsymbol{k} = \boldsymbol{0}$.

5.A.4 Self-energy at $k = 0$

When $\boldsymbol{k} = \boldsymbol{0}$ both $\Sigma_1^L(\omega,\boldsymbol{0})$ and $\Sigma_1^T(\omega,\boldsymbol{0})$ yield zero because they reduce to an odd integral over $\boldsymbol{q}$, as can be seen explicitly in Eqs. (5.24b) and (5.23) for the latter. Furthermore, the longitudinal and transverse contribution to $\Sigma_0(\omega,\boldsymbol{0})$ are given by the same integral. We find from Eq. (5.24a)

$$\Sigma_0(\omega) \equiv \Sigma_0^L(\omega,\boldsymbol{0}) + \Sigma_0^T(\omega,\boldsymbol{0}) = 2\hat{b}^i\hat{b}^j \int_{k_D>|\boldsymbol{q}|} \hat{q}^i\hat{q}^j|\boldsymbol{q}|H_+(\omega,\boldsymbol{q},\boldsymbol{q}). \tag{5.34}$$

The integrand in Eq. (5.34) has to be proportional to δ^{ij}, leading to

$$\begin{aligned} \Sigma_0(\omega) = \frac{1}{3\pi^2}\int_0^{k_D} \mathrm{d}q\, q^3 \Bigg[& \frac{\vartheta(\mu-q)}{\omega^+ - (1-\varepsilon)q} - \frac{\vartheta(\mu-q)}{\omega^+ - (1+\varepsilon)q} \\ & + \frac{1}{\omega^+ - (1+\varepsilon)q} + \frac{1}{\omega^+ + (1+\varepsilon)q}\Bigg], \end{aligned} \tag{5.35}$$

where we went to spherical coordinates with $q \equiv |\boldsymbol{q}|$ and the trivial angular integral yielded 4π. By using the identity

$$\lim_{\eta\to 0} \frac{1}{x+i\eta} = \mathcal{P}\left(\frac{1}{x}\right) - i\pi\delta(x), \tag{5.36}$$

where $\mathcal{P}$ indicates the principal value, we can write separate expressions for the real and imaginary part of the self-energy. For the imaginary part we find[c]

$$\begin{aligned}
\mathrm{Im}\big[\Sigma_0(\omega)\big] &= -\frac{1}{3\pi}\int_0^{k_D} \mathrm{d}q\, q^3 \Big[\vartheta(\mu-q)\delta(\omega-(1-\varepsilon)q) \\
&\quad - \vartheta(\mu-q)\delta(\omega-(1+\varepsilon)q) + \delta(|\omega|-(1+\varepsilon)q)\Big] \\
&= -\frac{\omega^3}{3\pi}\Bigg\{\vartheta(k_D-\mu)\vartheta(\omega)\left[\frac{\vartheta\big(\mu-\omega_{\max}\big)}{(1-\varepsilon)^4} - \frac{\vartheta\big(\mu-\omega_{\min}\big)}{(1+\varepsilon)^4}\right] \\
&\quad + \vartheta(\mu-k_D)\vartheta(\omega)\left[\frac{\vartheta\big(k_D-\omega_{\max}\big)}{(1-\varepsilon)^4} - \frac{\vartheta\big(k_D-\omega_{\min}\big)}{(1+\varepsilon)^4}\right] \\
&\quad + \frac{\mathrm{sign}(\omega)}{(1+\varepsilon)^4}\vartheta(k_D-|\omega_{\min}|)\Bigg\},
\end{aligned} \tag{5.37}$$

in terms of the frequencies

$$\omega_{\min/\max} \equiv \frac{\omega}{1\pm\varepsilon}, \tag{5.38}$$

which obey $\omega_{\max} \geq \omega_{\min}$ because $0 \leq \varepsilon < 1$. The real part of the self-energy now follows from the imaginary part by using the Kramers-Kronig relation

$$\mathrm{Re}\big[\Sigma_0(\omega)\big] = \frac{1}{\pi}\mathcal{P}\int_{-\infty}^{\infty} \mathrm{d}\omega'\, \frac{\mathrm{Im}\big[\Sigma_0(\omega')\big]}{\omega'-\omega}. \tag{5.39}$$

[c] Note that for the imaginary part of the third and fourth term in Eq.(5.35) we can use that for any function $f(q)$

$$\int_0^{\infty} \mathrm{d}q\, f(q)\big[\delta(\omega-(1+\varepsilon)q) + \delta(\omega+(1+\varepsilon)q)\big] = \int_0^{\infty} \mathrm{d}q\, f(q)\delta(|\omega|-(1+\varepsilon)q).$$

Using this relation, we find

$$\begin{aligned}\mathrm{Re}\big[\Sigma_0(\omega)\big] = -\frac{1}{3\pi^2}\Bigg\{ &\vartheta(k_D-\mu)\left[\frac{\omega_{\max}^3 f(\mu/\omega_{\max})}{1-\varepsilon} - \frac{\omega_{\min}^3 f(\mu/\omega_{\min})}{1+\varepsilon}\right] \\ &+ \vartheta(\mu-k_D)\left[\frac{\omega_{\max}^3 f(k_D/\omega_{\max})}{1-\varepsilon} - \frac{\omega_{\min}^3 f(k_D/\omega_{\min})}{1+\varepsilon}\right] \\ &+ \frac{\omega_{\min}^3}{1+\varepsilon}\left[\frac{k_D^2}{\omega_{\min}^2} + \log\left|1-\frac{k_D^2}{\omega_{\min}^2}\right|\right]\Bigg\}, \end{aligned} \tag{5.40}$$

in terms of the function

$$f(x) \equiv x + \frac{x^2}{2} + \frac{x^3}{3} + \log|1-x|. \tag{5.41}$$

From the expressions Eqs. (5.37) and (5.40) for the imaginary and real part of the self-energy, it becomes clear that there are two distinct regimes: $\mu/k_D > 1$ and $\mu/k_D < 1$, as we discussed in Section 5.3.

The expression in Eq. (5.40) has singularities at $\omega_{\min/\max} = k_D$ because we implemented a hard cut-off at the Debye frequency. This is important for the numerics that led to Fig. 5.1, because the hard cut-off turns out to be a problem when verifying the sum-rule, especially when doing the same calculation at $|\boldsymbol{k}| \neq 0$. We therefore implement the Debye frequency with a smooth mollifier. For this mollifier, we choose the Fermi-Dirac distribution and make the replacement $\vartheta(k_D - |\boldsymbol{q}|) \to \left(e^{\hbar v_F(|\boldsymbol{q}|-k_D)/k_B T_{\text{fict.}}} + 1\right)^{-1}$ in Eq. (5.34). We stress that T_{fict} is a fictitious temperature which only serves to smoothen out the hard cut-off set by the Debye frequency. In Fig. 5.1 we used $k_B T_{\text{fict}}/\hbar v_F k_D = 10^{-2}$.

Bibliography

[1] E. C. I. van der Wurff and H. T. C. Stoof, Phys. Rev. B **94**, 155118 (2016).

[2] E. C. I. van der Wurff and H. T. C. Stoof, Phys. Rev. B **96**, 121116 (2017).

[3] E. C. I. van der Wurff and H. T. C. Stoof, arXiv preprint 1903.10985 (2019).

[4] E. C. I. van der Wurff and A. Cortijo, arXiv preprint 1905.00908 (2019).

[5] E. C. I. van der Wurff, A.-W. de Leeuw, R. A. Duine, and H. T. C. Stoof, Phys. Rev. Lett. **113**, 135301 (2014).

[6] A.-W. de Leeuw, E. C. I. van der Wurff, R. A. Duine, and H. T. C. Stoof, Phys. Rev. A **90**, 043627 (2014).

[7] A.-W. de Leeuw, E. C. I. van der Wurff, R. A. Duine, D. van Oosten, and H. T. C. Stoof, Phys. Rev. A **94**, 013615 (2016).

[8] L. Liao, E. C. I. van der Wurff, D. van Oosten, and H. T. C. Stoof, Phys. Rev. A **99**, 023850 (2019).

[9] R. P. Feynman, R. B. Leighton, and M. Sands, Am. J. Phys. **33**, 750 (1965).

[10] F. Wilczek, Physics Today **51**, 11 (1998).

[11] N. Ashcroft and N. Mermin, *Solid State Physics* (Saunders College, Philadelphia, 1976).

[12] Y. Yao, L. Kleinman, A. H. MacDonald, J. Sinova, T. Jungwirth, D.-S. Wang, E. Wang, and Q. Niu, Phys. Rev. Lett. **92**, 037204 (2004).

[13] Q. Si and F. Steglich, Science **329**, 1161 (2010).

[14] L. Landau, J. Exptl. Theoret. Phys. **8**, 1058 (1956).

[15] A. Abrikosov and I. Khalatnikov, Rep. Progr. Phys. **22**, 329 (1959).

[16] P. A. M. Dirac, Proc. Royal Soc. A **117**, 610 (1928).

[17] H. Weyl, Z. Phys. **56**, 330 (1929).

[18] J. von Neumann and E. Wigner, Physik. Z. **30**, 467470 (1929).

[19] C. Herring, Phys. Rev. **52**, 365 (1937).

[20] K. Asano and C. Hotta, Phys. Rev. B **83**, 245125 (2011).

[21] G. van Miert and C. M. Smith, Phys. Rev. B **93**, 035401 (2016).

[22] P. R. Wallace, Phys. Rev. **71**, 622 (1947).

[23] K. S. Novoselov, A. K. Geim, S. V. Morozov, D. Jiang, Y. Zhang, S. V. Dubonos, I. V. Grigorieva, and A. A. Firsov, Science **306**, 666 (2004).

[24] J. Zak, Phys. Rev. Lett. **62**, 2747 (1989).

[25] G. Volovik, *The Universe in a Helium Droplet*, International Series of Monographs on Physics (OUP Oxford, 2009).

[26] H. Nielsen and M. Ninomiya, Phys. Lett. B **105**, 219 (1981).

[27] D. Xiao, M.-C. Chang, and Q. Niu, Rev. Mod. Phys. **82**, 1959 (2010).

[28] M. Prez-Victoria, Phys. Rev. Lett. **83**, 2518 (1999).

[29] R. Jackiw and V. A. Kosteleck, Phys. Rev. Lett. **82**, 3572 (1999).

[30] A. G. Grushin, Phys. Rev. D **86**, 045001 (2012).

[31] B. Yan and C. Felser, Annu. Rev. Condens. Matter Phys. **8**, 337 (2017).

[32] M. Z. Hasan and C. L. Kane, Rev. Mod. Phys. **82**, 3045 (2010).

[33] Y. Sun, S.-C. Wu, and B. Yan, Phys. Rev. B **92**, 115428 (2015).

[34] N. P. Armitage, E. J. Mele, and A. Vishwanath, Rev. Mod. Phys. **90**, 015001 (2018).

[35] A. A. Burkov and L. Balents, Phys. Rev. Lett. **107**, 127205 (2011).

[36] X. Wan, A. M. Turner, A. Vishwanath, and S. Y. Savrasov, Phys. Rev. B **83**, 205101 (2011).

[37] H. Weng, C. Fang, Z. Fang, B. A. Bernevig, and X. Dai, Phys. Rev. X **5**, 011029 (2015).

[38] S.-M. Huang, S.-Y. Xu, I. Belopolski, C.-C. Lee, G. Chang, B. Wang, N. Alidoust, G. Bian, M. Neupane, C. Zhang, *et al.*, Nat. Comm. **6**, 7373 (2015).

[39] S.-Y. Xu, I. Belopolski, N. Alidoust, M. Neupane, G. Bian, C. Zhang, R. Sankar, G. Chang, Z. Yuan, C.-C. Lee, S.-M. Huang, H. Zheng, J. Ma, D. S. Sanchez, B. Wang, A. Bansil, F. Chou, P. P. Shibayev, H. Lin, S. Jia, and M. Z. Hasan, Science **349**, 613 (2015).

[40] B. Lv, H. Weng, B. Fu, X. Wang, H. Miao, J. Ma, P. Richard, X. Huang, L. Zhao, G. Chen, Z. Fang, X. Dai, T. Qian, and H. Ding, Phys. Rev. X **5**, 031013 (2015).

[41] L. Yang, Z. Liu, Y. Sun, H. Peng, H. Yang, T. Zhang, B. Zhou, Y. Zhang, Y. Guo, M. Rahn, *et al.*, Nat. Phys. **11**, 728 (2015).

[42] B. Q. Lv, N. Xu, H. M. Weng, J. Z. Ma, P. Richard, X. C. Huang, L. X. Zhao, G. F. Chen, C. E. Matt, F. Bisti, V. N. Strocov, J. Mesot, Z. Fang, X. Dai, T. Qian, M. Shi, and H. Ding, Nat. Phys. **11**, 724 (2015).

[43] S.-Y. Xu, N. Alidoust, I. Belopolski, Z. Yuan, G. Bian, T.-R. Chang, H. Zheng, V. N. Strocov, D. S. Sanchez, G. Chang, C. Zhang, D. Mou, Y. Wu, L. Huang, C.-C. Lee, S.-M. Huang, B. Wang, A. Bansil, H.-T. Jeng, T. Neupert, A. Kaminski, H. Lin, S. Jia, and M. Zahid Hasan, Nat. Phys. **11**, 748 (2015).

[44] N. Xu, H. Weng, B. Lv, C. Matt, J. Park, F. Bisti, V. Strocov, D. Gawryluk, E. Pomjakushina, K. Conder, *et al.*, Nat. Comm. **7**, 11006 (2016).

[45] E. Liu, Y. Sun, N. Kumar, L. Muechler, A. Sun, L. Jiao, S.-Y. Yang, D. Liu, A. Liang, Q. Xu, *et al.*, Nat. Phys. **14**, 1125 (2018).

[46] J.-R. Soh, F. de Juan, M. Vergniory, N. Schröter, M. Rahn, D. Yan, M. Bristow, P. Reiss, J. Blandy, Y. Guo, *et al.*, arXiv preprint 1901.10022 (2019).

[47] L.-L. Wang, N. H. Jo, B. Kuthanazhi, Y. Wu, R. J. McQueeney, A. Kaminski, and P. C. Canfield, arXiv preprint 1901.08234 (2019).

[48] C. Beenakker, Science **353**, 539 (2016).

[49] Z. Wang, A. Alexandradinata, R. J. Cava, and B. A. Bernevig, Nature **532**, 189 (2016).

[50] I. Lifshitz *et al.*, Sov. Phys. JETP **11**, 1130 (1960).

[51] T. Qin, Q. Niu, and J. Shi, Phys. Rev. Lett. **107**, 236601 (2011).

[52] R. Karplus and J. M. Luttinger, Phys. Rev. **95**, 1154 (1954).

[53] Y. D. Chong, Phys. Rev. B **81**, 052303 (2010).

[54] A. A. Zyuzin and A. A. Burkov, Phys. Rev. B **86**, 115133 (2012).

[55] A. A. Burkov, Phys. Rev. Lett. **113**, 187202 (2014).

[56] V. Jacobs, *Dirac and Weyl semimetals with holographic interactions*, Ph.D. thesis, Utrecht University, the Netherlands (2015).

[57] M. A. Stephanov and Y. Yin, Phys. Rev. Lett. **109**, 162001 (2012).

[58] D. T. Son and N. Yamamoto, Phys. Rev. D **87**, 085016 (2013).

[59] M. E. Peskin and D. V. Schroeder, *An Introduction to quantum field theory* (Addison-Wesley, Reading, USA, 1995).

[60] D. E. Kharzeev and H.-U. Yee, Phys. Rev. D **84**, 045025 (2011).

[61] D. T. Son and B. Z. Spivak, Phys. Rev. B **88**, 104412 (2013).

[62] F. Arnold, C. Shekhar, S.-C. Wu, Y. Sun, R. D. Dos Reis, N. Kumar, M. Naumann, M. O. Ajeesh, M. Schmidt, A. G. Grushin, *et al.*, Nat. Commun. **7**, 11615 (2016).

[63] Y. Wang, E. Liu, H. Liu, Y. Pan, L. Zhang, J. Zeng, Y. Fu, M. Wang, K. Xu, Z. Huang, *et al.*, Nat. Comm. **7**, 13142 (2016).

[64] X. Huang, L. Zhao, Y. Long, P. Wang, D. Chen, Z. Yang, H. Liang, M. Xue, H. Weng, Z. Fang, X. Dai, and G. Chen, Phys. Rev. X **5**, 031023 (2015).

[65] J. Behrends and J. H. Bardarson, Phys. Rev. B **96**, 060201 (2017).

[66] S. V. Syzranov, Y. I. Rodionov, and B. Skinner, Phys. Rev. B **98**, 081114 (2018).

[67] Y. Li, Z. Wang, P. Li, X. Yang, Z. Shen, F. Sheng, X. Li, Y. Lu, Y. Zheng, and Z.-A. Xu, Front. Phys. **12**, 127205 (2017).

[68] D. Kharzeev, J. Liao, S. Voloshin, and G. Wang, Prog. Part. Nucl. Phys. **88**, 1 (2016).

[69] J. M. Margutti, *Rotating planes, fluctuating shapes: Anisotropic flow and magnetic fields in heavy-ion collisions*, Ph.D. thesis, Utrecht University, the Netherlands (2015).

[70] Y. Ferreiros and A. Cortijo, Phys. Rev. B **93**, 195154 (2016).

[71] S. Das Sarma and E. H. Hwang, Phys. Rev. Lett. **102**, 206412 (2009).

[72] S. S. Schweber, *QED and the men who made it: Dyson, Feynman, Schwinger, and Tomonaga* (Princeton University Press, 1994).

[73] B. Odom, D. Hanneke, B. D'Urso, and G. Gabrielse, Phys. Rev. Lett. **97**, 030801 (2006).

[74] J. Bardeen, L. N. Cooper, and J. R. Schrieffer, Phys. Rev. **108**, 1175 (1957).

[75] D. I. Pikulin, A. Chen, and M. Franz, Phys. Rev. X **6**, 041021 (2016).

[76] R. Ilan, A. G. Grushin, and D. I. Pikulin, arXiv preprint 1903.11088 (2019).

[77] H. Shapourian, T. L. Hughes, and S. Ryu, Phys. Rev. B **92**, 165131 (2015).

[78] J. Behrends, S. Roy, M. H. Kolodrubetz, J. H. Bardarson, and A. G. Grushin, Phys. Rev. B **99**, 140201 (2019).

[79] N. Levy, S. Burke, K. Meaker, M. Panlasigui, A. Zettl, F. Guinea, A. C. Neto, and M. Crommie, Science **329**, 544 (2010).

[80] H. B. Nielsen and M. Ninomiya, Phys. Lett. B **130**, 389 (1983).

[81] D. Kharzeev, Phys. Lett. B **633**, 260 (2006).

[82] L. Lu, Z. Wang, D. Ye, L. Ran, L. Fu, J. D. Joannopoulos, and M. Soljai, Science **349**, 622 (2015).

[83] S. L. Adler, Phys. Rev. **177**, 2426 (1969).

[84] J. S. Bell and R. Jackiw, Il Nuovo Cimento A (1965-1970) **60**, 47 (1969).

[85] J. Behrends, A. G. Grushin, T. Ojanen, and J. H. Bardarson, Phys. Rev. B **93**, 075114 (2016).

[86] Q. Li, D. E. Kharzeev, C. Zhang, Y. Huang, I. Pletikosić, A. Fedorov, R. Zhong, J. Schneeloch, G. Gu, and T. Valla, Nat. Phys. **12**, 550 (2016).

[87] C.-l. Zhang, S.-y. Xu, I. Belopolski, Z. Yuan, Z. Lin, B. Tong, G. Bian, N. Alidoust, C.-c. Lee, S.-m. Huang, *et al.*, Nat. Commun. **7**, 10735 (2016).

[88] M. O. Goerbig, J.-N. Fuchs, G. Montambaux, and F. Pichon, Phys. Rev. B **78**, 045415 (2008).

[89] M. Trescher, B. Sbierski, P. W. Brouwer, and E. J. Bergholtz, Phys. Rev. B **91**, 115135 (2015).

[90] A. A. Soluyanov, D. Gresch, Z. Wang, Q. Wu, M. Troyer, X. Dai, and B. A. Bernevig, Nature **527**, 495 (2015).

[91] S. Tchoumakov, M. Civelli, and M. O. Goerbig, Phys. Rev. Lett. **117**, 086402 (2016).

[92] Y. Xu, F. Zhang, and C. Zhang, Phys. Rev. Lett. **115**, 265304 (2015).

[93] M. Trescher, B. Sbierski, P. W. Brouwer, and E. J. Bergholtz, Phys. Rev. B **95**, 045139 (2017).

[94] T. S. Sikkenk and L. Fritz, Phys. Rev. B **96**, 155121 (2017).

[95] Y. Chen, S. Wu, and A. A. Burkov, Phys. Rev. B **88**, 125105 (2013).

[96] M.-C. Chang and M.-F. Yang, Phys. Rev. B **91**, 115203 (2015).

[97] S. Zhong, J. E. Moore, and I. Souza, Phys. Rev. Lett. **116**, 077201 (2016).

[98] J. Ma and D. A. Pesin, Phys. Rev. B **92**, 235205 (2015).

[99] M. M. Vazifeh and M. Franz, Phys. Rev. Lett. **111**, 027201 (2013).

[100] Y. V. Nazarov, Zh. Eksp. Teor. Fiz. **91**, 332 (1986).

[101] F. Detassis, L. Fritz, and S. Grubinskas, Phys. Rev. B **96**, 195157 (2017).

[102] D. E. Kharzeev and H. J. Warringa, Phys. Rev. D **80**, 034028 (2009).

[103] J. Steiner, A. Andreev, and D. Pesin, Phys. Rev. Lett. **119**, 036601 (2017).

[104] S. P. Mukherjee and J. P. Carbotte, Phys. Rev. B **96**, 085114 (2017).

[105] A. A. Zyuzin and R. P. Tiwari, JETP Lett. **103**, 717 (2016).

[106] Y. Alavirad and J. D. Sau, Phys. Rev. B **94**, 115160 (2016).

[107] G. Baar, D. E. Kharzeev, and H.-U. Yee, Phys. Rev. B **89**, 035142 (2014).

[108] D. E. Kharzeev, Y. Kikuchi, and R. Meyer, Eur. Phys. J. B **91**, 83 (2018).

[109] K. Landsteiner, Phys. Rev. B **89**, 075124 (2014).

[110] N. Yamamoto, Phys. Rev. D **92**, 085011 (2015).

[111] H. T. Stoof, K. B. Gubbels, and D. B. Dickerscheid, *Ultracold quantum fields*, Vol. 1 (Springer, 2009).

[112] Z. Wang, D. Gresch, A. A. Soluyanov, W. Xie, S. Kushwaha, X. Dai, M. Troyer, R. J. Cava, and B. A. Bernevig, Phys. Rev. Lett. **117**, 056805 (2016).

[113] J. P. Carbotte, Phys. Rev. B **94**, 165111 (2016).

[114] K. Das and A. Agarwal, Phys. Rev. B **99**, 085405 (2019).

[115] O. Pozo, Y. Ferreiros, and M. A. H. Vozmediano, Phys. Rev. B **98**, 115122 (2018).

[116] S. Tchoumakov, M. Civelli, and M. O. Goerbig, Phys. Rev. B **95**, 125306 (2017).

[117] Y. Ferreiros, A. A. Zyuzin, and J. H. Bardarson, Phys. Rev. B **96**, 115202 (2017).

[118] S. Kaushik, D. E. Kharzeev, and E. J. Philip, Phys. Rev. B **99**, 075150 (2019).

[119] A. Cortijo, D. Kharzeev, K. Landsteiner, and M. A. H. Vozmediano, Phys. Rev. B **94**, 241405 (2016).

[120] K. Landsteiner, E. Megías, and F. Pena-Benitez, Phys. Rev. Lett. **107**, 021601 (2011).

[121] A. Berdyugin, S. Xu, F. Pellegrino, R. K. Kumar, A. Principi, I. Torre, M. B. Shalom, T. Taniguchi, K. Watanabe, I. Grigorieva, *et al.*, Science **364**, 162 (2019).

[122] A. Vilenkin, Phys. Lett. B **80**, 150 (1978).

[123] A. Vilenkin, Phys. Rev. D **20**, 1807 (1979).

[124] K. Landsteiner, E. Megías, and F. Peña-Benitez, "Anomalous transport from kubo formulae," in *Strongly Interacting Matter in Magnetic Fields* (Springer, Berlin, Heidelberg, 2013).

[125] M. N. Chernodub, A. Cortijo, A. G. Grushin, K. Landsteiner, and M. A. H. Vozmediano, Phys. Rev. B **89**, 081407 (2014).

[126] P. Goswami and S. Tewari, Phys. Rev. B **88**, 245107 (2013).

[127] R. Lundgren, P. Laurell, and G. A. Fiete, Phys. Rev. B **90**, 165115 (2014).

[128] E. V. Gorbar, V. A. Miransky, I. A. Shovkovy, and P. O. Sukhachov, Phys. Rev. B **96**, 155138 (2017).

[129] S. P. Mukherjee and J. P. Carbotte, J. Phys. Condens. Matter **30**, 115702 (2018).

[130] G. Sharma, P. Goswami, and S. Tewari, Phys. Rev. B **93**, 035116 (2016).

[131] G. Sharma, C. Moore, S. Saha, and S. Tewari, Phys. Rev. B **96**, 195119 (2017).

[132] S. Saha and S. Tewari, Eur. Phys. J. B Condens. Matter **91**, 4 (2018).

[133] D. Xiao, Y. Yao, Z. Fang, and Q. Niu, Phys. Rev. Lett. **97**, 026603 (2006).

[134] N. R. Cooper, B. I. Halperin, and I. M. Ruzin, Phys. Rev. B **55**, 2344 (1997).

[135] C.-L. Zhang, S.-Y. Xu, C. Wang, Z. Lin, Z. Du, C. Guo, C.-C. Lee, H. Lu, Y. Feng, S.-M. Huang, *et al.*, Nat. Phys. **13**, 979 (2017).

[136] J. M. Luttinger, Phys. Rev. **135**, A1505 (1964).

[137] C. P. Herzog, J. Phys. A-Math. Theor. **42**, 343001 (2009).

[138] G. D. Mahan, *Many-particle physics* (Springer Science & Business Media, 2013).

[139] D. E. Kharzeev and H.-U. Yee, Phys. Rev. D **83**, 085007 (2011).

[140] L. Adamczyk et al. (STAR Collaboration), Phys. Rev. Lett. **114**, 252302 (2015).

[141] E. V. Gorbar, V. A. Miransky, I. A. Shovkovy, and P. O. Sukhachov, Phys. Rev. B **95**, 115202 (2017).

[142] E. V. Gorbar, V. A. Miransky, I. A. Shovkovy, and P. O. Sukhachov, Phys. Rev. B **95**, 205141 (2017).

[143] D. O. Rybalka, E. V. Gorbar, and I. A. Shovkovy, Phys. Rev. D **99**, 016017 (2019).

[144] K. Landsteiner, E. Megías, and F. Peña Benítez, Phys. Rev. D **90**, 065026 (2014).

[145] J.-Y. Chen, D. T. Son, M. A. Stephanov, H.-U. Yee, and Y. Yin, Phys. Rev. Lett. **113**, 182302 (2014).

[146] T. Thonhauser, Int. J. Mod. Phys. A **25**, 1429 (2011).

[147] G. Sundaram and Q. Niu, Phys. Rev. B **59**, 14915 (1999).

[148] W. Gerlach and O. Stern, Z. Phys. **9**, 349 (1922).

[149] E. Schrödinger, Phys. Rev. **28**, 1049 (1926).

[150] W. Pauli, Z. Phys. **43**, 601 (1927).

[151] D. E. Nagle, R. S. Julian, and J. R. Zacharias, Phys. Rev. **72**, 971 (1947).

[152] J. E. Nafe, E. B. Nelson, and I. I. Rabi, Phys. Rev. **71**, 914 (1947).

[153] J. Schwinger, Phys. Rev. **73**, 416 (1948).

[154] E. J. Ferrer and V. de la Incera, Nucl. Phys. B **824**, 217 (2010).

[155] Z. K. Liu, B. Zhou, Y. Zhang, Z. J. Wang, H. M. Weng, D. Prabhakaran, S.-K. Mo, Z. X. Shen, Z. Fang, X. Dai, Z. Hussain, and Y. L. Chen, Science **343**, 864 (2014).

[156] M. Neupane, S.-Y. Xu, R. Sankar, N. Alidoust, G. Bian, C. Liu, I. Belopolski, T.-R. Chang, H.-T. Jeng, H. Lin, A. Bansil, F. Chou, and M. Z. Hasan, Nat. Commun. **5**, 4786 (2014).

[157] S. Borisenko, Q. Gibson, D. Evtushinsky, V. Zabolotnyy, B. Büchner, and R. J. Cava, Phys. Rev. Lett. **113**, 027603 (2014).

[158] Z. K. Liu, J. Jiang, B. Zhou, Z. J. Wang, Y. Zhang, H. M. Weng, D. Prabhakaran, S.-K. Mo, H. Peng, P. Dudin, T. Kim, M. Hoesch, Z. Fang, X. Dai, Z. X. Shen, D. L. Feng, Z. Hussain, and Y. L. Chen, Nat. Mater. **13**, 677 (2014).

[159] S. Jeon, B. B. Zhou, A. Gyenis, B. E. Feldman, I. Kimchi, A. C. Potter, Q. D. Gibson, R. J. Cava, A. Vishwanath, and A. Yazdani, Nat. Mater. **13**, 851 (2014).

[160] P. Hosur, S. A. Parameswaran, and A. Vishwanath, Phys. Rev. Lett. **108**, 046602 (2012).

[161] W. Witczak-Krempa, M. Knap, and D. Abanin, Phys. Rev. Lett. **113**, 136402 (2014).

[162] A. Sekine and K. Nomura, J. Phys. Conf. Ser. **603**, 012017 (2015).

[163] J. González, Phys. Rev. B **92**, 125115 (2015).

[164] J. González, J. High Energy Phys. **2015**, 190 (2015).

[165] S. Das Sarma, E. H. Hwang, and H. Min, Phys. Rev. B **91**, 035201 (2015).

[166] J. Hofmann and S. Das Sarma, Phys. Rev. B **91**, 241108 (2015).

[167] J. Zhou, H.-R. Chang, and D. Xiao, Phys. Rev. B **91**, 035114 (2015).

[168] I. Panfilov, A. A. Burkov, and D. A. Pesin, Phys. Rev. B **89**, 245103 (2014).

[169] A. Thakur, R. Sachdeva, and A. Agarwal, J. Phys. Condens. Matter **29**, 105701 (2017).

[170] J. Hofmann, E. Barnes, and S. Das Sarma, Phys. Rev. B **92**, 045104 (2015).

[171] R. E. Throckmorton, J. Hofmann, E. Barnes, and S. Das Sarma, Phys. Rev. B **92**, 115101 (2015).

[172] V. P. J. Jacobs, P. Betzios, U. Gürsoy, and H. T. C. Stoof, Phys. Rev. B **93**, 195104 (2016).

[173] A. A. Zyuzin and V. A. Zyuzin, Phys. Rev. B **92**, 115310 (2015).

[174] G. Bihlmayer, Y. Koroteev, P. Echenique, E. Chulkov, and S. Blgel, Surf. Sci. **600**, 3888 (2006).

[175] S. Kourtis, J. Li, Z. Wang, A. Yazdani, and B. A. Bernevig, Phys. Rev. B **93**, 041109 (2016).

[176] A. K. Mitchell and L. Fritz, Phys. Rev. B **93**, 035137 (2016).

[177] G. Chang, S.-Y. Xu, H. Zheng, C.-C. Lee, S.-M. Huang, I. Belopolski, D. S. Sanchez, G. Bian, N. Alidoust, T.-R. Chang, C.-H. Hsu, H.-T. Jeng, A. Bansil, H. Lin, and M. Z. Hasan, Phys. Rev. Lett. **116**, 066601 (2016).

[178] B. I. Lundqvist, Phys. Kond. Mater. **6**, 193 (1967).

[179] L. Hedin, B. I. Lundqvist, and S. Lundqvist, Solid State Comm. **5**, 237 (1967).

[180] V. V. Klimov, Sov. J. Nucl. Phys. **33**, 934 (1981).

[181] H. A. Weldon, Phys. Rev. D **40**, 2410 (1989).

[182] G. Baym, J.-P. Blaizot, and B. Svetitsky, Phys. Rev. D **46**, 4043 (1992).

[183] J.-P. Blaizot and J.-Y. Ollitrault, Phys. Rev. D **48**, 1390 (1993).

[184] C. Manuel, Phys. Rev. D **62**, 076009 (2000).

[185] M. Polini, R. Asgari, G. Borghi, Y. Barlas, T. Pereg-Barnea, and A. H. MacDonald, Phys. Rev. B **77**, 081411 (2008).

[186] R. Sensarma, E. H. Hwang, and S. Das Sarma, Phys. Rev. B **84**, 041408 (2011).

[187] J. P. F. LeBlanc, J. P. Carbotte, and E. J. Nicol, Phys. Rev. B **84**, 165448 (2011).

[188] J. P. F. LeBlanc, J. Hwang, and J. P. Carbotte, Phys. Rev. B **85**, 115126 (2012).

[189] P. Chudzinski and T. Giamarchi, Phys. Rev. B **84**, 125105 (2011).

[190] A. Bostwick, F. Speck, T. Seyller, K. Horn, M. Polini, R. Asgari, A. H. MacDonald, and E. Rotenberg, Science **328**, 999 (2010).

[191] R. Tediosi, N. P. Armitage, E. Giannini, and D. van der Marel, Phys. Rev. Lett. **99**, 016406 (2007).

[192] N. Sadooghi and F. Taghinavaz, Phys. Rev. D **89**, 125005 (2014).

[193] H. A. Weldon, Phys. Rev. D **26**, 2789 (1982).

[194] V. N. Kotov, B. Uchoa, V. M. Pereira, F. Guinea, and A. H. Castro Neto, Rev. Mod. Phys. **84**, 1067 (2012).

[195] V. Kozii and L. Fu, Phys. Rev. B **98**, 041109 (2018).

[196] A. Cortijo, Y. Ferreirós, K. Landsteiner, and M. A. H. Vozmediano, Phys. Rev. Lett. **115**, 177202 (2015).

[197] B. Vanderheyden and J.-Y. Ollitrault, Phys. Rev. D **56**, 5108 (1997).

[198] M. Le Bellac and C. Manuel, Phys. Rev. D **55**, 3215 (1997).

[199] L. D. Landau, E. M. Lifshitz, V. Berestetskii, and L. Pitaevskii, *Course of Theoretical Physics: Theory of Elasticity* (1995).

[200] V. Arjona and M. A. H. Vozmediano, Phys. Rev. B **97**, 201404 (2018).

[201] M. Le Bellac, *Thermal field theory* (Cambridge University Press, 2000).

[202] A. A. Abrikosov, L. P. Gorkov, and I. E. Dzyaloshinski, *Methods of quantum field theory in statistical physics* (Courier Corporation, 2012).

[203] M. V. Sadovskii, *Diagrammatics: lectures on selected problems in condensed matter theory* (World Scientific, 2006).

[204] J. M. Luttinger, Phys. Rev. **121**, 942 (1961).

[205] B. Roy, J. D. Sau, and S. Das Sarma, Phys. Rev. B **89**, 165119 (2014).

[206] J.-P. Blaizot and E. Iancu, Nucl. Phys. B **390**, 589 (1993).

[207] J.-P. Blaizot and E. Iancu, Phys. Rev. Lett. **70**, 3376 (1993).

Nederlandse samenvatting

Dit hoofdstuk is bedoeld om vrienden, familie en andere geïnteresseerden die niet zo vertrouwd zijn met de theoretische natuurkunde, een idee te geven waar dit proefschrift over gaat. Bij het bladeren door dit proefschrift kan het de lezer niet ontgaan zijn dat er behoorlijk wat wiskundige vergelijkingen in staan. Dit is inherent aan de theoretische natuurkunde. Het doel van deze tak van de natuurwetenschappen is namelijk verschijnselen die we waarnemen in de wereld om ons heen in een wiskundig jasje te gieten en zo beter te begrijpen. Voorbeelden van het brede scala aan vragen die (theoretisch) natuurkundigen zichzelf stellen zijn: *"Waarom geleidt koper wel stroom en plastic niet?"* en *"Hoe is ons heelal ontstaan?"*. Het beantwoorden van zulke vragen gebeurt in samenwerking met collega's uit de experimentele natuurkunde. Soms wordt er een theorie opgesteld die vooruitloopt op de experimenten van vandaag de dag en soms wordt er iets onverwachts gemeten waarvoor een wiskundig model dient te worden opgesteld. Beide routes dragen bij aan de ontwikkeling van de natuurkunde.

Dit proefschrift is van een theoretische aard en draagt een steentje bij aan het begrip van een speciaal soort materialen genaamd *Weyl halfmetalen*. Dit zijn materialen waarin de elektronen zich anders gedragen dan in normale metalen. Hierdoor hebben ze bijzondere (en nuttige) eigenschappen. Zo kan een magneetveld bijvoorbeeld een verliesloze stroom opwekken in een Weyl halfmetaal. Dit is een heel gunstige materiaaleigenschap voor technologische toepassingen. Om beter te begrijpen waarom een Weyl halfmetaal zulke bijzondere eigenschappen heeft, beginnen we met het beantwoorden van een variant van de eerste vraag die we hierboven hebben gesteld: wat maakt een stuk koper en een stuk plastic zo verschillend?

Alles is gemaakt van ...

Om te begrijpen waarin koper en plastic verschillen, helpt het om eerst te begrijpen waarin ze juist wél op elkaar lijken. De beroemde Amerikaanse

natuurkundige Richard Feynman schreef ooit dat als, door een catastrofale gebeurtenis, alle wetenschappelijke kennis zou worden vernietigd, hij de volgende boodschap zou doorgeven aan de volgende generatie: "*Alles is gemaakt van atomen - kleine deeltjes die eeuwig in beweging zijn en elkaar aantrekken wanneer ze zich een kleine afstand uit elkaar bevinden, maar elkaar afstoten wanneer ze op elkaar geperst worden.*".[a] De overeenkomst tussen koper en plastic is dus dat beide materialen uit atomen zijn opgebouwd: koper uit koperatomen en plastic voornamelijk uit koolstof- en waterstofatomen.

Maar wat maakt dan het verschil tussen een koper- en, bijvoorbeeld, een koolstofatoom? Een atoom doet denken aan een miniatuur zonnestelsel waarin een piepkleine kern (de zon) wordt omcirkeld door negatief geladen *elektronen* (de planeten) in vaste banen, zoals is geïllustreerd in Figuur 1. De kern bestaat op zijn beurt uit positief geladen en neutrale deeltjes, genaamd *protonen* en *neutronen*. Het soort atoom wordt bepaald door het aantal protonen in de kern. Een koperatoom bevat bijvoorbeeld 29 protonen in de kern, terwijl koolstof er maar 6 herbergt.[b] Aangezien atomen elektrisch gezien neutraal zijn, bevatten ze evenveel elektronen als protonen.

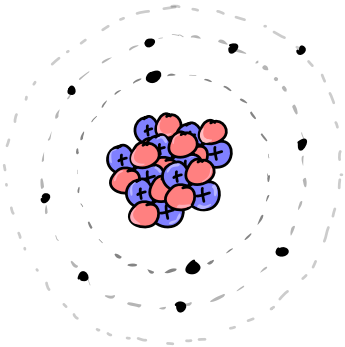

Fig. 1: Illustratie van een atoom, bestaande uit een kern van neutronen (rood) en protonen (blauw), die omcirkeld wordt door elektronen (zwart).

Een vaste stof zoals een stuk koper bestaat uit een gigantische hoeveelheid atomen die minutieus gerangschikt zijn in een zogenaamd *kristal*. Dergelijke kristallen kunnen allerlei symmetrieën tentoonstellen en variëren van kubisch in drie dimensies tot een honingraatpatroon in twee dimensies, zoals geïllustreerd is in Figuur 2(a) en (b). Het is belangrijk om je te realiseren dat de typische afstand tussen de atomen in een kristal ongeveer even groot is als één miljoenste van de dikte van een menselijke haar![c] Doordat de atomen

[a] Dit is een letterlijke vertaling van het Engelse citaat uit de inleiding in Hoofdstuk 1.

[b] Er bestaan vier zogenaamde koperisotopen en ook vier koolstofisotopen die verschillende aantallen neutronen bevatten. We beschrijven hier de meest voorkomende isotopen.

[c] Om preciezer te zijn: de afstand tussen de atomen in een kristal is typisch een halve nanometer, oftewel de helft van één duizendste van één miljoenste van een meter. De diameter van een menselijke haar ligt tussen de 0.02 en 0.2 millimeter.

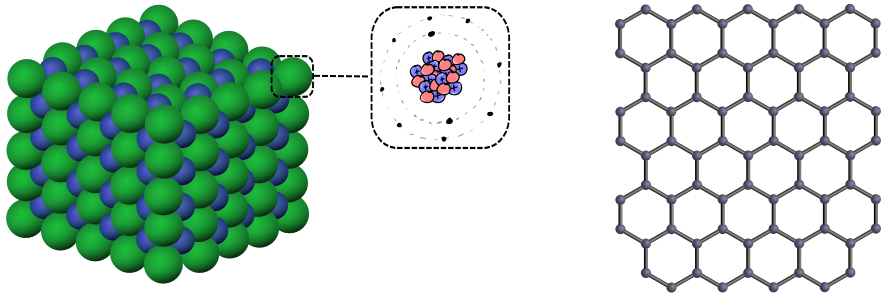

(a) (b)

Fig. 2: Voorbeelden van kristallen. (a) Driedimensionale kristalstructuur van tafelzout (NaCl). Groene bolletjes stellen chlooratomen voor en blauwe bolletjes natriumatomen. (b) Tweedimensionale kristalstructuur van koolstofatomen in een honingraatpatroon. De bolletjes stellen koolstofatomen voor en de balkjes chemische verbindingen.

zich zó dicht naast elkaar bevinden, gaan de banen van elektronen van verschillende atomen overlappen en ontstaat er een soort 'soep' van elektronen die niet meer tot slechts één atoom behoren.

Elektronensoep in een vaste stof

De eigenschappen van deze elektronensoep verschillen per materiaal en bepalen onder andere of een materiaal wel of niet stroom geleidt. Een stroom bestaat namelijk uit een hoop negatief geladen elektronen die zich door het materiaal voortbewegen. Dit wordt mogelijk gemaakt door het aansluiten van een batterij, die fungeert als een soort pomp van elektronen. Een normale batterij kan echter alleen de elektronen in een stuk metaal zoals koper rondpompen en niet in een isolator zoals plastic. Het kost namelijk veel meer energie om de elektronen in een isolator rond te pompen dan om hetzelfde te doen in een metaal. In het geval van een isolator is de vereiste energie zó hoog dat een normale batterij die energie niet kan leveren en het materiaal dus geen stroom geleidt.

De hoeveelheid energie die vereist is om een elektron in beweging te krijgen is geëncodeerd in de zogenaamde *bandenstructuur* van het materiaal. De bandenstructuur legt namelijk vast welke energieën de elektronen in een materiaal kunnen hebben en dus ook hoeveel energie er minimaal moet wor-

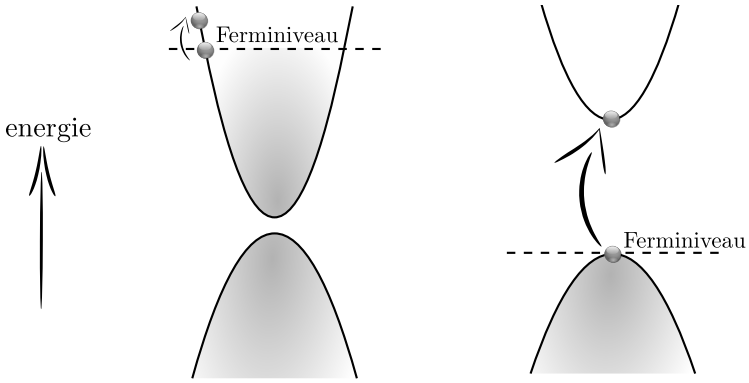

Fig. 3: Voorbeelden van bandenstructuren. De grijstint geeft aan welke energieën opgevuld zijn met elektronen. Witte gebieden binnen de dikke zwarte lijnen zijn gebieden waar elektronen zich mogen bevinden. (a) Vereenvoudigde bandenstructuur van een metaal als koper en van (b) een isolator als plastic. Voor een metaal kost het heel weinig energie (kleine pijl) om een elektron naar een hogere, toegestane energie te brengen (hetgeen nodig is om een stroom te laten lopen), terwijl het voor een isolator heel veel energie kost (grote pijl).

den toegevoegd (door een batterij) om een elektron deel te laten namen aan een stroom. De precieze vorm van een bandenstructuur is moeilijk om uit te rekenen, maar ze wordt uiteindelijk bepaald door twee dingen: het soort atomen waaruit het materiaal bestaat en het type kristal waarin de atomen zijn gerangschikt, waarvan we twee voorbeelden gaven in Figuur 2.

In Figuur 3 illustreren we heel schematisch waarin de bandenstructuur van een metaal en isolator verschillen. De dikke zwarte lijnen geven de gebieden aan waarbinnen elektronen zich mogen bevinden en grijskleurig gebieden zijn daadwerkelijk opgevuld met elektronen. De maximale energie waar zich nog een elektron bevindt, heet het *Ferminiveau*.[d] Als het Ferminiveau in een gedeeltelijk gevulde band ligt, zoals in Figuur 3(a) is weergegeven voor een metaal, dan kost het maar heel weinig energie (kleine pijl) om een elektron naar een leeg (wit) plekje te brengen. Zo'n energieverschil kan aangeleverd worden door een normale batterij en dus kan het material stroom geleiden. In het geval van een isolator is het minimale energieverschil om een elektron

[d] Genoemd naar en bedacht door de invloedrijke Italiaanse natuurkundige Enrico Fermi.

van het Ferminiveau naar een leeg plekje te brengen veel groter (grote pijl). Zo'n grote energie kan een batterij niet voorzien en dus zal een materiaal met zo'n bandenstructuur geen stroom geleiden.

Of een materiaal stroom geleidt, wordt dus bepaald door de vorm en opvulling van de bandenstructuur. Het is daarom van groot belang de bandenstructuur te weten om de eigenschappen van een materiaal te begrijpen. De hoofdrolspeler van dit proefschrift, het Weyl halfmetaal, heeft een speciaal type bandenstructuur. Dit leidt uiteindelijk tot bijzondere materiaaleigenschappen.

Weyl halfmetalen

Soms lijkt de bandenstructuur op twee kegels die elkaar in één punt raken, zoals geïllustreerd is in Figuur 4. Omdat de banden elkaar raken, is de eerstvolgende lege plek voor een elektron dichtbij, onafhankelijk van waar het Ferminiveau ligt. Als het Ferminiveau dichtbij het punt ligt waar de twee kegels elkaar raken, dan zijn er slechts weinig lege plekjes beschikbaar vlak boven het Ferminiveau omdat de kegel daar erg smal is. Het materiaal geleidt dan wel stroom, maar niet zo goed als een metaal. We spreken in dit geval van een *halfmetaal*.

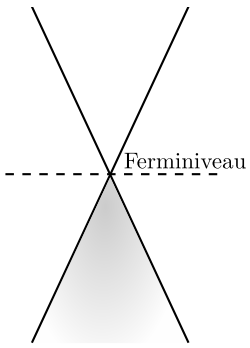

Fig. 4: Een halfmetaal met een kegelvormig bandenstructuur.

Het bekendste voorbeeld van een halfmetaal met kegelvormige bandenstructuur is *grafeen*. Dit materiaal bestaat uit een tweedimensionaal laagje koolstof in een honingraatpatroon, zoals weergegeven in Figuur 2(b). Grafeen werd voor het eerst geïsoleerd in 2004 en heeft een aantal bijzondere eigenschappen. Zo bewegen de elektronen erin zich uitzonderlijk snel voort. Daarnaast is het zó sterk dat een stukje grafeen van één vierkante meter niet zou breken onder de druk van een potlood met een balancerende olifant erbovenop![e]

Aangezien grafeen een tweedimensionaal materiaal is, is het niet altijd even bruikzaam. Gelukkig werd in 2015 experimenteel aangetoond dat het

[e] Voor een uitgebreide uitleg van deze bizarre uitspraak, zie het stuk *"Elephant Illustrates Important Point"* van Steve Mirsky in Scientific American (2011).

driedimensionale materiaal tantaalarsenide (TaAs) veel op grafeen lijkt. De bandenstructuur van dit materiaal is ook kegelvormig en we noemen een materiaal als tantaalarsenide een *Weyl halfmetaal*, naar de Duitse wiskundige Hermann Weyl.

Deze wiskundige heeft namelijk theoretisch laten zien dat elektron-achtige deeltjes zonder massa ook een kegelvormige bandenstructuur hebben. De elektronen in een Weyl halfmetaal hebben wel degelijk een massa, maar gedragen zich alleen alsof ze massaloos zijn. Het is precies deze effectieve massaloosheid van de elektronen die ervoor zorgt dat Weyl halfmetalen interessante eigenschappen hebben.

We gaan nu kort in op het onderzoek in dit proefschrift aan deze interessante eigenschappen.

Transporteigenschappen

In Hoofdstukken 2 en 3 bestuderen we hoe de elektronen in een Weyl halfmetaal met *gekantelde* kegels zich gedragen wanneer we externe verstoringen aanleggen. De verstoringen die we hebben onderzocht zijn het aanleggen van een voltage door een batterij, een magnetisch veld, temperatuurverschillen tussen de uiteindes van een stuk Weyl halfmetaal en ten slotte het roteren van zo'n stuk metaal.

Het blijkt dat al deze verstoringen leiden tot een bijzonder soort elektrische stroom die verliesloos is. Met verliesloos bedoelen we dat de elektronen geen energie verliezen terwijl ze door het materiaal stromen. Dit is in tegenstelling tot bijvoorbeeld een gloeilamp, waar een hoop energie verloren wordt door de elektronen, doordat de draad waardoor de stroom loopt, opwarmt. Het spreekt voor zich dat verliesloze stroom een aantrekkelijke materiaaleigenschap is voor technologische toepassingen, omdat het onnodig energieverlies voorkomt.

Een andere interessante eigenschap van Weyl halfmetalen is dat ze een stroom in de richting van het externe magneetveld mogelijk maken. Dit is opmerkelijk[f], omdat een magneetveld normaal gezien een stroom opwekt die loodrecht op zichzelf staat. Wanneer we bijvoorbeeld met behulp van een batterij een stroom door een koperen kabel laten lopen, wordt er een magneetveld gegenereerd dat circuleert rondom de kabel. Ook dit is een

[f] Ofwel onverwachts of 'anomaal', zoals we in de titel van dit proefschrift gebruiken.

interessante materiaaleigenschap die wellicht in de toekomst zal leiden tot nieuwe technologische toepassingen.

Interactie-effecten

In de eerste helft van dit proefschrift hebben we gekeken naar elektronen die niet wisselwerken. Dit doen ze in de praktijk wel: ze stoten elkaar af en kunnen botsen met de trillende atomen waaruit een kristal bestaat. In Hoofdstukken 4 en 5 hebben we deze zogenaamde interactie-effecten nader bestudeerd.

In Hoofdstuk 4 onderzoeken we wat er gebeurt als we meenemen dat de negatief geladen elektronen elkaar afstoten. In het bijzonder hebben we de invloed van deze interacties op het zogenaamde *magnetisch moment* uitgerekend. Dit magnetisch moment is grofweg een maat voor hoe hevig de elektronen reageren op een extern magneetveld. Uit onze berekeningen blijkt dat de bijdrage aan het magnetische moment door interacties in Weyl halfmetalen een stuk groter is dan in materialen met massieve elektronen.

Naast onderlinge interacties, kunnen de elektronen ook wisselwerken met de trillende atomen in een kristal. Naarmate de temperatuur hoger wordt, bewegen de atomen in een kristal namelijk steeds heftiger rond hun gemiddelde plek. Deze situatie lijkt op een voetbalwedstrijd in een groot stadion. Als de wedstrijd saai is (lage temperatuur), dan zitten de meeste supporters (atomen) braaf op hun stoeltje (roosterplek) en gebeurt er weinig. Wanneer de spanning van de wedstrijd echter oploopt (hogere temperatuur), dan worden de supporters onrustig en staan ze af en toe op uit hun stoeltje. Als de thuisspelende ploeg ten slotte een beslissend doelpunt maakt, dan kunnen de uitzinnige supporters besluiten om allemaal samen een 'wave' te doen.

Zo'n wave van trillende atomen in een kristal wordt een *fonon* genoemd. Een fonon beïnvloedt op zijn beurt de elektronen die zich door het kristal van atomen voortbewegen. In Hoofdstuk 5 laten we zien dat er een speciaal soort fononen bestaat in Weyl halfmetalen wanneer we het halfmetaal lichtelijk mechanisch vervormen. De onconventionele wisselwerking tussen dit speciale type fonon en de elektronen in een Weyl halfmetaal blijkt de eigenschappen van het halfmetaal te veranderen. De gevolgen hiervan kunnen wellicht in de toekomst experimenteel geobserveerd worden.

Tot slot

In deze Nederlandstalige samenvatting zijn we in de natuurkunde van materialen gedoken en hebben we uitgelegd wat dit proefschrift aan deze tak van sport heeft bijgedragen. Vaste materialen blijken te zijn opgebouwd uit periodiek gesorteerde atomen in een kristal. De bandenstructuur van de elektronen in zo'n kristal bepaalt hoe het materiaal reageert op externe verstoringen zoals het aanleggen van een voltage door middel van een batterij. Afhankelijk van de vorm en opvulling van de bandenstructuur geleidt een material wel (metaal) of geen (plastic) stroom.

Het onderzoek in dit proefschrift heeft zich gericht op materialen waarin de elektronen zich gedragen alsof ze massaloos zijn. Dit blijkt te leiden tot interessante eigenschappen met potentieel nuttige toepassingen, zoals verliesloze stroom en de mogelijkheid om een stroom parallel aan een magneetveld te laten lopen. Misschien zitten onze smartphones over tien jaar wel vol met Weyl halfmetalen! Maar voor het zo ver is, is er wel nog wat meer onderzoek nodig.

Acknowledgments

With the completion of this thesis, my time as a researcher in theoretical physics has come to a definite end. Over the past few years, I have spent a lot of time working alone, but finishing this thesis would not have been possible without the support of a lot of different people in their own unique ways. The following people played a particularly important role.

- ◇ Allereerst natuurlijk mijn begeleider **Henk**, die me de kans heeft gegeven om een promotietraject te starten. Je fysische intuïtie, betrokkenheid én vastberadenheid zijn ongeëvenaard. Iedere keer als we weer eens vastzaten, kon ik erop vertrouwen dat je de volgende dag met een nieuwe invalshoek kwam aanzetten. Ik heb veel van je geleerd, zowel op natuurkundig als op persoonlijk vlak. Bedankt voor een mooie tijd!

- ◇ **Alberto**, muchas gracias por estar abierto a empezar una colaboración, y tu hospitalidad en Madrid. Me gustaron mucho nuestras discusiones científicas, con las que me has dado una nueva perspectiva de cosas que pensaba que ya había entendido.

- ◇ My colleagues at the Institute for Theoretical Physics were instrumental in creating a wonderful working environment. It is a common misconception that all physicists are solely interested in science. Our animated, and sometimes heated, lunch discussions on a myriad of topics are a testament to this. Honorable mentions go out to **Rembert**, **Arie-Willem**, **Mathijs**, **Watse**, **Bram**, **Guido**, **Scott**, **Benedikt**, **Tycho**, **Stefano**, **Etienne**, **Camilo**, the **Sanders**, **Raffaele** and **Niccolò**. I also enjoyed the excellent questions posed by **Richard**, **Thijs** and **Casper**, who wrote their master thesis under the supervision of Henk and me.

- ◇ De pentbois wil ik bedanken voor het accepteren van een vreemde eend in de bijt. Specifieker bedank ik **Max** voor het zijn van mijn paranimf, twaalf jaar vriendschap en het altijd vinden van een goed

feestje, **Marco** voor het aanprijzen van de kunst van het "gewoon even normaal doen" en het voorzien van een broodnodige nuchtere kijk op de wereld, **Joram** voor het altijd stellen van de juiste vraag en het delen van promoveerleed, en tenslotte **Tom** en **Oskar** voor de gezelligheid, wandelingen en luisterende oren. In de categorie goede vrienden verdient ook **Koen** een expliciete vermelding; er zijn weinig mensen met wie ik over werkelijk álles een goed gesprek kan voeren. Tenslotte is daar **Nick**, bedankt voor het zijn van mijn paranimf en het delen van bijna tien jaar natuurkunde en vriendschap, dat ons samen van Eindhoven naar Utrecht bracht.

◇ All the wonderful housemates I have had in the Lordsroad flat over the years contributed to a house that I enjoyed coming home to and where I always felt at ease. Vooral **Bastiaan**, **Gert** en **Lisette** ben ik dankbaar voor vier jaar plezierig samenwonen en het delen van lief en leed. Ook ben ik Bastiaan dankbaar voor zijn hulp bij het ontwerpen van de omslag van dit proefschrift.

◇ De leden van tafeltennisvereniging SVE dank ik voor het faciliteren van een sportieve, doch zeker niet gezonde, maar wel zeer gezellige vrijetijdsbesteding. Ook heeft lid zijn van een tafeltennisteam dat uit maar liefst vier generaties bestaat me de afgelopen seizoenen veel plezier gedaan.

◇ Mien pap en mam **Frans** en **Marleen**, en mien broor **Bart** en zuster **Inge**, wèl iech bedaanke veur unne fiene, zörgeloeze jäög en netuurlek veur 't op peil hawwe vaan mie Mestreechs. Ouch bin iech behuurlek content mèt euze recentere aonwinste **Rianne** en **Saar**. Tenslotte vin iech 't verrèks zun dat miene opa **Marinus** en mien omi **Tita** neet bij dit belaankrieke momint höbbe mage zien.

◇ Finally, for discovering tasty sea creatures with me, tantalizing my taste buds with Bolivian dishes, always questioning my implicit assumptions, providing me with fresh perspectives, pushing me out of my comfort zone when necessary, supporting me when I felt overwhelmed and for making my life all the more fun, I thank **Lucía**. I am excited to see what the future holds for us.

About the author

Erik van der Wurff was born on August 23rd, 1991 in Maastricht, the Netherlands. He obtained his high-school gymnasium diploma *cum laude* at the Porta Mosana College in Maastricht in 2009, specializing in the natural sciences with the extra subject French. In that same year, he started with a bachelor in applied physics at Eindhoven University of Technology. During the third year of his bachelor he followed a minor in theoretical physics and did research on the self-assembly of biological viruses. In 2012 he successfully completed his bachelor with a thesis on Rydberg crystals in ultracold gases.

In the same year, he enrolled in the master's program in theoretical physics at Utrecht University. He obtained his master's degree *cum laude* in 2014 with a thesis on Bose-Einstein condensates of photons, written under the supervision of prof. dr. ir. Henk Stoof. For his thesis, he received the national Lorentz prize for theoretical physics and the prize for best master thesis in the department of physics at Utrecht University.

Following his master's, he was visiting researcher for half a year at the Max Planck Institute for Complex Systems in Dresden, Germany. Afterwards he returned to Utrecht University as a PhD candidate under the supervision of prof. dr. ir. Henk Stoof at the Institute for Theoretical Physics. The results of the research are presented in this thesis. During his time as a PhD candidate, he was referee for the journal *Physica A* and visting scientist at the Instituto de Ciencia de Materiales in Madrid, Spain. Next to that, he was PhD representative in the Board of Studies of the Graduate School of Natural Sciences, co-supervised four master theses and he was teaching assistant to several master and bachelor courses.

In his spare time Erik enjoys doing sports, especially running and playing table tennis. In addition, he likes to spend time reading books with topics ranging from fiction to economics and history.